LBNL-39779
UC-419

ERNEST ORLANDO LAWRENCE
BERKELEY NATIONAL LABORATORY

Heavy Ion Beam Propagation Through a Gas-Filled Chamber for Inertial Confinement Fusion

RECEIVED
MAR 25 1997
OSTI

Nigel Oswald Barboza
Accelerator and Fusion Research Division

October 1996
Ph.D. Thesis

LBNL-39779
UC-419

Heavy Ion Beam Propagation Through a Gas-Filled Chamber for Inertial Confinement Fusion

Nigel Oswald Barboza
Ph.D. Thesis

Department of Nuclear Engineering
University of California, Berkeley

and

Accelerator and Fusion Research Division
Ernest Orlando Lawrence Berkeley National Laboratory
University of California
Berkeley, CA 94720

October 1996

This work was supported by the U.S. Department of Energy under Contract No. DE-AC03-76SF00098.

Heavy Ion Beam Propagation Through a Gas-Filled Chamber for Inertial Confinement Fusion

by

Nigel Oswald Barboza

B.S. (University of California, Berkeley) 1987

A dissertation submitted in partial satisfaction of the

requirements for the degree of

Doctor of Philosophy

in

Engineering - Nuclear Engineering

in the

GRADUATE DIVISION

of the

UNIVERSITY of CALIFORNIA, BERKELEY

Committee in charge:

T. Kenneth Fowler (Chair)
Edward P. Lee
Charles K. Birdsall

1996

Heavy Ion Beam Propagation Through a Gas-Filled Chamber
for Inertial Confinement Fusion

by

Nigel Oswald Barboza

Abstract

Heavy Ion Beam Propagation in a Gas-Filled Chamber for Inertial Confinement Fusion*

by

Nigel Oswald Barboza

Doctor of Philosophy in Nuclear Engineering

University of California, Berkeley

Professor T. K. Fowler, Chair

The work presented here evaluates the dynamics of a beam of heavy ions propagating through a chamber filled with gas. The motivation for this research stems from the possibility of using heavy ion beams as a driver in inertial confinement fusion reactors for the purpose of generating electricity. Such a study is important in determining the constraints on the beam which limit its focus to the small radius necessary for the ignition of thermonuclear microexplosions which are the source of fusion energy.

Nuclear fusion is the process of combining light nuclei to form heavier ones. One possible fusion reaction combines two isotopes of hydrogen, deuterium and tritium, to form an alpha particle and a neutron, with an accompanying release of $\sim 17.6\,MeV$ of energy. Generating electricity from fusion requires that we create such reactions in an efficient and controlled fashion, and harness the resulting energy. In the inertial confinement fusion (ICF) approach to energy production, a small spherical target, a few millimeters in radius, of deuterium and tritium fuel is compressed so that the density and temperature of the fuel are high enough, $\sim 200\,g/cm^3$ and $\sim 20\,keV$, that

---

* This work was supported by the Director, Office of Energy Research, Office of Fusion Energy, U.S. Department of Energy, under Contract No. DE-AC03-76SF00098

a substantial number of fusion reactions occur; the pellet microexplosion typically releases $\sim 350\,MJ$ of energy in optimized power plant scenarios.

In order to compress and heat the pellet, some current ICF power plant designs call for using high energy, $\sim 10\,GeV$, heavy ion, $\sim 200\,amu$, beams to ablate, either directly or indirectly, by generating x-rays, the outside layer of the fuel pellet, thus causing it to compress via a rocket-like action. The heavy ion beams are focused into a fusion chamber, a few meters in radius, at the target located in its center. In the "liquid-wall" type of chamber, exposed liquid flows, consisting of liquid lithium or lithium compounds, surround the central region within the chamber where the subsequent microexplosion of the pellet occurs. The resultant energy from this explosion heats and partially vaporizes the liquid which is then used to generate steam for driving conventional electric generators. This process is repeated approximately ten times a second for a $\sim 1000\,MW_e$ power plant.

The heavy ion beams must be focused to a small spot-size radius on target; $\sim 2\,mm$ for some target designs. The final beam focusing elements can only be placed outside the chamber, $\sim 5\,m$ away from the target, or they will be damaged by neutrons from the microexplosion. Immediately after the explosion, the background gas density in the chamber can reach as high as $\sim 10^{18}$ molecules per cm^{-3}. Because the time between subsequent shots is on the order of a tenth of a second, it may not be possible, without employing various mechanisms such as cold liquid sprays, to lower the density to $\sim 10^{13}\,cm^{-3}$, essentially vacuum, needed for beam propagation under conservative assumptions. The ability to focus the beam in higher density gas, therefore, has considerable advantages, in that it eases this stringent requirement on the chamber recovery to substantially reduce the background gas density, leading to simplified reactor designs. It also allows for operation at higher temperatures, improving the thermodynamic efficiencies of the plant. In this thesis we examine the propagation of a beam through vapor densities of $\sim 10^{14}$ to 10^{15} molecules per cm^3 of both lithium and Flibe, a molten salt mixture of LiF and BeF_2. The focal spot radius of the beam is expected to be strongly influenced by collisions of the beam ions with the background gas. The predominant collision processes are beam stripping, where the charge state of the beam ions increases due to the loss of electrons, and ionization of the background gas. These processes can significantly alter and amplify the electrodynamic interaction of the beam ions with the collective electromagnetic field of the combined beam-plasma system.

The collisions of the beam ions with the background gas result in a highly random distribution of beam charge states and complicated plasma phenomena, making analytic methods inadequate for qualitatively describing the dynamics of the beam. We have therefore developed a new computer code, BTRAC, consisting of a fully electromagnetic $2\frac{1}{2}$D particle-in-cell (PIC) simulation coupled to a Monte Carlo collision (MCC) model. The PIC code simulates the complete dynamics of the interaction of the various charged particle species: beam ions, electrons and background gas ions, with the self-generated fields; while the MCC code follows the collisions between the beam ions and the background gas atoms. The cross sections for stripping the beam ions and for ionizing the background gas were calculated using systematic semi-empirical corrections to the classical Bohr formula based on the Bethe quantum mechanical results for fast atomic collisions.

The BTRAC simulation of a $4.3\,kA$ beam of $10\,GeV$, Hg^+ ions focused by a typical final focus system achieves the requisite spot radius of $\sim 2.1\,mm$ on target in a vacuum. For propagation through Flibe background gas with densities in the range of $\sim 10^{14}$ to 10^{15} molecules per cm^3, the same beam achieves spot radii of a few cm: from $\sim 3.1\,cm$ in $2\times10^{14}\,cm^{-3}$ density gas, to $\sim 5.5\,cm$ in $1\times10^{15}\,cm^{-3}$ gas. The heavy fluorine atoms in the vapor cause the beam to strip substantially, to average charge-states of ~ 11.4 to ~ 20. These highly stripped beam ions greatly ionize the background gas leading to gas ion charge densities in the vicinity of the beam that are comparable to that of the beam. In undertaking this study, it was initially hoped that the electrons generated from both these processes, stripping and ionization, would be confined within the beam and adequately neutralize the net charge, thereby reducing the repulsive electric forces that tend to defocus the beam. However, it was discovered that a substantial fraction of the electrons gain transverse kinetic energies that are comparable to or larger than the potential "well" of the beam. These electrons are not adequately confined by the beam and therefore cannot contribute effectively to its neutralization. However, there exists a central "core" of the beam within which the electrons are better confined, leading to a higher degree of neutralization and better focusing that the rest of the beam. Indeed the *rms* radius of the beam continues to decrease well past the point at which the edge radius reaches a "waist", and achieves a minimum of $\sim 1.7\,cm$ when the edge radius has expanded to $\sim 6.9\,cm$. Propagation through low-density, 1×10^{13} molecules per cm^3, Flibe background gas leads to average charge-states of ~ 1.7, and does allow the beam to focus to a spot radius of $\sim 8\,mm$, with a minimum *rms* radius of $\sim 2.2\,mm$. The beam also focuses to *mm* size spot-radii in high-density, $\sim 10^{14}$ to 10^{15} atoms per cm^3, lithium background gas: from $\sim 3.8\,mm$ in $2\times10^{14}\,cm^{-3}$ density gas, to $\sim 6.9\,mm$ in $\sim 1\times10^{15}\,cm^{-3}$ gas. Because lithium has a lower atomic number than fluorine, the stripping cross sections are generally an order of magnitude lower, leading to average charge-states of ~ 1.9 to ~ 4.

We therefore conclude that although conventional focusing and propagation of heavy ion beams through low-density, $\sim 10^{13}$ molecules per cm^3, Flibe background gas can achieve the *mm* size spot radii on target that are needed for heavy ion driven inertial confinement fusion, propagation through high-density Flibe, $\sim 10^{14}$ to 10^{15}

molecules per cm^3, where the beam ions become highly stripped, cannot. Perhaps some mechanism of injecting "cold" electrons into the beam to replenish the high-energy electrons lost during propagation could provide the necessary neutralization allowing the beam to focus in this high-density regime. Another possibility for high-density propagation is to use working fluids that contain atoms with low atomic numbers, such as liquid lithium. Ultimately, however, these various approaches to propagating a beam of heavy ions through background gas in a liquid-wall chamber of an inertial confinement fusion power plant must all be weighed with respect to the cost and safety of the power plant. For example allowing for higher density background gas in the chamber may lead to simpler chamber designs, but this must be weighed against the disadvantages of larger focal-spot radii, such as lower target gain, etc; and although using liquid-lithium instead of Flibe allows the beam to focus to smaller radii in higher background gas densities, lithium has several disadvantages when compared with Flibe, such as its fire hazard and large tritium inventory.

T. Kenneth Fowler

I dedicate this work to my parents,
whose love makes all things possible.

Contents

Figures

Tables

Acknowledgements

I wish to acknowledge the intellectual, emotional, and spiritual generosity of my family, friends, colleagues and teachers that has made my years at graduate school ones of constant discovery, full of the tears and laughter (mostly laughter) of life. Here then, in roughly biographical order, are words inadequate to express my heartfelt gratitude to them.

First and foremost I wish to thank my parents whose unconditional love for their children compelled them to uproot themselves from their homeland and undertake a journey in search of a better life. The sacrifices they made and continue to make serve as the torch that lights the path of my own journey. I also wish to thank my brothers, Ashley and Darren, and sister, Patricia, whose personal accomplishments have always been a source inspiration to me. Their constant support forms the bedrock of my life.

I shall always cherish the continual friendship of my co-conspirators in the Lincoln Times, Ramsen Betfarhad, Zue-Long (James) Wu, Bill Tsanakas, Winifred Lo, Daisy Khoo-Miyaki, and Mehdi Maghsoodnia — our discussions on the "metaphysics of politics" on several Berkeley steps were always, to say the least, interesting. But most especially I'd like to thank one of my earliest mentors and teachers, Eileen Kennedy-Brandt. Her devotion to her students, sense of humor and insight have challenged and inspired me to always try to live an examined and deliberate life.

I would also like to thank my friends and co-workers at IBM/ROLM Systems: Edith Feng and Susan Hubbard. Their faith in my abilities gave me the confidence to apply to graduate school, and they have continued to encourage me ever since.

My friends Lisa Gorman, Irum Shiekh, Julie Hayden and Nathan Martin, have been extremely supportive during my years in graduate school; ever-present to listen to me in both my happiness and despair. Our gourmet food and therapy sessions, which doubled as a reading club, were more than oases of fun and intellection, they were essential to my survival. I would also like to thank Anita Comelo, Tom Leininger, Abby Smuckler, Leanne Good — whose tips on "how to take a vacation while writing your thesis" will soon be published — Vicky Nacif de Brey and Chris Brey, and Michael Ames — whose generosity is not merely limited to the shirt on his back, but extends to the socks on his feet — for all their support through the years and for the fun times we've shared on our many trips together.

I'd also like to acknowledge my friends on the Student Leadership and Retreat Teams at Newman Hall, Tina Ialongo, Joe Morris, Alan Segui, Lucely Escamilla, Chad Paavola, and Gisèle Giorgi — our animated conversations often challenged me to be much more emotionally honest with myself. I thank them for inspiring and allowing me to explore the spiritual dimensions of my being and to grow in my relationship with God. I'd especially like to thank Father Frank Sabatté for welcoming me to the Newman "family" and encouraging me to give more than I thought I could; I always received much more in return. I also wish to thank Greta Rosenberger, whose spiritually uplifting conversations were the life-lines that literally carried me through many a week; and Heather Janes and Erica Padilla, who, in sharing of themselves, helped me define myself.

I also wish to express my gratitude to my friends and fellow-students at the University, my office-mate, Caron Jantzen, for putting-up with my often childish antics and shenanigans these past three years and for making the long hours spent in front of my computer screen far more bearable than they should have been, Micah Lowenthal, Jón Gudmundsson and Eric Coomer for helping me prepare for my qualifying examination, and for their willingness to discuss my research, Jin Hui, Joe Fitzpatrick and Matthieu Longeot, who, as my house-mates, shared many of my joys and sorrows throughout these years — our discussions on religion, science, politics and just about every other topic under the sun (or moon) frequently extended into the wee hours of the morning. I would also like to thank Ali Mansouri, whose generous words of advice advice often consisted of a unique blend of pragmatism and idealism; and Kimberly Anderson, Noam Tene, Parvaneh Borhani and Steve Asztalos, for all the wonderful times we shared together, whether it was just over dinner or a camp-fire.

Among my teachers in the Department of Nuclear Engineering, I wish to thank Professor T. Kenneth Fowler, the chairman of my thesis committee. His intuitive insights into my research were frequently helpful in enabling me to see the "bigger picture", and his sense of humor always reminded me not to take myself too seriously. I would also like to thank Professor Jasmina Vujic, chairwoman of my qualifying examination committee. Her precise and detailed lectures were my first introduction to numerical methods and computational physics, and were extremely useful in developing the Monte Carlo collision model. I would also like to thank Professor Stanley Prussin; his presense on my qualifying examination committee definitely reduced the stress. It was a great pleasure working for him as a graduate student instructor; his dedication to his students was an inspiration to me. The cross section calcula-

tions benefited from his lectures and discussions on the interaction of radiation with matter. I also wish to thank our departmental graduate assistants, Luda Requadt and Sara Hill, who with the wave of their magic pens were able to untangle many a bureaucratic web.

At Lawrence Berkeley National Laboratory, I wish to thank Edward Lee, my principal advisor, for giving me the opportunity to work on this thesis. His technical expertise and guidance were invaluable in carrying out the research; and his open-door, non-intrusive style best suited my own. I would also like to thank other members of the Fusion Energy Research Group, in particular, Kyoung Hahn, who was always willing to help me "debug" a piece of code long after it began to look like nothing more than a jumble of loops to me — we spent many late-night hours analyzing some finer point of a particular numerical method, William Fawley and Enrique Henestroza for their help with computational techniques, and Andris Faltens for his assistance in compiling cross section data. I would also like to thank Sue Bowen, our program and budget administrator, who was ever watchful for the best interests of the graduate students in the group. At Lawrence Livermore National Laboratory, I wish to thank Ralph Moir for discussions concerning the the HYLIFE reactor design, and Debra Callahan Miller for sharing her numerical simulation expertism.

In the Department of Electrical Engineering, I wish to thank Professor Charles Birdsall for giving me my first introduction to particle simulation. His sense of humor and good nature immediately puts one at ease. I am deeply indebted to his lectures, seminars and discussions on particle-in-cell techniques. I would also like to thank other members of the Plasma Simulation and Theory Group, in particular, Vahid Vahedi, Peter Mardhal and John Verboncoeur for their suggestions regarding numerical simulation techniques. In the Physics Department, I wish to thank Professor Allan Kaufman, for his excellent and thorough introduction to particle dynamics. His hand can be seen in many of the governing equations.

To you, O God, I give thanks for gently leading me in the dance of life and for bringing into it these generous and wonderful companions.

Berkeley, California Nigel Oswald Barboza
December, 1996

1 Introduction

Nuclear fusion of hydrogen isotopes has long been viewed as a potential source of safe, relatively clean energy to meet the increasing demands projected for the future. Inertial confinement fusion (ICF) is one concept currently being pursued as a means of harnessing this energy for the production of electricity. In this approach, small, spherical capsules containing deuterium and tritium, two isotopes of hydrogen, are compressed and heated until fusion occurs. The use of heavy ion beams to initiate these fusion microexplosions looks extremely promising in principle; however, it requires that such beams be focused to a small spot in a fusion chamber that may be filled with a low density gas. The research presented here is concerned with the fundamentals of ion beam dynamics in the fusion chamber. Collisions between the beam ions and the residual background gas in the chamber will strip the ions to higher charge states and generate a background plasma. These processes will affect the feasibility of propagating the beam to a small spot-size needed for heavy ion driven ICF.

1.1 Heavy Ion Driven Inertial Confinement Fusion

Nuclear fusion is the process of combining light nuclei to form heavier ones. One possible fusion reaction combines two isotopes of hydrogen, deuterium (D) and tritium (T), to form helium and a neutron. This reaction releases $17.6\,MeV$ of energy, with the neutron carrying away $14.1\,MeV$ and the alpha particle $3.5\,MeV$:

$$^2H + {}^3H \rightarrow {}^4He + n \; (17.6 \; MeV) \; . \tag{1}$$

Figure (1)* shows the Maxwellian averaged reaction rate parameters $\langle \sigma v \rangle$ for various

---

* Taken from Keefe (1982).

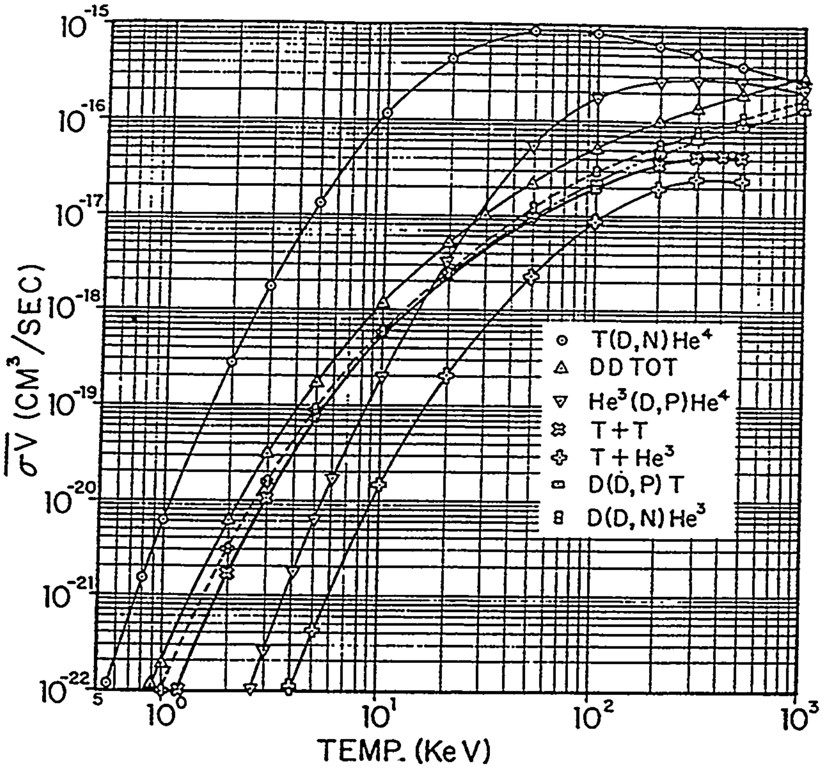

Figure 1: Values of $\langle\sigma v\rangle$ averaged over a Maxwellian distribution for a variety of fusion reactions.

fusion reactions as a function of temperature. As can be seen, $\langle\sigma v\rangle$ for the $T(D,n)\alpha$ reaction peaks when the reactant temperature is in the range 20 to 100 keV, and is $\sim 4\times 10^{-16}\,cm^3/s$ at 20 keV. Using this reaction for the purposes of generating energy requires not only that we raise the temperature of the fuel, a mixture of deuterium and tritium, to $\sim 20\,keV$, but also that the density be high enough for a significant number of reactions to occur before cooling or disassembly. If the fuel consists of a 50-50 mixture of D and T (DT), then the number of fusion reactions that occur per unit volume, f, can be given by:

$$\frac{df}{dt} = \frac{n^2}{4}\langle\sigma v\rangle \ , \tag{2}$$

where n is the total number density of D and T at time t. If we now let n_0 be the total initial number density, then assuming there is no transport of particles, $n = n_0 - 2f$; and if we define the burn-up fraction as $\phi \equiv 2f/n_0$, then we can solve (2) for ϕ at some time τ:

$$\frac{\phi}{1-\phi} = \frac{\langle\sigma v\rangle}{2} n_0\tau \; . \tag{3}$$

The burn-up fraction increases with the $n_0\tau$ product. For $n_0\tau \gtrsim 2\times10^{15}\ s/cm^3$, we get a burn-up fraction of $\gtrsim$30%.

The basic physics challenges facing any approach to fusion energy production are to attain a certain $n_0\tau$ product, referred to as the Lawson criterion, and to heat the fuel to the desired temperature. In the inertial confinement fusion concept, a laser or ion beam driver is used to deliver energy to a target containing a small spherical capsule of cold DT fuel causing it to compress substantially, thereby greatly increasing both its temperature and density. The subsequent fusion reactions will "burn-up" a significant fraction of the fuel, releasing energy in a microexplosion.

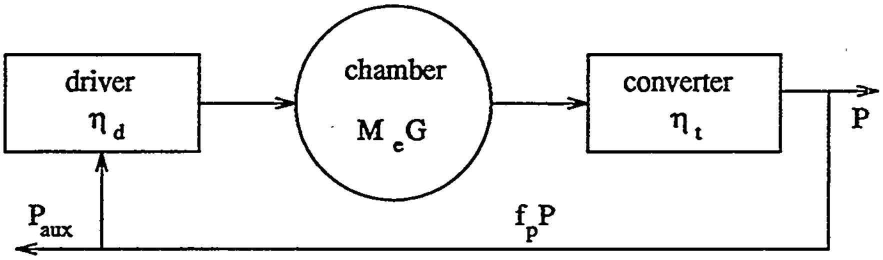

Figure 2: Power flow diagram for a typical inertial fusion plant.

A typical inertial confinement fusion facility would contain, in addition to other components, a driver for delivering the necessary energy to the target, a chamber to contain the subsequent capsule microexplosion, and provide a mechanism for carrying away the generated energy, and generators for converting this thermal energy to electric power. Figure (2) shows a block diagram of the power flow for such a plant. From this diagram we can write

$$\eta_t E_d \left(M_e G + 1\right) \nu = \left(f_p + 1\right) P \; , \tag{4}$$

where G, the target gain, is defined as the ratio between the energy released by the capsule microexplosion and the energy delivered to the capsule by the driver, E_d, P is the output electric power of the plant to the grid, f_p is the recirculating power fraction of P that is used to power the driver and run other plant equipment, η_t is the thermal conversion efficiency, ν is the plant repetition rate, and M_e is the energy multiplication factor that results from neutron induced nuclear reactions that take place in the chamber. We can also write

$$\nu E_d = (f_p P - P_{aux})\, \eta_d \ , \tag{5}$$

where η_d is the wall-plug to output driver efficiency, and P_{aux} is the amount of recirculating power that is used to drive plant equipment other than the driver. The idea behind any feasible power plant is to reduce the cost of the plant for a given output power, P. Zukerman, et al., (1988) do a detailed study of the cost of a heavy-ion fusion power plant versus various physical parameters. The cost increases as the driver energy, E_d, and the recirculating fraction, f_p, are increased; therefore, for fixed efficiencies and energy multiplication factor, we generally want to lower E_d and f_p. We can solve for f_p, by dividing equations (4) and (5):

$$f_p = \frac{1 + \eta_d \eta_t \left(M_e G + 1\right) \tilde{P}_{aux}}{\eta_d \eta_t \left(M_e G + 1\right) - 1} \ , \tag{6}$$

where $\tilde{P}_{aux} \equiv P_{aux}/P$. As can be seen f_p decreases as the gain, G, is increased. However for a typical value of $\tilde{P}_{aux} \simeq 0.05$, f_p does not decrease much for $\eta_d \eta_t (M_e G + 1) \gtrsim 10$. We can also solve for E_d in equations (5) and (4):

$$E_d = \frac{\left(1 + \tilde{P}_{aux}\right) P \eta_d}{\nu} \left[\frac{1}{\eta_d \eta_t \left(M_e G + 1\right) - 1}\right] . \tag{7}$$

The target gain, G, as we will see later, is not independent of the driver energy, E_d, but nevertheless, we can see from equation (7) that increasing the plant repetition rate, ν, will decrease the driver energy and hence the cost of the plant. However, making the repetition rate too high will not allow enough time to "clear" the chamber between subsequent microexplosions; this point will be discussed in more detail later. We can solve for this repetition rate in (7):

$$\nu = \frac{\left(1+\tilde{P}_{aux}\right) P\eta_d}{E_d}\left[\frac{1}{\eta_d\eta_t\left(M_eG+1\right)-1}\right] . \qquad (8)$$

For a $\sim 1000\,MW_e$ power plant, with $P_{aux}=0$, $M_e=1$ and $\eta_t \simeq 35\%$, and a heavy ion accelerator as the driver with energy $E_d \simeq 5\,MJ$ and an efficiency of $\eta_d \simeq 25\%$, and a target gain of $G \simeq 70$, equation (8) yields a repetition rate of $\sim 9.6\,Hz$, which is reasonable.

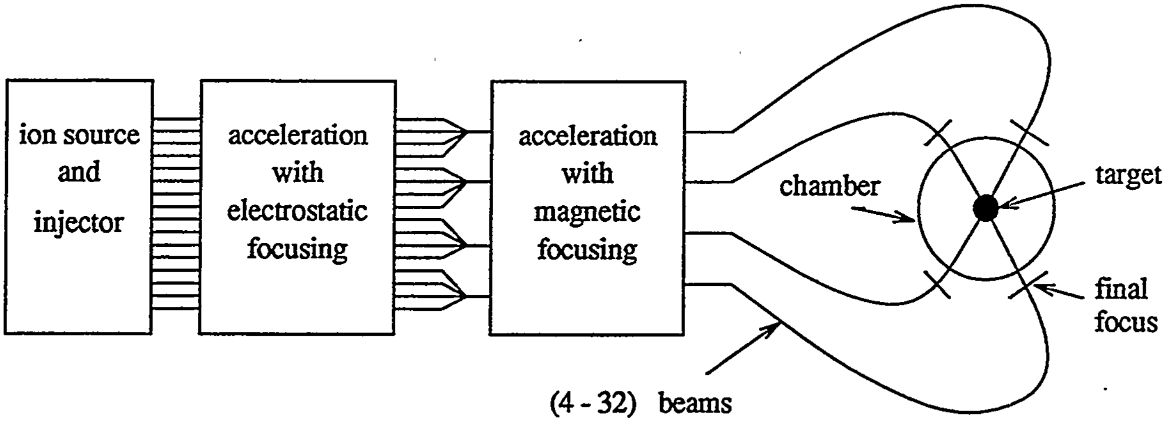

Figure 3: A block diagram of an induction linac for heavy ion driven ICF.

Up to now we have alluded to a driver, and mentioned in passing that this could be a heavy ion accelerator. One possible high current accelerator technology that could be used as a driver is the heavy ion induction linac. In such a system beams of heavy ions, like Cs^+ or Hg^+, are accelerated through induction cores, and focused using electrostatic and magnetic quadrupoles. Figure (3) shows a block diagram of an induction accelerator. Many beams are accelerated in parallel, combined, and further accelerated until they reach the energy and power necessary to compress and heat the fusion capsule. They are then focused onto the target in a chamber.

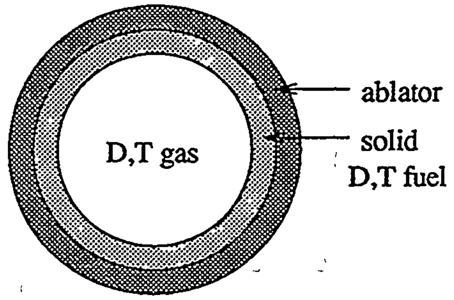

Figure 4: Schematic of a typical inertial confinement fusion capsule.

In one type of capsule design, this compression is accomplished by delivering energy to an outer shell, causing it to ablate off thereby imparting inward momentum to the fuel in much the same way as a rocket. Figure (4) shows a schematic of such a capsule, that consists of the shell, or ablator, a solid *DT* fuel layer and *DT* gas fill. The capsule radius is typically only a few *mm*.

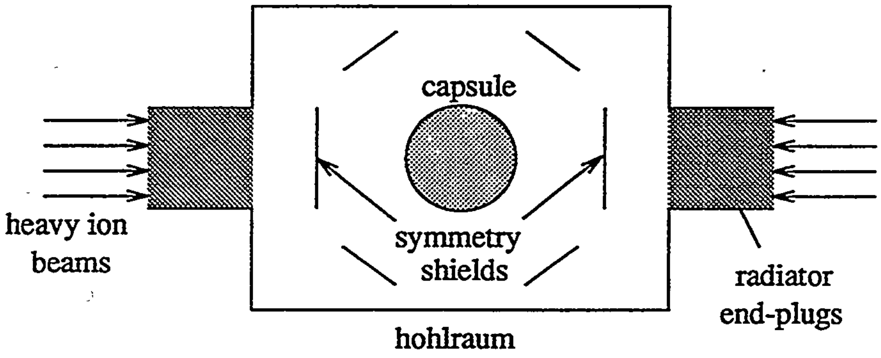

Figure 5: Schematic of an indirect drive target for heavy ion driven ICF.

In order to achieve uniform compression, the capsule must be symmetrically illuminated. It may be possible to achieve this uniformity by having several heavy ion beams impinge on the ablator in some symmetrical configuration. In this method, called “direct-drive”, the capsule is the target, and the ablator absorbs the energy of the heavy ions directly. Another method of obtaining symmetrical illumination, called “indirect drive”, is to enclose the capsule within a cylindrical case, or “hohlraum”. Fig

(5) shows a schematic of a hohlraum for heavy ion driven ICF. Here the hohlraum is the target and the heavy ions are stopped in the end plugs of the hohlraum. This material, heated by the ions, then radiates x-rays that, with the appropriate hohlraum design, can be made to symmetrically illuminate the outside shell of the capsule. Lindl (1995) provides a good overview of various target concepts.

1.1.1 Focal Spot-Size

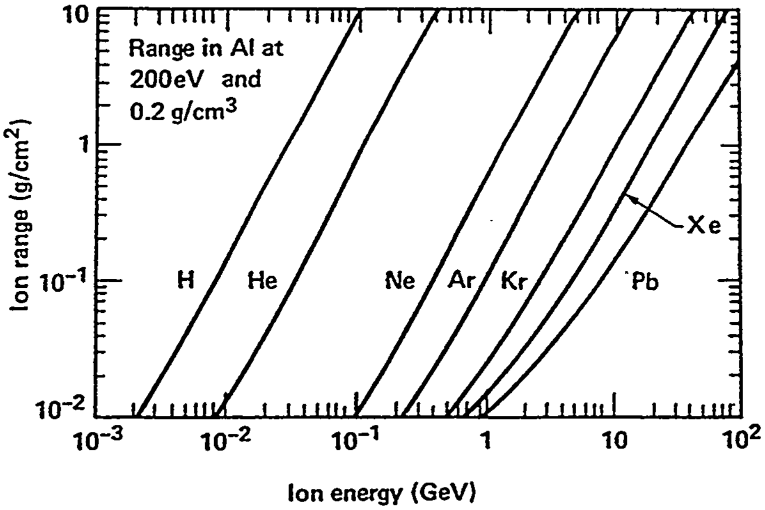

Figure 6: The range-energy relation for several ion species in hot matter ($200\,eV$).

In both the direct and indirect methods of capsule illumination, the stopping range of the ions in either the ablator or radiator and the spot-size, or radius, to which the beams can be focused are important in determining the energy gain of the target. Figure (6)* shows the range of various ions in aluminum as a function of ion energy. Bangerter (1988) discusses the results of gain analysis for indirectly driven

---

* Taken from Keefe (1982).

targets that are illuminated from two sides as shown in figure (5). Figure (7) * shows curves for gain versus driver energy, for various spot-sizes and ion ranges, and figure (8)* shows the peak driver power, P_d, as a function of driver energy corresponding to the curves in figure (7).

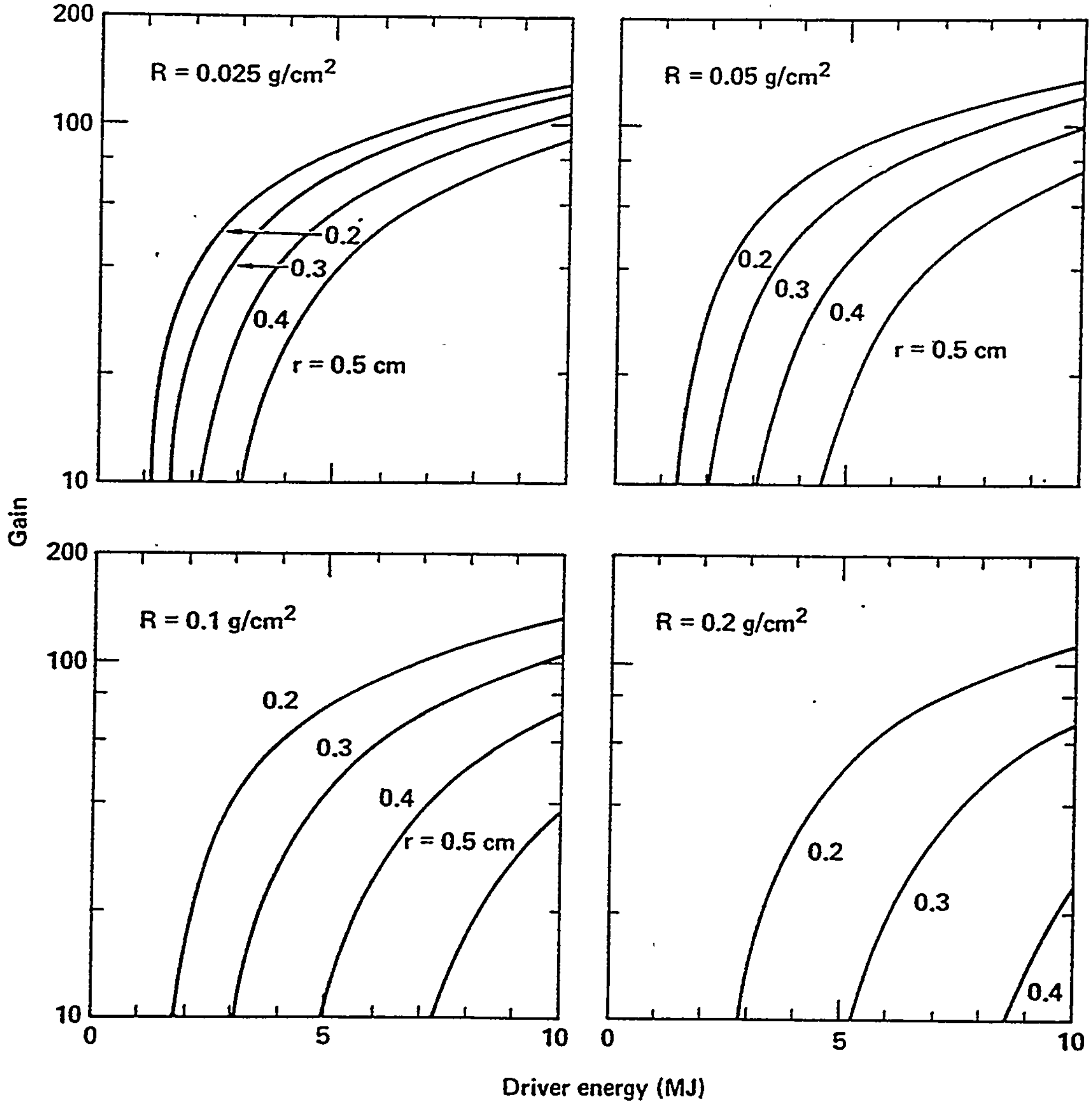

Figure 7: Curves for radiatively driven targets giving gain as a function of driver energy, focal spot radius and ion range.

---

* Taken from Bangerter (1988).

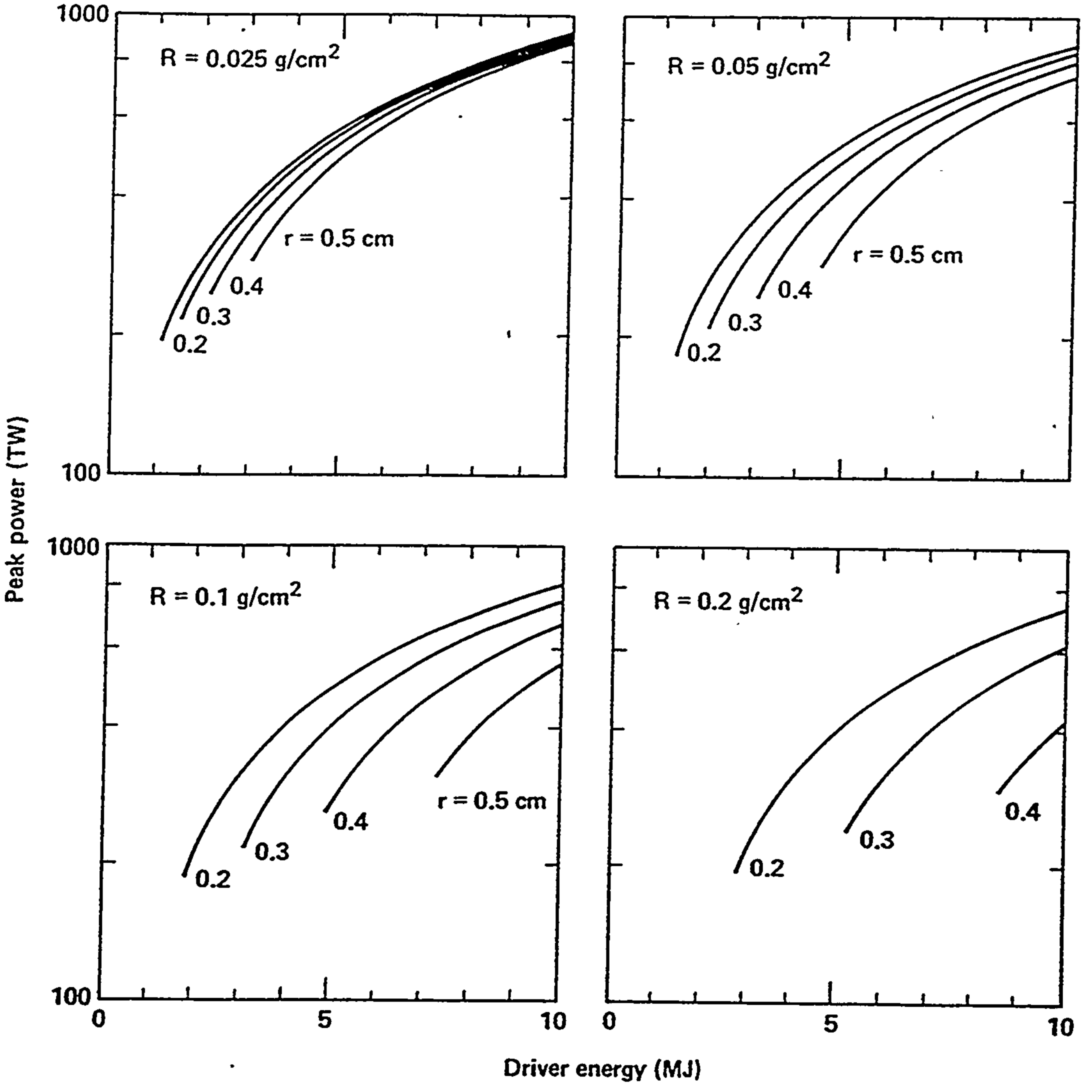

Figure 8: Peak driver power requirements corresponding to the gain curves in figure (7).

We can use the results in these graphs to discuss the relationship between the target gain and the focal spot-size of the beams. The general idea behind heavy-ion fusion is to produce the required high driver power with a relatively low beam current that can be accelerated and focused by conventional means, as we'll see later. This translates to ions with high kinetic energy and, to match the required short ion range, high mass. Consider ions that have a range of $\sim 0.1\, g/cm^2$. As can be seen from figure (6), this corresponds to heavy ions, $\sim 200\, amu$, with kinetic energy around $E_b \simeq 10\, GeV$. Some plausible ion species are mercury, which has a mass of $200.59\, amu$, or cesium, with a mass of $132.91\, amu$, among others. For a $\sim 5\, MJ$ driver, with a spot-radius of $\sim 2\, mm$, figure (7) predicts a gain of ~ 70. As before, equation (8) gives a plant repetition rate of $\nu \simeq 10\, Hz$ for a $\sim 1000\, MW_e$ power plant. And finally figure (8) gives a peak driver power of $\sim 500\, TW$. Smaller spot sizes are more difficult to achieve due to intrinsic limitations of a focal system; therefore let us examine what happens if we increase the spot-size to $\sim 3\, mm$, but keep the driver energy and ion range the same. We expect that this will decrease the gain since a greater mass of radiator material must be heated. From figure (7) we see that the gain drops to ~ 40, leading to a repetition rate of $\sim 20\, Hz$, which, in turn, would stress the fusion chamber dynamics. In order to lower the repetition rate, we need to increase the gain. We can accomplish this in one of two ways, by either increasing the driver energy or decreasing the range. From figure (7), we see that to regain $G \simeq 70$, for the same ion range, we would have to increase the driver energy to $\sim 7\, MJ$, and from figure (8) the peak power would become $\sim 600\, TW$. Following the second approach and decreasing the range to $\sim 0.05\, g/cm^2$ for the same driver energy of $\sim 5\, MJ$ would also increase the gain to ~ 65 but leave the peak power at $\sim 500\, TW$. However, now from figure (6) we see that the kinetic energy of a $\sim 200\, amu$ ion would need to be lowered to $\sim 4.5\, GeV$. Table (1) summarizes these results. As we'll see later, the price for either raising the peak power or lowering the ion kinetic energy to compensate for a larger spot size is paid for by increasing the driver current, which makes final focus more difficult. Therefore it is necessary to make the focal spot size of the beam as small as possible. However, from a cost point of view, although increasing the peak driver power increases the accelerator cost, lowering the ion kinetic energy may substantially reduce the accelerator cost. For a general discussion of these economic tradeoffs see Hovingh, et al., (1988).

spot-size (mm)	range (g/cm^2)	G	E_d (MJ)	P_d (TW)	E_b (GeV)
2	0.1	70	5	500	10
3	0.1	70	7	600	10
3	0.05	65	5	500	4.5

Table 1: Beam, driver and target parameters as a function of focal spot size for a $1000\,MW_e$ *power plant.*

1.1.2 Beam Current

The total current that needs to be delivered by the driver to the target is given by

$$I_d = \frac{qP_d}{E_b}\ (kA)\ . \tag{9}$$

where P_d is the driver power in TW, q is the ion charge state, and E_b is the kinetic energy of the ions in GeV. As can be seen, this current increases if we either raise the peak power or lower the ion kinetic energy. Typically, the driver current is on the order of tens of kiloamps and cannot be delivered by a single beam. Indeed for double-sided, indirect drive targets, and more so for direct drive targets where symmetry of irradiation is important, we need to have considerably more than one beam, perhaps $N_b \simeq 4$–32. However, the complexity and expense of the hardware that will be needed to bend and focus several beams, in conventional final focus designs, limits us to few tens of beams.

The maximum amount of current that can be focused in a single beam without neutralization is determined by solving for the "free-flight" of the beam in the reaction chamber. The radius of the beam, a, as a function of the axial position, z, in a vacuum chamber is governed by the "envelope" equation. For an axisymmetric beam with mono-energetic ions, where there are no external forces present, this is:

$$\frac{d^2a}{dz^2} = \frac{Q}{a} + \frac{\epsilon^2}{a^3} \, . \tag{10}$$

We shall discuss this equation in more detail later when we analyze the beam transport in the chamber. The terms on the right-hand-side of equation (10) represent the defocusing space-charge and transverse thermal forces of the beam. The first term represents the defocusing effect due to the space-charge of the beam. For a long, narrow, cylindrical beam, with uniform transverse distribution, the dimensionless perveance, Q, is given by

$$Q = \frac{qeI_b}{2\pi\epsilon_0 m_b m_o (\beta\gamma c)^3} \, , \tag{11}$$

where q as before is the charge state of the beam ion, I_b is the beam current, m_b is the beam ion mass in *amu*, and $\beta\gamma$ is the relativistic factor. It is related to the ion kinetic energy by:

$$(\beta\gamma)^2 = \tilde{E}_b \left(\tilde{E}_b + 2\right) \, , \tag{12}$$

where $\tilde{E}_b \simeq 1.07 E_b/m_b$ and E_b is in GeV. The factor of γ^{-3} instead of γ^{-1} in equation (11) reflects the partial cancellation of the beam's electric repulsion by magnetic attraction. The second term in (10) is a measure of the defocusing effect due to the thermal forces of the beam. The emittance is defined as:

$$\epsilon^2 \equiv \left(\frac{4}{\beta^2 c^2}\right) \left[\langle r^2 \rangle \left(\langle v_r^2 \rangle + \langle v_\theta^2 \rangle\right) - \langle r v_r \rangle^2\right] \, , \tag{13}$$

where v_r and v_θ are the transverse radial and azimuthal velocities of the beam ions respectively, and $\langle \, \rangle$ denotes moments of the beam taken at a given position z and time, t. This emittance is usually determined by the ion source, and beam manipulations in the accelerator; for example combining several beams to form a single beam may lead to a large growth in the emittance.

We can now integrate equation (10) with the initial conditions, $a(0) = a_l$, the radius of the beam at the last focusing lens, and $da/dz(0) = \Theta$, the focusing half-angle of the beam emerging from the lens:

$$\Theta^2 = 2Q \ln\left(\frac{a_l}{a_s}\right) + \epsilon^2 \left(\frac{1}{a_s^2} - \frac{1}{a_l^2}\right) , \tag{14}$$

where a_s is the minimum beam radius, or "waist" of the beam, where $da/dz = 0$. Consider a beam with initial radius $a_l \simeq 10\,cm$, emittance $\epsilon \simeq 2.0 \times 10^{-5}\,m-rad$, and a convergence angle of $\Theta \simeq 0.02\,rad$. Then we get a spot-size, or minimum beam radius, of $a_s \simeq 2\,mm$ with a beam perveance of $Q \simeq 3.8 \times 10^{-5}$. For a $\sim 200\,amu$, $\sim 10\,GeV$, $^{+}1$ ion, equation (11) yields a beam current of $I_b \simeq 4.3\,kA$. Finally for a $\sim 500\,TW$ peak power machine (9) gives a driver current of $I_d \simeq 50\,kA$, resulting in $N_b \simeq 12$ beams. We now look at the case where we increased the spot size to $\sim 3\,mm$. Then equation (14) yields $Q \simeq 5.1 \times 10^{-5}$. If we wish to keep the peak driver power at $\sim 500\,TW$, table (1) predicts a beam kinetic energy of $\sim 4.5\,GeV$. Using equation (9) gives $I_d \simeq 111\,kA$, and equation (11) yields $I_b \simeq 1.7\,kA$, leading to $N_b \simeq 66$ beams. Therefore smaller spot-sizes result in fewer beams on target due to the lower peak power requirement. However, one must remember that this analysis was done for the transport of a beam in a vacuum chamber. As mentioned above, the background gas in the chamber will partially strip the beam ions and introduce other atomic and plasma processes which will affect the spot size of the beam and consequently the maximum transportable current.

1.1.3 Chamber Characteristics

Although the basic function of the chamber is to provide a means for transporting the energy produced in the explosion, via some working fluid, to an electricity generating facility, it also has to meet some other requirements in order to be viable for a commercial power plant. As an example, we consider, one of the most recent

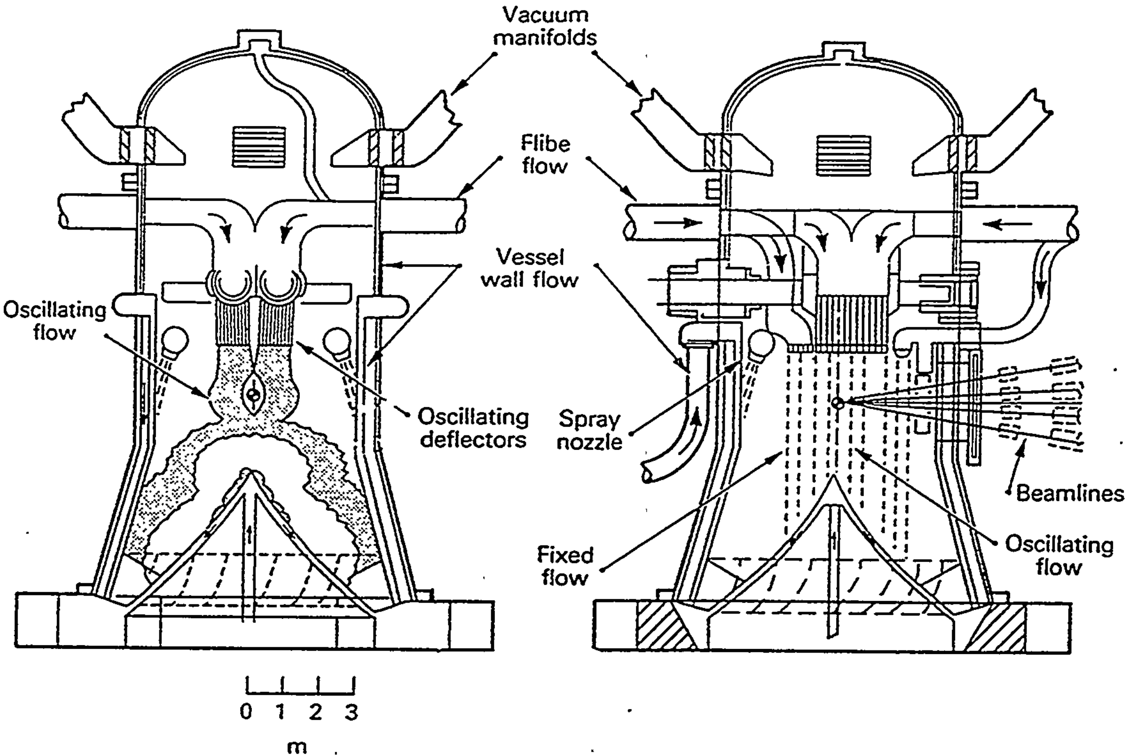

Figure 9: HYLIFE-II inertial confinement fusion reaction chamber. One view is rotated 90 deg. from the other.

and detailed liquid-wall chamber designs, HYLIFE-II by Moir, et al. (1994). Figure (9) * shows two views of this chamber, one rotated 90 degrees from the other.

The working fluid that is used to carry away the heat in the HYLIFE-II chamber is Flibe, a molten-salt mixture of 66.7 mol % LiF and 33.3 mol % BeF_2. As mentioned above, the fuel for fusion power plants consists of deuterium and tritium. Deuterium is very abundant in nature, constituting about 0.015% of natural hydrogen, however, the amount of tritium is negligible. Both isotopes of lithium in LiF can be used to breed tritium via the reactions:

$$^{6}Li + n \rightarrow {}^{4}He + T \ (4.8\ MeV) \ ,$$

$$^{7}Li + n \rightarrow {}^{4}He + T + n \ (-2.5\ MeV)$$

---

* Taken from Moir, et al., (1994).

Therefore, lithium plays a vital role as a breeder of the necessary tritium as well as being a working fluid component.

In the HYLIFE-II design, the fusion target is injected into a "pocket" of Flibe created in the center of the chamber by oscillating nozzles. This pocket, which has a Flibe thickness of about $\sim 1\,m$, and various other configurations of Flibe jets within the chamber serve to protect the chamber walls from neutrons. After the microexplosion the pocket disintegrates. A $1000\,MW_e$ reactor design with a driver energy of $5\,MJ$ and a gain of 70, results in a capsule output energy of $\sim 350\,MJ$. This explosion can vaporize several kg of liquid, resulting in background gas densities on the order of 10^{18} molecules per cm^{-3} immediately after a microexplosion. The background gas density in the chamber at the time of the next shot is an important parameter in determining the spot-size to which the ion beams can be focused. And as we have seen above, it is important that we try to focus the beam to a spot small enough to allow the high gains needed for an economically attractive fusion plant.

The HYLIFE-II design assumes a driver efficiency of $\eta_d \sim 35\%$, and a thermal conversion efficiency of $\eta_t \sim 43\%$. With an energy multiplication factor, $M_e = 1.18$ and $50\,MW$ of auxiliary power, equation (8) predicts a repetition rate of $\sim 6.3\,Hz$. This means that a target must be injected into the chamber, a fresh pocket of liquid formed, and any conditions that are necessary for the propagation of the beam through the chamber, in particular the original density of the background gas, must be restored every sixth of a second.

For $E_d \sim 5\,MJ$ and $G \sim 70$, we can use figures (7) and (8) to determine a set of spot-sizes, ion ranges, and driver powers, P_d. Then, with these ion ranges, figure (6) can be used to give a set of beam kinetic energies, E_b, and driver currents, I_d, for

spot-size (mm)	range (g/cm^2)	P_d (TW)	E_b (GeV)	I_d (kA)	I_b (kA)	N_b
2	0.1	500	10	50	4.3	12
2.75	0.05	525	4.5	117	1.6	73
3.25	0.025	550	2.5	220	0.7	314

Table 2: Beam and driver parameters as a function of various focal spot sizes for a $5\,MJ$ *driver.*

$\sim 200\,amu$, $^{+}1$ ions. Then we can use equations (10) and (11) to calculate the beam currents, I_b, and number of beams. Table (2) lists the results of such calculations; as an example, for a 12 beam design, like HYLIFE-II, the focal spot radius for $\sim 4.3\,kA$, $\sim 10\,GeV$ beams is $\sim 2\,mm$. It must be stressed that these calculations are predicated on the target gain calculations shown in figures (7) and (8) by Bangerter (1988). More recent results by Bangerter and Ho (1990) show that target gains of ~ 60 can be achieved with $\sim 5\,MJ$ drivers and spot radii of $\sim 3\,mm$. Lindl (1995) gives an overview of ongoing experimental and theoretical work in target physics and design that may allow for even larger spot-sizes.

1.2 Purpose of this Thesis

As we have seen above, the spot radius of the beam on the target is a key parameter in determing the target gain and peak driver power. Since the kinetic energy of the ions and the total beam current, and ultimately the cost of the power plant, are influenced adversely by increasing spot-size, the beams must be focused to a small spot radius. This spot radius is affected by the density of background vapor present in the chamber at the time of the beam propagation.

As mentioned above, the background gas density immediately following a microexplosion can reach as high as $\sim 10^{18}$ molecules per cm^{-3}. In the HYLIFE-II design study by Moir, et al., (1994), 205 spray heads of cold Flibe, $843\,K$, are employed to condense the background gas and reduce the density in the chamber to $\sim 10^{13}$ molecules per cm^3 within the $\sim 0.17\,s$ between shots. The ability to focus the beam in higher density vapor, $\sim 10^{14}\,cm^{-3}$, has considerable advantages, in that it eases these stringent requirements on the chamber, reducing or perhaps even eliminating the need for sprays and other mechanisms to condense the vapor, leading to simplified reactor designs. Methods for propagating the beam through lower density, $\lesssim 10^{13}\,cm^{-3}$, gas have been explored by Callahan (1995). Beam propagation as a magnetic pinch through higher density, $\gtrsim 10^{15}\,cm^{-3}$, gas are being studied by Hahn and Lee (1995) and Tauschwitz, et al., (1995), and are very advantageous if physically feasible. However, some neutralized transport schemes lead to more complicated designs requiring, for example, the formation of stable plasma channels within the chamber, etc.

The purpose of this thesis is to determine if a beam of heavy ions can be focused to the necessary *mm* size spot radii on target through background gas densities in the range of $\sim 10^{14}$ to 10^{15} molecules per cm^3. We will explore chambers that use Flibe or liquid-lithium, which was proposed in the original HYLIFE design by Blink, et al., (1985), and also meets the basic requirements of breeding tritium and protecting the first structural wall from neutrons, as the working fluid. Collisions of the beam ions with the background gas will result in a highly random distribution of beam charge states due to stripping, and complicated plasma phenomena due to ionization of the background gas. Analytic formulations, such as the simple envelope equation, (10), used earlier are inadequate for describing the dynamics of the beam under these conditions. We therefore turn to numerical methods based on particle-in-cell and Monte Carlo techniques to solve the basic equations of motion for the beam ions.

2 Beam Propagation Theory

In this thesis we wish to determine the spot radius to which a heavy ion beam can be conventionally focused through a chamber filled with background gas. In particular we wish to determine the positions and velocities of the beam ions as they move through the chamber as this will determine the position and radius of the focal spot. In order to do this we first need to understand the physical processes that affect the motion of the beam ions, and then write a set of equations that describe this motion.

Beam ion	Hg^+
Ion kinetic energy (E_b)	$10\,GeV$
Particle velocity (β)	0.32
Beam current (I_b)	$4\,kA$
Pulse length (L_b)	$1\,m$
Beam emittance (ϵ)	$20\,mm - mrad$
Beam radius at final lens (a_l)	$10\,cm$
Beam convergence half-angle (Θ)	$20\,mrad$

Table 3: Some typical beam parameters.

Before proceeding, we summarize, in table (3), a set of beam parameters based on the discussion in the previous chapter and adapted from Lee (1991). We shall use these parameters to determine the order of magnitude of various dynamical quantities throughout this thesis.

2.1 Physical Processes

We separate the interactions of the particles in the chamber into two types. Discrete, or particle-particle, interactions where the charged and neutral particles in the chamber undergo collisions; and collective, or particle-field, interactions, where the charged particles are affected by the self-generated electromagnetic fields. As mentioned above, inertial confinement fusion may require that multiple beams, ~ 4 to 32, be focused onto the target; in this thesis however, we study the transport of a single beam and neglect the forces of the other beams. Interactions between these multiple beams has been studied by Callahan (1995).

2.1.1 Particle-Particle Interactions

As mentioned above, the background gas neutrals, beam ions, background gas ions, and electrons can interact with each other via collisions. These collisions can be elastic scattering collisions or inelastic charge-changing and excitation collisions. The charge-changing collisions are responsible for the creation of electrons and gas ions, and for the alteration of the beam ion charge state. It is hoped that the electrons generated by ionizing collisions with the background gas will be entrained by the beam, while the background gas ions, being heavier than the electrons, will remain essentially at the location of their creation. These electrons may be sufficient to compensate for the increase in charge state of the beam ions due to stripping and any gas ions in the vicinity of the beam, allowing the beam to be focused to spot radii comparable to those in a pure vacuum chamber.

The densities of the charged species, electrons, beam ions and gas ions, are generally orders of magnitude lower than that of the background gas neutral density; even the electrons, which are the most prolific of the charged species, reach densities of $\sim 10^{13}\, cm^{-3}$ only when the background gas density is at the high end, $\sim 10^{15}\, cm^{-3}$, and the beam is at the target. Therefore we can ignore collisions between the charged species. Within the scope of this thesis, we also ignore collisions between the secondary charged species, electrons and gas ions, and background gas neutrals; although such collisions will result in the generation of electrons and background gas ions, they will not change the charge state of the beam ions.

We are therefore left with collisions between the beam ions and background gas neutrals. As mentioned above, these collisions can be elastic scattering or inelastic. Elastic scattering collisions result in an angular deflection of the beam ions. Jackson (1975) has shown that after several collisions, the distribution in angle will be approximately Gaussian with a mean square angle:

$$\langle \theta^2 \rangle \simeq 4\pi n_g L \left(\frac{2qZ_g e^2}{\gamma m_b m_o \beta^2 c^2} \right)^2 \ln \left(\frac{240}{Z_g^{1/3}} \right) , \tag{15}$$

where Z_g is the background gas atomic number, n_g is the background gas density, q and m_b are the charge-state and mass of the beam ion in *amu* respectively, β is its velocity in units of c, and γ is the relativistic factor. L is the distance that the beam ion travels, and is approximately given by $\sim a_l/\Theta$, where a_l is the radius of the beam at the lens and Θ is the convergence angle from the lens. For example consider the typical beam parameters given in table (3) with an average charge state of $q \simeq {}^{+}3$ propagating through fluorine gas with density $n_g \simeq 10^{15}\, cm^{-3}$; as we will see later, fluorine is the dominant background gas component for reactors that use Flibe. The root mean square deflection angle is then $\sim 2.3\, \mu rad$. From emittance considerations, the minimum mean square angle can be given by: $\langle \theta^2 \rangle \simeq \epsilon^2 / 2a_l^2$, where ϵ is the emittance of the beam. Again using the parameters given in table (3) we get a mean square angle of $\sim 0.14\, mrad$. This is more than sixty times larger than the deflection angle from scattering, therefore we can ignore elastic scattering collisions.

We are left then with inelastic collisions between the beam ions and background gas neutrals. These collisions can be divided into excitation collisions, where the beam ion or the background gas neutral is left in an excited state after the collision, and charge-changing collisions, where the charge states of the beam ions and background gas atoms are altered by the collision. Viewed from a classical perspective, the excitation process is one where an electron in a lower-lying level in the atom is excited to a higher level via the absorption of energy; this leaves a "hole" in the lower level where the electron used to be. The time to fill this hole, and return the atom to its ground state can be given by $\hbar/\Gamma$, where Γ is the natural line width of the level. From compilations by Keski-Rahkonen and Krause (1974) we see that the outer-most atomic levels generally have the smallest line-widths. For example for the N_7 shell in mercury, $\Gamma \simeq 0.2\,eV$, which yields a de-excitation time of $3.3\,fs$. Similarly the lifetime for a hole in the L_2 shell of fluorine is $\sim 1.3\,ps$. As will be seen later, these times are generally much smaller than the mean time between charge-changing collisions, therefore we can neglect excitation.

We are now left with charge-changing collisions between the beam ions and background gas neutrals. These collisions are of two types, electron loss, where the charge state of the beam ion or the background gas neutral increases, and electron capture, where the charge state of the beam ion decreases due to the capture of an electron from the background gas neutral. These collisions can be described by a "cross section", such that the probability for a beam ion to undergo a particular type of collision in a small distance, δs, is given by

$$P = \sigma n_g \delta s \ , \tag{16}$$

where n_g is the neutral density of the background gas. The cross section, σ, for this collision has the dimensions of area.

Schlachter, et al., (1983) have shown that the capture cross section, $\sigma_{c,q}$, the cross section for a beam ion of charge state q to capture an electron from the background gas, follows the approximate empirical scaling law:

$$\sigma_{c,q} \simeq 8.6 \times 10^{-21} \frac{a_0^2 q^{3.9} Z_g^{4.2}}{\tilde{E}_b^{4.8}} , \tag{17}$$

where q and Z_g, as before, are the charge-state of the beam ion and atomic number of the background gas respectively, and $\tilde{E}_b \simeq 1.07 E_b/m_b$ where E_b is the kinetic energy of the beam ion in GeV and m_b is its mass in amu. a_0 is the Bohr radius. For example with the values in table (3) with an average charge state of $q \simeq {}^{+}3$ and fluorine background gas, we calculate a capture cross section $\sigma_{c,q} \sim 2.2 \times 10^{-25}\, cm^2$. As will be shown this is much less than the cross sections for electron loss and therefore can be ignored.

We are then left only with the electron loss collisions between the beam ions and the background gas neutrals. There are two types of electron loss collisions, those that result in the loss of electrons from the beam ions, stripping, and those that result in the loss of electrons from the background gas, ionization; these generally occur simultaneously. We quote here the results of a semi-empirical method for calculating the single-electron loss cross sections for fast collisions, i.e. collisions where only a single electron is lost from either the background gas or the beam ion; this method is described in detail in a later section. For example, the ionization of an almost fully stripped mercury ion, Hg^{79+}, due to a collision with a neutral fluorine atom has the smallest cross section, $\sim 2.5 \times 10^{-22}\, cm^2$. Although we would never expect a mercury beam ion to reach this high a charge state, this cross section is still more than three orders of magnitude larger than the capture cross section, so we are justified in ignoring electron capture. The largest cross section is for the ionization of a neutral fluorine atom by a fully stripped mercury ion, $\sim 2.7 \times 10^{-14}\, cm^2$; and with a background gas density of $n_g \simeq 10^{15}\, cm^{-3}$, the mean time between collisions, $\sim 1/\sigma n_g \beta c$, is $\sim 3.9\, ps$. Although this is only three times larger than the largest de-excitation time, as mentioned above, we do not expect the mercury beam ions to become fully stripped. For the more realistic $^{+}20$ charge state ions, the collision time increases to $\sim 32.5\,ps$ which is more than twenty-five times larger than the de-excitation time; therefore the beam ions and the background gas neutrals are assumed to be in their ground states when they undergo electron loss collisions.

Finally, a few words must be said about multiple electron loss cross sections. As will be shown later, for fast collisions the electron loss cross sections are independent of a detailed knowledge of the structure of the projectile, and depend only on its charge state. Therefore at high velocities, the electron loss cross sections will be approximately the same whether the projectile is an electron, proton, or Hg^{+} ion. Schram, et al., (1966) have reported single and multiple electron loss cross sections for electron impact on noble gases. Their data go as high as $15\,keV$ electrons, which correspond to a velocity of $0.24c$, slightly lower than the $0.32c$ velocity for $10\,GeV$ mercury. For the ionization of helium, the ratio of the cross section for the loss of two electrons to that for one electron is $\sim 0.27\%$. For neon this ratio is $\sim 2.4\%$ and gets much lower for the loss of more than two electrons. For the heavier gases, krypton and xenon, the ratios are $\sim 8.8\%$ and $\sim 18\%$ respectively. Clearly, for heavier atoms that have many loosely bound outer electrons, the multiple electron loss cross sections are a significant fraction of the single electron loss cross sections, but for lighter atoms they are only a few percent of the single electron loss cross sections. Therefore in the case of the ionization of the background gas we can safely neglect the multiple loss cross sections. For mercury stripping, however, it seems that we may not be able to neglect multiple electron loss since it forms about $\sim 20\%$ of the single electron loss cross section. But, single electron stripping is never a major component of the total collision cross section; for $^{+}10$ mercury ions colliding with fluorine, it's about $\sim 7\%$. Consequently the multiple electron stripping cross section will be even smaller, $\sim 1.5\%$ of the total cross section, and therefore can be ignored.

2.1.2 Particle-Field Interactions

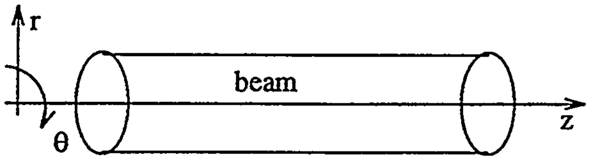

Figure 10: The beam coordinate system.

Besides collisional interactions, the charged species in the chamber can also interact with the collective, self-generated electromagnetic fields. In order to discuss these fields and their effect on the velocities and positions of the particles, it becomes necessary to specify a coordinate system. The most natural system is cylindrical, with the axis running through the center line of the beam as shown in figure (10).

The computations to be presented here are axisymmetric, therefore, by assumption, the space charge of the beam will generate only radial and axial electric fields. Also the beams of concern here have no net angular momentum around the z axis, therefore the only bulk currents that exist are radial and axial; consequently, by symmetry, only azimuthal magnetic fields exist. Therefore, we retain only the transverse magnetic field set: the radial and axial electric fields, E_r and E_z respectively, and the azimuthal magnetic field, B_θ.

The motions of all the charged particles in the chamber: beam ions, background gas ions and electrons are coupled to these fields via the Lorentz force. Since the system is taken to be axisymmetric, we are only concerned with the radial and axial positions of the particles, r and z, respectively. Although the beam itself has no net angular momentum, each individual beam ion does have an azimuthal velocity, therefore we keep all three velocity components, radial, axial and azimuthal, v_r, v_z and v_θ, respectively.

For some types of particles, one or more of these velocity components may remain invariant under the influence of the fields discussed above. We first look at the beam ions. For the values in table (3) both v_r and v_θ are much less than v_z; therefore $\beta \simeq v_z/c$, and the change in the axial velocity can be written as $\Delta v_z \simeq (qe\Delta t/\gamma^3 m_b m_o)(E_z + v_r B_\theta)$, where m_b is the mass in *amu* and q is the charge state of the ion. Again for the values in table (3) we get maximum fields of around, $B_\theta \simeq 0.01\,T$ and $E_z \simeq 4.2\,MV/m$ for an ellipsoidal beam, and $\Delta t \simeq 53\,ns$ for the beam to traverse a distance of $\sim 5\,m$. Then $\Delta v_z/v_z \simeq 0.1\%$. Therefore v_z and γ, which is only a function of v_z, are taken to be invariant. For the beam ions then we only need equations for v_r and v_θ. We now look at the gas ions; as mentioned before, these are created via ionizing collisions between the beam ions and background gas atoms, and essentially have zero initial velocity. The radial and axial velocities are given by $\Delta v \simeq (q_g e\Delta t/m_g m_o)E$, where q_g and m_g are the charge state and mass of the background gas ion in amu respectively. For a $^{+}1$ fluorine ion, and the values in table (3) we get maximum fields of around $E \simeq 8.6\,MV/m$ and $\Delta v \simeq 0.007c$. Therefore the gas ions never reach relativistic velocities. Also with the transverse magnetic field set, there are no forces in the azimuthal direction; therefore angular momentum is conserved and the azimuthal velocity remains zero. For the background gas ions then we keep only v_r and v_z. The electrons however, are created with some initial velocity; this velocity is dependent on whether the electron is created via ionizing a background gas atom or stripping a beam ion, and will be discussed in more detail later. Therefore all three electron velocity components, v_r, v_z and v_θ, must be maintained.

2.2 Governing Equations

An analysis of the particle-field interactions will allow us to write a set of time-evolution equations for the dynamic quantities discussed above: the radial and axial positions of all the particles, the radial, axial and azimuthal velocity components of the electrons, the radial and axial velocities of the gas ions, and the radial and azimuthal velocities of the beam ions. We also need to write equations for the transverse magnetic field set: the radial and axial electric fields, and the azimuthal magnetic field. The formalism presented here benefits from lectures by Kaufman (1995).

The particle-particle interactions, as discussed above, will result in the creation of electrons and gas ions, and an increase in the charge states of the beam ions. Because we only allow for single electron loss collisions between background gas neutrals and beam ions, all the gas ions created have charge state $^{+}1$; but the beam ions can undergo several successive stripping collisions with background gas neutrals, and therefore can have any charge state from an initial value to fully stripped. We can then write evolution equations for the number of electrons, gas ions, and beam ions of a particular charge state. The resulting equations will form a complete set that can, in theory, be solved with the appropriate initial and boundary conditions to determine the dynamics of the beam.

2.2.1 Particle Position Equations

The positions of the particles are given by:

$$\frac{d\mathbf{r}_{s,i}}{dt} = \mathbf{v}_{s,i} \ , \tag{18}$$

where $\mathbf{r}_{s,i}$ is the position of a particle and $\mathbf{v}_{s,i}$ is its velocity. The subscript $s = (q, e, g)$ is a species label refering to beam ions of charge state q, electrons, and gas ions respectively, and the subscript i denotes a particular particle. As mentioned above, we keep only the radial and axial positions of the particles. Then for the radial position (18) becomes:

$$\frac{dr_{s,i}}{dt} = v_{r,s,i} \; . \tag{19}$$

$r_{s,i}$ refers to the radial position of a particle. And for the axial position, $z_{s,i}$:

$$\frac{dz_{s,i}}{dt} = v_{z,s,i} \; , \tag{20}$$

2.2.2 Particle Velocity Equations

The fully relativistic time evolution equations for the velocities is the Newton-Lorentz equation:

$$\frac{d\mathbf{p}_{s,i}}{dt} = q_s e\left(\mathbf{E}(\mathbf{r}_{s,i}) + \mathbf{v}_{s,i} \times \mathbf{B}(\mathbf{r}_{s,i})\right) \; , \tag{21}$$

where $\mathbf{p}_{s,i}$ is the particle momentum defined as $m_s m_o \gamma_{s,i} \mathbf{v}_{s,i}$, where m_s is the particle mass in *amu*, $\gamma_{s,i}$ is the relativistic factor, q_s is the charge state of the particle, $\mathbf{E}(\mathbf{r}_{s,i})$ and $\mathbf{B}(\mathbf{r}_{s,i})$ are the electric and magnetic fields at the position of the particles.

Now for the radial velocity of the electrons we can write:

$$\frac{d\gamma_{e,i} v_{r,e,i}}{dt} = \frac{\gamma_{e,i} v_{\theta,e,i}^2}{r_{e,i}} - \frac{e}{m_e m_o}\left(E_r(\mathbf{r}_{e,i}) - v_{z,e,i} B_\theta(\mathbf{r}_{e,i})\right) \; , \tag{22}$$

where the subscript s is written as e, and m_e is the mass of the electron in units of *amu*. Similarly for the axial velocity:

$$\frac{d\gamma_{e,i} v_{z,e,i}}{dt} = -\frac{e}{m_e m_o}\left(E_z(\mathbf{r}_{e,i}) + v_{r,e,i} B_\theta(\mathbf{r}_{e,i})\right) \; , \tag{23}$$

and for the azimuthal velocity:

$$\frac{d\gamma_{e,i} v_{\theta,e,i}}{dt} = -\frac{\gamma_{e,i} v_{\theta,e,i} v_{r,e,i}}{r_{e,i}} \; , \tag{24}$$

As mentioned in the previous section, for the beam ions, we only need equations for the radial and azimuthal velocities. Using equation (21) we can write the radial velocity of a beam ion of charge state q as:

$$\frac{dv_{r,q,i}}{dt} = \frac{v_{\theta,q,i}^2}{r_{q,i}} + \frac{qe}{\gamma_{q,i} m_b m_o} \left(E_r(\mathrm{r}_{q,i}) - v_{z,q,i} B_\theta(\mathrm{r}_{q,i}) \right) , \tag{25}$$

where now the subscirpt s is written as q, the charge state of a particular beam ion, and m_b is its mass in *amu*. Notice that the relativistic factor $\gamma_{q,i}$ is taken to be invariant. The azimuthal velocity is given by:

$$\frac{dv_{\theta,q,i}}{dt} = -\frac{v_{\theta,q,i} v_{r,q,i}}{r_{q,i}} . \tag{26}$$

And finally for the non-relativistic, $\gamma_{g,i} \sim 1$, background gas ions, we write the radial and axial velocities as:

$$\frac{dv_{r,g,i}}{dt} = \frac{e}{m_g m_o} \left(E_r(\mathrm{r}_{g,i}) - v_{z,g,i} B_\theta(\mathrm{r}_{g,i}) \right) , \tag{27}$$

$$\frac{dv_{z,g,i}}{dt} = \frac{e}{m_g m_o} \left(E_z(\mathrm{r}_{g,i}) + v_{r,g,i} B_\theta(\mathrm{r}_{g,i}) \right) , \tag{28}$$

where the charge-state of all gas ions, as discussed above, is $^+1$, and where m_g is the mass of the gas atom in units of *amu*.

2.2.3 Field Equations

As can be seen, in order to solve the time evolution of the velocities, we need to know the electric and magnetic fields at the positions of the particles. The time evolution of the magnetic field is given by the Faraday-Maxwell equation:

$$\frac{\partial \mathbf{B}}{\partial t} = -\nabla \times \mathbf{E} . \tag{29}$$

For the azimuthal magnetic field then:

$$\frac{\partial B_\theta}{\partial t} = \frac{\partial E_z}{\partial r} - \frac{\partial E_r}{\partial z} . \tag{30}$$

And the time evolution of the electric field is be given by the Ampère-Maxwell equation:

$$\frac{\partial \mathbf{E}}{\partial t} = \frac{1}{\mu_0 \epsilon_0} \nabla \times \mathbf{B} - \frac{1}{\epsilon_0} \mathbf{J} \ , \tag{31}$$

where J is the current density. For the radial and axial electric fields, equation (31) yields:

$$\frac{\partial E_r}{\partial t} = \frac{-1}{\mu_0 \epsilon_0} \frac{\partial B_\theta}{\partial z} - \frac{1}{\epsilon_0} J_r \ , \tag{32}$$

$$\frac{\partial E_z}{\partial t} = \frac{1}{\mu_0 \epsilon_0} \frac{1}{r} \frac{\partial (r B_\theta)}{\partial r} - \frac{1}{\epsilon_0} J_z \ . \tag{33}$$

The divergence of B equation, $\nabla \cdot \mathbf{B} = 0$, is trivially satisfied with the azimuthally symmetric transverse magnetic field set used here, and we substitute the continuity equation for Gauss' law, $\nabla \cdot \mathbf{E} = \rho / \epsilon_0$.

2.2.4 Current Density Equations

Equations (32) and (33) contain the source terms J_r and J_z, the radial and axial current densities respectively. Later we will show how we can get these by evaluating the continuity equation:

$$\nabla \cdot \mathbf{J} = -\frac{\partial \rho}{\partial t} \ , \tag{34}$$

where ρ is the charge density defined as:

$$\rho \equiv \sum_{q=1}^{Z_b} qe \sum_{i=1}^{N_q} \delta^3(\mathbf{r} - \mathbf{r}_{q,i}) + \sum_{i=1}^{N_e} -e\delta^3(\mathbf{r} - \mathbf{r}_{e,i}) + \sum_{i=1}^{N_g} e\delta^3(\mathbf{r} - \mathbf{r}_{g,i}) \ , \tag{35}$$

where Z_b is the atomic number of the beam ion, and N_q, N_e, and N_g are the number of beam ions of charge state q, the number of electrons, and the number of gas ions respectively. δ^3 is a three-dimensional delta function, such that the integral of ρ over all space would result in $e(N_g - N_e + \sum_{q=1}^{Z_b} qN_q)$. For the geometry of concern, equation (34) becomes:

$$\frac{1}{r} \frac{\partial (r J_r)}{\partial r} + \frac{\partial J_z}{\partial z} = \frac{\partial \rho}{\partial t} \ . \tag{36}$$

2.2.5 Particle Number Equations

Finally we need a method for calculating the total number of particles of a given species. The derivation presented here benefits from lectures by Vujic (1992). As mentioned above, these numbers are determined by the collisions. The only collisions of concern are those between beam ions and background gas neutrals. If we write δs for the beam ions in equation (16) as $v_z \delta t$, since, as discussed above, $v_r, v_\theta \ll v_z$, then the probability that a beam ion of charge state q will undergo a particular type of collision, x, in the time interval δt is given by:

$$\delta P_{x,q,i} = \sigma_{x,q} n_g v_{z,q,i} \delta t \ , \tag{37}$$

where $\sigma_{x,q}$ is the cross section for this type of collision, n_g is the background gas density, and $v_{z,q,i}$ is the velocity of the beam ion. Therefore the probability that no collision will occur in this time is:

$$\delta \tilde{P}_{q,i} = 1 - \sigma_{t,q} n_g v_{z,q,i} \delta t \ , \tag{38}$$

where $\sigma_{t,q}$ is now the total cross section and is given by $\sum_x \sigma_{x,q}$. Then the probability that no collision has occurred after a time $t = n\delta t$ has elapsed is given by $\tilde{P}_{q,i} = (\delta \tilde{P}_{q,i})^n$, or in the limit of $n \to \infty$:

$$\tilde{P}_{q,i} = \exp\left(-\sigma_{t,q} n_g v_{z,q,i} t\right) \ . \tag{39}$$

Then the probability that a collision of type x will take place between some time t and $t+\delta t$ is simply given by $\tilde{P}_{q,i} \delta P_{x,q,i}$. Finally the probability distribution function, or the probability density for a collision of type x to occur at time t is given by:

$$\pi_{x,q,i} = \sigma_{x,q} n_g v_{z,q,i} \exp\left(-\sigma_{t,q} n_g v_{z,q,i} t\right) \ . \tag{40}$$

This probability density is normalized over the interval $0 \le t \le \infty$. We now define a cumulative distribution, $P_{x,q,i}(t)$, or the probability that a collision of type x will take place over the interval $0 \leq t' \leq t$:

$$P_{x,q,i} \equiv \int_0^t \pi_{x,q,i}(t')dt' \ . \tag{41}$$

Substituting from (40) into (41) yields:

$$P_{x,q,i} = \frac{\sigma_{x,q}}{\sigma_{t,q}} \left[1 - \exp\left(-\sigma_{t,q} n_g v_{z,q,i} t\right)\right] \ , \tag{42}$$

where $P_{x,q,i}(0) = 0$ and $P_{x,q,i}(\infty) = 1$.

Since we have concluded that the only two types of collisions that can occur are stripping and ionization, we can write:

$$\sigma_t = \sigma_{in,0} + \sigma_{st,0} + \sigma_{in,st} \ . \tag{43}$$

where we have suppressed the subscript q for convenience. $\sigma_{in,0}$ is the cross section for ionizing the background gas but not stripping the beam ion; likewise, $\sigma_{st,0}$ is the cross section for stripping the beam ion without ionizing the background gas atom; and $\sigma_{in,st}$ is the cross section for both these processes to occur simultaneously. In the case of collisions between fast, heavy particles, like the beam ions, and light projectiles, such as the background gas atoms, almost all collisions will result in some ionization of the background gas atom; therefore $\sigma_{st,0} \simeq 0$, and we can write (43) as:

$$\sigma_t = \sigma_{in,0} + \sigma_{in,st} \ , \tag{44}$$

If we now define the ionization cross section as, $\sigma_{in} \equiv \sigma_{in,0} + \sigma_{in,st}$, then the probability equation (42) becomes:

$$P_{x,q,i} = \frac{\sigma_{x,q}}{\sigma_{in,q}} \left[1 - \exp\left(-\sigma_{in,q} n_g v_{z,q,i} t\right)\right] \ , \tag{45}$$

where for ionizing collisions we replace σ_x by σ_{in}, and for stripping collisions, by $\sigma_{st} \equiv \sigma_{st,0} + \sigma_{in,st} \simeq \sigma_{in,st}$. As discussed above, every ionizing collision between a beam ion q, i and a background gas neutral leads to the creation of a background gas ion of charge state $^{+}1$ and an electron; and every stripping collision will result in the conversion of the beam ion charge state from q to $q+1$ and the creation of an electron. The probability function (45) can then be solved to calculate the number of background gas ions, N_g, electrons, N_e, and beam ions of charge state q, N_q at time t.

We now have a complete set of equations for the following unknows. Particle radial positions, $r_{q,i}$, $z_{q,i}$, $r_{e,i}$: equation (19); axial positions, $z_{e,i}$, $r_{g,i}$, $z_{g,i}$: equation (20); electron velocities, $v_{r,e,i}$, $v_{z,e,i}$, $v_{\theta,e,i}$: equations (22), (23) and (24); beam ion velocities, $v_{r,q,i}$, $v_{\theta,q,i}$: equations (25) and (26); background gas ion velocities, $v_{r,g,i}$, $v_{z,g,i}$: equations (27) and (28); azimuthal magnetic field, B_θ: equation (30); radial and axial electric fields, E_r, E_z: equations (32) and (33); radial and axial current densities, J_r, J_z: equation (36); and particle numbers, N_g, N_e, N_q: equation (45). Given a set of boundary and initial conditions, we can solve these equations for the dynamics of the beam, in particular for the positions of the beam ions. The constant parameters that appear in these equations are the axial velocities for the beam ions, $v_{z,q,i}$, the beam ion and gas atom masses, m_b and m_g, the atomic number of the beam ions, Z_b, the background gas density, n_g, and the stripping and ionization cross sections, $\sigma_{st,q}$ and $\sigma_{in,q}$.

3 Numerical Equations

The equations in the previous section can be grouped into four categories. The particle equations for the positions and velocities; the field equations for the electric and magnetic fields; the particle-field interaction equations for the current densities and the field interpolation to the particle positions; and the particle-particle interaction equation for the particle numbers. Solving these equations is impossible analytically without making many simplifying assumptions. We therefore turn to numerical methods. The resulting numerical equations can be "solved" using a computer.

For the particle position and velocity equations we impose a temporal grid and employ a central differencing scheme to reduce the temporal derivatives to algebraic quantities. In addition to this we impose a spatial mesh and finite differencing techniques to reduce the spatial derivatives in the field equations. Particle-in-cell (PIC) techniques are used to interpolate the fields to the particle positions and calculate the current densities. Finally Monte Carlo collision (MCC) techniques are employed to calculate the particle numbers. A study of the boundary and initial conditions needed to solve these equations is deferred until later.

We first describe the geometry used to model the target chamber. In a liquid-wall chamber such as HYLIFE-II by Moir, et al., (1994), shown in figure (9), a pocket of liquid Flibe surrounds the target. Figure (11) * shows a top and side view of this pocket, the location of the target and the beams in the chamber. As mentioned before, in this thesis we study the transport of a single beam through the chamber, neglecting the other beams. We then replace the complex geometry shown in figure (11) by a large open-ended cylinder with a conducting wall, as shown in figure (12).

---

* Taken from Moir, et al., (1994).

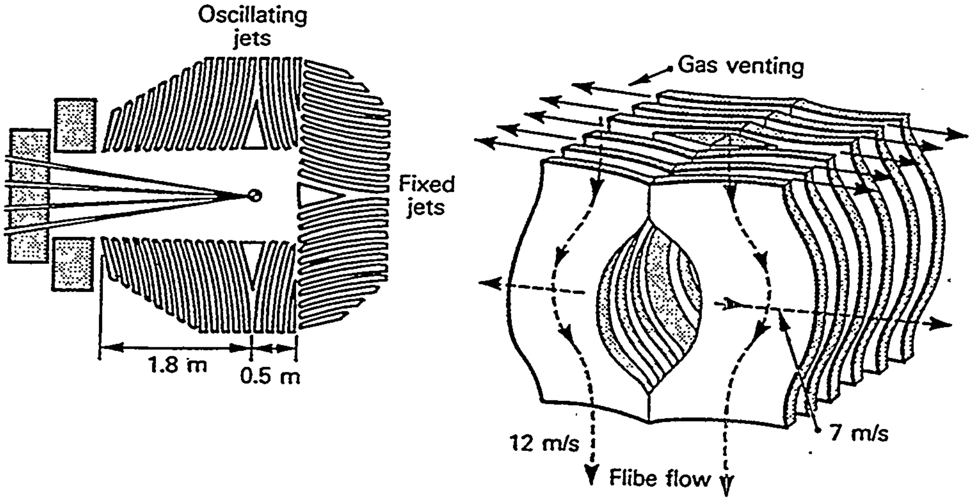

Figure 11: The oscillating and stationary jets of liquid Flibe in the HYLIFE-II chamber. Top and side views.

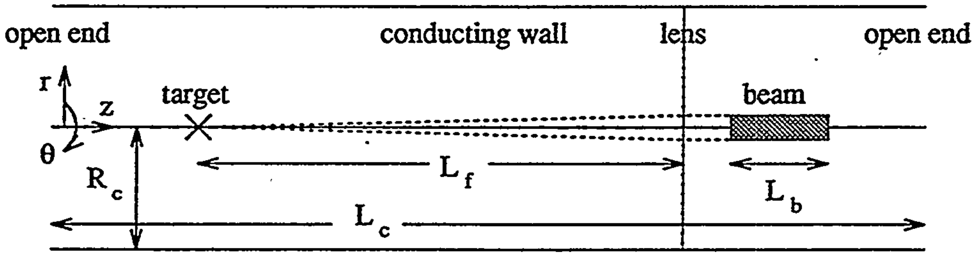

Figure 12: The simplified chamber geometry used to solve the system of equations.

The final focus system is included in the model as a thin lens located a distance $L_f \simeq a_l/\Theta$ from the target; where a_l is the radius of the beam at the lens, and Θ is the beam convergence angle. The radius of the cylinder, R_c is tens of centimeters; in the HYLIFE-II chamber, for example, the closest "structure" to the beam, once it enters the chamber, is the Flibe pocket which has $\sim 50\,cm$ inner radius around the target. The length of the cylinder, L_c, is several meters; it includes the distance from the lens to the target plus a few beam lengths, L_b, to the right of the lens and the left of the target as shown in figure (12). The beam starts behind the lens; as the simulation progresses, it travels down the axis of the cylinder, through the lens, towards the target. The background gas only exists in front of the lens.

3.1 Superparticle Equations

Evaluating the governing equations for every particle in the system, s, i, is computationally impractical; for the parameters given in table (3), the number of beam ions of charge state $^{+}1$ initially is $N_1 \simeq 2.6 \times 10^{14}$. Therefore we need to first discretize the number of particles. The discussion presented here follows that of Hockney and Eastwood (1988). The equations that need to be discretized are the particle position and velocity equations, (18) and (21). For each species, s, we group a number of particles together, and define:

$$\mathbf{r}_p \equiv \frac{1}{\Delta N} \sum_{i=1}^{\Delta N} \mathbf{r}_i \; , \tag{46}$$

where $\mathbf{r}_p$ is now the position of a group of ΔN particles at positions $\mathbf{r}_i$ indexed by p. The species subscript has been suppressed for convenience. Given any function of $\mathbf{r}$, $f(\mathbf{r})$, we approximate its value at the group position $\mathbf{r}_p$ by:

$$f(\mathbf{r}_p) \simeq \frac{1}{\Delta N} \sum_{i} f(\mathbf{r}_i) \; . \tag{47}$$

The validity of this approximation will be discussed in detail later, when we analyze the numerical methods.

We can use equation (47) for the velocities of the particles to write:

$$\mathbf{v}_p = \frac{1}{\Delta N} \sum_{i} \mathbf{v}_i \; , \tag{48}$$

where $\mathbf{v}_p$ is the velocity of a hypothetical particle at location $\mathbf{r}_p$, and $\mathbf{v}_i$ are, as before, the velocities of the particles located at $\mathbf{r}_i$. If we now take the time derivative of (46), we get:

$$\frac{d\mathbf{r}_p}{dt} = \mathbf{v}_p \ , \tag{49}$$

so that (18) retains its original form if we interpret $\mathbf{v}_p$ as the velocity of group p.

Taking the derivative of (48) results in:

$$\frac{d\mathbf{v}_p}{dt} + \frac{1}{\Delta N}\sum_i \frac{\mathbf{v}_i}{\gamma_i}\frac{d\gamma_i}{dt} = \frac{qe}{mm_o}\frac{1}{\Delta N}\sum_i \frac{1}{\gamma_i}\left(\mathbf{E}(\mathbf{r}_i) + \mathbf{v}_i \times \mathbf{B}(\mathbf{r}_i)\right) \ , \tag{50}$$

where we have substituted from (21). The relativistic factor, γ, is simply a function of velocity, therefore using (47) and interpolating the fields to the group position, $\mathbf{r}_p$, we can write:

$$\frac{\gamma_p d\mathbf{v}_p}{dt} + \mathbf{v}_p\frac{d\gamma_p}{dt} = \frac{qe}{mm_o}\left(\mathbf{E}(\mathbf{r}_p) + \mathbf{v}_p \times \mathbf{B}(\mathbf{r}_p)\right) \ . \tag{51}$$

If we define $m_p \equiv \Delta N m_o$ and $e_p \equiv \Delta N e$, then equation (51) can be written as:

$$\frac{d\mathbf{p}_p}{dt} = qe_p\left(\mathbf{E}(\mathbf{r}_p) + \mathbf{v}_p \times \mathbf{B}(\mathbf{r}_p)\right) \ , \tag{52}$$

and we see that (21) retains its form with $\mathbf{p}_p \equiv mm_p\gamma_p\mathbf{v}_p$.

We see that if we can approximate the value of a function at the position of a group of particles, $\mathbf{r}_p$, by (47), then the equations that describe the motion of the particles, (18) and (45) also describe the motion of these groups of particles, or "superparticles". Therefore all the subsequent equations derived from these also remain the same, provided we replace the particle index i by the superparticle index p, the mass m_o by the "super-mass" m_p, and the charge e by the "super-charge" e_p. From this point on, particles are to be thought of as superparticles with positions and velocities, $\mathbf{r}_{s,p}$ and $\mathbf{v}_{s,p}$, where s is the species label, $s = (q, e, g)$; and the summation over the particle numbers, N_s, is now done over superparticle numbers, $K_s \equiv N_s/\Delta N$.

3.2 Particle and Field Equations

We now describe the the method for differencing the three sets of time-evolution equations. The equations for the radial and axial positions of the superparticles: (19) and (20); the superparticle velocity equations: (22), (23), (24), (25), (26), (27) and (28); and the electric and magnetic field equations: (30), (32) and (33). Many of the techniques used here are described quite thoroughly in the definitive text by Birdsall and Langdon (1985) and the review article by Dawson (1983).

3.2.1 Particle Position Equations

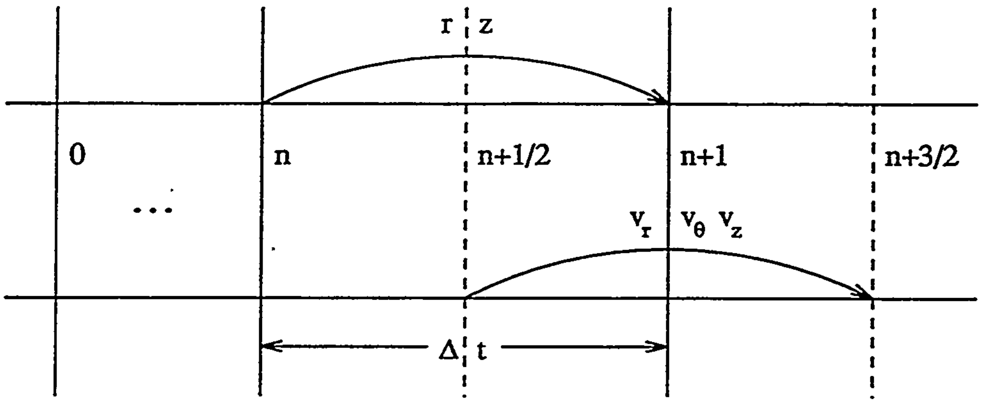

Figure 13: The temporal grid showing the particle positions and velocities.

To difference the particle position equations, (19) and (20), we temporally "stagger" the particle velocities from the positions as shown on the grid in figure (13). Δt is the temporal division over which the quantities are advanced, and n is an index used to refer to a particular location in time. This allows us to employ a "central differencing" scheme for the derivatives, which will be discussed in more detail later, when we analyze the numerical methods. The method is called "leap-frog" because the particle velocities at $n + 1/2$ are used to advance the positions from n to $n + 1$, and then the positions at $n+1$ are used to advance the velocities from $n+1/2$ to $n+3/2$.

Differencing the axial position equation (20) yields:

$$z_{s,p}^{n+1} = z_{s,p}^{n} + v_{z,s,p}^{n+1/2}\Delta t \ , \tag{53}$$

where the superscripts refer to the time-index. Thus if the axial position is know at time n and the axial velocity is known at time $n+1/2$ then we can find the position at time $n+1$, thereby advancing it by one time-division, Δt. For the beam ions $v_{z,s,p}^{n+1/2}$ is replaced by the invariant quantity $v_{z,q,p}$. Thus:

$$z_{q,p}^{n+1} = z_{q,p}^{n} + v_{z,q,p}\Delta t \ . \tag{54}$$

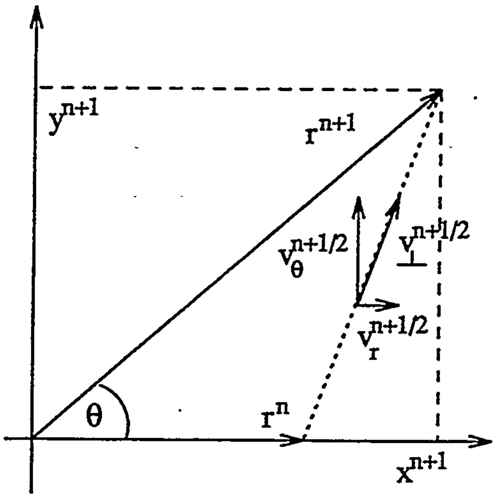

Figure 14: The Cartesian transverse plane for the radial position advance.

Differencing the radial position equation (19) presents some problems in cylindrical coordinates. Consider a particle that is close to the origin and has some finite radial and azimuthal velocity; by conservation of angular momentum, such a particle would be prevented from passing through the origin. If, however, we were to simply difference equation (19) in a fashion similar to equation (53), then, because the resulting equation would have no accommodation for the azimuthal velocity of the particle, the radial velocity could cause the particle to go through the origin in time Δt, clearly violating the conservation of angular momentum. Boris (1970) describes a method for overcoming this problem by performing the radial position advance in the Cartesian transverse plane. Figure (14) shows this transverse plane and the particle's position and velocity at the various times. Notice that the transverse velocity at $n + 1/2$, $v_{\perp,s,p}^{n+1/2}$, is resolved with respect to the position at n. The Cartesian coordinates of the particle are then given by:

$$x_{s,p}^{n+1} = r_{s,p}^{n} + v_{r,s,p}^{n+1/2} \Delta t \, , \tag{55}$$

and

$$y_{s,p}^{n+1} = v_{\theta,s,p}^{n+1/2} \Delta t \, . \tag{56}$$

Then the advanced radial position is calculated from:

$$r_{s,p}^{n+1} = \sqrt{(x_{s,p}^{n+1})^2 + (y_{s,p}^{n+1})^2} \, . \tag{57}$$

Since the background gas ions do not have any azimuthal velocity, this Cartesian advance is superfluous; equation (56) vanishes and equation (57) simply becomes the differenced version of equation (19), with the caveat that r always be positive. Thus

$$r_{g,p}^{n+1} = \sqrt{(r_{g,p}^{n} + v_{r,g,i}^{n+1/2} \Delta t)^2} \, . \tag{58}$$

Equations (55) and (56) imply that the particle lies on the x axis at time n. While the orientation of this axis is arbitrary initially, it cannot remain so, and if we wish the particle at time $n+1$ to also be located on the x axis in preparation for the advance to time $n+2$, then clearly we must rotate the Cartesian system by the angle

θ shown in figure (14). In particular this rotation will affect the orientation of the velocities at time $n+1/2$, therefore we defer this calculation till we study the particle velocity equations.

3.2.2 Field Equations

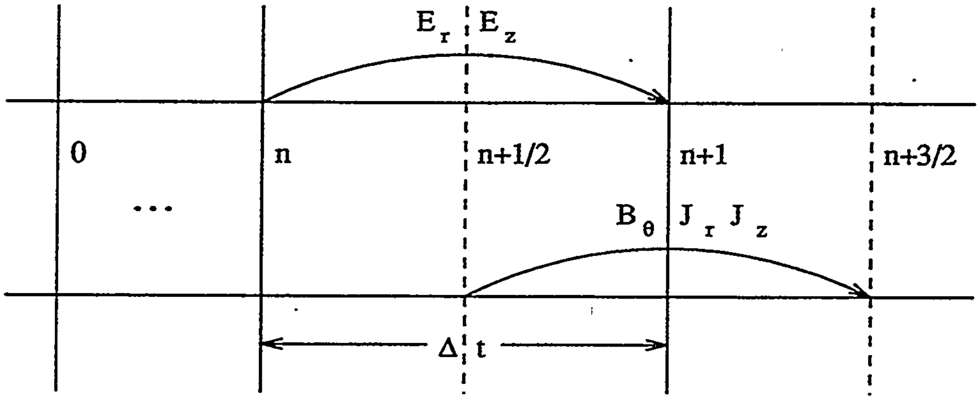

Figure 15: The temporal grid showing the electric and magnetic fields.

The field equations (30), (32) and (33) have both spatial and temporal derivatives. Therefore, in addition to imposing a temporal mesh, similar to the one employed for the particle positions as shown in figure (13), we also need to impose a spatial grid. The temporal mesh is shown in figure (15). We now "leap-frog" between the radial and axial electric fields, which are known at integral time-steps, and the azimuthal magnetic field and current densities, which are known at half-integral time-steps.

Since the spatial derivatives of the fields are needed in equations (30) to (33), we impose a rectangular (r, z) mesh, figure (16), on the cylindrical system shown in figure (12). This mesh is similar to the Cartesian grid used by Yee (1966), and allows us to use a "three-point finite difference" scheme for the spatial derivatives, described by Birdsall and Langdon (1985), and discussed in more detail later, when we analyze

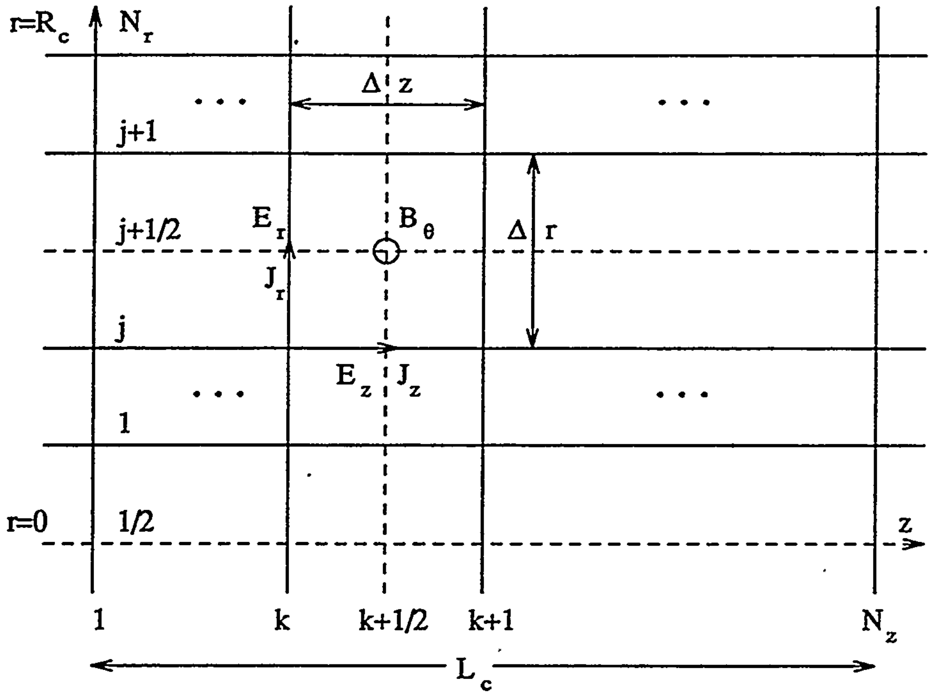

Figure 16: The spatial grid showing the locations of the electric and magnetic fields and the current densities.

the numerical methods. The radial mesh division is Δr and the axial division is Δz. The radial index, j, runs from 1/2 on axis, $r=0$, to N_r at the conducting wall, $r=R_c$. The axial grid index, k, runs from 1 at the open end on the left of the target to N_z at the open end on the right of the lens. The radial electric field, E_r, and current density, J_r, are computed on integral axial nodes and half-integral radial nodes; the axial electric field, E_z, and current density, J_z, are computed on half-integral axial nodes and integral radial nodes; and the azimuthal magnetic field, B_θ, is known at half-integral axial and radial nodes.

The Ampére-Maxwell equations (32) and (33) can be differenced as:

$$E^{n+1}_{r,j+1/2,k} = E^{n}_{r,j+1/2,k} - \frac{\Delta t \left(B^{n+1/2}_{\theta,j+1/2,k+1/2} - B^{n+1/2}_{\theta,j+1/2,k-1/2} \right)}{\mu_0 \epsilon_0 \Delta z} - \frac{\Delta t}{\epsilon_0} J^{n+1/2}_{r,j+1/2,k} , \quad (59)$$

$$E^{n+1}_{z,j,k+1/2} = E^{n}_{z,j,k+1/2} + \frac{2\Delta t\left(r_{j+1/2}B^{n+1/2}_{\theta,j+1/2,k+1/2} - r_{j-1/2}B^{n+1/2}_{\theta,j-1/2,k+1/2}\right)}{\mu_0\epsilon_0\left(r^2_{j+1/2} - r^2_{j-1/2}\right)} - \frac{\Delta t}{\epsilon_0}J^{n+1/2}_{z,j,k+1/2} , \tag{60}$$

where the additional subscripts on the fields and current densities refer to the spatial location on the mesh shown in figure (16), the superscripts, as before, refer to the temporal location in figure (15), and $r_{j+1/2}$, for instance, is the radius of the grid location $j+1/2$. Equations (59) and (60) advance the radial and axial electric fields from n to $n+1$ given the current densities and magnetic fields at $n+1/2$. The method for calculating these current densities is discussed later.

To advance the magnetic field we difference the Faraday-Maxwell equation (30):

$$B^{n+3/2}_{\theta,j+1/2,k+1/2} = B^{n+1/2}_{\theta,j+1/2,k+1/2} - \frac{\Delta t}{\Delta z}\left(E^{n+1}_{r,j+1/2,k+1} - E^{n+1}_{r,j+1/2,k}\right) + \frac{\Delta t}{\Delta r}\left(E^{n+1}_{z,j+1,k+1/2} - E^{n+1}_{z,j,k+1/2}\right) , \tag{61}$$

Therefore we advance the azimuthal magnetic field from $n+1/2$ to $n+3/2$ given the radial and axial electric fields at $n+1$.

3.2.3 Particle Velocity Equations

Finally, we turn to the velocity evolution equations (22), (23) and (24) for the electrons, (25) and (26) for the ions, and (27) and (28) for the background gas ions. The temporal locations of the velocities are shown in figure (13). We first look at the beam ions. The azimuthal velocity equation (26) is nothing more than the conservation of angular momentum:

$$\frac{d(r_{q,p}v_{\theta,q,p})}{dt} = 0 . \tag{62}$$

With the help of figure (17), the same as figure (14) with more detail, we can finite difference equation (62):

$$r^{n+3/2}_{q,p}v^{n+3/2}_{\perp,q,p}\sin\left(\chi' - \psi'\right) = r^{n+1/2}_{q,p}v^{n+1/2}_{\perp,q,p}\sin\left(\chi - \psi\right) , \tag{63}$$

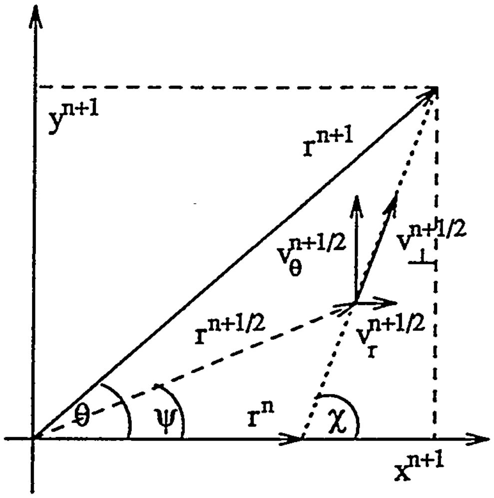

Figure 17: The Cartesian transverse plane for the velocity advance.

where $v_{\perp,q,p}^{n+1/2}$ is the transverse velocity of the beam ion, χ, as shown, is the angle between $r_{q,p}^{n}$ and $v_{\perp,q,p}^{n+1/2}$, and ψ is the angle between $r_{q,p}^{n}$ and $r_{q,p}^{n+1/2}$; similarly the primed quantities are these values at $n+3/2$. The problem with this equation is that $r_{q,p}^{n+1/2}$ and $r_{q,p}^{n+3/2}$ are "pseudo" positions, in that we do not actually have the particle positions at these half-integral temporal locations. As mentioned before $v_{\perp,q,p}^{n+1/2}$ is resolved with respect to the position at n, therefore the right-hand-side of equation (63) becomes:

$$r_{q,p}^{n+1/2} v_{\perp,q,p}^{n+1/2} \sin(\chi - \psi) = v_{\theta,q,p}^{n+1/2} \left[r_{q,p}^{n+1/2} \cos\psi - \frac{r_{q,p}^{n+1/2}}{\tan\chi} \sin\psi \right] ,$$

and from figure (17) we see that the term in the square brackets is nothing more than $r_{q,p}^{n}$. Similarly the left-hand-side of equation (63) becomes $v_{\theta,q,p}^{n+3/2} r_{q,p}^{n+1}$, and we can write (63) as:

$$v_{\theta,q,p}^{n+3/2} = \frac{r_{q,p}^{n}}{r_{q,p}^{n+1}} v_{\theta,q,p}^{n+1/2} . \tag{64}$$

We now have an equation for the advance of the azimuthal velocity from $n+1/2$ to $n+3/2$ given the particle positions at n and $n+1$. We can write this in a more insightful form if we realize the following:

$$\sin\theta_{q,p} \equiv \frac{y_{q,p}^{n+1}}{r_{q,p}^{n+1}} = \frac{v_{\theta,q,p}^{n+1/2}\Delta t}{r_{q,p}^{n+1}} \, , \qquad \cos\theta_{q,p} \equiv \frac{x_{q,p}^{n+1}}{r_{q,p}^{n+1}} = \frac{r_{q,p}^{n} + v_{r,q,p}^{n+1/2}\Delta t}{r_{q,p}^{n+1}} \, . \tag{65}$$

where $\theta_{q,p}$ is the angle between $r_{q,p}^{n}$ and $r_{q,p}^{n+1}$ shown in figure (17). Then equation (64) becomes:

$$v_{\theta,q,p}^{n+3/2} = v_{\theta,q,p}^{n+1/2}\cos\theta_{q,p} - v_{r,p}^{n+1/2}\sin\theta_{q,p} \, . \tag{66}$$

In this form equation (66) can be recognized as the the azimuthal component of the velocity that results from a rotation of $v_{\perp,q,p}^{n+1/2}$ by the angle θ, and accounts for the rotation of described by Boris (1970) and mentioned in the section on the position advance.

We now look at the radial velocity equation (25) for the beam ions. We can rewrite this as:

$$\frac{1}{r_{q,p}}\frac{d(r_{q,p}v_{r,q,p})}{dt} = \frac{v_{\perp,q,p}^{2}}{r_{q,p}} + \frac{qe_p}{\gamma_{q,p}m_b m_p}\left(E_r(\mathbf{r}_{q,p}) - v_{z,q,p}B_\theta(\mathbf{r}_{q,p})\right) \, . \tag{67}$$

Performing the same manipulations as we did with the azimuthal velocity equation, and remembering that $v_{\perp,q,p}^{n+1/2}$ is resolved with respect to the position at n, we finite difference (67) as

$$v_{r,q,p}^{n+3/2} = \frac{r_{q,p}^{n}v_{r,q,p}^{n+1/2}}{r_{q,p}^{n+1}} + \frac{\Delta t\left(v_{\perp,q,p}^{n+1/2}\right)^2}{r_{q,p}^{n+1}} + \frac{qe_p\Delta t}{\gamma_{q,p}m_b m_p}\left(E_{r,q,p}^{n+1} - v_{z,q,p}B_{\theta,q,p}^{n+1}\right) \, , \tag{68}$$

where $E_{r,q,p}^{n+1}$ is the radial electric field at $n+1$ at the position of the particle $\mathbf{r}_{q,p}^{n+1}$, and similarly for the azimuthal magnetic field; we'll discuss these fields in more detail later. Again, we can gain some insight if we define the rotated radial velocity as:

$$v_{r,q,p}^{\times} \equiv v_{r,q,p}^{n+1/2}\cos\theta_{q,p} + v_{\theta,q,p}^{n+1/2}\sin\theta_{q,p} \, , \tag{69}$$

where $\theta_{q,p}$ is the rotation angle shown in figure (17) and defined in equations (65). Then (68) becomes:

$$v_{r,q,p}^{n+3/2} = v_{r,q,p}^{\times} + \frac{qe_p\Delta t}{\gamma_{q,p}m_b m_p}\left(E_{r,q,p}^{n+1} - v_{z,q,p}B_{\theta,q,p}^{n+1}\right) \ . \tag{70}$$

Equation (70) completes the rotation described by Boris (1970) and advances the radial velocity from $n+1/2$ to $n+3/2$.

We now turn our attention to the gas ions. The time-evolution of the radial and axial velocities of these non-relativistic particles is given by equations (27) and (28). If we central difference these equations we get:

$$v_{r,g,p}^{n+3/2} = v_{r,g,p}^{n+1/2} + \frac{e_p\Delta t}{m_g m_p}\left(E_{r,g,p}^{n+1} - \frac{v_{z,g,p}^{n+3/2} + v_{z,g,p}^{n+1/2}}{2}B_{\theta,g,p}^{n+1}\right) \ , \tag{71}$$

$$v_{z,g,p}^{n+3/2} = v_{z,g,p}^{n+1/2} + \frac{e_p\Delta t}{m_g m_p}\left(E_{z,g,p}^{n+1} + \frac{v_{r,g,p}^{n+3/2} + v_{r,g,p}^{n+1/2}}{2}B_{\theta,g,p}^{n+1}\right) \ , \tag{72}$$

The problem with these equations, unlike that of the beam ions, is that they are coupled in the velocities through the force terms. In the case of the beam ions, the force term contains only the axial velocity which is assumed to be invariant. Boris (1970) provides an elegant solution to this problem by decoupling the electric and magnetic forces. We first define a velocity advance based on half the electric force:

$$\begin{aligned} v_{r,g,p}^{-} &\equiv v_{r,g,p}^{n+1/2} + \frac{e_p\Delta t}{2m_g m_p}E_{r,g,p}^{n+1} \ , \\ v_{z,g,p}^{-} &\equiv v_{z,g,p}^{n+1/2} + \frac{e_p\Delta t}{2m_g m_p}E_{z,g,p}^{n+1} \ . \end{aligned} \tag{73}$$

Then, anticipating that we will have to end the velocity advance by conducting a similar operation for the remaining half of the magnetic field we write:

$$v_{r,g,p}^{n+3/2} = v_{r,g,p}^{+} + \frac{e_p\Delta t}{2m_g m_p}E_{r,g,p}^{n+1} \ , \tag{74}$$

$$v_{z,g,p}^{n+3/2} = v_{z,g,p}^{+} + \frac{e_p\Delta t}{2m_g m_p}E_{z,g,p}^{n+1} \ . \tag{75}$$

These equations, (74) and (75), are sufficient to advance the radial and axial velocities of the particles provided we know the quantities $v^+_{r,g,p}$ and $v^+_{z,g,p}$. Clearly we need to solve for these quantities in terms of the known values $v^-_{r,g,p}$ and $v^-_{z,g,p}$ defined by equations (73). If we substitute (74), (75) and (73) into (71) and (72) we get what look like a set of rotation formulae:

$$\begin{aligned} v^+_{r,g,p} &= v^-_{r,g,p}\cos\phi_{g,p} - v^-_{z,g,p}\sin\phi_{g,p} \ , \\ v^+_{z,g,p} &= v^-_{r,g,p}\sin\phi_{g,p} + v^-_{z,g,p}\cos\phi_{g,p} \ , \end{aligned} \tag{76}$$

where $\sin\phi_{g,p}$ and $\cos\phi_{g,p}$ are defined as:

$$\begin{aligned} \sin\phi_{g,p} &\equiv \frac{\left(\frac{e_p B^{n+1}_{\theta,g,p}\Delta t}{m_g m_p}\right)}{1+\left(\frac{e_p B^{n+1}_{\theta,g,p}\Delta t}{2m_g m_p}\right)^2} \ , \\ \cos\phi_{g,p} &\equiv \frac{1-\left(\frac{e_p B^{n+1}_{\theta,g,p}\Delta t}{2m_g m_p}\right)^2}{1+\left(\frac{e_p B^{n+1}_{\theta,g,p}\Delta t}{2m_g m_p}\right)^2} \ . \end{aligned} \tag{77}$$

We expect (76) to be a rotation because the azimuthal magnetic field will indeed rotate the radial and axial velocities; the significance of this will be discussed in more detail later. These equations then provide the desired relations between $v^+_{r,g,p}$ and $v^-_{r,g,p}$, and $v^+_{z,g,p}$ and $v^-_{z,g,p}$, where $v^-_{r,g,p}$ and $v^-_{z,g,p}$ are given by (73). Then equations (74) and (75) can be used to advance the radial and axial velocities of the gas ions from $n+1/2$ to $n+3/2$.

Finally, we look at the velocity advance of the fully relativistic electrons, given by equations (22), (23) and (24). As in Birdsall and Langdon (1985) we proceed by defining a "generalized velocity", $u_{e,p} \equiv \gamma_{e,p} v_{e,p}$, where $v_{e,p}$ is any velocity component, and $\gamma_{e,p}$, as before, is the relativistic factor. We now deal with this quantity instead of the velocities and convert after the advance is complete. The azimuthal velocity equation (24) can then be written as:

$$\frac{d(r_{e,p}u_{\theta,e,p})}{dt} = 0 \ . \tag{78}$$

This is similar to the azimuthal velocity equation for the beam ions; therefore using the method of Boris (1970) we write the following difference equation:

$$u_{\theta,e,p}^{n+3/2} = u_{\theta,e,p}^{n+1/2} \cos\theta_{e,p} - u_{r,p}^{n+1/2} \sin\theta_{e,p} \ , \tag{79}$$

where the angle of rotation $\theta_{e,p}$ is defined, as in the case of the ions, by:

$$\begin{aligned} \sin\theta_{e,p} &\equiv \frac{u_{\theta,e,p}^{n+1/2}\Delta t}{\gamma_{e,p}^{n+1/2} r_{e,p}^{n+1}} \ , \\ \cos\theta_{e,p} &\equiv \frac{r_{e,p}^{n}}{r_{e,p}^{n+1}} + \frac{u_{r,e,p}^{n+1/2}\Delta t}{\gamma_{e,p}^{n+1/2} r_{e,p}^{n+1}} \ , \end{aligned} \tag{80}$$

and the relativistic factor can be written as:

$$\left(\gamma_{e,p}^{n+1/2}\right)^2 \equiv 1 + \frac{(u_{r,e,p}^{n+1/2})^2 + (u_{z,e,p}^{n+1/2})^2 + (u_{\theta,e,p}^{n+1/2})^2}{c^2} \ . \tag{81}$$

Equation (79) advances the azimuthal velocity from $n+1/2$ to $n+3/2$.

The coupled radial and axial velocity equations (22) and (23) become:

$$\frac{1}{r_{e,p}} \frac{d(r_{e,p}u_{r,e,p})}{dt} = \frac{u_{\perp,e,p}^2}{r_{e,p}\gamma_{e,p}} - \frac{e_p}{m_e m_p}\left(E_r(\mathrm{r}_{e,p}) - \frac{u_{z,e,p}}{\gamma_{e,p}} B_\theta \mathrm{r}_{e,p})\right) \ , \tag{82}$$

$$\frac{du_{z,e,p}}{dt} = -\frac{e_p}{m_e m_p}\left(E_z(\mathrm{r}_{e,p}) + \frac{u_{r,e,p}}{\gamma_{e,p}} B_\theta(\mathrm{r}_{e,p})\right) \ . \tag{83}$$

Using the same manipulations as we did for the radial velocity of the beam ions, we can difference these two equations as:

$$u_{r,e,p}^{n+3/2} = u_{r,e,p}^{\times} - \frac{e_p\Delta t}{m_e m_p}\left(E_{r,e,p}^{n+1} - \frac{u_{z,e,p}^{n+3/2} + u_{z,e,p}^{n+1/2}}{2\gamma_{e,p}^{n+1}} B_{\theta,e,p}^{n+1}\right) \ , \tag{84}$$

$$u_{z,e,p}^{n+3/2} = u_{z,e,p}^{n+1/2} - \frac{e_p\Delta t}{m_e m_p}\left(E_{z,e,p}^{n+1} + \frac{u_{r,e,p}^{n+3/2} + u_{r,e,p}^{n+1/2}}{2\gamma_{e,p}^{n+1}} B_{\theta,e,p}^{n+1}\right) \ , \tag{85}$$

where, as in the case of the beam ions,

$$u_{r,e,p}^{\times} = u_{r,e,p}^{n+1/2} \cos\theta_{e,p} + v_{\theta,e,p}^{n+1/2} \sin\theta_{e,p} \ , \tag{86}$$

and $\sin\theta_{e,p}$ and $\cos\theta_{e,p}$ are given by equations (80). Then employing the concept described by Boris (1970) of using half the electric force, followed by a magnetic rotation, and then the remaining half of the electric force to advance the velocities as we did for the gas ions, we can write equations (84) and (85) as:

$$u_{r,e,p}^{n+3/2} = u_{r,e,p}^{+} - \frac{e_p\Delta t}{2m_e m_p} E_{r,e,p}^{n+1} \,, \tag{87}$$

$$u_{z,e,p}^{n+3/2} = u_{z,e,p}^{+} - \frac{e_p\Delta t}{2m_e m_p} E_{z,e,p}^{n+1} \,, \tag{88}$$

where

$$\begin{aligned} u_{r,e,p}^{+} &= u_{r,e,p}^{-}\cos\phi_{e,p} - u_{z,e,p}^{-}\sin\phi_{e,p} \,, \\ u_{z,e,p}^{+} &= u_{r,e,p}^{-}\sin\phi_{e,p} + u_{z,e,p}^{-}\cos\phi_{e,p} \,, \end{aligned} \tag{89}$$

where

$$\begin{aligned} \sin\phi_{e,p} &\equiv \frac{-\left(\dfrac{e_p B_{\theta,e,p}^{n+1}\Delta t}{\gamma_{e,p}^{n+1} m_e m_p}\right)}{1+\left(\dfrac{e_p B_{\theta,e,p}^{n+1}\Delta t}{2\gamma_{e,p}^{n+1} m_e m_p}\right)^2} \,, \\ \cos\phi_{e,p} &\equiv \frac{1-\left(\dfrac{e_p B_{\theta,e,p}^{n+1}\Delta t}{2\gamma_{e,p}^{n+1} m_e m_p}\right)^2}{1+\left(\dfrac{e_p B_{\theta,e,p}^{n+1}\Delta t}{2\gamma_{e,p}^{n+1} m_e m_p}\right)^2} \,, \end{aligned} \tag{90}$$

and

$$\begin{aligned} u_{r,e,p}^{-} &\equiv u_{r,e,p}^{\times} - \frac{e_p\Delta t}{2m_e m_p} E_{r,e,p}^{n+1} \,, \\ u_{z,e,p}^{-} &\equiv u_{z,e,p}^{n+1/2} - \frac{e_p\Delta t}{2m_e m_p} E_{z,e,p}^{n+1} \,. \end{aligned} \tag{91}$$

We now need to determine $\gamma_{e,p}^{n+1}$ in equations (90). However, the velocities are defined at half-integral temporal nodes and are not known at $n+1$; but since the magnetic force serves only to rotate the velocities, we can determine the "pseudo" velocities at integral nodes by the half electric advance. Then:

$$\gamma_{e,p}^{n+1} \equiv 1 + \frac{(u_{r,e,p}^{-})^2 + (u_{z,e,p}^{-})^2 + (u_{\theta,e,p}^{n+3/2})^2}{c^2} \,. \tag{92}$$

Finally the actual velocities are defined as $v_{e,p}^{n+3/2} \equiv u_{e,p}^{n+3/2}/\gamma_{e,p}^{n+3/2}$, where $\gamma_{e,p}^{n+3/2}$ is given by an equation similar to (81), except that the velocities at $n+1/2$ are now replaced by those at $n+3/2$.

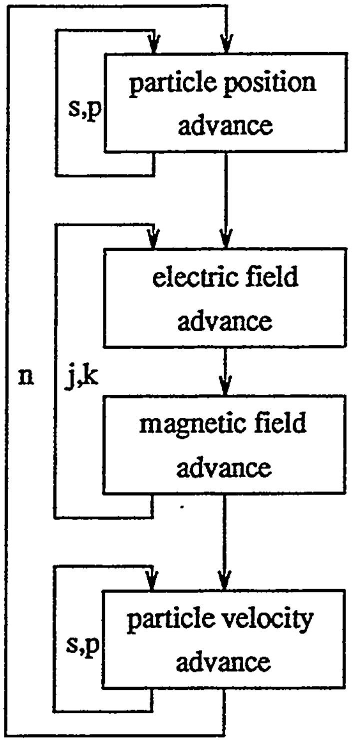

Figure 18: Flow-chart of the algorithm for advancing particle and field quantities.

This concludes the differencing of the time evolution equations for the superparticle positions, (19) and (20), superparticle velocities, (22), (23), (24), (25), (26), (27) and (28), and the fields, (30), (32) and (33). Given a set of superparticle positions, $r^n_{s,p}$, $z^n_{s,p}$, beam ion velocities, $v^{n+1/2}_{r,q,p}$, $v^{n+1/2}_{\theta,q,p}$, $v_{z,q,p}$, gas ion velocities, $v^{n+1/2}_{r,g,p}$, $v^{n+1/2}_{z,g,p}$, electron velocities, $v^{n+1/2}_{r,e,p}$, $v^{n+1/2}_{\theta,e,p}$, $v^{n+1/2}_{z,e,p}$, and fields, $E^n_{r,j+1/2,k}$, $E^n_{r,j,k+1/2}$, $B^{n+1/2}_{\theta,j+1/2,k+1/2}$, the algorithm for advancing these quantities to the next temporal index, Δt in time away, proceeds as follows. We first use equations (53) and (54) to advance the axial positions, and equations (57) and (58) to advance the radial positions of the particles from n to $n+1$. This is done for every single superparticle indexed by s, p. We then use equations (59) and (60) to advance the radial and axial electric fields from n to $n+1$, and equation (61) to advance the azimuthal magnetic field from $n+1/2$ to $n+3/2$. This is done for every grid point indexed by j, k. Finally we use equations (66) and (70) to advance the azimuthal and radial velocities of the beam ions, equations (74) and (75) to advance the radial and axial velocities of the gas ions, and equations (79), (87) and (88) to advance the azimuthal, radial and axial velocities of the electrons from $n + 1/2$ to $n + 3/2$. Again we do this for every particle, s, p. Figure (18) shows the flow-chart for this procedure. At the end of this series of operations we have all the particle positions, particle velocities, and fields at a time Δt later. We repeat this for every time-step, n, "leap-frogging" forward in time.

3.3 Particle-Field and Particle-Particle Interactions

The particles affect the fields through the current densities, $J^{n+1/2}_{r,j+1/2,k}$, $J^{n+1/2}_{z,j,k+1/2}$, which are used to advance the electric fields. And the fields affect the particles through the Lorentz force which requires a knowledge of the fields at the superparticle locations, $E^{n+1}_{r,s,p}$, $E^{n+1}_{z,s,p}$, $B^{n+1}_{\theta,s,p}$, in order to advance the velocities. Particle-in-cell (PIC) techniques, where the particles occupy certain locations within the spatial mesh "cells", are used to evaluate both these quantities.

In order to calculate the current densities, we need to know the number of superparticles, K_s. The number of particles of any given species will change due to the collisions between particles. These collisions are described by the collision probability equation (45). We shall use Monte Carlo collision (MCC) techniques to solve the probability equations and determine the particle numbers.

3.3.1 Field Interpolation

We now discuss a method for interpolating the fields to the particle positions. In general these fields are defined as:

$$\mathbf{F}(\mathbf{r}_{s,p}) \equiv \int \mathbf{F}(\mathbf{r})\delta^3(\mathbf{r}-\mathbf{r}_{s,p})dV \ . \tag{93}$$

Since we do not know the fields at all positions in space, $\mathbf{r}$, but only at certain grid locations, $\mathbf{r}_{j,k}$, we follow Hockney and Eastwood (1988) and approximate (93) by:

$$\mathbf{F}(\mathbf{r}_{s,p}) = \sum_{j,k} \mathbf{F}(\mathbf{r}_{j,k})W(\mathbf{r}_{s,p}-\mathbf{r}_{j,k})dV \ , \tag{94}$$

where W is some "weighting" function which, like the delta function, determines to what extent regions of space, now defined by the grid points $\mathbf{r}_{j,k}$, contribute to the particle position, $\mathbf{r}_{s,p}$. The validity of this approximation will be discussed in more detail later, when we analyze the numerical methods.

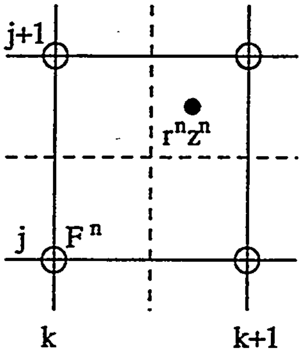

Figure 19: Spatial mesh for the interpolation of the fields to the particle positions.

In order to determine the weighting functions, W, we impose some constraints on their form and function. The first of these is that only the fields from the four nearest grid points will be used in the interpolation, then equation (94) becomes:

$$\begin{aligned} F^n_{s,p} = {} & F^n_{j,k}W(r^n_{s,p}, z^n_{s,p}; r_j, z_k) + F^n_{j+1,k}W(r^n_{s,p}, z^n_{s,p}; r_{j+1}, z_k) + \\ & F^n_{j+1,k+1}W(r^n_{s,p}, z^n_{s,p}; r_{j+1}, z_{k+1}) + F^n_{j,k+1}W(r^n_{s,p}, z^n_{s,p}; r_j, z_{k+1}) \ , \end{aligned} \tag{95}$$

where $F^n_{s,p}$ is the interpolated field to the particle location, $(r^n_{s,p}, z^n_{s,p})$ at time n, and $F^n_{j,k}$ are the fields at the spatial grid points, (r_j, z_k), and temporal location n. With the above constraint then, the grid point j, k in equation (95) is such that $r_j < r^n_{s,p} < r_{j+1}$, $z_k < z^n_{s,p} < z_{k+1}$ as shown in figure (19). We now stipulate that these weighting functions be bilinear in r^2, z. This is also referred to as "volume weighting" because the weight associated with any grid point will then be related to the volume of space between the particle and the grid point; where, for example, the volume of space between the particle shown in figure (19) and the grid point j, k is $\pi((r^n_{s,p})^2 - (r_j)^2)(z^n_{s,p} - z^k)$. Using this volume to interpolate the forces from the grid points to the particles yields:

$$
\begin{aligned}
W(r^n_{s,p}, z^n_{s,p}; r_j, z_k) &= \left(\frac{(r_{j+1})^2 - (r^n_{s,p})^2}{(r_{j+1})^2 - (r_j)^2}\right)\left(\frac{z_{k+1} - z^n_{s,p}}{z_{k+1} - z_k}\right) ,\\
W(r^n_{s,p}, z^n_{s,p}; r_{j+1}, z_k) &= \left(\frac{(r^n_{s,p})^2 - (r_j)^2}{(r_{j+1})^2 - (r_j)^2}\right)\left(\frac{z_{k+1} - z^n_{s,p}}{z_{k+1} - z_k}\right) ,\\
W(r^n_{s,p}, z^n_{s,p}; r_{j+1}, z_{k+1}) &= \left(\frac{(r^n_{s,p})^2 - (r_j)^2}{(r_{j+1})^2 - (r_j)^2}\right)\left(\frac{z^n_{s,p} - z_k}{z_{k+1} - z_k}\right) ,\\
W(r^n_{s,p}, z^n_{s,p}; r_j, z_{k+1}) &= \left(\frac{(r_{j+1})^2 - (r^n_{s,p})^2}{(r_{j+1})^2 - (r_j)^2}\right)\left(\frac{z^n_{s,p} - z_k}{z_{k+1} - z_k}\right) .
\end{aligned}
\tag{96}
$$

More generally, for all nodes in the system, equation (96) can be written as:

$$
W(r^n_{s,p}, z^n_{s,p}; r_j, z_k) = \begin{cases}
\left(\frac{(r_{j+1})^2-(r^n_{s,p})^2}{(r_{j+1})^2-(r_j)^2}\right)\left(\frac{z_{k+1}-z^n_{s,p}}{z_{k+1}-z_k}\right) & \text{if } r_j < r^n_{s,p} < r_{j+1} \text{ and} \\
 & z_k < z^n_{s,p} < z_{k+1} , \\
\left(\frac{(r_{j+1})^2-(r^n_{s,p})^2}{(r_{j+1})^2-(r_j)^2}\right)\left(\frac{z^n_{s,p}-z_{k-1}}{z_k-z_{k-1}}\right) & \text{if } r_j < r^n_{s,p} < r_{j+1} \text{ and} \\
 & z_{k-1} < z^n_{s,p} < z_k , \\
\left(\frac{(r^n_{s,p})^2-(r_{j-1})^2}{(r_j)^2-(r_{j-1})^2}\right)\left(\frac{z^n_{s,p}-z_{k-1}}{z_k-z_{k-1}}\right) & \text{if } r_{j-1} < r^n_{s,p} < r_j \text{ and} \\
 & z_{k-1} < z^n_{s,p} < z_k , \\
\left(\frac{(r^n_{s,p})^2-(r_{j-1})^2}{(r_j)^2-(r_{j-1})^2}\right)\left(\frac{z_{k+1}-z^n_{s,p}}{z_{k+1}-z_k}\right) & \text{if } r_{j-1} < r^n_{s,p} < r_j \text{ and} \\
 & z_k < z^n_{s,p} < z_{k+1} , \\
0 & \text{otherwise} ,
\end{cases}
\tag{97}
$$

It must be mentioned that this is only one type of weighting; there are other schemes that involve more or less grid points, other than the nearest four. Hockney and Eastwood (1988) present a good discussion of the various weighting schemes. For instance the "nearest-grid-point", or NGP, method interpolates the field from only the nearest single grid point to the particle. We'll discuss these weighting functions in more detail later.

We can now interpolate the fields at grid points, $F^n_{j,k}$, to the particle position, $(r_{s,p}, z_{s,p})$, using equation (94):

$$F^n_{s,p} = \sum_{j,k} F^n_{j,k} W(r^n_{s,p}, z^n_{s,p}; r_j, z_k) \ , \tag{98}$$

where $W(r^n_{s,p}, z^n_{s,p}; r_j, z_k)$ are given by equations (97). $F^n_{j,k}$ can be either the radial or axial electric fields or azimuthal magnetic fields. The electric fields are known at the same temporal index, n, as the particle positions and so can be used directly in equation (98). However the magnetic fields are known at half-integral temporal indices, $n-1/2$, and $n+1/2$, and therefore must be time-averaged before they can be used in equation (98):

$$B^n_{\theta,j+1/2,k+1/2} = \frac{1}{2}\left(B^{n-1/2}_{\theta,j+1/2,k+1/2} + B^{n+1/2}_{\theta,j+1/2,k+1/2}\right) \ . \tag{99}$$

This is done for every superparticle, s, p, in the system.

3.3.2 Current Density Equations

We now turn to the current density calculations. Verboncoeur, et al. (1995), present a charge conserving method for calculating the current densities. We start by solving the continuity equation (34). If we finite difference this equation around the

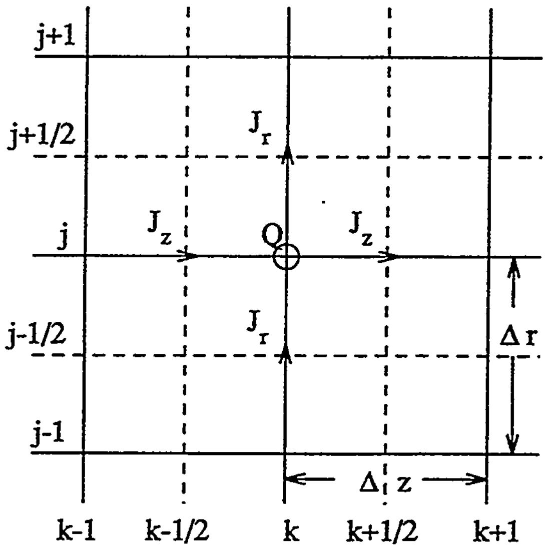

Figure 20: Spatial mesh showing the locations of the current densities and charge.

location (j,k) as shown in figure (20) we get:

$$\frac{-\left(Q^{n+1}_{j,k}-Q^{n}_{j,k}\right)}{\pi\left(r^2_{j+1/2}-r^2_{j-1/2}\right)\Delta z\Delta t}=\frac{2\left(r_{j+1/2}J^{n+1/2}_{r,j+1/2,k}-r_{j-1/2}J^{n+1/2}_{r,j-1/2,k}\right)}{r^2_{j+1/2}-r^2_{j-1/2}}+\frac{J^{n+1/2}_{z,j,k+1/2}-J^{n+1/2}_{z,j,k-1/2}}{\Delta z}\,, \tag{100}$$

where $Q_{j,k}$ is the charge at location j,k and is defined as:

$$Q(\mathrm{r}_{j,k})\equiv\int\rho(\mathrm{r})dV_{j,k}\ , \tag{101}$$

where the integration is performed over a small volume surrounding the grid location, $\mathrm{r}_{j,k}$. If we substitute for the charge density, ρ, from (35), and use the same argument as we did for interpolating the fields in the previous section, where we replaced the integration over the delta function by some weighting function, W, described by Hockney and Eastwood (1988), we get:

$$Q^{n}_{j,k}=qe_pW(r^n,z^n;r_j,z_k)\ . \tag{102}$$

where, for simplicity, we have assumed that we have a particle of charge state q located at (r^n,z^n); we have suppressed the subscripts, s,p, denoting a single particle.

We can define:

$$\Delta Q_{j,k} \equiv Q_{j,k}^{n+1} - Q_{j,k}^{n} = q e_p \left(W_{j,k}^{n+1} - W_{j,k}^{n} \right) \ , \tag{103}$$

where $W_{j,k}^n$ is used as a shorthand notation for $W(r^n, z^n; r_j, z_k)$. To solve for the current densities we write a set of equations (100) for each node in the spatial mesh, substituting from (103) for the charge, and then solve this set with appropriate boundary conditions.

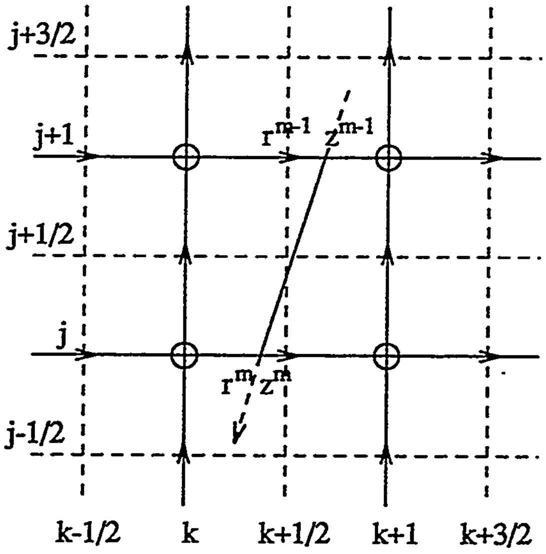

Figure 21: Spatial mesh showing the trajectory of a hypothetical particle.

Consider a hypothetical particle that starts at position (r^n, z^n) at time index n and ends at (r^{n+1}, z^{n+1}) at time index $n+1$ after having crossed several "cell" boundaries, where a cell is defined by the solid lines marked by integral grid indices in figure (21). The location at which the particle crosses the cell boundary is given by $(r^{n,m}, z^{n,m})$, $m = 0, 1, 2, 3, \cdots, M+1$, where $m = 1$ is the location of the first cell boundary crossing, $m = M$ is the location of the last crossing, and $(r^{n,0}, z^{n,0}) \equiv (r^n, z^n)$ and $(r^{n,M+1}, z^{n,M+1}) \equiv (r^{n+1}, z^{n+1})$. A segment of such a particle's trajectory is shown in figure (21). Then we can rewrite equation (103) as:

$$\Delta Q_{j,k} = q e_p \sum_{m=1}^{M+1} \left(W_{j,k}^{n,m} - W_{j,k}^{n,m-1} \right) \ , \tag{104}$$

where $W_{j,k}^{n,m}$ are the weighting functions with (r^n, z^n) replaced by the boundary crossings $(r^{n,m}, z^{n,m})$. We now attempt to solve for the current densities by writing a set of equations similar to (100) for each node on the mesh for a given particle. From (104) we see that we can replace $\Delta Q_{j,k}$ in these equations by a summation over cell traversals, m. Therefore we can break a particle's trajectory from (r^n, z^n) to (r^{n+1}, z^{n+1}) into a series of cell traversals and treat each of these independently, summing the current densities at the end. If we now choose W to be the same functions as were used to interpolate the fields, (97), then $W_{j,k}^{n,m}$ and $W_{j,k}^{n,m-1}$ are nonzero only for the four integral nodes surrounding the cell. For the hypothetical particle shown in figure (21), these nodes are (j,k), $(j+1,k)$, $(j+1,k+1)$, and $(j,k+1)$. Therefore for every cell traversal we can write the following equations for each node in the system by substituting for $\Delta Q_{j,k}$ from (104) into (100):

$$\begin{aligned}
\frac{q e_p}{\pi \Delta t} \left(W_{j,k}^{n,m-1} - W_{j,k}^{n,m} \right) &= 2\Delta z \left(r_{j+1/2} J_{r,j+1/2,k}^{n+1/2,m} - r_{j-1/2} J_{r,j-1/2,k}^{n+1/2,m} \right) + \\
&\quad \left(r_{j+1/2}^2 - r_{j-1/2}^2 \right) \left(J_{z,j,k+1/2}^{n+1/2,m} - J_{z,j,k-1/2}^{n+1/2,m} \right) \ , \\
\frac{q e_p}{\pi \Delta t} \left(W_{j+1,k}^{n,m-1} - W_{j+1,k}^{n,m} \right) &= 2\Delta z \left(r_{j+3/2} J_{r,j+3/2,k}^{n+1/2,m} - r_{j+1/2} J_{r,j+1/2,k}^{n+1/2,m} \right) + \\
&\quad \left(r_{j+3/2}^2 - r_{j+1/2}^2 \right) \left(J_{z,j+1,k+1/2}^{n+1/2,m} - J_{z,j+1,k-1/2}^{n+1/2,m} \right) \ , \\
\frac{q e_p}{\pi \Delta t} \left(W_{j+1,k+1}^{n,m-1} - W_{j+1,k+1}^{n,m} \right) &= 2\Delta z \left(r_{j+3/2} J_{r,j+3/2,k+1}^{n+1/2,m} - r_{j+1/2} J_{r,j+1/2,k+1}^{n+1/2,m} \right) + \\
&\quad \left(r_{j+3/2}^2 - r_{j+1/2}^2 \right) \left(J_{z,j+1,k+3/2}^{n+1/2,m} - J_{z,j+1,k+1/2}^{n+1/2,m} \right) \ , \\
\frac{q e_p}{\pi \Delta t} \left(W_{j,k+1}^{n,m-1} - W_{j,k+1}^{n,m} \right) &= 2\Delta z \left(r_{j+1/2} J_{r,j+1/2,k+1}^{n+1/2,m} - r_{j-1/2} J_{r,j-1/2,k+1}^{n+1/2,m} \right) + \\
&\quad \left(r_{j+1/2}^2 - r_{j-1/2}^2 \right) \left(J_{z,j,k+3/2}^{n+1/2,m} - J_{z,j,k+1/2}^{n+1/2,m} \right) \ ,
\end{aligned} \tag{105}$$

where grid point j,k is such that $r_j < r^{n,m-1} < r_{j+1}$, $z_k < z^{n,m-1} < z_{k+1}$. For the rest of the nodes on the spatial mesh we have homogeneous equations of the form:

$$\begin{aligned} 0 =& 2\Delta z \left(r_{j-1/2} J^{n+1/2,m}_{r,j-1/2,k} - r_{j-3/2} J^{n+1/2,m}_{r,j-3/2,k} \right) + \\ & \left(r^2_{j-1/2} - r^2_{j-3/2} \right) \left(J^{n+1/2,m}_{z,j-1,k+1/2} - J^{n+1/2,m}_{z,j-1,k-1/2} \right) \ , \end{aligned} \tag{106}$$

where $\mathbf{J}^{n+1/2,m}$ are the current densities calculated from this particular traversal, so that the total current density on mesh points for each particle is given by a sum over all cell crossings. We can solve this set of equations with appropriate boundary conditions. The simplest boundary condition is to set all current densities on mesh points not immediately surrounding the cell to zero. We can then reduce this set of equations, one for each node, to four equations for the four nodes surrounding the cell:

$$\begin{aligned} \frac{qe_p}{\pi\Delta t} \left(W^{n,m-1}_{j,k} - W^{n,m}_{j,k} \right) &= 2\Delta z r_{j+1/2} J^{n+1/2,m}_{r,j+1/2,k} + \left(r^2_{j+1/2} - r^2_{j-1/2} \right) J^{n+1/2,m}_{z,j,k+1/2} \ , \\ \frac{qe_p}{\pi\Delta t} \left(W^{n,m-1}_{j+1,k} - W^{n,m}_{j+1,k} \right) &= -2\Delta z r_{j+1/2} J^{n+1/2,m}_{r,j+1/2,k} + \left(r^2_{j+3/2} - r^2_{j+1/2} \right) J^{n+1/2,m}_{z,j+1,k+1/2} \ , \\ \frac{qe_p}{\pi\Delta t} \left(W^{n,m-1}_{j+1,k+1} - W^{n,m}_{j+1,k+1} \right) &= -2\Delta z r_{j+1/2} J^{n+1/2,m}_{r,j+1/2,k+1} - \left(r^2_{j+3/2} - r^2_{j+1/2} \right) J^{n+1/2,m}_{z,j+1,k+1/2} , \\ \frac{qe_p}{\pi\Delta t} \left(W^{n,m-1}_{j,k+1} - W^{n,m}_{j,k+1} \right) &= 2\Delta z r_{j+1/2} J^{n+1/2,m}_{r,j+1/2,k+1} - \left(r^2_{j+1/2} - r^2_{j-1/2} \right) J^{n+1/2,m}_{z,j,k+1/2} \ . \end{aligned} \tag{107}$$

Solving these equations for the four current densities surrounding this cell yields:

$$\begin{aligned} J^{n+1/2,m}_{r,j+1/2,k} &= \frac{qe_p}{4\pi\Delta t \Delta r (\Delta z)^2} \left(\frac{(r^{n,m})^2 - (r^{n,m-1})^2}{r_{j+1/2}(2r_j + \Delta r)} \right) \left(2z_{k+1} - z^{n,m} - z^{n,m-1} \right) \ , \\ J^{n+1/2,m}_{z,j+1,k+1/2} &= \frac{qe_p}{2\pi\Delta t (\Delta r)^2 \Delta z} \left(\frac{2(r_j)^2 - (r^{n,m})^2 - (r^{n,m-1})^2}{(2r_{j+1/2} + \Delta r)(2r_j + \Delta r)} \right) \left(z^{n,m-1} - z^{n,m} \right) \ , \\ J^{n+1/2,m}_{r,j+1/2,k+1} &= \frac{qe_p}{4\pi\Delta t \Delta r (\Delta z)^2} \left(\frac{(r^{n,m-1})^2 - (r^{n,m})^2}{r_{j+1/2}(2r_j + \Delta r)} \right) \left(2z_k - z^{n,m} - z^{n,m-1} \right) \ , \\ J^{n+1/2,m}_{z,j,k+1/2} &= \frac{qe_p}{2\pi\Delta t (\Delta r)^2 \Delta z} \left(\frac{2(r_{j+1})^2 - (r^{n,m})^2 - (r^{n,m-1})^2}{(2r_{j-1/2} + \Delta r)(2r_j + \Delta r)} \right) \left(z^{n,m} - z^{n,m-1} \right) \ , \end{aligned} \tag{108}$$

where we have substituted for the weights from (97). We remind the reader that $m=0,1,2,\cdots,M+1$ where $(r^{n,m},z^{n,m})$ are the coordinates of each cell boundary crossing for $1\leq m\leq M$, and $(r^{n,0},z^{n,0})=(r^n,z^n)$ and $(r^{n,M+1},z^{n,M+1})=(r^{n+1},z^{n+1})$.

Therefore with equations (108) we can solve for the current densities associated with a segment of a given particle's trajectory. As mentioned before, to get the current density for a superparticle we need to sum over all segments, $J_{s,p}^{n+1/2}=\sum_m J_{s,p}^{n+1/2,m}$, where we have added the subscripts s,p denoting a particular superparticle, p, of species $s=q,e,g$, and suppressed the subscripts denoting the component and grid location. Then the total current density is given by summing over all particles:

$$J^{n+1/2}=\sum_{q=1}^{Z_b}\sum_{p=1}^{K_q^{n+1/2}} J_{q,p}^{n+1/2}+\sum_{p=1}^{K_e^{n+1/2}} J_{e,p}^{n+1/2}+\sum_{p=1}^{K_g^{n+1/2}} J_{g,p}^{n+1/2}\,. \tag{109}$$

where Z_b is the atomic number of the beam ions, $K_q^{n+1/2}$, $K_e^{n+1/2}$, and $K_g^{n+1/2}$ are respectively the number of "super-beam ions" of charge state q, "super-electrons", and "super-gas ions" at time $n+1/2$. J can be either component, radial or axial, at a particular grid location.

3.3.3 Particle Number Equations

As can be seen, equation (109) involves a summation over the superparticles. Therefore we need to determine the number of superparticles of a given species, $K_s^{n+1/2}$, that exist in the system at time $n+1/2$. Birdsall (1991) and Vahedi and Surendra (1995) describe an MCC method for evaluating the collision probability equation (45).

This equation determines the probability, $P_{x,q,p}(t)$, for a collision of type x to take place between a beam ion, q,p and a background gas neutral over the interval

$0 \le t \le \infty$ so that $P_{x,q,p}(0) = 0$ and $P_{x,q,p}(\infty) = 1$. Therefore if we choose a number ξ between 0 and 1, and then set $\xi = P_{x,q,p}(t)$, we can invert (45) to find the time within which collision x will occur:

$$t_{x,q,p} = \frac{-1}{\sigma_{in,q} n_g v_{z,q,p}} \ln\left(1 - \frac{\sigma_{in,q}}{\sigma_{x,q}}\xi\right) \ . \tag{110}$$

In the MCC method, the number ξ is chosen randomly from a list of numbers that are uniformly distributed over the interval 0 to 1. We'll discuss this in more detail later, when we analyze the numerical methods.

As mentioned above, every collision between a beam ion and a background gas atom will result in ionization of the background gas atom. Therefore to calculate the time it takes for a beam ion to ionize a background gas atom, we assign particle q, p a number $\xi_{in,q,p}$. Then setting $\xi = \xi_{in,q,p}$ in equation (110) yields:

$$t_{in,q,p} = \frac{-1}{\sigma_{in,q} n_g v_{z,q,p}} \ln\left(1 - \xi_{in,q,p}\right) \ . \tag{111}$$

where we have replaced $\sigma_{x,q}$ with $\sigma_{in,q}$. Clearly if $t_{in,q,p} \le \Delta t$ then the ion will undergo an ionizing collision in the time interval Δt. Therefore we can define a discrete probability function:

$$D_{in,q,p} \equiv \begin{cases} 1 & \text{if } \xi_{in,q,p} \le 1 - \exp\left(-\sigma_{in,q} n_g v_{z,q,p} \Delta t\right) \ , \\ 0 & \text{otherwise} \ , \end{cases} \tag{112}$$

so that $D_{in,q,p}$ is the probability that particle q, p will undergo an ionizing collision within time Δt. We also need to determine if the beam ion strips. Therefore we assign a second number $\xi_{st,q,p}$ to the beam ion and calculate the time to strip as:

$$t_{st,q,p} = \frac{-1}{\sigma_{in,q} n_g v_{z,q,p}} \ln\left(1 - \frac{\sigma_{in,q}}{\sigma_{st,q}}\xi_{st,q,p}\right) \ . \tag{113}$$

where we have replaced $\sigma_{x,q}$ with $\sigma_{st,q}$ in equation (110). If we set $t_{st,q,p} \le t_{in,q,p} \le \Delta t$, and substitute for $t_{in,q,p}$ from (111), then we can write:

$$D_{st,q,p} \equiv \begin{cases} 1 & \text{if } \frac{\sigma_{in,q}}{\sigma_{st,q}}\xi_{st,q,p} \le \xi_{in,q,p} \le 1 - \exp\left(-\sigma_{in,q} n_g v_{z,q,p} \Delta t\right) \ , \\ 0 & \text{otherwise} \ . \end{cases} \tag{114}$$

where $D_{st,q,p}$ is the discrete probability that this particle will undergo a stripping collision.

We can now use these probabilities to advance the superparticle numbers, $K_s^{n+1/2}$, to the next temporal index, $n+3/2$, as follows. At time n we assign two numbers, $\xi_{in,q,p}$ and $\xi_{st,q,p}$, and then evaluate $D_{in,q,p}$ and $D_{st,q,p}$ using equations (112) and (114) respectively, for every super-beam ion q, p. The numbers of superparticles at $n+3/2$ are then given by:

$$\begin{aligned}
K_q^{n+3/2} &= K_q^{n+1/2} + \sum_{p=1}^{K_{q-1}^{n+1/2}} D_{st,q-1,p} - \sum_{p=1}^{K_q^{n+1/2}} D_{st,q,p} \; , \\
K_e^{n+3/2} &= K_e^{n+1/2} + \sum_{q=1}^{Z_b} \sum_{p=1}^{K_p^{n+1/2}} D_{in,q,p} + \sum_{q=1}^{Z_b} \sum_{p=1}^{K_p^{n+1/2}} D_{st,q,p} \; , \qquad (115) \\
K_g^{n+3/2} &= K_g^{n+1/2} + \sum_{q=1}^{Z_b} \sum_{p=1}^{K_p^{n+1/2}} D_{in,q,p} \; .
\end{aligned}$$

With the evaluation of the particle-field interactions, using PIC techniques, and the particle-particle interactions, using MCC methods, we have provided a complete set of numerical equations that correspond to the analytical governing equations presented in the previous chapter. After advancing the particle positions we use equation (109) to calculate the current densities. These current densities are then used to advance the fields. Given a set of superparticle numbers, $K_q^{n+1/2}$, $K_e^{n+1/2}$, and $K_g^{n+1/2}$, we use equations (115) to advance them. And finally equation (98) is used to interpolate the fields to the particle positions, before advancing the velocities. Figure (22) shows the expanded version of the flow-chart, figure (18), that includes these calculations. The constant parameters that appear in the complete set of equations are now the beam ion and gas atom masses in units of *amu*, m_b and m_g; the atomic number of the beam ions, Z_b; the background gas density, n_g; and the stripping and ionization

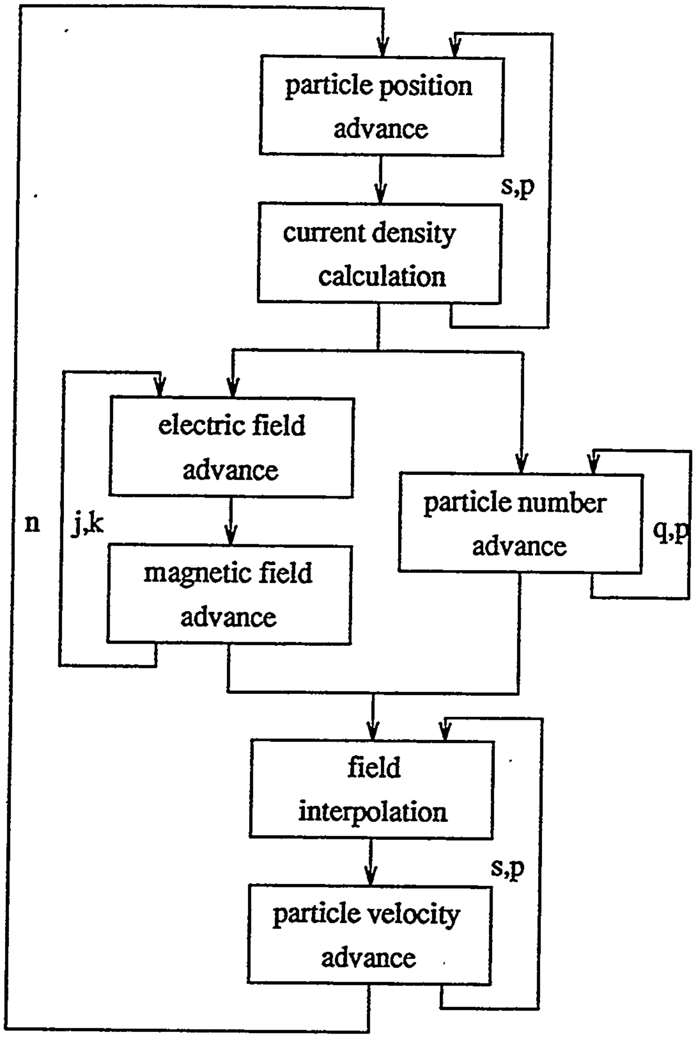

Figure 22: Flow-chart of the algorithm for advancing particle and field quantities, showing the current density calculations and field interpolations.

cross sections, $\sigma_{st,q}$ and $\sigma_{in,q}$. In addition, the numerical equations also contain a set of "non-physical" discrete parameters: the time-step, Δt; the grid sizes, Δr and Δz; and the particle-to-superparticle ratio, ΔN. We also remind the reader that we need a set of initial and boundary conditions for the fields and particle positions and velocities to solve these equations.

4 Numerical Analysis, Initial and Boundary Conditions

The numerical equations derived in the previous section form a complete set of equations for the superparticle positions and velocities, the electromagnetic fields, and the particle-particle and particle-field interactions. As mentioned in the previous section, in order to solve these equations we need to supply a set of initial and boundary conditions.

We also need to supply a set of discrete parameters: the time-step, Δt; the spatial mesh sized, Δr and Δz; and the superparticle ratio, ΔN. Clearly, from a computational point of view, we would like to make these quantities as large as possible because the number of superparticles, mesh-points, and time-steps are all inversely proportional to them. However, if we require that the solutions to the numerical equations be both stable and accurate, in that they do not undergo "non-physical" growth or damping, and that they be as close to the analytic solutions as possible, then these parameters tend to zero. An analysis of the stability and accuracy will allow us to put realistic upper bounds on the difference quantities.

4.1 Numerical Analysis and Discrete Parameters

We first discuss the methods used in the previous section to derive the numerical equations for the particle positions and velocities, the electromagnetic fields, and the particle-field and particle-particle interactions. We then analyze the solutions to these equations for their accuracy and stability. This will provide us with a set of conditions for the choice of the temporal and spatial grid sizes and the superparticle ratio. Many of the methods presented here and their analysis can be found in Birdsall and Langdon (1985), and Isaacson and Keller (1966); lectures by Vujic (1992) were also very helpful.

4.1.1 Superparticle Equations

We discuss now the approximations used to derive the superparticle equations, in particular (47). Consider a function $f(\mathbf{r})$, then we can expand this function in a Taylor series about a particle position $\mathbf{r}_i$ (in this section "particles" refer specifically to real particles; and "superparticles" to a group of real particles):

$$f(\mathbf{r}_p) = f(\mathbf{r}_i) + \nabla f \cdot (\mathbf{r}_i - \mathbf{r}_p) + \cdots \ , \qquad (116)$$

where $\mathbf{r}_p$ is the superparticle position defined by (46), and the derivatives of f are evaluated at $\mathbf{r}_i$. If we now expand $f(\mathbf{r})$ for all particles in a superparticle group and then sum over these particles, we can write:

$$f(\mathbf{r}_p) = \frac{1}{\Delta N} \sum_i f(\mathbf{r}_i) + \frac{1}{\Delta N} \sum_i \nabla f \cdot (\mathbf{r}_i - \mathbf{r}_p) + \cdots \ , \qquad (117)$$

where ΔN is the number of particles in the superparticle group. If we assume that the first derivative of the function, ∇f, is constant and that the higher derivatives vanish for all particle positions $\mathbf{r}_i$ in the superparticle group, in equation (117), then we arrive at the superparticle equation (47). If the function varies with wavelength λ, then clearly the summation should be done over particles in a region defined approximately by this wavelength.

We now attempt to determine the minimum number of particles that must be included in the superparticle group given the above approximation. The analysis used here is similar to that presented by Lewis and Miller (1984) and Nakamura

(1977). Let N_0 be the number of particles in the small region. We can now define an average:

$$\langle f\rangle \equiv \frac{1}{N_0}\sum_{i=1}^{N_0} f_i \; , \tag{118}$$

where, $f_i \equiv f(\mathbf{r}_i)$, is the function at the particle location $\mathbf{r}_i$, and the summation is done over all particle positions in the region. We can also define the variance:

$$\sigma^2 \equiv \frac{1}{N_0}\sum_{i} (f_i - \langle f\rangle)^2 \; ; \tag{119}$$

which is a measure of the spread of the function at individual particle locations f_i about the average value $\langle f\rangle$. For large N_0 and linear fields in the region, $\nabla f \simeq \langle f\rangle/\lambda$, we can evaluate this as $\sigma^2 = \langle f\rangle^2/12$.

We now do the same for the superparticles. We define an average quantity over the superparticles in this region as:

$$\langle f\rangle_i \equiv \frac{1}{K_0}\sum_{p=1}^{K_0} f_{p,i} \; , \tag{120}$$

where $f_{p,i}$ is the field at the particle location $\mathbf{r}_i$ belonging to superparticle group p, and K_0 is the total number of superparticles in the region, $K_0 \equiv N_0/\Delta N$. We can also define a variance of this average quantity with respect to the "true" average as:

$$\sigma_p^2 \equiv \frac{1}{\Delta N}\sum_{i=1}^{\Delta N} (\langle f\rangle_i - \langle f\rangle)^2 \; . \tag{121}$$

Clearly if the superparticles in the region are to be an accurate representation of the actual particles, then this variance should vanish. If we evaluate σ_p^2 in equation (121), we get $\sigma_p^2 = \sigma^2/K_0$; or as K_0 becomes large, the superparticle representation becomes more accurate. However, as mentioned above, making the number of superparticles large is computationally expensive.

We now evaluate the error between $\langle f\rangle_i$ and $\langle f\rangle$. The central limit theorem states that the probability of having $\langle f\rangle_i$ fall between $\langle f\rangle - \delta$ and $\langle f\rangle + \delta$ approaches the normal distribution:

$$C = \frac{1}{\sqrt{2\pi}} \int_{-\delta/\sigma_p}^{+\delta/\sigma_p} \exp\left(\frac{-z^2}{2}\right) dz \ , \tag{122}$$

where $z \equiv (\langle f \rangle_i - \langle f \rangle)/\sigma_p$. C is also called the confidence level. Carrying out the integration, and substituting for σ_p and σ yields:

$$C = \mathrm{erf}\left(\sqrt{6K_0}\frac{\delta}{\langle f \rangle}\right) \ , \tag{123}$$

where erf is the error function. If we now define the error as $\varepsilon \equiv (\langle f \rangle_i - \langle f \rangle)/\langle f \rangle$, then we can write

$$K \equiv \frac{N}{\Delta N} = \frac{N}{6N_0}\left(\frac{\mathrm{erf}^{-1}(C)}{\varepsilon}\right)^2 \ , \tag{124}$$

where N is the total number of particles in the system. Making ε smaller, or decreasing the allowable error, increases the number of superparticles, K, needed to establish a given confidence level C. The number of beam ions in a small region defined by λ can be approximated by $N_0 \simeq I_b\lambda/qev$, where I_b is the beam current; q is the charge state of the beam ions, and v is the beam velocity, while the total number of beam ions is given by $N \equiv I_bL_b/qev$, where L_b is the length of the beam; then (124) becomes:

$$K \simeq \frac{L_b}{6\lambda}\left(\frac{\mathrm{erf}^{-1}(C)}{\varepsilon}\right)^2 \ . \tag{125}$$

This equation gives us a condition for the number of superparticles, K, in relation to the spatial variation of the fields, λ. (In the sections that follow, "particles" will once again be synonymous with "superparticles").

4.1.2 Particle Position and Velocity Equations

We now look at the particle position and velocity equations (49) and (52). These equations are both first-order ordinary differential equations in time, of the form:

$$\frac{df}{dt} = g \ . \tag{126}$$

If we expand any function $\mathbf{f}$ around the temporal point $n+1/2$, we can evaluate $\mathbf{f}^{n+1}$ as:

$$\mathbf{f}^{n+1} = \mathbf{f}^{n+1/2} + \frac{d\mathbf{f}}{dt}\left(\frac{\Delta t}{2}\right) + \frac{1}{2!}\frac{d^2\mathbf{f}}{dt^2}\left(\frac{\Delta t}{2}\right)^2 + \frac{1}{3!}\frac{d^3\mathbf{f}}{dt^3}\left(\frac{\Delta t}{2}\right)^3 + \cdots , \tag{127}$$

where all derivatives are evaluated at $n+1/2$; and Δt is, as before, the difference in time between n and $n+1$. We can also evaluate $\mathbf{f}^n$:

$$\mathbf{f}^{n} = \mathbf{f}^{n+1/2} - \frac{d\mathbf{f}}{dt}\left(\frac{\Delta t}{2}\right) + \frac{1}{2!}\frac{d^2\mathbf{f}}{dt^2}\left(\frac{\Delta t}{2}\right)^2 - \frac{1}{3!}\frac{d^3\mathbf{f}}{dt^3}\left(\frac{\Delta t}{2}\right)^3 + \cdots . \tag{128}$$

Subtracting (128) from (127) and discarding terms of order $(\Delta t)^3$ or higher yields:

$$\mathbf{f}^{n+1} - \mathbf{f}^{n} = \mathbf{g}^{n+1/2}\Delta t , \tag{129}$$

where we have substituted from (126) remembering that the derivatives are evaluated at $n+1/2$. This result is known as "central differencing", and is second-order accurate, in that the largest term discarded is third-order. Clearly, the smaller Δt, the more accurate the result; indeed in the limit that $\Delta t \to 0$, (129) reduces to (126). If we substitute the differential equations (19) and (20) for the radial and axial positions into (129) we get the numerical equations for the particle position advance (57) and (53). Similarly substituting the differential equations (22), (23) and (24) for the electron velocities, (25) and (26) for the beam ion velocities, and (27) and (28) for the gas ion velocities into (129) yields the numerical equations for the velocity advance: (87), (88) and (79) for the electrons, (70) and (66) for the beam ions, and (74) and (75) for the gas ions respectively.

To see the affect this approximation, and hence the affect that the introduction of the finite time-step, Δt, has on the motion of the particles, we evaluate these difference equations under some special circumstances. First we look at the force-free motion of a particle in the transverse plane, that has azimuthal velocity v_θ, but no radial velocity. The equation of motion is then:

$$\frac{d\theta}{dt} = \omega_r , \tag{130}$$

where θ is the angle of rotation around the z axis. The solution to this equation is $\theta = \omega_r t$, where the frequency $\omega_r = v_\theta / r$. The numerical solution with no radial velocity is given by equation (57):

$$(r^{n+1})^2 = (r^n)^2 \left(1 + \omega_r^2 \Delta t^2\right) \ , \tag{131}$$

where we have substituted $\omega_r = v_\theta^{n+1/2} / r^n$. Using $\cos\theta = r^n / r^{n+1}$, where θ is given by equations (65), equation (131) becomes:

$$\theta = \tan^{-1}\left(\omega_r \Delta t\right) \ . \tag{132}$$

If we assume that the numerical solution also describes a rotating particle, $\theta = \omega t$, but with some frequency ω different from ω_r, then we can solve (132):

$$\omega = \frac{1}{\Delta t} \tan^{-1}\left(\omega_r \Delta t\right) \ . \tag{133}$$

Therefore we have an equation that relates the numerical frequency ω to the actual frequency ω_r. This equation is unconditionally stable, in that as long as ω_r is real, no choice of Δt will make ω imaginary. For the numerical result to be accurate, however, we require that these two frequencies be close. Expanding the right-hand-side of (133) in a Taylor series yields:

$$\omega = \frac{1}{\Delta t} \left[\omega_r \Delta t - \frac{1}{3} \left(\omega_r \Delta t\right)^3 + \cdots \right] \ , \tag{134}$$

and the error is then:

$$\varepsilon \equiv \frac{\omega - \omega_0}{\omega_0} \simeq \frac{1}{3} \left(\omega_r \Delta t\right)^2 \ . \tag{135}$$

This equation gives us a condition on the time-step, Δt, relative to the particle rotation frequency ω_r. For a given error, the time-step is inversely proportional to the frequency, as expected; that is, the resolution of higher frequencies requires smaller time-steps.

Next we consider a non-relativistic electron moving, with no azimuthal velocity in the radial electric field of a long beam, $E_r = kr$, where k is some constant determined by the parameters of the beam. If we ignore the azimuthal magnetic field, then the equation of motion is:

$$\frac{d^2r}{dt^2} = -\frac{e_p k}{m_e m_p} r \,. \tag{136}$$

The solution to this equation is of the form $r \sim \cos(\omega_p t)$, where the frequency of oscillation is $\omega_p^2 = ke_p/m_e m_p$. We now write the numerical solution for this problem. With no azimuthal velocity, the radial position is given by equation (57):

$$r^{n+1} = r^n + v_r^{n+1/2} \Delta t \,, \tag{137}$$

and with no azimuthal magnetic magnetic field, the non-relativistic velocity equation, (87), becomes:

$$v_r^{n+3/2} = v_r^{n+1/2} - \omega_p^2 r^{n+1} \Delta t \,, \tag{138}$$

where we have substituted ω_p for the electric field. If we now eliminate the velocity in equation (137) we get:

$$r^{n+1} = r^n + r^{n+2} + r^{n+1} \left(\omega_p^2 \Delta t^2 - 1 \right) \,. \tag{139}$$

Again we assume that the numerical solutions are also oscillatory, $r \sim \cos(\omega t)$, but with some frequency ω different from ω_p; then, as in Birdsall and Langdon (1985), we can solve for the frequency, ω, in equation (139):

$$\omega = \frac{2}{\Delta t} \sin^{-1} \left(\frac{\omega_p \Delta t}{2} \right) \,, \tag{140}$$

This result is numerically unstable, i.e. ω becomes imaginary for real ω_p, when $\Delta t \geq 2/\omega_p$. However, the accuracy condition is more stringent; Expanding the right-hand-side of (140) in a Taylor series, we get:

$$\omega = \frac{2}{\Delta t} \left[\frac{\omega_p \Delta t}{2} + \frac{1}{6} \left(\frac{\omega_p \Delta t}{2} \right)^3 + \cdots \right] \,. \tag{141}$$

and the error is:

$$\varepsilon \equiv \frac{\omega - \omega_p}{\omega_p} \simeq \frac{1}{24} \left(\omega_p \Delta t \right)^2 \,. \tag{142}$$

This equation gives us a condition on the time-step, Δt, relative to the plasma frequency, ω_p.

Finally, we look at a non-relativistic electron in an azimuthal magnetic field, B_θ. The equations of motion are:

$$\begin{aligned} \frac{dv_r}{dt} &= \frac{e_p B_\theta}{m_e m_p} v_z \ , \\ \frac{dv_z}{dt} &= -\frac{e B_\theta}{m_e m_p} v_r \ . \end{aligned} \tag{143}$$

The solutions to this equation are of the form $v_r \sim \cos(\omega_c t)$ and $v_z \sim sin(\omega_c t)$, where the frequency of rotation in the r, z plane is, $\omega_c = -e_p B_\theta / m_e m_p$. The numerical solutions are given by (88) for no electric field:

$$v_z^{n+3/2} \left[1 + \left(\frac{\omega_c \Delta t}{2} \right)^2 \right] = v_r^{n+1/2} \omega_c \Delta t + v_z^{n+1/2} \left[1 - \left(\frac{\omega_c \Delta t}{2} \right)^2 \right] \ . \tag{144}$$

where we have substituted ω_c for the magnetic field. As in Birdsall and Landgon (1985), we assume that the numerical solutions also describe a rotating electron, $v_r \sim \cos(\omega t)$ and $v_z \sim \sin(\omega t)$, but with frequency ω different from ω_c. Then equation (144) becomes:

$$\omega = \frac{2}{\Delta t} \tan^{-1} \left(\frac{\omega_c \Delta t}{2} \right) \ . \tag{145}$$

This equation is also unconditionally stable. Expanding the right-hand-side in a Taylor series yields:

$$\omega = \frac{2}{\Delta t} \left[\frac{\omega_c \Delta t}{2} - \frac{1}{3} \left(\frac{\omega_c \Delta t}{2} \right)^3 \cdots \right] \ , \tag{146}$$

and the error becomes:

$$\varepsilon \equiv \frac{\omega - \omega_c}{\omega_c} \simeq \frac{1}{12} (\omega_c \Delta t)^2 \ , \tag{147}$$

This equation gives us a condition on the time-step, Δt, relative to the cyclotron frequency, ω_c.

4.1.3 Field Equations

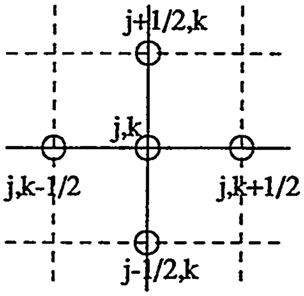

Figure 23: The spatial grid used to difference the field equations.

We now turn to the field equations (29) and (31). These are both first-order partial differential equations of the form:

$$\frac{\partial \mathrm{g}}{\partial t} = \nabla \times \mathrm{f} \ . \tag{148}$$

If we use the central difference technique described above for the temporal derivative, we can write this as:

$$\frac{\mathrm{g}^{n+1} - \mathrm{g}^{n}}{\Delta t} = (\nabla \times \mathrm{f})^{n+1/2} \ . \tag{149}$$

We now look at the right-hand-side of this equation. In the cylindrical coordinate system of concern here, the "curl" operation results in the following derivatives: $\partial f/\partial z$, $\partial f/\partial r$ and $(1/r)\partial(rf)/\partial r$. We can evaluate these using a "three-point" spatial finite difference scheme on the mesh shown in figure (23); this is similar to the central differencing scheme used above for the temporal derivatives in the position and velocity equations. Then

$$\begin{aligned} \left(\frac{\partial f}{\partial z}\right)_{j,k} &= \frac{f_{j,k+1/2} - f_{j,k-1/2}}{\Delta z} \ , \\ \left(\frac{\partial f}{\partial r}\right)_{j,k} &= \frac{f_{j+1/2,k} - f_{j-1/2,k}}{\Delta r} \ , \\ \left(\frac{1}{r}\frac{\partial (rf)}{\partial r}\right)_{j,k} &= \frac{2\left(r_{j+1/2}f_{j+1/2,k} - r_{j-1/2}f_{j-1/2,k}\right)}{\left(r^2_{j+1/2} - r^2_{j-1/2}\right)} \ . \end{aligned} \tag{150}$$

where the subscripts, as before, represent the radial and axial positions on the spatial mesh respectively, and r_j is the radius at the mesh point j. As in the case of the central difference equations, these finite difference results are also second-order accurate, in that the largest terms discarded are of order $(\Delta r)^3$ and $(\Delta z)^3$. Clearly, if we let Δr and Δz approach zero, equations (150) will reduce to the corresponding differential equations; but since the number of mesh points is inversely proportional to the grid sizes, for computational reasons we want to make these quantities as large as possible. If we substitute (32) and (33) for the electric fields and (30) for the magnetic field into (150) and (149) we arrive at the difference equations for the field advance: (59) and (60) for the electric fields and (61) for the magnetic field.

As before, we now look at the stability and accuracy of these numerical solutions. The analysis presented here benefited from lectures by Mei (1994). The azimuthal magnetic field of a free-space transverse magnetic wave can be found from, $B_\theta = (\partial A/\partial r)$, where the potential function A satisfies the Helmholtz equation:

$$\nabla^2 A = \frac{1}{c^2}\frac{\partial^2 A}{\partial t^2} \, . \tag{151}$$

In an axisymmetric cylinder, such as that used for the simulation environment, figure (12), the solution is of the form $B_\theta \sim J_1(p_0 r)\exp(\pm ik_0 z)\exp(-i\omega_0 t)$, where the frequency of the wave, ω_0, the axial wave number, k_0, and p_0 are related by the dispersion relation, $\omega_0^2 = c^2(k_0^2 + p_0^2)$, such that $p_0 R_c = \zeta_0$ are zeroes of the J_0 Bessel function where R_c is the radius of the cylinder. We now consider the numerical solution for the azimuthal magnetic field. With no source terms, equations (59), (60) and (61) become:

$$\frac{E^{n+1}_{r,j+1/2,k} - E^{n}_{r,j+1/2,k}}{\Delta t} = -c^2\left(\frac{B^{n+1/2}_{\theta,j+1/2,k+1/2} - B^{n+1/2}_{\theta,j+1/2,k-1/2}}{\Delta z}\right) , \tag{152}$$

$$\frac{E^{n+1}_{z,j,k+1/2} - E^{n}_{z,j,k+1/2}}{\Delta t} = 2c^2 \left(\frac{r_{j+1/2} B^{n+1/2}_{\theta,j+1/2,k+1/2} - r_{j-1/2} B^{n+1/2}_{\theta,j-1/2,k+1/2}}{r^2_{j+1/2} - r^2_{j-1/2}} \right), \tag{153}$$

and

$$\begin{aligned} \frac{B^{n+3/2}_{\theta,j+1/2,k+1/2} - B^{n+1/2}_{\theta,j+1/2,k+1/2}}{\Delta t} = - \left(\frac{E^{n+1}_{r,j+1/2,k+1} - E^{n+1}_{r,j+1/2,k}}{\Delta z} \right) + \\ \left(\frac{E^{n+1}_{z,j+1,k+1/2} - E^{n+1}_{z,j,k+1/2}}{\Delta z} \right), \end{aligned} \tag{154}$$

Substituting (152) and (153) into (154) yields:

$$\begin{aligned} \frac{1}{c^2} \left(\frac{B^{n+3/2}_{\theta,j+1/2,k+1/2} - 2B^{n+1/2}_{\theta,j+1/2,k+1/2} + B^{n-1/2}_{\theta,j+1/2,k+1/2}}{\Delta t^2} \right) = \\ \left(\frac{B^{n+1/2}_{\theta,j+1/2,k+3/2} - 2B^{n+1/2}_{\theta,j+1/2,k+1/2} + B^{n+1/2}_{\theta,j+1/2,k-1/2}}{\Delta z^2} \right) + \\ \frac{2}{\Delta r^2} \left[B^{n+1/2}_{\theta,j+3/2,k+1/2} \left(\frac{r_{j+3/2}}{r_{j+3/2} + r_{j+1/2}} \right) - \right. \\ B^{n+1/2}_{\theta,j+1/2,k+1/2} \left(\frac{r_{j+1/2}}{r_{j+3/2} + r_{j+1/2}} + \frac{r_{j+1/2}}{r_{j+1/2} + r_{j-1/2}} \right) + \\ \left. B^{n+1/2}_{\theta,j-1/2,k+1/2} \left(\frac{r_{j-1/2}}{r_{j+1/2} + r_{j-1/2}} \right) \right]. \end{aligned} \tag{155}$$

Taking the numerical solution to have the same form as the analytic solution, $B_\theta \sim J_1(pr)\exp(\pm ikz)\exp(-i\omega t)$, but with a different frequency, ω, and wave numbers k and p, yields from (155):

$$\begin{aligned} \left(\frac{2}{c\Delta t}\right)^2 \sin^2\left(\frac{\omega \Delta t}{2}\right) = \left(\frac{2}{\Delta z}\right)^2 \sin^2\left(\frac{k\Delta z}{2}\right) + \\ p^2 \left(\frac{2}{\Delta x}\right)^2 \left[\frac{(\Delta x^2 - 2x^2)(J_1^+ + J_1^-) + x\Delta x (J_1^- - J_1^+) + 4x^2 J_1}{2(4x^2 - \Delta x^2) J_1} \right], \end{aligned} \tag{156}$$

where $J_1 = J_1(x)$, $J_1^+ = J_1(x+\Delta x)$ and $J_1^- = J_1(x - \Delta x)$, and $x \equiv \zeta r_{j+1/2}/R_c$ and $\Delta x \equiv \zeta \Delta r / R_c$, where we recall that $\zeta \equiv pR_c$ are the zeroes of the J_0 Bessel function.

We now focus on the spatial parts of this equation. If we take the temporal derivatives to be exact, or $\Delta t \to 0$, then the frequency of the numerical solution will be equivalent to that of the exact solution, $\omega = \omega_0$, and (156) will become:

$$k_0^2 + p_0^2 = \left(\frac{2}{\Delta z}\right)^2 \sin^2\left(\frac{k\Delta z}{2}\right) + p^2\left(\frac{2}{\Delta x}\right)^2 \left[\frac{\left(\Delta x^2 - 2x^2\right)\left(J_1^+ + J_1^-\right) + x\Delta x\left(J_1^- - J_1^+\right) + 4x^2 J_1}{2(4x^2 - \Delta x^2)J_1}\right], \tag{157}$$

where we have substituted for c^2 from the dispersion relation. If we now take the radial derivatives to be exact, or $\Delta r \to 0$, then $p = p_0$, and in the limit that $\Delta x \to 0$ equation (157) reduces to:

$$k = \frac{2}{\Delta z} \sin^{-1}\left(\frac{k_0 \Delta z}{2}\right) . \tag{158}$$

With $\lambda_z \equiv 2\pi/k_0$, we can expand the right-hand-side of (158) in a Taylor series to give:

$$\varepsilon = \frac{k - k_0}{k_0} \simeq \frac{1}{24}\left(\frac{2\pi\Delta z}{\lambda_z}\right)^2 . \tag{159}$$

This equation sets a limit on the axial grid division, Δz, relative to the axial variations of the fields, λ_z.

Similarly if instead of taking the radial derivatives to be exact in (157), we take the axial derivatives to be exact, or $\Delta z \to 0$, then $k = k_0$, and we get:

$$\varepsilon + 1 = \left(\frac{1}{\sqrt{2}}\right)\sqrt{\frac{\Delta x^2(4x^2 - \Delta x^2)J_1}{\left(\Delta x^2 - 2x^2\right)\left(J_1^+ + J_1^-\right) + x\Delta x\left(J_1^- - J_1^+\right) + 4x^2 J_1}}, \tag{160}$$

where the error is given by, $\varepsilon \equiv (p/p_0) - 1$. For any radial wavelength, λ_r, we can find ζ, the zero of the J_0 Bessel function that will support this wave in a cylinder of radius R_c; we can then use equation (160) to find the Δx, for $0 \le x \le \zeta$, that will result in a given error ε; and finally we can find $\Delta r \simeq \Delta x R_c/\zeta$.

We now look at the stability of (156) without assuming exact spatial or temporal derivatives. For this equation to be stable, we require that ω be real, or that the $\sin^2$

term on the left-hand-side be less than or equal to unity:

$$\begin{aligned}\left(\frac{1}{c\Delta t}\right)^2 > \left(\frac{1}{\Delta z}\right)^2 \sin^2\left(\frac{k\Delta z}{2}\right) + \\ \left(\frac{1}{\Delta r}\right)^2 \left[\frac{\left(\Delta x^2 - 2x^2\right)\left(J_1^+ + J_1^-\right) + x\Delta x\left(J_1^- - J_1^+\right) + 4x^2 J_1}{2(4x^2 - \Delta x^2)J_1}\right] ,\end{aligned} \tag{161}$$

We now find the maximum values of the expressions on the right-hand-side. For the axial term the maximum value is simply $1/\Delta z^2$. For large zeroes, we can write $\zeta \simeq 2\pi R_c/\lambda_r$; then for λ_r/R_c varying from ~ 0.02 to 1 the radial term in [] approximately evaluates to unity. So that (161) becomes:

$$\left(\frac{1}{\Delta z^2} + \frac{1}{\Delta r^2}\right) \lesssim \frac{1}{c^2\Delta t^2} . \tag{162}$$

Equation (162) is a condition for stability that relates the temporal and spatial divisions; it is commonly referred to as the Courant-Friedrichs-Lewy stability criterion.

4.1.4 Particle-Field Interactions

The PIC methods used to calculate the current densities and to interpolate the fields to the particle positions are defined by the weighting functions (97). We now examine the accuracy of these weighting functions. The analysis presented here follows that of Hockney and Eastwood (1988). From conservation, we require that:

$$\sum_{j,k} W(r_p, z_p; r_j, z_k) = 1 , \tag{163}$$

where, as before, (r_p, z_p) is the location of the particle and (r_j, z_k) is the location of the grid point j, k. If we now also require that the first volume, $\pi r^2 z$, moment be satisfied, then:

$$\sum_{j,k} r_j^2 z_k W(r_p, z_p; r_j, z_k) = r_p^2 z_p , \tag{164}$$

Invoking separability in the radial and axial coordinates yields from (163):

$$\begin{aligned}\sum_j w(r_p; r_j) = 1 , \\ \sum_k w(z_p; z_k) = 1 ,\end{aligned} \tag{165}$$

and from (164):

$$\sum_j r_j^2 w(r_p;r_j) = r_p^2 \ , \qquad \sum_k z_k w(z_p;z_k) = z_p \ . \tag{166}$$

where $W(r_p,z_p;r_j,z_k) = w(r_p;r_j)w(z_p;z_k)$. We now have a total of four equations. To solve we must have only four unknowns; hence we limit the summation over grid points to the four grid points that surround the particle, $r_j < r_p < r_{j+1}$ and $z_k < z_p < z_{k+1}$. Then equations (165) and (166) become:

$$w(r_p;r_j) + w(r_p;r_{j+1}) = 1 \ , \qquad w(z_p;z_k) + w(z_p;z_{k+1}) = 1 \ , \tag{167}$$

and

$$r_j^2 w(r_p;r_j) + r_{j+1}^2 w(r_p;r_{j+1}) = r_p^2 \ , \qquad z_k w(z_p;z_k) + z_{k+1} w(z_p;z_{k+1}) = z_p \ . \tag{168}$$

Solving these four equations yields the weighting functions given by (97). In this analysis, we stopped after the first order moment; the maximum error in not satisfying the second order moment is first order in the grid divisions, Δr and Δz. The accuracy of the scheme increases with the number of moments we choose to satisfy; however, the number of grid points that must be used in the weighting scheme also increases leading to greater computational expense. If, for instance, we choose to satisfy only the zeroth order moment, then we are left with equations (167), and we must therefore limit ourselves to a single grid point; as mentioned before, this is referred to as the NGP weighting scheme. The accuracy of this scheme is zeroth order, which means that the error is infinite for any finite grid division.

Another advantage, besides accuracy, of satisfying higher moments and thereby including more grid points is that the charge assignment and field interpolation both become "smoother". Consider a particle of charge state q located at $r_p = r_j$ and $z_{k-1} \le z_p \le z_{k+1}$. Then the charge assigned to the grid points is given by substituting the weighting functions (97) into (102):

$$
\begin{aligned}
Q_{j,k-1} &= \begin{cases} qe_p\left(\frac{z_k - z_p}{\Delta z}\right) & \text{if } z_{k-1} < z_p < z_k \ , \\ 0 & \text{if } z_k < z_p < z_{k+1} \ , \end{cases} \\
Q_{j,k} &= \begin{cases} qe_p\left(\frac{z_p - z_{k-1}}{\Delta z}\right) & \text{if } z_{k-1} < z_p < z_k \ , \\ qe_p\left(\frac{z_{k+1} - z_p}{\Delta z}\right) & \text{if } z_k < z_p < z_k + 1 \ , \end{cases} \\
Q_{j,k+1} &= \begin{cases} 0 & \text{if } z_{k-1} < z_p < z_k \ , \\ qe_p\left(\frac{z_p - z_k}{\Delta z}\right) & \text{if } z_k < z_p < z_{k+1} \ . \end{cases}
\end{aligned}
\tag{169}
$$

As the particle moves axially and crosses the grid location j, k, say from $z_k < z_p < z_{k+1}$ to $z_{k-1} < z_p < z_k$, the charge weighted to any grid point, given by (169), is continuous, although its derivative is not. Similarly, if we take the grid fields to be such that $F_{j,k}$ is the only non-zero field, and ignore the effect of the particle, then the interpolated field is given by substituting the weighting functions (97) into (98):

$$
F_p = \begin{cases} F_{j,k}\left(\frac{z_{k+1} - z_p}{\Delta z}\right) & \text{if } z_k < z_p < z_{k+1} \ , \\ F_{j,k}\left(\frac{z_p - z_{k-1}}{\Delta z}\right) & \text{if } z_{k-1} < z_p < z_k \ . \end{cases}
\tag{170}
$$

And again as the particle moves axially and crosses the grid location j, k, the interpolated field to the particle position, given by (170), is continuous. However, with the NGP weighting scheme where only a single grid point is used, both the charge and field quantities are discontinuous as the particle moves across the grid. Therefore using more grid points allows us to "smooth" both the charge assignment and the field interpolation.

Hockney and Eastwood (1988) show that using the same weighting scheme to weight the particle to the grid and to interpolate the fields to the particle positions, as is done here, eliminates any self-force that the particle would otherwise feel. Consider a single particle of charge state q located at (r_p, z_p), then the weighted charge at the grid points is given by (102):

$$
Q_{j,k} = qe_p W(r_p, z_p; r_j, z_k) \ . \tag{171}
$$

We can calculate the grid fields from these charge assignments through some discrete Green function:

$$F_{j,k} = \sum_{j',k'} d(r_j, z_k; r_{j'}, z_{k'}) Q_{j',k'} \ , \tag{172}$$

where $d(r_j, z_k; r_{j'}, z_{k'})$ is the Green function that relate the charge at grid location j', k' to the field at grid location j, k. Clearly this function must be properly symmetric, so that when the charge and field locations are interchanged, $d(r_j, z_k; r_{j'}, z_{k'}) = -d(r_{j'}, z_{k'}; r_j, z_k)$. The force at the particle position is given by $f_p = qe_pF_p$, or substituting from (98):

$$f_p = qe_p \sum_{j,k} F_{j,k} W(r_p, z_p; r_j, z_k) \ . \tag{173}$$

In order to calculate the self-force, or the force that the particle experiences due to its own charge weighted to the grid, we substitute (171) into (172) and then into (173), to get:

$$f_p = q^2 e_p^2 \sum_{j,k} \sum_{j',k'} d(r_j, z_k; r_{j'}, z_{k'}) W(r_p, z_p; r_{j'}, z_{k'}) W(r_p, z_p; r_j, z_k) \ . \tag{174}$$

Interchanging j, k and j', k' and using the symmetry condition of the Green function gives the desired result: $f_p = 0$.

4.1.5 Particle-Particle Interactions

Finally, we turn to the particle-particle interactions. The discrete collision probability equations (112) and (114) depend on the numbers $\xi_{in,q,p}$ and $\xi_{st,q,p}$ respectively. We now discuss a method, similar to that described by Hammersley and Handscomb (1964) and Lewis and Miller (1984), for choosing these numbers. Given a probability density, $\pi_{x,q,p}(t)$ as a function of time, for a collision of type x to occur between a beam ion q, p and a background gas neutral within time t and $t+dt$, we can transform to some other variable ξ, where $\xi \equiv f(t)$, some function of time, so that $t = f^{-1}(\xi)$, where f^{-1} is the inverse of f:

$$\Pi_{x,q,p}(\xi) = \frac{\pi_{x,q,p}(f^{-1}(\xi))}{f'(f^{-1}(\xi))} \ , \tag{175}$$

where $f' = df(t)/dt$. $\Pi_{x,q,p}(\xi)$ is the probability density that $\xi = f(t)$ will correspond to the time, t, at which a collision occurs. If we now take the special case of $f(t) = P_{x,q,p}(t)$, the probability that collision x will occur within 0 and some time t; then using the differential form of equation (42):

$$\frac{dP_{x,q,p}(t)}{dt} = \pi_{x,q,p}(t) \ , \tag{176}$$

equation (175) becomes:

$$\Pi_{x,q,p}(\xi) = 1 \ , \tag{177}$$

where $\xi = P_{x,q,p}(t)$. We recall that since $\pi_{x,q,p}$ is normalized over $0 \le t \le \infty$, $P_{x,q,p}$ ranges from 0 to 1. Therefore equation (177) means that ξ is uniformly distributed over the interval 0 to 1. In deriving equations (112) and (114) we set $\xi_{in,q,p} = P_{in,q,p}(t)$, and $\xi_{st,q,p} = P_{st,q,p}(t)$, therefore $\xi_{in,q,p}$ and $\xi_{st,q,p}$ are also uniformly distributed over the interval 0 to 1, and we can randomly choose them from a set of such numbers.

We now discuss the accuracy of the MCC method used here to calculate the particle-particle interactions. The first approximation stems from the fact that we allow each beam ion to undergo only one ionizing collision in every time-step. As discussed by Vahedi and Surendra (1995), this approximation puts a limit on the size of the time-step; clearly the smaller the time-step, the more accurate the result. The probability that a single beam ion, q, p, will undergo at least one ionizing collision in time-step Δt, $P_{in,q,p}$, is given by (45):

$$P_{in,q,p} = 1 - \exp\left(-\sigma_{in,q} n_g v_{z,q,p} \Delta t\right) \ . \tag{178}$$

Therefore the probability that a particle will undergo $m \ge 2$ collisions in this time-step is simply $(P_{in,q,p})^m$, and the total probability that this particle will undergo more than one ionizing collision, or the error in ignoring these collisions, is:

$$\varepsilon = \sum_{m=2}^{\infty} (P_{in,q,p})^m = \frac{(P_{in,q,p})^2}{1 - P_{in,q,p}} \, . \tag{179}$$

If we wish to keep this error, ε, to less than 2%, then we get $P_{in,q,p} \lesssim 0.13$, and $\Delta t \lesssim 0.14/\nu_{in,q,p}$, where $\nu_{in,q,p} \equiv \sigma_{in,q} n_g v_{z,q,p}$.

The second approximation is a result of using a small number of particles to represent the the collision probability. The analysis presented here is similar to that discussed by Lewis and Miller (1984) and Nakamura (1977). If there are a large number of total particles of charge state q, $K_q \to \infty$, then the average number of particles that undergo an ionizing collision is simply given by the probability:

$$\langle k \rangle_{\infty} = P_{in,q,p} \, , \tag{180}$$

where $P_{in,q,p}$ is, as before, the probability for a single particle q,p to undergo an ionizing collision in time Δt, and is given by (178); the ∞ subscript denotes the fact that this is an average for large K_q. For a finite number of particle, K_q, the probability of having k particles collide in time Δt is given by the binomial distribution:

$$p_k = \frac{K_q!}{k!(K_q - k)!} P_{in,q,p} (1 - P_{in,q,p})^{K_q - k} \, . \tag{181}$$

And the average number of particles that collide is simply:

$$\langle k \rangle_K = \frac{k}{K_q} \, , \tag{182}$$

where now the K subscript reminds us that this is the average for a finite K_q. Clearly we wish this average to be as close to the probability $P_{in,q,p}$ as possible. We now find the variance of $\langle k \rangle_K$ with respect to $\langle k \rangle_{\infty}$:

$$\sigma_K^2 = \sum_{k=0}^{K_q} p_k \left(\langle k \rangle_K - \langle k \rangle_{\infty} \right)^2 \, . \tag{183}$$

Substituting from (180), (181) and (182) and carrying out the summation yields $\sigma_K^2 = (P_{in,q,p}(1 - P_{in,q,p}))/K_q$; therefore we see that as K_q becomes large this variance vanishes, as expected. As before, we use the central limit theorem to find the probability, or confidence level, that $\langle k\rangle_K$ will fall between $\langle k\rangle_\infty - \delta$ and $\langle k\rangle_\infty + \delta$:

$$C = \frac{1}{\sqrt{2\pi}} \int_{-\delta/\sigma_K}^{+\delta/\sigma_K} \exp\left(\frac{-z^2}{2}\right) dz \ , \tag{184}$$

where $z \equiv (\langle k\rangle_K - \langle k\rangle_\infty)/\sigma_k$. Carrying out the integration, and substituting from σ_K and $P_{in,q,p}$ from (178), yields:

$$K_q = \frac{2\exp(-\nu_{in,q,p}\Delta t)}{1 - \exp(-\nu_{in,q,p}\Delta t)} \left(\frac{\mathrm{erf}^{-1} C}{\varepsilon}\right)^2 \ , \tag{185}$$

where erf^{-1} is the inverse error function, and $\varepsilon \equiv \delta/\langle k\rangle_\infty$ is the error. As the collision frequency ν becomes smaller, more particles are needed to compensate for the low statistics, if we wish to keep the same error and confidence level.

In summary, we collect some of the more stringent accuracy and stability relations derived here. These essentially set upper-bounds to the difference quantities: the time-step, Δt; the spatial mesh sizes, Δr and Δz; and the superparticle ratio, ΔN. To ensure accuracy of the superparticle approximation, we have equation (125). If we set $\lambda \simeq \beta c/\omega_b$, where β is, as before, the velocity of the beam and ω_b is the beam frequency, $\omega_b^2 \equiv n_b e^2/\epsilon_0 m_b m_o$ where n_b is the beam ion density and m_b is the beam ion mass; then for an error of less than 1% and a confidence level $C \gtrsim 98\%$, equation (125) becomes:

$$\Delta N \lesssim 1.4 \times 10^{15} \left(\frac{I_b}{q\omega_b}\right) \ , \tag{186}$$

where, as before, I_b is the beam current, and q is the charge-state of the beam ions. For the parameters given in table (3), the beam frequency at the target, when the radius of the beam is $\sim 2\,mm$, is $\omega_b \simeq 4.4 \times 10^8\, s^{-1}$; this gives $\Delta N \lesssim 1.4 \times 10^{10}$ and $K_1 \simeq 19{,}000$, a manageable number number from a computational point of view. To resolve the plasma frequency accurately, we have a limit on the time-step, equation (142); for an error of less than 0.2%, this equation yields:

$$\Delta t \lesssim \frac{0.2}{\omega_{pe}} , \tag{187}$$

where ω_{pe} is the electron plasma frequency, $\omega_{pe}^2 \equiv n_e e^2/\epsilon_0 m_e m_o$ where n_e is the electron density and m_e is the electron mass. Again, for the parameters given in (3), if we assume that the electron density is the same as the beam ion density, then at the lens, when the radius of the beam is $a_l \simeq 10\,cm$, we get $\omega_{pe} \simeq 5.13 \times 10^9\,s^{-1}$, so that $\Delta t \lesssim 39\,ps$; this leads to about 1,400 time-steps for the beam to reach the target. Accuracy of the electric and magnetic fields sets limits on the spatial mesh sizes. For Δz, if we again take $\lambda_z \simeq \beta c/\omega_b$, then for an error of less than 0.2%, equation (159) becomes:

$$\Delta z \lesssim 0.03 \frac{\beta c}{\omega_b} . \tag{188}$$

With the parameters given in table (3), the beam frequency at the end of the simulation is $\omega_b \simeq 4.4 \times 10^8\,s^{-1}$, and $\Delta z \lesssim 0.7\,cm$. For a simulation length, $L_c \simeq 8\,m$, shown in figure (12), this gives the total number of axial mesh points, $N_z \simeq 1,140$. For the radial mesh size, if we specify $\varepsilon \lesssim 0.2\%$, equation (160) becomes:

$$\frac{\Delta x^2 (4x^2 - \Delta x^2) J_1}{(\Delta x^2 - 2x^2)\left(J_1^+ + J_1^-\right) + x\Delta x \left(J_1^- - J_1^+\right) + 4x^2 J_1} \lesssim 2.01 , \tag{189}$$

where we recall that $x \equiv \zeta r/R_c$, $\Delta x \equiv \zeta \Delta r/R_c$, $J_1 = J_1(x)$, $J_1^+ = J_1(x + \Delta x)$, and $J_1^- = J_1(x - \Delta x)$. Equation (189) is satisfied for all $0 \lesssim x \lesssim 100$ if $\Delta x \lesssim 0.22$ or $\Delta r \lesssim 0.22 R_c/\zeta$. If we now take $\lambda_r \simeq \beta c \Theta/\omega_b$, where Θ is the convergence angle, then for the parameters in table (3), the beam frequency at the lens, when the radius of the beam is $a_l \simeq 10\,cm$, is $\omega_b \simeq 8.5 \times 10^6\,s^{-1}$ and $\lambda_r \simeq 22.6\,cm$. In order to support such a wave in a $R_c \simeq 30\,cm$ cylinder, ζ would have to be the third zero of the J_0 Bessel function, $\zeta = 8.65$. Therefore we get $\Delta r \lesssim 0.8\,cm$, and the number of radial mesh points $N_r \simeq 38$. The Courant-Friedrichs-Lewy (CFL) stability criterion (162) relates the time-step and spatial mesh sizes:

$$\left(\frac{1}{\Delta z^2}+\frac{1}{\Delta r^2}\right) \lesssim \frac{1}{c^2 \Delta t^2} . \tag{190}$$

For the mesh sizes given above, $\Delta t \lesssim 17\,ps$. Although this condition is more stringent than the plasma frequency limit of $\sim 39\,ps$, if the electron density becomes several times the beam ion density, then the plasma frequency could become the limiting condition. Indeed towards the end, when the beam is at the target, and the number of electrons is large, perhaps as much as ~ 10 times the number of beam ions, and the radius of the beam is small, $\sim 2\,mm$, the electron plasma frequency could get as high as $\sim 8 \times 10^{11}\,s^{-1}$ and $\Delta t \lesssim 0.2\,ps$. Finally the collision frequency can also limit the time-step (179):

$$\Delta t \lesssim \frac{0.14}{\nu} , \tag{191}$$

where ν is the collision frequency, $\nu \equiv \sigma n_g \beta c$ where σ is a particular collision cross section and n_g is the background gas density. For the parameters given in table (3), and $n_g \simeq 10^{15}\,cm^{-3}$ and the cross section for a Hg^+ ion to ionize a fluorine atom, $\sigma_{in} \simeq 4.1 \times 10^{-17}\,cm^2$, we get $\nu \simeq 3.8 \times 10^8\,s^{-1}$, and $\Delta t \lesssim 0.4\,ns$. This is certainly less stringent than either the plasma frequency of CFL condition; however if the beam ions reach charge states in excess of a few, as a result of stripping in high density gas, then the ionization cross section can get large enough to make this a limiting condition. For example for an Hg^{15+} ion $\sigma_{in} \simeq 1.5 \times 10^{-15}\,cm^2$, then $\Delta t \lesssim 9.7\,ps$.

4.2 Initial and Boundary Conditions

As mentioned above, in addition to values for the discrete parameters, in order to solve the numerical equations, we also need to supply a set of initial and boundary conditions. Since the particle equations have only temporal derivatives, they only need initial conditions. The fields however need both initial and boundary conditions.

4.2.1 Particle Initial Conditions

The only particles that need to be initialized are the beam ions. For the system being studied in this thesis, there are no initial electrons or background gas ions, $N_e = 0$ and $N_g = 0$; these are created via ionizing and stripping collisions between the beam ions and background gas neutrals. The number of beam particles that need to be initialized is simply given by $K_q = N_q/\Delta N$, where N_q is the total number of real beam ions of charge-state q in the system.

Birdsall and Langdon (1985) describe a method for initializing these particles by inverting a given initial distribution, $f_q(\mathrm{r}, \mathrm{v})$, where the total number of beam ions of charge-state q is now given by:

$$N_q = \int dx \int dy \int dz \int dv_x \int dv_y \int dv_z f_q(\mathrm{r}, \mathrm{v}, t) \ , \tag{192}$$

We first find the density of a single variable by integrating over the other variables; for instance:

$$\tilde{f}_q(x) = \frac{1}{N_q} \int dy \int dz \int dv_x \int dv_y \int dv_z f_q(\mathrm{r}, \mathrm{v}, t) \ , \tag{193}$$

where $\tilde{f}_q(x)$ is the normalized particle density in the spatial variable x. We now construct the cumulative distribution, similar to the method used to invert the probability density for the MCC calculations:

$$\tilde{F}_q(x) \equiv \int_{x_{min}}^{x} \tilde{f}_q(x')dx' \ , \tag{194}$$

where, because $\tilde{f}_q(x)$ is normalized, $\tilde{F}_q(x_{min}) = 0$ and $\tilde{F}_q(x_{max}) = 1$. Then as was done in the MCC method above, we assign a random number $\xi_{x,q,p}$ from a uniform distribution over the interval 0 to 1, and then invert $\tilde{F}_q$ to find the position of particle q, p:

$$x_{q,p} = \tilde{F}_q^{-1}(\xi_{x,q,p}) \ . \tag{195}$$

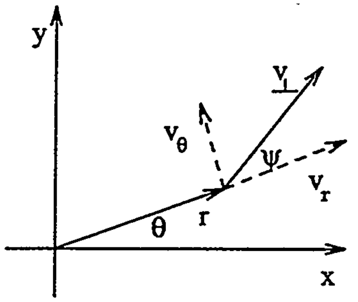

Figure 24: The transverse plane of the beam showing the position and velocity vectors.

This is then repeated for all K_q beam particles, for each variable, y, z, etc.

For the solutions presented in this thesis, we assume that the beam initially consists of particles of a single charge-state q, that are singular in axial velocity, v_z, and have K-V, Kapchinskij and Vladimirskij (1959), distribution in transverse phase-space:

$$f_q(r,\theta,z,v_\perp,\psi,v_z) = \frac{N_q}{\pi^2\epsilon^2 v_z^2}\delta\left(\frac{r^2}{a_l^2}+\frac{a_l^2 v_\perp^2}{\epsilon^2 v_z^2}-1\right)\delta\left(v_z-\beta c\right)\tilde{f}_q(z)\ , \tag{196}$$

where δ is the Dirac delta function. The beam radius, a_l, and emittance, ϵ, can vary along the length of the beam; and $\tilde{f}_q(z)$ is the normalized axial distribution of the beam. If we now assume that we can divide the beam into several axial slizes, each of thickness δz, across which the radius and emittance of the beam can be taken to be approximately constant, then for each slice μ we can write:

$$\begin{aligned} f_{q,\mu}(r,\theta,z,v_\perp,\psi,v_z) = \frac{N_{q,\mu}}{\pi^2\epsilon_\mu^2 v_z^2\delta z}\delta\left(\frac{r^2}{a_\mu^2}+\frac{a_\mu^2 v_\perp^2}{\epsilon_\mu^2 v_z^2}-1\right)\ \times \\ \delta\left(v_z-\beta c\right)H\left(z-z_h-(\mu-1)\delta z\right)H\left(z_h+\mu\delta z-z\right)\ , \end{aligned} \tag{197}$$

where H is the Heaviside step function, $\mu = 1, 2, \cdots, L_b/\delta z$, a_μ and ϵ_μ are the radius and emittance of each slice, and $N_{q,\mu}$ is the number of beam ions in slice μ:

$$N_{q,\mu} \equiv N_q \int_{z_h+(\mu-1)\delta z}^{z_h+\mu\delta z} \tilde{f}_q(z)dz\ , \tag{198}$$

where z_h is the axial position of the "head" of the beam, and L_b is the pulse length. The geometry in the transverse plane of the beam is shown in figure (24). As mentioned before, the only coordinates that need to be initialized are, $r_{q,p}$, $z_{q,p}$, $v_{r,q,p}$, $v_{\theta,q,p}$, and $v_{z,q,p}$; where $v_{r,q,p}=v_{\perp,q,p}\sin(\psi_{q,p})$ and $v_{\theta,q,p}=v_{\perp,q,p}\cos(\psi_{q,p})$. Therefore we find densities, and cumulative distributions for each beam slice using (193) and (194):

$$\begin{aligned}\tilde{f}_{q,\mu}(r) &= \frac{2}{a_\mu^2}H\left(1-\frac{r^2}{a_\mu^2}\right) \ , \\ \tilde{F}_{q,\mu}(r) &= \frac{r^2}{a_\mu^2} \ ,\end{aligned} \tag{199}$$

where $0 \le r \le a_\mu$, so that $\tilde{F}_{q,\mu}(0)=0$ and $\tilde{F}_{q,\mu}(a_\mu)=1$. Then we choose a random number $\xi_{r,q,p}$ for particle q,p from a uniform distribution over the interval 0 to 1, and invert (199) to get, $r_{q,p}=a_\mu\sqrt{\xi_{r,q,p}}$. For the axial position:

$$\begin{aligned}\tilde{f}_{q,\mu}(z) &= \frac{1}{\delta z}H\left(z-z_h-(\mu-1)\delta z\right)H\left(z_h+\mu\delta z-z\right) \ , \\ \tilde{F}_{q,\mu}(z) &= \frac{1}{\delta z}\left(z-z_h-(\mu-1)\delta z\right) \ ,\end{aligned} \tag{200}$$

where $z_h+(\mu-1)\delta z \le z \le z_h+\mu\delta z$, so that $\tilde{F}_{q,\mu}(z_h+(\mu-1)\delta z)=0$ and $\tilde{F}_{q,\mu}(z_h+\mu\delta z)=1$. Again we choose another random number $\xi_{z,q,p}$ and invert (200) to get, $z_{q,p}=z_h+(\mu+\xi_{z,q,p}-1)\delta z$. For the transverse velocity:

$$\begin{aligned}\tilde{f}_{q,\mu}(v_\perp) &= \frac{2a_\mu^2}{\epsilon_\mu^2\beta^2c^2}H\left(1-\frac{a_\mu^2v_\perp^2}{\epsilon_\mu^2\beta^2c^2}\right) \ , \\ \tilde{F}_{q,\mu}(v_\perp) &= \frac{a_\mu^2v_\perp^2}{\epsilon_\mu^2\beta^2c^2} \ ,\end{aligned} \tag{201}$$

where $0 \le v_\perp \le \epsilon_\mu\beta c/a_\mu$, so that $\tilde{F}_{q,\mu}(0)=0$ and $\tilde{F}_{q,\mu}(\epsilon_\mu\beta c/a_\mu)=1$. Choosing a random number $\xi_{vp,q,p}$, and inverting (201) yields, $v_{\perp,q,p}=(\epsilon_\mu\beta c/a_\mu)\sqrt{\xi_{vp,q,p}}$. From the distribution function, (197), we see that $\xi_{vq,q,p}$ and $\xi_{r,q,p}$ are correlated. Substituting (199) and (201) into (197), and focusing on the delta function gives, $f_{q,\mu}(r,v_\perp) \sim \delta(\xi_{r,q,p}+\xi_{vp,q,p}-1)$; therefore $\xi_{vp,q,p}=1-\xi_{r,q,p}$. Then $v_{\perp,q,p}=(\epsilon_\mu\beta c/a_\mu)\sqrt{1-\xi_{r,q,p}}$. For the angle ψ we get:

$$\begin{aligned} \tilde{f}_{q,\mu}(\psi) &= \frac{1}{2\pi} \,, \\ \tilde{F}_{q,\mu}(\psi) &= \frac{\psi}{2\pi} \,, \end{aligned} \tag{202}$$

where $0 \leq \psi \leq 2\pi$, so that $\tilde{F}_{q,\mu}(0) = 0$ and $\tilde{F}_{q,\mu}(2\pi) = 1$. Therefore inverting (202) yields, $\psi_{q,p} = 2\pi\xi_{\psi,q,p}$, where $\xi_{\psi,q,p}$ is a uniformly distributed random number between 0 and 1. Then $v_{r,q,p} = v_{\perp,q,p}\sin(2\pi\xi_{\psi,q,p})$ and $v_{\theta,q,p} = v_{\perp,q,p}\cos(2\pi\xi_{\psi,q,p})$. Finally we look at the axial velocity:

$$\begin{aligned} \tilde{f}_{q,\mu}(v_z) &= \delta(v_z - \beta c) \,, \\ \tilde{F}_{q,\mu}(v_z) &= H(v_z - \beta c) \,, \end{aligned} \tag{203}$$

where $-\infty \leq v_z \leq \infty$, so that $\tilde{F}_{q,\mu}(-\infty) = 0$ and $\tilde{F}_{q,\mu}(\infty) = 1$. Then choosing a random number and inverting (203) yields $v_{z,q,p} = \beta c$. We carry out these operations for each super-beam ion $K_{q,\mu} \equiv N_{q,\mu}/\Delta N$ in each slice μ. Therefore given a set of initial parameters for the beam: its velocity, β; pulse length, L_b; and the number of ions of charge state q, $N_{q,\mu}$, initial radius, a_μ, and emittance, ϵ_μ, of each beam slice μ; we can use a set of random numbers uniformly distributed over the interval 0 to 1 to find the initial positions and velocities of the beam particles.

4.2.2 Field Initial Conditions

We initialize the fields by first solving the electrostatic problem in the frame of the beam, and then performing a Lorentz transformation of the results to the frame of the cylinder. The electrostatic problem is defined by the Poisson equation for the potential:

$$\nabla^2 V' = -\frac{\rho}{\epsilon_0} \,, \tag{204}$$

where the prime superscripts denote that we are solving this potential in the frame of the beam, and ρ is the charge density of the beam. Using a Green function formulation, we can write:

$$V'(\mathbf{r}'_0) = \int \rho(\mathbf{r}) G(\mathbf{r}'_0, \mathbf{r}) d\mathbf{r} + F(\mathbf{r}'_0) \ , \tag{205}$$

where $\mathbf{r}'_0$ is the point at which we wish to find the potential in the beam frame and $\mathbf{r}$ is the variable of integration over the beam. $F(\mathbf{r}'_0)$ is a function that satisfies the Laplace equation, $\nabla^2 F = 0$, inside the volume, and is therefore defined by the boundary condition, and $G(\mathbf{r}'_0, \mathbf{r})$ is the so-called Green's function that satisfies the condition,

$$\nabla^2 G(\mathbf{r}'_0, \mathbf{r}) = -\frac{\delta(\mathbf{r}'_0 - \mathbf{r})}{\epsilon_0} \ , \tag{206}$$

where the derivative is taken with respect to $\mathbf{r}$. If we substitute (206) into (205) we recover (204). Using Dirichlet boundary conditions, where the potential on the conducting wall surface of the cylinder shown in figure (12) is zero, reduces (205) to:

$$V'(\mathbf{r}'_0) = \int \rho(\mathbf{r}) G(\mathbf{r}'_0, \mathbf{r}) d\mathbf{r} \ . \tag{207}$$

And the Green function equation, (206), for the geometry of concern here becomes:

$$\nabla^2 G(\mathbf{r}'_0, \mathbf{r}) = -\frac{1}{r'_0 \epsilon_0} \delta(r'_0 - r) \delta(\theta'_0 - \theta) \delta(z'_0 - z) \ , \tag{208}$$

where (r'_0, z'_0, θ'_0) is the coordinate at which we wish to find the potential. Jackson (1975) solves this equation for a cylinder of radius R_c:

$$G(\mathbf{r}'_0, \mathbf{r}) = \frac{1}{2\pi^2 \epsilon_0} \sum_{m=-\infty}^{\infty} \exp\left(im(\theta'_0 - \theta)\right) \int_0^\infty dk \cos\left[k(z'_0 - z)\right] \times \\ \left\{ \frac{I_m(kr_<)}{I_m(kR_c)} \left[I_m(kR_c) K_m(kr_>) - K_m(kR_c) I_m(kr_>) \right] \right\} \ , \tag{209}$$

where I_m and K_m are the modified Bessel functions of order m, and:

$$r_< = \begin{cases} r \ , & \text{if } r < r'_0 \ , \\ r'_0 \ , & \text{if } r > r'_0 \ , \end{cases}$$

$$r_> = \begin{cases} r'_0 \ , & \text{if } r < r'_0 \ , \\ r \ , & \text{if } r > r'_0 \ . \end{cases} \tag{210}$$

Substituting (209) into (207) yields:

$$V'(r_0', \theta_0', z_0') = \frac{1}{2\pi^2 \epsilon_0} \int_0^{2\pi} d\theta \int_{-\infty}^{\infty} dz \int_0^{R_c} dr r \rho(r, \theta, z) \times \\ \sum_{m=-\infty}^{\infty} \exp\left(im(\theta_0' - \theta)\right) \int_0^{\infty} dk \cos\left[k(z_0' - z)\right] \times \\ \left\{ \frac{I_0(kr_<)}{I_0(kR_c)} \left[I_0(kR_c)K_0(kr_>) - K_0(kR_c)I_0(kr_>)\right] \right\} , \tag{211}$$

In the axisymmetric geometry of concern here $m = 0$. For a K-V distribution (196), we can write:

$$\rho(r, \theta, z) = qe \int d^3v \tilde{f}_q(\mathbf{r}, \mathbf{v}) = \frac{N_q qe}{\pi a_l^2} f_q(z) H\left(1 - \frac{r^2}{a_l^2}\right) . \tag{212}$$

where the beam consists of ions with a single charge-state q. Substituting (212) into (211) and carrying out the radial and azimuthal integrations yields:

$$V'(r_0', z_0') = \frac{N_q qe}{\pi^2 \epsilon_0} \int_{-\infty}^{\infty} dz \left(\frac{\tilde{f}_q(z)}{a_l^2}\right) \times \\ \left[V_>'(r_0', z_0', z) H\left(\frac{r_0'}{a_l}^2 - 1\right) + V_<'(r_0', z_0', z) H\left(1 - \frac{r_0'}{a_l}^2\right)\right] , \tag{213}$$

where for $r_0' > a_l$ we get:

$$V_>'(r_0', z_0', z) = \int_0^{\infty} \frac{dk}{k^2} \cos\left[k(z_0' - z)\right] \left[\frac{K_0(kr_0')}{I_0(kr_0')} - \frac{K_0(kR_c)}{I_0(kR_c)}\right] ka I_0(kr_0') I_1(ka_l) , \tag{214}$$

and for $r_0' < a_l$ we get:

$$V_<'(r_0', z_0', z) = \int_0^{\infty} \frac{dk}{k^2} \cos\left[k(z_0' - z)\right] \left\{ \begin{array}{c} \left[\frac{K_1(kr_0')}{I_1(kr_0')} + \frac{K_0(kr_0')}{I_0(kr_0')}\right] kr_j' I_0(kr_0') I_1(kr_0') - \\ \left[\frac{K_1(ka_l)}{I_1(ka_l)} + \frac{K_0(kR_c)}{I_0(kR_c)}\right] kr_j' I_0(kr_0') I_1(ka_l) \end{array} \right\} . \tag{215}$$

The electric fields are evaluated by substituting (213) into $\mathbf{E}' = -\nabla V$. For the electric fields in the beam frame, we can write:

$$\begin{aligned}
E'_r(r_0, z_0) &= \frac{N_q q e}{\pi^2 \epsilon_0} \int_{-\infty}^{\infty} dz \left(\frac{\tilde{f}_q(z)}{a_l^2} \right) \times \\
&\qquad \left[E'_{r,>}(r_0, z_0, z) H\left(\frac{r_0^2}{a_l^2} - 1 \right) + E'_{r,<}(r_0, z_0, z) H\left(1 - \frac{r_0^2}{a_l^2} \right) \right] , \\
E'_z(r_0, z_0) &= \frac{N_q q e}{\pi^2 \epsilon_0} \int_{-\infty}^{\infty} dz \left(\frac{\tilde{f}_q(z)}{a_l^2} \right) \times \\
&\qquad \left[E'_{z,>}(r_0, z_0, z) H\left(\frac{r_0^2}{a_l^2} - 1 \right) + E'_{z,<}(r_0, z_0, z) H\left(1 - \frac{r_0^2}{a_l^2} \right) \right] ,
\end{aligned} \tag{216}$$

where we have transformed the location at which we compute the electric fields to the frame of the cylinder from that of the beam, $r'_0 = r_0$ and $z'_0 = \gamma z_0$, where γ is, as before, the relativistic factor. Then for $r_0 > a_l$ we get:

$$\begin{aligned}
E'_{r,>}(r_0, z_0, z) &= \int_0^{\infty} dk \cos\left[k(\gamma z_0 - z)\right] \left[\frac{K_0(kR_c)}{I_0(kR_c)} I_1(kr_0) - K_1(kr_0) \right] a_l I_1(ka_l) , \\
E'_{z,>}(r_0, z_0, z) &= \int_0^{\infty} \frac{dk}{k} \sin\left[k(\gamma z_0 - z)\right] \left[\frac{K_0(kr_0)}{I_0(kr_0)} - \frac{K_0(kR_c)}{I_0(kR_c)} \right] k a_l I_0(kr_0) I_1(ka_l) ,
\end{aligned} \tag{217}$$

and for $r_0 < a_l$ we get:

$$\begin{aligned}
E'_{r,<}(r_0, z_0, z) &= \int_0^{\infty} dk \cos\left[k(\gamma z_0 - z)\right] \left[\frac{K_0(kR_c)}{I_0(kR_c)} I_1(ka_l) - K_1(ka_l) \right] a_l I_1(kr_0) , \\
E'_{z,<}(r_0, z_0, z) &= \int_0^{\infty} \frac{dk}{k} \sin\left[k(\gamma z_0 - z)\right] \times \\
&\qquad \left\{ 1 - \frac{I_0(kr_0)}{I_0(ka_l)} + \left[\frac{K_0(ka_l)}{I_0(ka_l)} - \frac{K_0(kR_c)}{I_0(kR_c)} \right] k a_l I_0(kr_0) I_1(ka_l) \right\} ,
\end{aligned} \tag{218}$$

We now convert the integrals in equations (216), (217) and (218) to Reimann sums. First the infinite integral over the axial dimension in (216) is non-vanishing only along the length of the beam, L_b, because $\tilde{f}_q(z)$, the normalized axial density of the beam, is non-vanishing only along the beam. As before, we divide the beam into several axial slices, each of thickness δz, across which the radius of the beam, a_l, can be taken to be approximately constant, then (216) becomes:

$$
\begin{aligned}
E'_z(r_0, z_0) &= \frac{qe}{\pi^2 \epsilon_0} \sum_{\mu=1}^{L_b/\delta z} \frac{N_{q,\mu}}{a_\mu^2} \times \\
&\qquad \left[E'_{z,\mu,<} H\left(1 - \frac{r_0^2}{a_\mu^2}\right) + E'_{z,\mu,>} H\left(\frac{r_0^2}{a_\mu^2} - 1\right)\right] , \\
E'_r(r_0, z_0) &= \frac{qe}{\pi^2 \epsilon_0} \sum_{\mu=1}^{L_b/\delta z} \frac{N_{q,\mu}}{a_\mu^2} \times \\
&\qquad \left[E'_{r,\mu,<} H\left(1 - \frac{r_0^2}{a_\mu^2}\right) + E'_{r,\mu,>} H\left(\frac{r_0^2}{a_\mu^2} - 1\right)\right] ,
\end{aligned}
\tag{219}
$$

where a_μ and $N_{q,\mu}$ are the radius and number of beam ions for each beam slice denoted by index $\mu = 1, 2, \cdots, L_b/\delta z$, and $E'_{r,\mu,>}$, for instance, is the shorthand notation for $E'_{r,>}(r_0, z_0, z_h + \mu\delta z)$, where z_h, as before, is the axial location for the head of the beam. The integral along the the axial wave number, k, is made finite by the imposition of the spatial grid. Since we are ultimately interested in the fields at grid locations, the smallest axial wavelength that can be resolved is $\lambda_{min} = 2\gamma\Delta z$, where Δz, as before, is the axial grid division, in the frame of the cylinder, and the factor of γ converts this to the frame of the beam. Then the maximum wave number is $k_{max} = 2\pi/\lambda_{min} = \pi/\gamma\Delta z$, and equation (217) becomes:

$$
\begin{aligned}
E'_{r,\mu,>}(r_0, z_0) =& \frac{\pi}{2\gamma L_c} \frac{a_\mu^2}{r_0} + \sum_{n=1}^{L_c/2\Delta z} \frac{2\pi}{\gamma L_c} \cos\left[k_n \gamma (z_0 - z_h - \mu\delta z)\right] \times \\
&\qquad \left[\frac{K_0(k_n R_c)}{I_0(k_n R_c)} I_1(k_n r_0) + K_1(k_n r_0)\right] a_\mu I_1(k_n a_\mu) , \\
E'_{z,\mu,>}(r_0, z_0) =& \sum_{n=1}^{L_c/2\Delta z} \frac{1}{n} \sin\left[k_n \gamma (z_0 - z_h - \mu\delta z)\right] \times \\
&\qquad \left[\frac{K_0(k_n r_0)}{I_0(k_n r_0)} - \frac{K_0(k_n R_c)}{I_0(k_n R_c)}\right] k_n a_\mu I_0(k_n r_0) I_1(k_n a_\mu) ,
\end{aligned}
\tag{220}
$$

and equation (218) becomes:

$$\begin{aligned}
E'_{r,\mu,<}(r_0,z_0) =& \frac{\pi}{2\gamma L_c} r_0 + \sum_{n=1}^{L_c/2\Delta z} \frac{2\pi}{\gamma L_c} \cos\left[k_n\gamma(z_0 - z_h - \mu\delta z)\right] \times \\
& \left[\frac{K_0(k_n R_c)}{I_0(k_n R_c)} I_1(k_n a_\mu) + K_1(k_n a_\mu)\right] a_\mu I_1(k_n r_0) \,, \\
E'_{z,\mu,<}(r_0,z_0) =& \sum_{n=1}^{L_c/2\Delta z} \frac{1}{n} \sin\left[k_n\gamma(z_0 - z_h - \mu\delta z)\right] \times \\
& \left\{ \begin{array}{c} 1 - \frac{I_0(k_n r_0)}{I_0(k_n a_\mu)} + \left[\frac{K_0(k_n a_\mu)}{I_0(k_n a_\mu)} - \frac{K_0(k_n R_c)}{I_0(k_n R_c)}\right] \times \\ k_n a_\mu I_0(k_n r_0) I_1(k_n a_\mu) \end{array} \right\} ,
\end{aligned} \tag{221}$$

where L_c, as before, is the length of the cylinder and $k_n = 2n\pi/\gamma L_c$ is the discretized wave number in the beam frame, where $n = 1, 2, \cdots, L_c/2\Delta z$. This conversion of an infinite integral over k to a finite sum over k_n makes the system periodic, and therefore introduces "ghost" beams to the front and back of the actual beam. We can reduce the effects of these beams on the fields in the cylinder by making the cylinder shown in figure (12) sufficiently long; perhaps by a few beam-lengths longer than the minimum simulation length.

Equations (219) give the electric fields in the beam frame; however, in order to solve the numerical equations, we require the initial fields in the frame of the cylinder. Therefore we perform a Lorentz transformation of these beam frame fields:

$$\begin{aligned}
\mathbf{E} &= \frac{\mathbf{E}' - \beta c\hat{z} \times \mathbf{B}'}{\sqrt{1-\beta^2}} - \frac{(\beta\hat{z}\cdot\mathbf{E}')\,\beta\hat{z}}{1-\beta^2+\sqrt{1-\beta^2}} \,, \\
\mathbf{B} &= \frac{\mathbf{B}' + \beta/c\hat{z} \times \mathbf{E}'}{\sqrt{1-\beta^2}} - \frac{(\beta\hat{z}\cdot\mathbf{B}')\,\beta\hat{z}}{1-\beta^2+\sqrt{1-\beta^2}} \,,
\end{aligned} \tag{222}$$

where β is the axial velocity of the beam in units of c. The "primed" quantities are the fields in the beam frame and the "unprimed" quantities are those in the frame of the cylinder. For the geometry of concern here (222) reduces to:

$$\begin{aligned} E_z(r_0, z_0) &= E'_z(r_0, z_0) \ , \\ E_r(r_0, z_0) &= \gamma E'_r(r_0, z_0) \ , \\ B_\theta(r_0, z_0) &= \frac{\beta\gamma}{c} E'_r(r_0, z_0) \ , \end{aligned} \tag{223}$$

where γ, as before, is the relativistic factor, $\gamma = 1/\sqrt{1-\beta^2}$. To find the fields on the spatial grid shown in figure (16) we set (r_0, z_0) to the grid location of interest. For instance if we wish to find the radial electric field at the grid location $j + 1/2, k$, $E_{r,j+1/2,k} \equiv E_r(r_{j+1/2}, z_k)$, we first set $r_0 = r_{j+1/2}$, and $z_0 = z_k$ where $(r_{j+1/2}, z_k)$ is the position of the grid point $j + 1/2, k$. We then use equations (219) to solve for the field in the frame of the beam, $E'_r(r_{j+1/2}, z_k)$; and then use equations (223) to transform to the frame of the cylinder, $E_r(r_{j+1/2}, z_k) = \gamma E'_r(r_{j+1/2}, z_k)$. Therefore given a set of initial parameters for the beam: its velocity, β; pulse length, L_b; the number of ions of charge state q, $N_{q,\mu}$, initial radius, a_μ, and emittance, ϵ_μ, of each beam slice, μ; we can use this method to initialize the radial and axial electric fields and the azimuthal magnetic field at all grid points in the cylinder shown in figure (12).

4.2.3 Field Boundary Conditions

Finally we discuss the boundary conditions for the fields. For the spatial grid shown in figure (16), these are the radial electric field and azimuthal magnetic field on the axis of the cylinder shown in figure (12), $E_{r,1/2,k}$ and $B_{\theta,1/2,k+1/2}$, the axial electric field on the surface of the cylinder, $E_{z,N_r,k+1/2}$, and the radial electric fields at the two open-ends, $E_{r,j+1/2,1}$ and $E_{r,j+1/2,N_z}$. From symmetry arguments we set the radial electric field and azimuthal magnetic field on the axis of the cylinder to zero; and because the cylinder has conducting walls, the axial electric field on the surface also vanishes. This leaves the radial electric field at the two open ends.

Mur (1981), discusses a boundary condition that absorbs the outgoing waves at the two open ends of the cylinder. The analytic free-space solution for the radial electric field of a transverse magnetic wave in a long cylinder is of the form $E_r \sim J_1(p_0 r)\exp(\pm i k_0 z)\exp(-i\omega_0 t)$, where, as before, the frequency of the wave, ω_0, the axial wave number, k_0, and p_0 are related by the dispersion relation, $\omega_0^2 = c^2(k_0^2 + p_0^2)$, such that $p_0 R_c = \zeta_0$ are zeroes of the J_0 Bessel function where R_c is the radius of the cylinder. For any transverse boundary in the cylinder, these solutions satisfy the condition:

$$\frac{\partial E_r}{\partial z} = \pm\left(\frac{k_0}{\omega_0}\right)\frac{\partial E_r}{\partial t}\,, \tag{224}$$

where a wave traveling in the direction of increasing z, or a right-going wave specified by the + sign in the axial exponent, satisfies the negative equation, while the left-going wave satisfies the positive equation. The propagation vector of the wave is given by $\mathrm{k} = k_0\hat{z} + p_0\hat{r}$; and the angle of incidence with respect to the axis of the cylinder is, $\cos\vartheta = k_0/|\mathrm{k}|$. Substituting from the dispersion relation, we can write (224) as:

$$\frac{\partial E_r}{\partial z} = \pm\left(\frac{\cos\vartheta}{c}\right)\frac{\partial E_r}{\partial t}\,. \tag{225}$$

If we now take $\vartheta \simeq 0$, or the waves to be normal-incident on the open-ends, then

$$\frac{\partial E_r}{\partial z} \simeq \pm\left(\frac{1}{c}\right)\frac{\partial E_r}{\partial t}\,. \tag{226}$$

The validity of this approximation is discussed later.

We now turn to the finite difference equations. If we assume that all stability and accuracy criterion are met rigorously, then the frequencies and wave numbers of the numerical solutions will be close to those of the analytic solutions. Using "central differencing" in time and "three-point" spatial differencing discussed earlier gives:

$$\begin{aligned}\frac{\partial E_r}{\partial t} &= \frac{1}{\Delta t}\left(\frac{E^{n+1}_{r,j+1/2,k} + E^{n+1}_{r,j+1/2,k-1}}{2} - \frac{E^{n}_{r,j+1/2,k} + E^{n}_{r,j+1/2,k-1}}{2}\right)\,,\\ \frac{\partial E_r}{\partial z} &= \frac{1}{\Delta z}\left(\frac{E^{n+1}_{r,j+1/2,k} + E^{n}_{r,j+1/2,k}}{2} - \frac{E^{n+1}_{r,j+1/2,k-1} + E^{n}_{r,j+1/2,k-1}}{2}\right)\,.\end{aligned} \tag{227}$$

Substituting (227) into (226) yields:

$$\begin{aligned} E^{n+1}_{r,j+1/2,k}\left(c\Delta t \mp \Delta z\right) - E^{n+1}_{r,j+1/2,k-1}\left(c\Delta t \pm \Delta z\right) \; &= \\ E^{n}_{r,j+1/2,k-1}\left(c\Delta t \mp \Delta z\right) &- E^{n}_{r,j+1/2,k}\left(c\Delta t \pm \Delta z\right) \ . \end{aligned} \tag{228}$$

where, as before, the left-going wave uses the upper signs and the right-going wave the lower signs. Separating this equation into a left-going wave for the left open end and a right-going wave for the right open end yields:

$$\begin{aligned} E^{n+1}_{r,j+1/2,1} &= E^{n}_{r,j+1/2,2} + \frac{c\Delta t - \Delta z}{c\Delta t + \Delta z}\left(E^{n+1}_{r,j+1/2,2} - E^{n}_{r,j+1/2,1}\right) \ , \\ E^{n+1}_{r,j+1/2,N_z} &= E^{n}_{r,j+1/2,N_z-1} + \frac{c\Delta t - \Delta z}{c\Delta t + \Delta z}\left(E^{n+1}_{r,j+1/2,N_z-1} - E^{n}_{r,j+1/2,N_z}\right) \ . \end{aligned} \tag{229}$$

Thus knowing the radial electric fields at one grid location inside the boundaries at both the current and previous time-steps, $E^{n+1}_{r,j+1/2,2}$ and $E^{n}_{r,j+1/2,2}$, and $E^{n+1}_{r,j+1/2,N_z-1}$ and $E^{n}_{r,j+1/2,N_z-1}$; and the field at the boundary at the previous time-step, $E^{n}_{r,j+1/2,1}$ and $E^{n}_{r,j+1/2,N_z}$, allows us to find the fields at the boundary for the current time-step, $E^{n+1}_{r,j+1/2,1}$ and $E^{n+1}_{r,j+1/2,N_z}$. This simple boundary condition absorbs all waves that are incident normal to the open-ends, $\vartheta \simeq 0$; waves that are incident at angles that are much different from this will be artificially reflected back into the cylinder. Since the waves are generated in the vicinity of the beam, if the distance between the beam and the open-ends of the cylinder shown in figure (12) is approximately the length of the beam, then the angle of incidence for a wave to reach the open-ends without reflecting off the walls of the cylinder is $\vartheta \simeq \tan^{-1}(R_c/L_b)$. For the parameters given in table (3) we get $\vartheta \simeq 0.29\, rad$, or $\cos\vartheta \simeq 0.96$, which is close to unity, satisfying the approximation made in equation (226).

This concludes the discussion of the initial and boundary conditions required to solve the numerical equations. Indeed with these and the conditions on the discrete parameters described above, we are in a position to use the equations to analyze the transport of a beam of ions through background gas. The algorithm proceeds

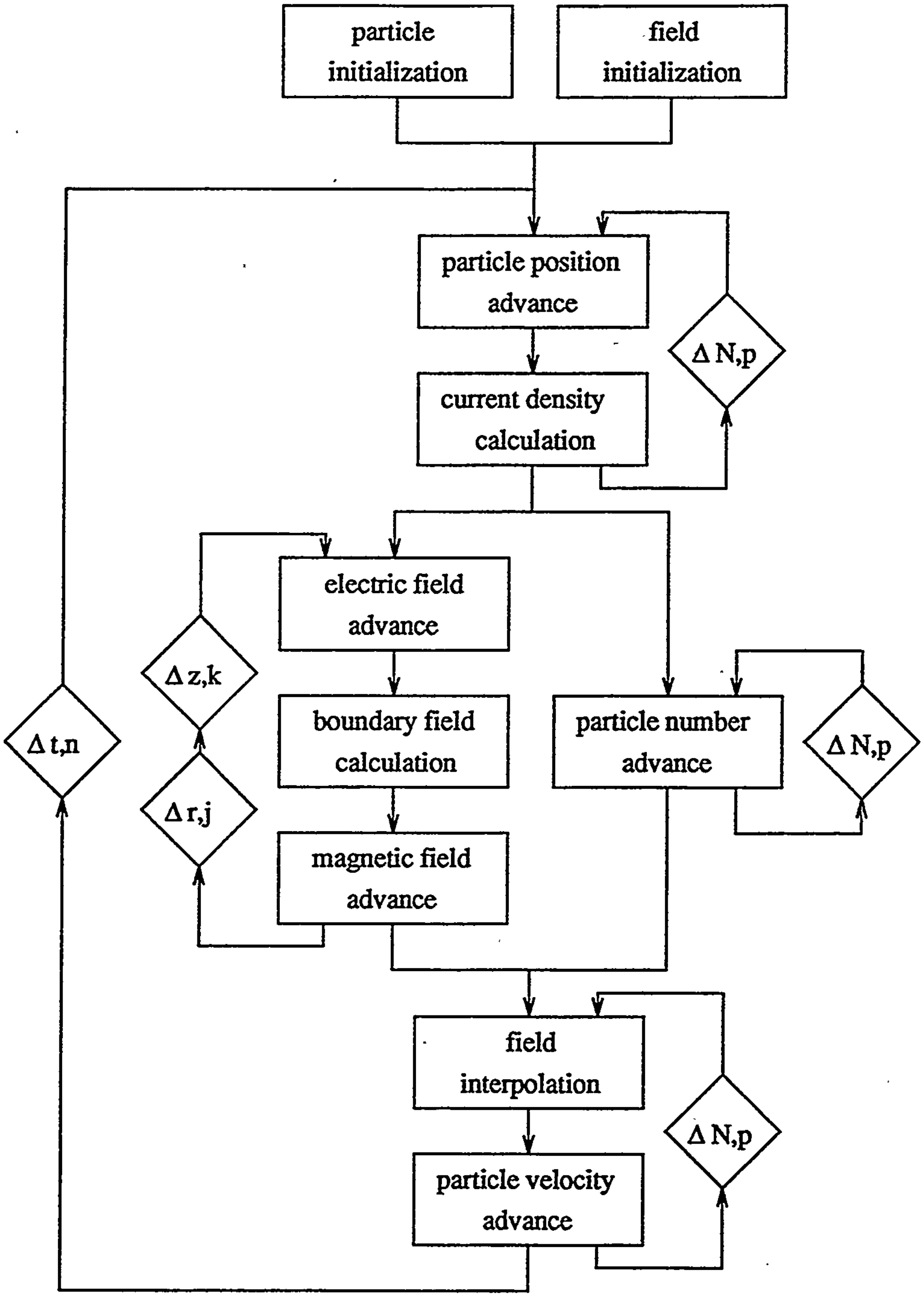

Figure 25: Flow-chart of the BTRAC code used to solve the numerical equations.

as follows. We start with a set of initial beam parameters, such as those outlined in table (3). We assume that the beam has a K-V transverse distribution; and convert the normalized axial distribution, $\tilde{f}_q(z)$, into a series of slices specified by equation

(198). We also specify the background gas density, n_g; the stripping and ionization cross sections for beam ions of various charge states, q, colliding with background gas neutrals, $\sigma_{st,q}$ and $\sigma_{in,q}$; and the size of the simulation environment shown in figure (12), L_c and R_c. We first use equation (186) to determine the superparticle ratio, ΔN. From this we can determine the number of super-beam ions for each charge state, K_q. Then using equation (195) and the beam parameters we can determine the initial positions, $r_{q,p}$ and $z_{q,p}$, and velocities, $v_{r,q,p}$, $v_{\theta,q,p}$ and $v_{z,q,p}$, of each particle, q, p. Using equations (200) and (199) we can determine the spatial mesh sizes, Δz and Δr. From these and the size of the simulation environment, we can find the number of radial and axial grid points, N_r and N_z. And using the distribution functions and equations (223) we can initialize the fields, $E_{r,j+1/2,k}$, $E_{z,j,k+1/2}$ and $B_{\theta,j+1/2,k+1/2}$, for each mesh point j, k on the grid shown in figure (16). After having initialized the fields and particles, we can now "push" the beam ions forward in time.

First using the most stringent of equations (187), (190) and (191) we can determine the size of the time-step, Δt. Then for every time-step we do the following. We use equations (53) and (57), and the present positions, $r^n_{s,p}$ and $z^n_{s,p}$, and velocities, $v^{n+1/2}_{r,q,p}$, $v^{n+1/2}_{\theta,q,p}$, $v_{z,q,p}$, $v^{n+1/2}_{r,e,p}$, $v^{n+1/2}_{\theta,e,p}$, $v^{n+1/2}_{z,e,p}$, $v^{n+1/2}_{r,g,p}$ and $v^{n+1/2}_{z,g,p}$ to advance the positions of the particles to the next time-step, $r^{n+1}_{s,p}$ and $z^{n+1}_{s,p}$. We then use equation (109), these present and advanced particle positions, the weighting functions, (97), and the present number of particles $K^{n+1/2}_s$, to calculate the current densities for each mesh point, $J^{n+1/2}_{r,j+1/2,k}$ and $J^{n+1/2}_{z,j,k+1/2}$. With these current densities and the present electric fields, $E^n_{r,j+1/2,k}$ and $E^n_{z,j,k+1/2}$, and magnetic fields, $B^{n+1/2}_{\theta,j+1/2,k+1/2}$, we can use equations (59) and (60) to advance the electric fields for each mesh point in the interior of the simulation environment to the next time-step, $E^{n+1}_{r,j+1/2,k}$ and $E^{n+1}_{r,j,k+1/2}$. These along with the boundary conditions specified by equations (229) are used to advance the radial electric fields on the two open-ends of the simulation environment shown in figure (12) to the next time-step, $E^{n+1}_{r,j+1/2,1}$ and $E^{n+1}_{r,j+1/2,N_z}$. Then with these electric fields and equation (61) we can advance the magnetic field to the next time-step, $B^{n+3/2}_{\theta,j+1/2,k+1/2}$. Using equations (115), the present number of particles, and the cross sections and background gas density we can determine the number of particles for each species for the next time-step, $K^{n+3/2}_s$. With the advanced fields on the mesh points, the particle positions, and the same weighting functions as were used for the current density calculations, (97), we can use equation (98) to interpolate the fields to the particles, $E^{n+1}_{r,s,p}$, $E^{n+1}_{z,s,p}$ and $B^{n+1}_{\theta,s,p}$. Finally we can use equations (66), (70), (74), (75), (79), (87) and (88), these interpolated fields, and the present particle velocities to advance the velocities to the next time-step, $v^{n+3/2}_{r,g,p}$, $v^{n+3/2}_{\theta,g,p}$, $v^{n+3/2}_{r,e,p}$, $v^{n+3/2}_{\theta,e,p}$, $v^{n+3/2}_{z,e,p}$, $v^{n+3/2}_{r,g,p}$ and $v^{n+3/2}_{z,g,p}$. In this way we advance all quantities from one time-step to the next; we repeat this for each time-step. Figure (25) shows the flow-chart for this algorithm. A computer code, BTRAC, described in detail in the appendix, was developed to "solve" the numerical equations by carrying out these operations.

5 Stripping and Ionization Cross Sections

As mentioned above, in order to use the method outlined in the previous chapters to solve for the propagation of a beam of heavy ions through background gas we need to provide, in addition to the beam parameters and system geometry, a set of stripping and ionization cross sections, $\sigma_{st,q}$ and $\sigma_{in,q}$, for the fast, $\beta \simeq 0.3$, collisions of interest in this thesis. Since most experimental data is for slow collisions, Lo and Fite (1970) and Dehmel, et al., (1973), we develop here a semi-empirical approach for calculating these cross sections. Betz (1972) presents a good survey of the various theories applicable to such calculations. We focus here on two theories that allow us to calculate the cross sections for electron loss collisions between the beam ions and background gas atoms: the Bohr classical theory and the Bethe quantum theory. The Bethe theory, based on the Born approximation, gives the "correct" velocity dependence, $(1/\beta^2)\ln(\beta^2)$, when compared with experimental data; however the parameters contained in this formulation are not easily calculated for atoms more complicated than helium. By contrast the Bohr theory, based on the "free electron" approximation, has parameters that depend only on the ionization energies of atomic orbitals, which are readily available; however, the velocity dependence it predicts is simply $(1/\beta^2)$. We therefore develop a semi-empirical method for obtaining the necessary parameters in the Bethe theory using the Bohr theory as a guide.

5.1 Cross Section Theories

Single-electron loss reactions can be described by:

$$A^{n+} + B^{k+} \to A^{(n+1)+} + B^{k+} + e \; . \tag{229}$$

In the following discussion we shall refer to the atom that looses the electron as the target, in this case A^{n+}, and the atom that causes this loss as the projectile, in this case B^{k+}. We can relate this to the ionization and stripping cross sections discussed earlier, if we let A^{n+} represent the beam ion of charge state n, so that $q=n$, and B^{k+} represent the neutral background gas atom, so that $k=0$, then the cross section for the loss of an electron from A is the stripping cross section, $\sigma_{st,n}$; alternatively, if we let A^{n+} represent the background gas atom, so that now $n=0$, and B^{k+} be the beam ion of charge state k, so that $q=k$, then the cross section for the loss of an electron from A is the ionization cross section, $\sigma_{in,k}$.

5.1.1 Bohr Classical Theory

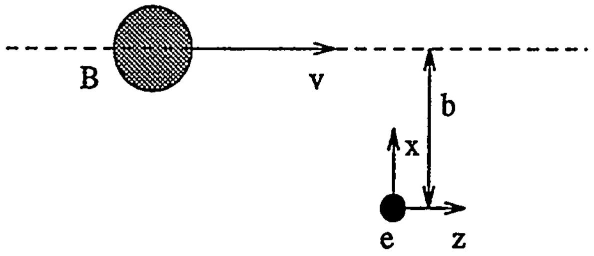

Figure 26:. The geometry for atomic collisions.

Following Bohr (1948) we calculate the cross section by viewing the system in the reference frame of the target atom, A. The derivation presented here also benefits from lectures by Prussin (1992). Figure (26) shows the geometry of the collision, where B is the projectile, and e is an electron to be lost in the target atom. Because the projectile is fast we can invoke the impulse approximation, then the electron remains instantaneously at rest in this reference frame. The change in momentum of the projectile can be written as:

$$\Delta \mathbf{p}_B = Z_{B,k} e \int \mathbf{E} dt \ , \tag{230}$$

where $\mathbf{E}$ is the electric field of the electron in this frame, and $Z_{B,k}$ is the effective charge state of the projectile, which depends on both the atomic number, Z_B, and the charge state, k. The electric field of the electron is simply:

$$\mathbf{E} = \frac{-e}{(x^2+z^2)^{3/2}}\left[x\hat{x} + z\hat{z}\right] , \tag{231}$$

where $\sqrt{x^2+z^2}$ is the distance between the projectile and the electron. If we now make the assumption that, the projectile maintains a straight-line trajectory with constant velocity, then substituting (231) into (230) and carrying out the integration yields:

$$\Delta\mathbf{p}_B = \frac{-2Z_{B,k}e^2}{\beta c b}\hat{x} , \tag{232}$$

where b is the so-called impact parameter as shown in figure (26), and β is the velocity of the projectile. From momentum conservation, the momentum transferred to the electron must be exactly equal to, but opposite in sign to the change in the momentum of the projectile, $\Delta\mathbf{p}_e = -\Delta\mathbf{p}_B$. The kinetic energy transferred to the electron is given non-relativistically by:

$$\Delta T = \frac{1}{2m_e}\left[\Delta\mathbf{p}_e^2 + 2\Delta\mathbf{p}_e\cdot\mathbf{p}_i\right] . \tag{233}$$

where $\mathbf{p}_i$ is the initial momentum of the electron in the target atom, and m_e is the electron mass. Because the direction of the initial momentum of the electrons in any given orbital is entirely random, if we take an ensemble average of the dot product in (233) we get zero; then substituting from (232) yields:

$$\langle\Delta T\rangle = \frac{2a_0^2 Z_{B,k}^2 \alpha^4 m_e c^2}{\beta^2 b^2} , \tag{234}$$

where $\langle\,\rangle$ denotes an ensemble average, α is the fine structure constant, and a_0 is the Bohr radius. The ionization cross section, or probability for the removal of any single electron, μ, in the target atom, is simply given by:

$$\sigma_\mu = 2\pi\int b\,db = \frac{2\pi a_0^2 Z_{B,k}^2 \alpha^4 m_e c^2}{\beta^2}\int_{B_{A,n,\mu}}^{\infty}\frac{d\langle\Delta T\rangle}{\langle\Delta T\rangle^2} , \tag{235}$$

where we have substituted for b from (234), and where $B_{A,n,\mu}$ is the electron's binding energy in the target atom, A. If we carry out the integration in (235) and sum over all the electrons in the target atom to get the total probability, then the Bohr cross section formula becomes:

$$\sigma_{Bohr} = \sum_{\mu=1}^{Z_A-n} \sigma_\mu = \left(\frac{4\pi a_0^2 Z_{B,k}^2 \alpha^2}{\beta^2} \right) \Sigma_{A,n} \ , \tag{236}$$

where:

$$\Sigma_{A,n} \equiv \sum_{\mu=1}^{Z_A-n} \frac{R}{B_{A,n,\mu}} \ , \tag{237}$$

where R is the Rydberg energy, 13.6 eV, and Z_A is the atomic number of the target atom. $\Sigma_{A,n}$ contains all the atomic information of the target; and the coefficient, in particular $Z_{B,k}$, contains the information about the projectile. The fact that the formula is a product of these two parts is a general characteristic of fast collisions where the projectile and the target do not intimately interact with each other.

5.1.2 Bethe Quantum Theory

Bethe (1930) gives the following cross section for the removal of a single electron, μ, based on the Born approximation for fast collisions:

$$\sigma_\mu = \frac{4\pi a_0^2 Z_{B,k}^2 \alpha^2}{\beta^2} \left(b_{A,n,\mu} \frac{R}{B_{A,n,\mu}} \right) \ln \left(4 \frac{\beta^2}{\alpha^2} \frac{R}{c_{A,n,\mu}} \right) \ , \tag{238}$$

where $b_{A,n,\mu}$ are some ionization factors and $c_{A,n,\mu}$ are roughly equivalent to the binding energies, $B_{A,n,\mu}$; R, as before, is the Rydberg energy. Carrying out the summation over all orbitals in (238) yields the Bethe cross section formula:

$$\sigma_{Bethe} = \sum_{\mu=1}^{Z_A-n} \sigma_\mu = \left(\frac{4\pi a_0^2 Z_{B,k}^2 \alpha^2}{\beta^2} \right) \left[M_{A,n}^2 \ln \left(4 \frac{\beta^2}{\alpha^2} \right) + C_{A,n} \right] \ , \tag{239}$$

where

$$M_{A,n}^2 \equiv \sum_{\mu=1}^{Z_A-n} \left(\frac{R}{B_{A,n,\mu}} \right) b_{A,n,\mu} \ , \tag{240}$$

and

$$C_{A,n} \equiv \sum_{\mu=1}^{Z_A-n} b_{A,n,\mu} \left(\frac{R}{B_{A,n,\mu}}\right) \ln\left(\frac{R}{c_{A,n,\mu}}\right) . \tag{241}$$

Again we see that the formula (239) is the product of two parts: one that contains the quantities $M^2_{A,n}$ and $C_{A,n}$ which are both functions of the target only, and a coefficient that contains the information of the projectile. It is interesting to note that the projectile parts of the Bohr and Bethe formulae, (236) and (239), are identical.

5.2 Semi-Empirical Analysis

The parameter, $\Sigma_{A,n}$, in the Bohr formula (236), is fairly easy to calculate since it depends on nothing more than the binding energies of the electrons in the target atom, $B_{A,n,\mu}$. On the other hand the parameters, $M^2_{A,n}$ and $C_{A,n}$, in the Bethe formula (239), are difficult to obtain since they require a detailed knowledge of the eigenfunctions of atom A^{n+} for the calculations of $b_{A,n,\mu}$ and $c_{A,n,\mu}$.

5.2.1 Experimental Comparison

In order to determine which of the two formulae, (236) or (239), has the "correct" velocity dependence, we write them as:

$$\left(\frac{\beta^2}{4\pi a_0^2 Z^2_{B,k}\alpha^2}\right) \sigma_{Bohr} = \Sigma_{A,n} \ , \tag{242}$$

and

$$\left(\frac{\beta^2}{4\pi a_0^2 Z^2_{B,k}\alpha^2}\right) \sigma_{Bethe} = M^2_{A,n} \left[\ln C_{A,n} + \ln\left(\frac{4\beta^2}{\alpha^2}\right)\right] \ , \tag{243}$$

If we now plot experimental data for the left hand side of these equations versus $\ln(4\beta^2/\alpha^2)$ we would either expect to see a constant, if the Bohr formula is "correct", or a straight line, if the Bethe formula is "correct"; such a plot is referred to as a Fano plot, after Fano and Cooper (1968). As mentioned above, there is not much

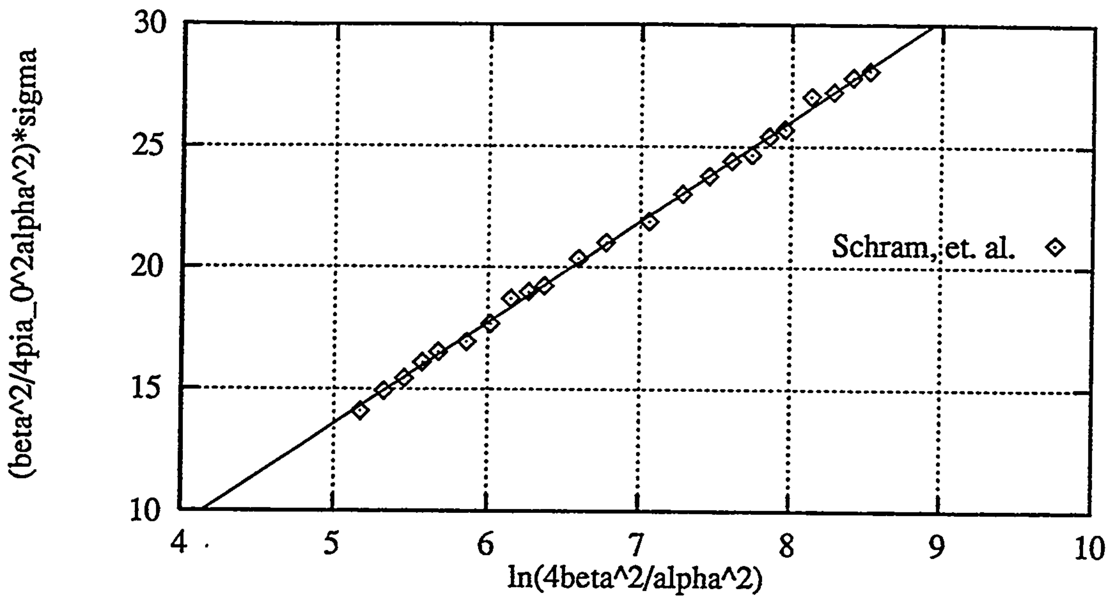

Figure 27: $\left(\frac{\beta^2}{4\pi a_0^2\alpha^2}\right)$ *σ vs. ln* $\left(\frac{4\beta^2}{\alpha^2}\right)$ *for single electron ionization of argon.*

experimental data available for fast atomic collisions; however fast collisions between electrons and atoms, and protons and atoms are more readily available. In this case $Z_{B,k}^2 = 1$. Figure (27) shows the Fano plot for electron impact ionization of argon; the experimental data is taken from Schram (1966). As can be seen the data is not approximated by a constant corresponding to $\sigma \sim (1/\beta^2)$, suggesting that the Bohr formula (242) is "incorrect". Indeed we can fit a diagonal straight line through the data, as shown, which means that the Bethe formula (243) contains an essential additional physics. Following Fano and Cooper (1968), we can use such plots to determine $M_{A,n}^2$ and $C_{A,n}$ which should be the slope and intercept of the line respectively as seen from (243). Table (4) shows the results of such an analysis for the electron impact ionization of various noble gas targets; the data is again taken from Schram, et al., (1966).

Target atom	$M^2_{A,n}$	$-C_{A,n}$
Helium	0.49	0.54
Neon	1.84	4.50
Argon	4.16	7.23
Krypton	5.95	9.58
Xenon	8.25	11.8

Table 4: $M^2_{A,n}$ and $C_{A,n}$ for noble gases.

5.2.2 Cross Section Formula

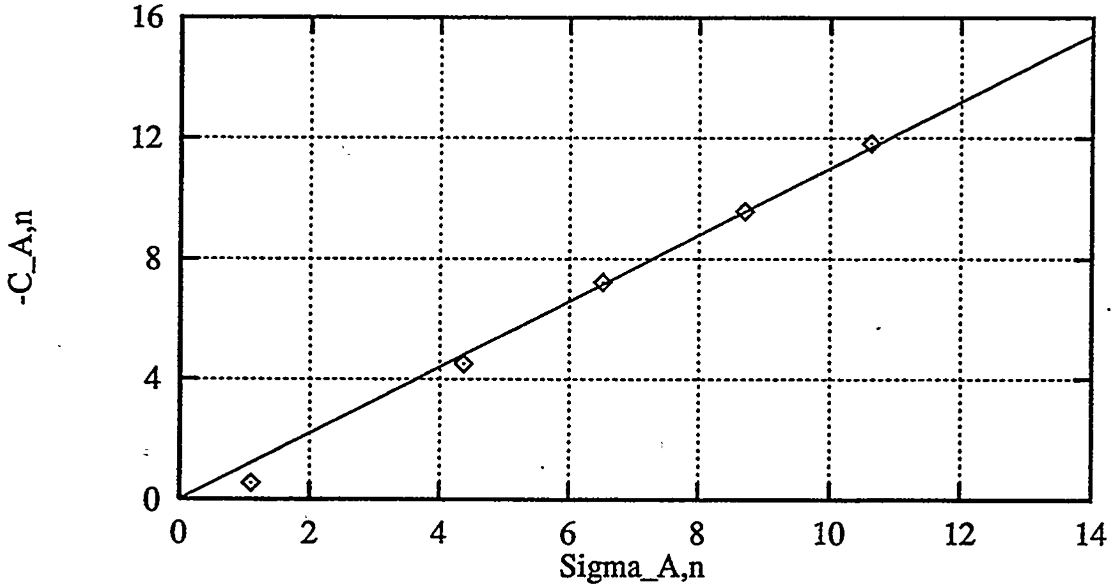

Figure 28: $-C_{A,n}$ vs. $\Sigma_{A,n}$ for the noble gases.

Using the data in table (4) and guided by equations (240) and (241) we look for relationships between the parameters in (239), $M^2_{A,n}$ and $C_{A,n}$, and the quantity $\Sigma_{A,n}$. Inokuti (1971) suggests the possibility of polynomial expansions in the inverse binding energy, $1/B_{A,n,\mu}$. Since $\Sigma_{A,n}$ is a function of these binding energies, we assume that the expansion can be given in terms of $\Sigma_{A,n}$. Figure (28) shows the plot of $-C_{A,n}$ vs. $\Sigma_{A,n}$ for each of the noble gases shown in table (4). The binding energies for the

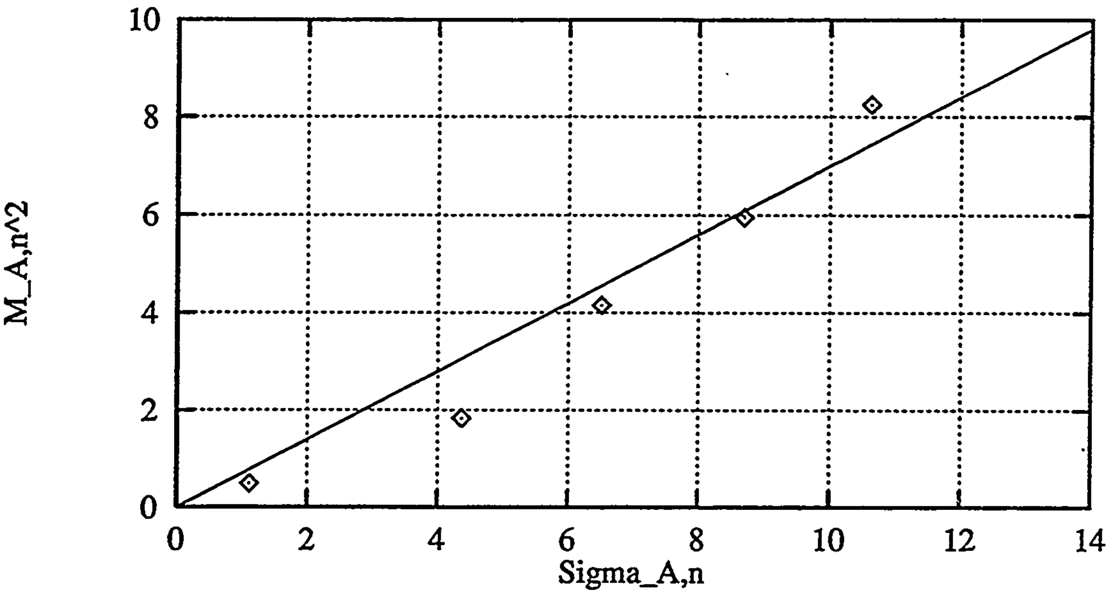

Figure 29: $M_{A,n}^2$ *vs.* $\Sigma_{A,n}$ *for the noble gases.*

calculation of $\Sigma_{A,n}$ were taken from Sevier (1979). If we assume a lowest order linear expansion, we can fit a straight line to the data, $c_2\Sigma_{A,n}$, where c_2 is some constant, in this case, $c_2 \simeq 1.1$. Similarly we can also plot $M_{A,n}^2$ vs. $\Sigma_{A,n}$, as shown in figure (29). Again using the data in table (4), and conducting a linear fit yields, $c_1\Sigma_{A,n}$, where for the noble gases $c_1 \simeq 0.7$.

If we now substitute these constants into (239) we get the following semi-empirical formula for the electron loss cross section, σ:

$$\sigma \simeq \frac{4\pi a_0^2 Z_{B,k}^2 \alpha^2}{\beta^2}\left[c_1 \ln\left(\frac{4\beta^2}{\alpha^2}\right) - c_2\right]\Sigma_{A,n} \ , \tag{244}$$

where $\Sigma_{A,n}$ is given by (237). Therefore given the constants c_1 and c_2, we can calculate the cross sections for single electron ionization.

5.3 Cross Section Calculations

Before we can use equation (244) we need to discuss methods for calculating the summation over the binding energies of the target atom, $\Sigma_{A,n}$, and the effective charge state of the projectile, $Z_{B,k}$.

As can be seen from equation (237), $\Sigma_{A,n}$ depends on the binding energies for the electrons in the target atom. The binding energies for neutral atoms are well tabulated, and can be found in Sevier (1979) for example; for non-neutral atoms, these are not so readily available. However, Carlson, et al., (1970) give the following simple formula for calculating these binding energies from those for the neutral atom:

$$B_{A,n,\mu} = \left(I_{A,n} - B_{A,0,\mu'}\right) + B_{A,0,\mu} \ , \tag{245}$$

where $I_{A,n}$ is the ionization energy of the ion A^{n+}, $B_{A,0,\mu'}$ is the binding energy in the neutral atom of the orbital, μ', that corresponds to the outer-most orbital of the ion, and $B_{A,0,\mu}$ is the binding energy in the neutral atom that corresponds to the orbital in question, μ. Thus knowing the binding energies of the neutral atom and the ionization energy of the ion we can compute the binding energies of the ion.

The effective charge of a bare ion is simply the atomic number of the atom, $Z_{B,Z_B} = Z_B$; however for non-bare ions the electrons would provide some screening. Therefore we write:

$$Z_{B,k} = Z_B - \epsilon_{B,k} \ , \tag{246}$$

where Z_B is the atomic number of the projectile and $\epsilon_{B,k}$ is some screening constant that depends on the charge-state k. Slater (1930) provides a semi-empirical method of calculating these screening constants. Although the calculations were made to determine the asymptotic form of the single-electron wave function by making the assumption that the electron is in a hydrogen-like atom of nuclear charge $(Z-\epsilon)$, they can be used to provide an estimate of the effective charge of the projectile. In this approach, the screening constant is a function of the number of occupied orbitals in the projectile atom, and is calculated by the following sum rules: we first group the shells so that the s and p orbitals of a given quantum number form the same group while the d and f orbitals form separate groups. Then we add screening numbers as follows: an amount 0.35 for each electron in the outermost group (except if this is a $1s$ group, then 0.30 is used); if this outermost group is an s,p group then 0.85 for each electron in the next group in and 1.00 for each of the rest of the electrons in the atom; if this outermost group is not an s,p group then we simply add 1.00 for each of the rest of the electrons in the atom. This sum is then the screening constant $\epsilon_{B,k}$.

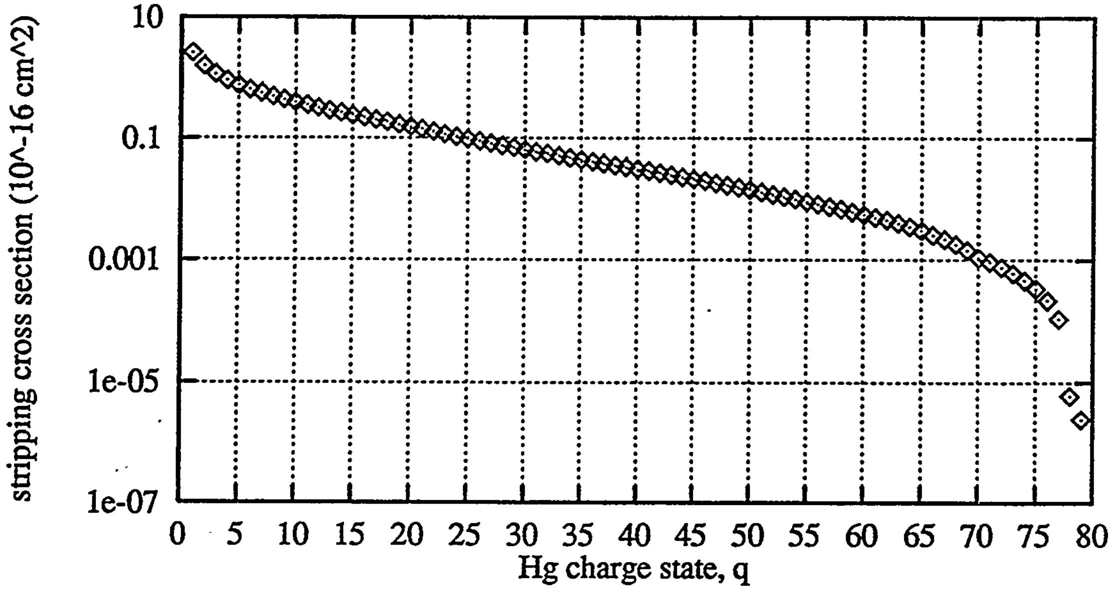

Figure 30: The stripping cross section, $\sigma_{st,q}$

for Hg^{q+} colliding with neutral fluorine at $\beta=0.315$.

We can now use equation (244) to calculate the stripping and ionization cross sections for various beam ions colliding with background gas. For this thesis we are

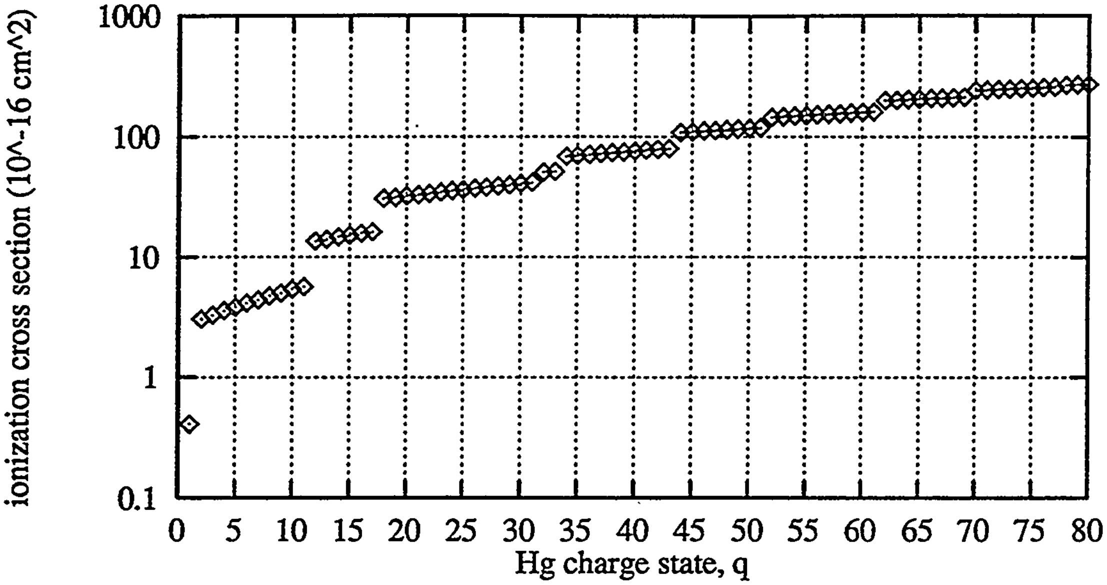

Figure 31: The ionization cross section, $\sigma_{in,q}$ *for* Hg^{q+} *colliding with neutral fluorine at* $\beta = 0.315$.

concerned with heavy ions, like Hg^{q+}, colliding with neutral background gas atoms like fluorine. In the case of the stripping cross sections, $\sigma_{st,q}$, as mentioned above, A represents the beam ion and B the background neutral; therefore we need to calculate $\Sigma_{Hg,q}$ and $Z_{F,0}$. Similarly for the ionization cross sections, $\sigma_{in,q}$, we need to calculate $\Sigma_{F,0}$ and $Z_{Hg,q}$:

$$\begin{aligned} \sigma_{st,q} &\simeq \frac{4\pi a_0^2 Z_{F,0}^2 \alpha^2}{\beta^2} \left[c_1 \ln\left(\frac{4\beta^2}{\alpha^2}\right) - c_2 \right] \Sigma_{Hg,q} \ , \\ \sigma_{in,q} &\simeq \frac{4\pi a_0^2 Z_{Hg,q}^2 \alpha^2}{\beta^2} \left[c_1 \ln\left(\frac{4\beta^2}{\alpha^2}\right) - c_2 \right] \Sigma_{F,0} \ , \end{aligned} \qquad (247)$$

where we use equation (245) for $\Sigma_{Hg,q}$ and $\Sigma_{F,0}$, and (246) for $Z_{Hg,q}$ and $Z_{F,0}$. Figures (30) and (31) show the results of equations (247) for $\beta \simeq 0.315$ as a function of the beam ion charge-state q, where we have assumed that the constants c_1 and c_2 are the same as those calculated for the noble gases, $c_1 \simeq 0.7$ and $c_2 \simeq 1.1$.

6 Results and Conclusions

In the previous sections we have shown that the focal spot radius of the heavy ion beam at the target is a crucial parameter in establishing the power plant feasibility and operating conditions. Target gain, driver energy and peak power, all depend on focal spot size. Generally the smaller this spot size for a given beam current the more favorable is the operating regime. The purpose of this thesis is to determine the spot radius to which a beam of heavy ions can be focused by a conventional lens system, followed by propagation through a chamber of background gas.

Beam ion	Hg^+
Beam ion mass (m_b)	$200.6\,amu$
Ion kinetic energy (E_b)	$10.02\,GeV$
Particle velocity (β)	0.315
Beam current (I_b)	$4.3\,kA$
Beam line-charge density (λ_b)	$45.6\,\mu C/m$
Pulse length (L_b)	$0.94\,m$
Beam emittance (ϵ)	$19.3\,mm-mrad$
Beam radius at final lens (a_l)	$10\,cm$
Beam convergence half-angle (Θ)	$20\,mrad$

Table 5: Beam parameters used for calculations.

We now analyze the transport of a beam of ions using the `BTRAC` code to solve the numerical equations described in the previous sections. We take the beam to be K-V in the transverse plane with uniform radius, a_l, and emittance, ϵ, along its length, L_b, singular axial velocity, β, and uniform axial dirstribution:

$$f(r,z,v_\perp,v_z)=\frac{\lambda_b}{\pi^2 q e\epsilon^2 v_z^2 L_b^2}\delta\left(\frac{r^2}{a_l^2}+\frac{a_l^2 v_\perp^2}{\epsilon^2 v_z^2}-1\right)\delta(v_z-\beta c)H(L_b-z)H(-z)\,. \quad (248)$$

The beam parameters, adapted from Lee (1991), are shown in table (5). We will first look at the case of transport through a vacuum chamber, and then at the more interesting case of transport through background gas.

6.1 Vacuum Propagation

The first case we consider is propagation of a beam through vacuum, $n_g = 0$. In this case we can derive an approximate analytic solution for the beam envelope radius; and then compare this to the results of the numerical solution.

6.1.1 Analytic Solution with Standard Beam Parameters

The analytic solution to the problem of a beam of ions propagating through a vacuum can be described by the "envelope" equation (10). Lee and Cooper (1976) derive a very general envelope equation for axisymmetric beams; we present a specific derivation for the case of concern here. We start by using the analytic governing equations for the motion of the beam ions derived earlier. If we substitute equation (25) into (19) we get

$$\frac{d^2r}{dt^2} = \frac{v_\theta^2}{r} + \frac{qe}{\gamma m_b m_o}\left(E_r - v_z B_\theta\right) , \tag{249}$$

where we have dropped the subscripts for convenience, and remind the reader that γ is the relativistic factor, and m_b is the mass of the beam ion in *amu*. With the same assumptions as were made before, that the velocity of the beam ion is primarily axial, $v_\perp \ll v_z \simeq \beta c$, and that this axial velocity doesn't change much over the course of the beam propagation, we can convert the temporal derivative in (249) to one over the axial position, z:

$$\frac{d^2r}{dz^2} = \frac{v_\theta^2}{r\beta^2c^2} + \frac{f_r}{\gamma m_b m_o \beta^2 c^2} , \tag{250}$$

where we define the radial force:

$$f_r \equiv qe\left(E_r - \beta c B_\theta\right) . \tag{251}$$

We now take moments defined over the transverse phase-space distribution. For a moving "disk" of beam particles with $z - \beta ct$ equal to a constant:

$$\langle r \rangle \equiv \int r dr \int d\theta \int v_\perp dv_\perp \int d\psi r f(r, \theta, v_\perp, \psi; z) \ , \tag{252}$$

where f is the particle distribution in the transverse plane shown in figure (24), evaluated at axial location, z. Using (250) we can find the following moment:

$$\langle r r'' \rangle = \frac{\langle v_\theta^2 \rangle}{\beta^2 c^2} + \frac{\langle r f_r \rangle}{\gamma m_b m_o \beta^2 c^2} \ , \tag{253}$$

where the primes signify derivates with respect to z. Substituting

$$\langle r^2 \rangle'' = 2\langle r'^2 \rangle + 2\langle r r'' \rangle \ , \tag{254}$$

and defining $a^2 \equiv 2\langle r^2 \rangle$ in (253) we get the envelope equation:

$$\frac{d^2 a}{dz^2} = \frac{\epsilon^2}{a^3} + \frac{Q}{a} \ , \tag{255}$$

where ϵ, called the emittance, is defined as:

$$\epsilon^2 \equiv \frac{4}{\beta^2 c^2} \left[\langle r^2 \rangle \left(\langle v_r^2 \rangle + \langle v_\theta^2 \rangle \right) - \langle r v_r \rangle^2 \right] \ , \tag{256}$$

and Q, the dimensionless perveance is defined as:

$$Q \equiv \frac{2\langle r f_r \rangle}{\gamma m_b m_o \beta^2 c^2} \ . \tag{257}$$

The envelope equation, (255), is identical to (10). The emittance equation, (256), is also identical to that given by (13). The variable a is interpreted as the radius of the beam, or its "envelope".

Using the moment equation (252), we can write the perveance, (257), as:

$$Q = \frac{4\pi}{\gamma m_b m_o \beta^2 c^2} \int r dr \tilde{f}(r; z) \left(r f_r \right) \ , \tag{258}$$

where $\tilde{f}(r;z)$, the normalized number density, is given by

$$\tilde{f}(r;z) \equiv \frac{qe}{\lambda_b} \int v_\perp dv_\perp \int d\psi f_q(r, v_\perp, \psi; z) \ , \tag{259}$$

and $f_q(r, v_\perp, \psi; z)$, as before, is the transverse axisymmetric distribution for particles of charge-state q in the beam. If we assume that all the particles in the beam are of charge-state q, then we can define a beam line-charge density at some radius, r, as:

$$\lambda(r;z) \equiv 2\pi qe \int v_\perp dv_\perp \int d\psi \int_0^r r' dr' f_q(r', v_\perp, \psi; z) \ , \tag{260}$$

so that λ_b is the total beam line-charge density:

$$\lambda_b \equiv 2\pi qe \int v_\perp dv_\perp \int d\psi \int_0^\infty r dr f_q(r, v_\perp, \psi; z) \ , \tag{261}$$

Substituting (260) and (259) into (258) yields:

$$Q = \frac{2qe}{\gamma m_b m_o \beta^2 c^2 \lambda_b} \int r dr \frac{\partial \lambda}{\partial r} (E_r - \beta c B_\theta) \ , \tag{262}$$

where we have substituted for the radial force from (251). The fields are given by:

$$\begin{aligned} E_r &= \frac{\lambda}{2\pi\epsilon_0 r} \ , \\ B_\theta &= \frac{\mu_0 \beta c \lambda}{2\pi r} \ , \end{aligned} \tag{263}$$

where λ is defined by (260). Substituting (263) into (262) and performing the integration yields:

$$Q = \frac{qeI_b}{2\pi\epsilon_0 m_b m_o (\beta\gamma c)^3} \ , \tag{264}$$

where I_b, the beam current, is given by $\lambda_b \beta c$; this equation is identical to (11).

Lee and Cooper (1976) have shown that in the case of self-similar expansion, the emittance of the beam is conserved. Given the initial conditions $a(0) = a_l$ and $a'(0) = -\Theta$, the beam convergence half-angle, we can solve equation (255) to obtain the radius of the beam, a, as a function of axial position z. For the parameters given

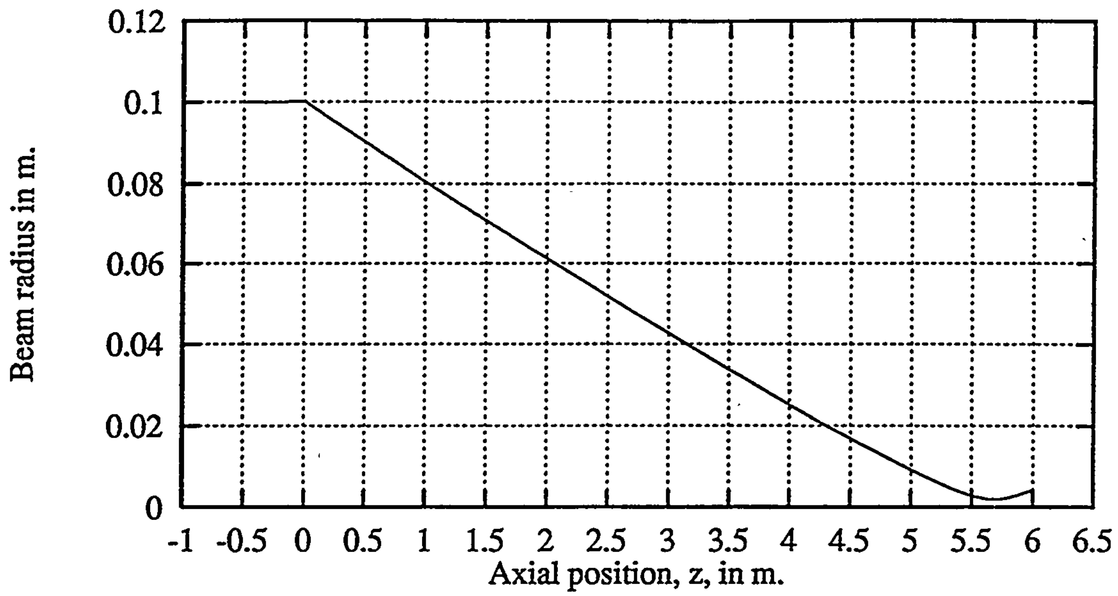

Figure 32: The envelope solution for the beam propagating through a vacuum.

in table (5) we get, $Q=3.78\times10^{-5}$, and with $\epsilon=1.93\times 10^{-5}\,m{-}rad$, $a_l=10\,cm$, and $\Theta=20\,mrad$, figure (32) displays the solution of equation (255) obtained by applying Stoermer's rule* for discretizing second-order, conservative differential equations. The beam is considered to be moving from left to right. As mentioned before, the effect of the final focus system is modeled by an artificial thin lens, located at $z=0$, which focuses the beam onto the target $(a_l/\Theta)\simeq5\,m$ away. The radius of the beam, initially at $\sim10\,cm$, gets focused to a spot-size of $a_s\simeq1.97\,mm$ at axial position $z\simeq\ 5.68\,m$, slightly beyond the nominal position of the target. The actual convergence angle, or target position, would be adjusted so that the minimum radius occurred at the target. This spot radius agrees with the analytic integral to the envelope equation, (14).

We can also make estimates for the radial electric and azimuthal magnetic fields

---

* See for example Press, et al., (1992).

at the edge of a long cylindrical beam by substituting a, the beam radius, for r in equations (263):

$$
\begin{aligned}
E_r &= \frac{\lambda_b}{2\pi\epsilon_0 a}\,, \\
B_\theta &= \frac{\mu_0 I_b}{2\pi a}\,,
\end{aligned}
\tag{265}
$$

where λ_b, the beam line charge density, is given by (261), and I_b, the beam current, is given by $\lambda_b \beta c$. For the parameters given in table (5), with $a \simeq 1.97\,mm$, we get $E_r \simeq 4.16 \times 10^8\,V/m$ and $B_\theta \simeq 4.37 \times 10^{-1}\,T$. These high fields are expected to strongly effect the motion of any electrons generated by collisions with background gas molecules.

6.1.2 Numerical Solution with Standard Beam Parameters

$\Delta r\,(mm)$	$\Delta t\,(ps)$	N_t
8	15	2,294
4	10	1,727
2	5	1,694
1	3	706
0.5	1.5	1,900

Table 6: Number of time steps used for numerical simulation of the beam for vacuum propagation.

Using the parameters in table (5) we set the length and radius of the simulation enviroment shown in figure (12) to $L_c \simeq 9\,m$ and $R_c \simeq 30\,cm$. Equation (186) yields $\Delta N \lesssim 1.4{\times}10^{10}$, and therefore $K_1 \simeq 19,080$ super-beam ions; the subscript "1" signifies that all these particles have initial charge state $q=1$. Using the "envelope" solution as a guide, we determine that at the end of the simulation, when the radius of the beam is approximately $\sim 2\,mm$, the beam plasma frequency will be $\omega_b \simeq 4.4{\times}10^8\,s^{-1}$; and using equation (188) we set $\Delta z \lesssim 6\,mm$ and $N_z \simeq 1,500$ grid divisions. Since the numerical simulation code, BTRAC, does not allow for reductions in the axial grid division, we will use this, more stringent, Δz throughout the simulation. Similarly, at the beginning of the simulation, where the radius of the beam is $\sim 10\,cm$, $\omega_b \simeq 8.9\times 10^6\,s^{-1}$; and using (189) we get $\Delta r \lesssim 8\,mm$ and $N_r \simeq 38$ grid divisions. Since there is no background gas, there are no collisions or electrons; therefore the only condition on the time-step comes from the CFL equation (190), which gives $\Delta t \lesssim 15\,ps$. As the simulation progresses the radius of the beam will decrease, this will force a smaller radial grid division and time-step; the BTRAC code does allow for reductions in Δr and Δt. Table (6) shows Δr and Δt and the number of time-steps, N_t, for each set of parameters. For instance, at the end of the first "run", the mid-point, i.e. the axial location of the center of the beam, will be at position $z \simeq -0.48 + 2294(\Delta t \beta c) \simeq 2.77\,m$, where the mid-point of the beam is initially at $\sim -0.48\,m$; at the end of the next run, the mid-point of the beam will have progressed to $z \simeq 2.77 - 1,727(\Delta t \beta c) \simeq 4.4\,m$; and so on.

Figure (33) shows the results of a BTRAC simulation with the parameters given above. The figure shows the beam at three different times, superimposed on the same graph, along with the envelope solution of figure (32). The first of these "snapshots" is at time "0", when the head of the beam is still behind the lens, at $z = 0\,m$; its radius is $\sim 10\,cm$, and the mid-point is seen to be $\sim 0.48\,m$ behind the lens. The second "snapshot" shows the beam at $\sim 34.4\,ns$, when the mid-point is at $\sim 2.77\,m$. And finally the last of these "snapshots" is at $\sim 65.1\,ns$, when the mid-point of the beam is now at $\sim 5.67\,m$. The "waist" or point of smallest beam "envelope" radius, given by $a \equiv \sqrt{2\langle r^2\rangle}$, occurs at $\sim 5.67\,m$, as opposed to $\sim 5.68\,m$ for the numerically integrated envelope solution, and has radius $\sim 2.08\,mm$ as opposed to $\sim 1.97\,mm$; this is a $\sim 5.6\%$ discrepancy between the envelope and numerical results. We can also calculate the

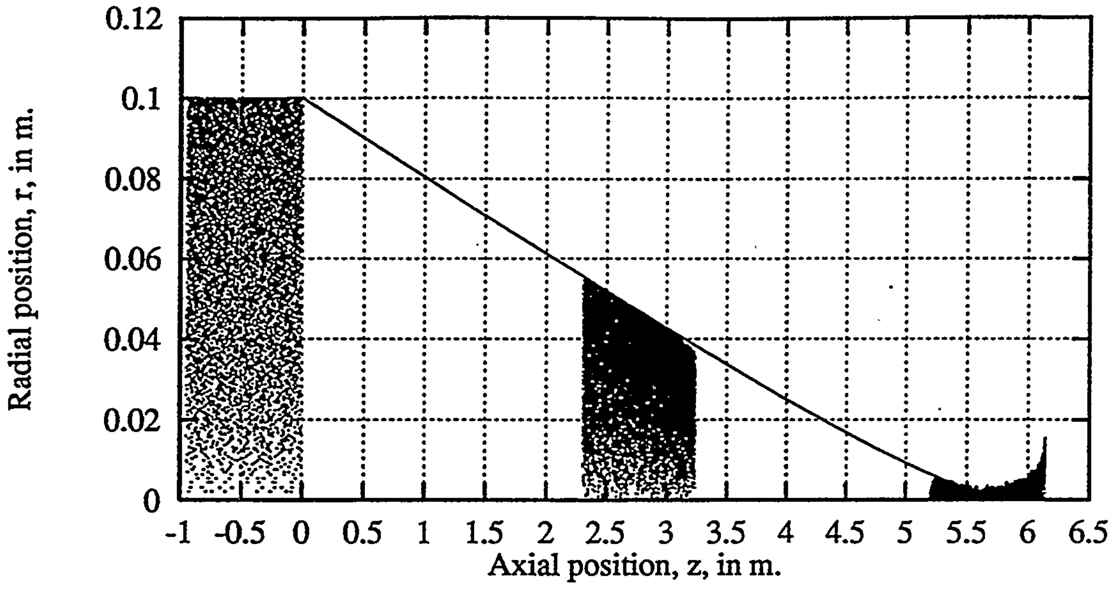

Figure 33: The beam ions for vacuum propagation.

emittance of the beam at the waist given by equation (256), $\epsilon \simeq 2.01 \times 10^{-5}\, m-rad$; this confirms the assumption of emittance conservation that was made when solving the envelope equation.

Figures (34) and (35) show the radial electric field and azimuthal magnetic field at a radius of $\sim 2.08\, mm$ as a function of axial position across the beam when its mid-point is at $\sim 5.67\, m$. These fields are obtained by carrying out the summation given by equation (98) that weights the fields to the particle positions:

$$F(r,z) = \sum_{j,k} F_{j,k} W(r,z;r_j,z_k) \ , \tag{266}$$

where $F(r,z)$ is either the radial electric field or the azimuthal magnetic field at location (r,z), $F_{j,k}$ is the field at the grid location (r_j, z_k) and W is the weighting function given by equation (97). As can be seen, the radial electric field at the mid-point of the beam, for location $z \sim 5.67\, m$ is $E_r \simeq 4.06 \times 10^8\, V/m$, which is within $\sim 2.29\%$ of the analytical value calculated above; and the azimuthal magnetic field

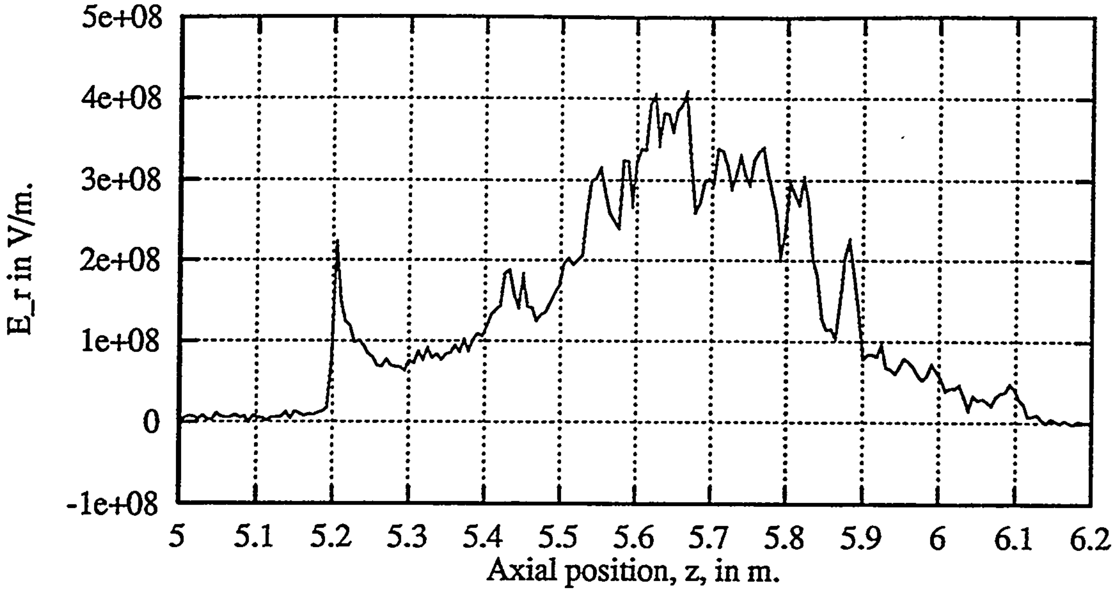

Figure 34: The radial electric field at 2.08 mm for vacuum propagation.

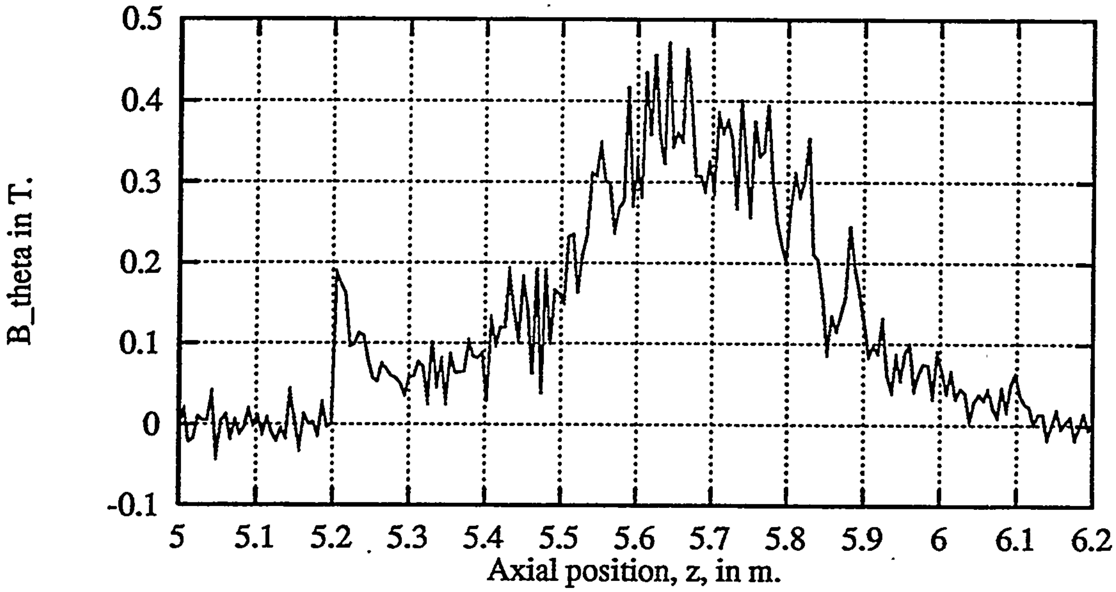

Figure 35: The azimuthal magnetic field at 2.08 mm for vacuum propagation.

is $4.63 \times 10^{-1}\,T$, which is within $\sim 5.93\%$ of the analytical value. Although the analytical theory assumes a long cylindrical beam with no axial electric field, E_z, the results obtained from the numerical solution are very close to those obtained from the analytic calculation.

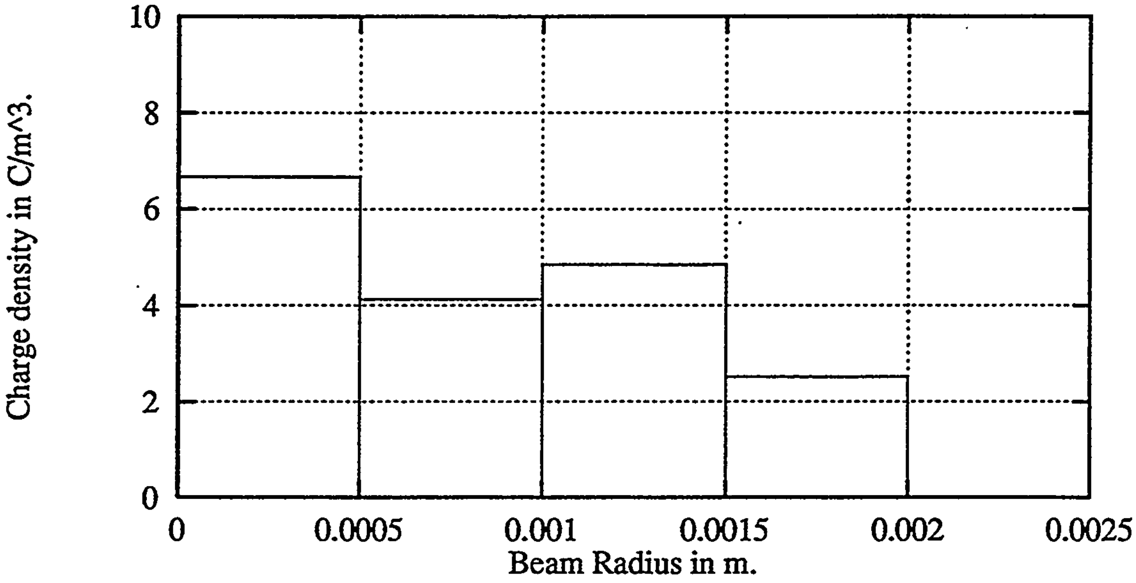

Figure 36: Charge density for vacuum propagation.

Figure (36) shows the charge density as a function of radius at the mid-point of the beam, at $\sim 5.67\,m$. This is done by counting the number of super-beam ions in a small annulus with thickness $\Delta r \simeq 0.5\,mm$ and length $\Delta z \simeq 6\,mm$ at the mid-point. If we integrate this charge density over the radius of the beam we get a line-charge density of $\lambda_b \simeq 4.79 \times 10^{-5}\,C/m$. Again we see that although the analytical solution did not include the effect of the axial electric field and therefore assumes that λ_b is a constant, it is very close, within $\sim 4.99\%$, to the numerical solution.

6.2 Propagation through Background Gas

We now turn our attention to propagation of the beam through background gas for reactor chambers theat use Flibe, a molten-salt mixture of 66.7 mol % LiF and 33.3 mol % BeF_2, or liquid-lithium as the working fluid. We first explore beam propagation through vapor densities of $\sim 10^{14}$ to 10^{15} molecules per cm^3 of Flibe. Moir, et al., (1991) report that these densities correspond to Flibe equilibrium temperatures of ~ 940 to $1038\,K$. Under these conditions the background gas consists of $\sim 99\%$ BeF_2 molecules, while the remaining $\sim 1\%$ contains other compounds, including LiF. Therefore we can take the vapor to be entirely BeF_2. There is almost no data for the stripping and ionization of BeF_2 molecules, however, estimates of atomic cross sections can be made using the semi-empirical methods described earlier in chapter 5. In view of this we take the gas to be composed of individual atoms, rather than molecules. The BTRAC code is currently only capable of simulating single-species background gas. There are twice as many fluorine atoms as there are beryllium atoms in the background gas, and the atomic number of fluorine is more than twice that of beryllium; consequently we expect the stripping of the beam ions to be dominated by fluorine. The stripping and ionization collision frequencies, $\sigma n_g \beta c$, for Hg^{3+} ions at $\beta \simeq 0.315$ colliding with the Be atoms in $\sim 5\times10^{14}$ molecules cm^{-3} BeF_2 are $\nu_{st} \simeq 5.9\times10^7\, s^{-1}$ and $\nu_{in} \simeq 1.1\times10^9\, s^{-1}$ respectively; similarly for F these frequencies are $\nu_{st} \simeq 1.1\times10^9\, s^{-1}$ and $\nu_{in} \simeq 3.1\times10^9\, s^{-1}$. As can be seen, the stripping frequency for beryllium is about $\sim 5\%$ that of fluorine, and the ionization frequency is about a third; therefore we ignore the Be and take the background gas to be composed of fluorine atoms at twice the Flibe molecular vapor density in the chamber.

6.2.1 Numerical Solution for

Flibe Vapor at 2×10^{14} Molecules per c.c

$\Delta r\,(mm)$	$\Delta t\,(ps)$	N_t
8	15	662
8	10	490
8	5	2937
8	3	1631
4	3	2263
4	2	5239
2	2	1005
2	1	182

Table 7: Number of time steps used for numerical simulation of the beam in $4\times10^{14}\,cm^{-3}$ fluorine.

We now look at the results of the numerical simulations for the beam passing through background gas at various densities. For background gas at 2×10^{14} molecules of BeF_2 per cm^3, we carry out the simulation with 4×10^{14} atoms of fluorine per cm^3, as described above. The stripping and ionization cross sections for Hg^+ beam ions colliding with F at $\beta\simeq0.315$ are shown in figures (30) and (31). The initial beam parameters are the same as those used for the vacuum case and listed in table (5). The reductions in the radial grid division, Δr, are performed at similar intervals to the case of vacuum transport shown in table (6). However, now the time-step is no longer simply limited by the CFL condition, (190); because there are collisions between the beam ions and the background gas, it can also be limited by the collision frequency, (191), and because of the presence of electrons, by the electron plasma frequency, (187). Table (7) shows the time-step sequence used for this simulation; except for the initial time division, which is set by the CFL condition, all subsequent Δt are set by the more stringent plasma frequency limit. The other simulation parameters are the same as were used in the vacuum case, $\Delta z \simeq 6\,mm$ and $\Delta N \simeq 1.4 \times 10^{10}$.

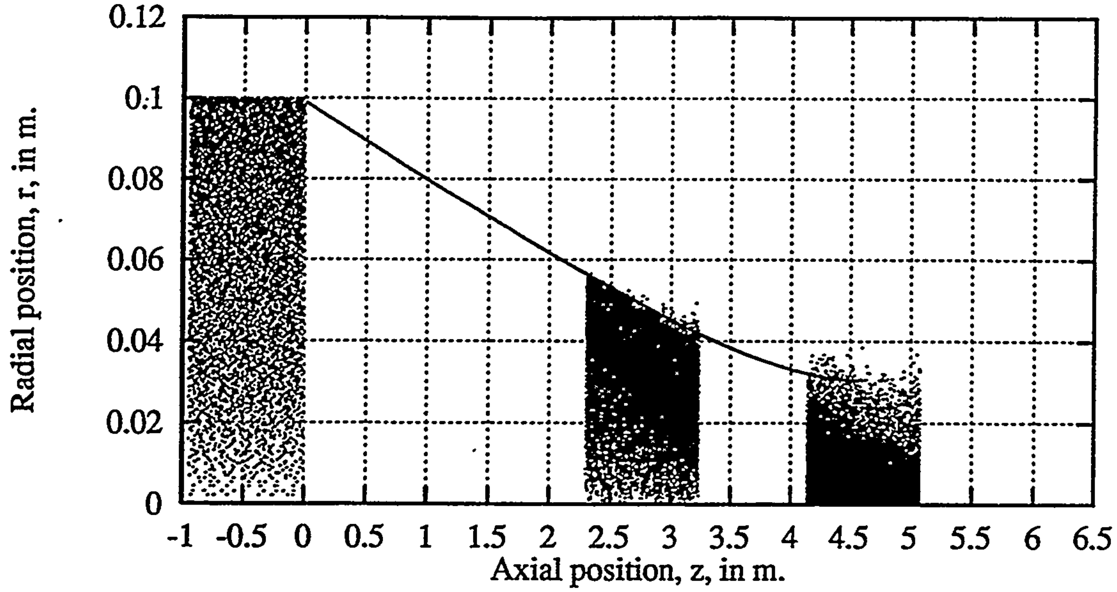

Figure 33: The beam ions for propagation through $4 \times 10^{14}\,cm^{-3}$ *fluorine.*

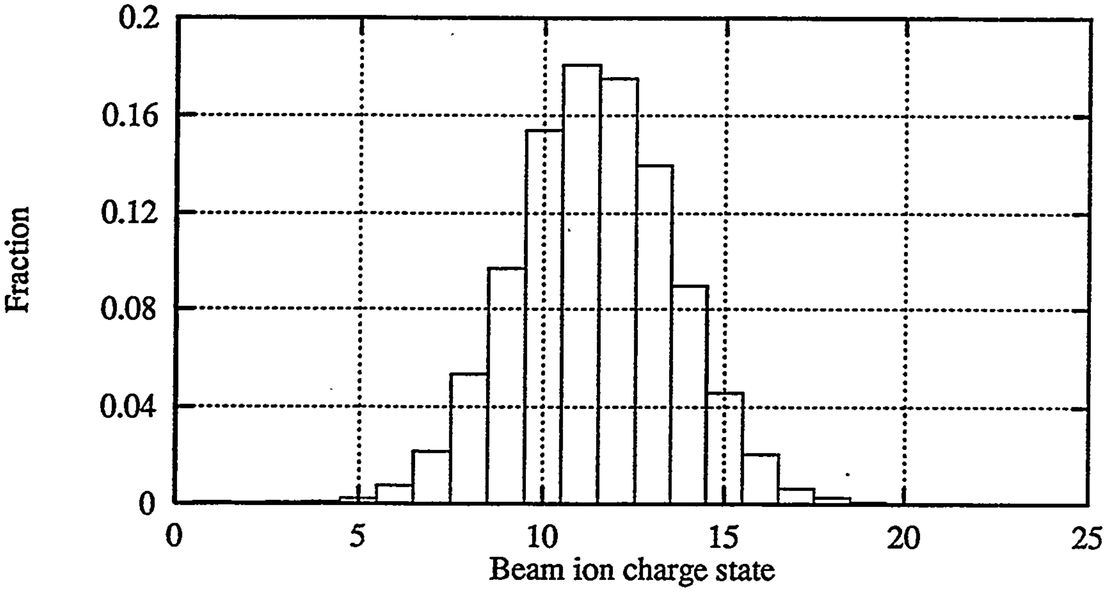

Figure 38: The distribution of beam ion charge states for propagation through $4 \times 10^{14}\,cm^{-3}$ *fluorine.*

Figure (37) shows the results of the BTRAC simulation for the beam ions at three different times superimposed on the same graph. The first of these "snapshots" is at time "0", the second is at time $\sim 34.4\,ns$, and the third "snapshot" is at the end of the simulation, $\sim 53.9\,ns$. The solid line plots the location of the particle with the maximum radial position within a thin, Δz, slice around the axial mid-point of the beam. As can be seen this "edge" radius of the beam reaches a waist, or spot size, of $\sim 3.05\,cm$, when the mid-point of the beam is at $\sim 4.61\,m$. This spot radius is much larger than the $\sim 2\,mm$ spot-size achievable in a vacuum. Also the position of the focal spot has shifted by $\sim 1.06\,m$ from the vacuum case as would be expected for a beam that has a larger focal spot. The distribution of charge states of the beam ions at the end of the simulation is shown in figure (38). The average charge state is ~ 11.41, so that the beam line-charge density increases from $\sim 4.79\times10^{-5}\,C/m$ to $\sim 5.47\times10^{-4}\,C/m$.

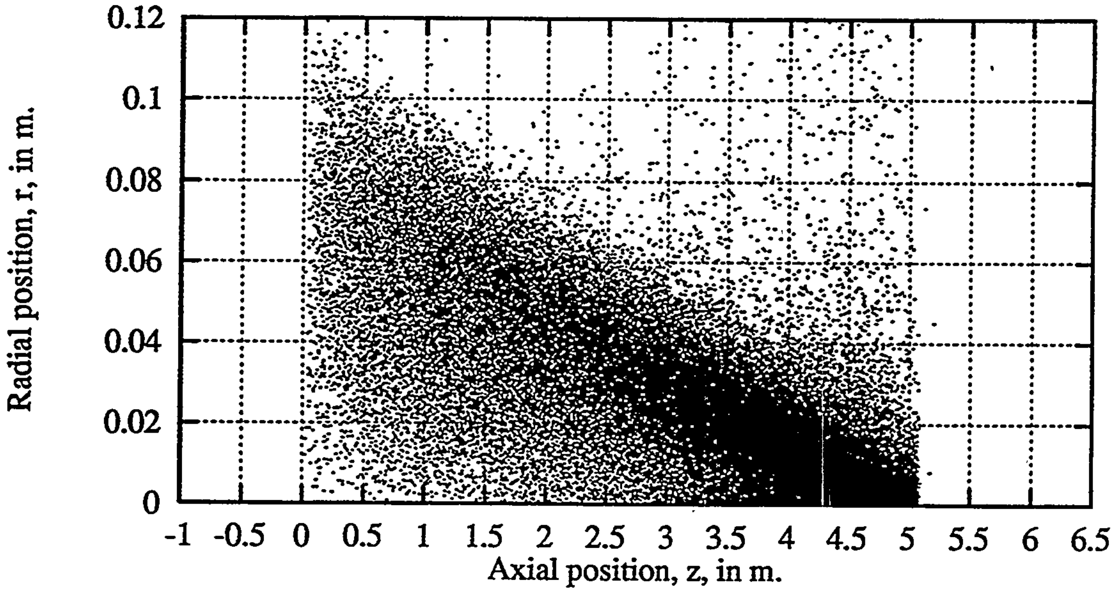

Figure 39: The electrons generated by the beam propagating through $4\times10^{14}\,cm^{-3}$ *fluorine.*

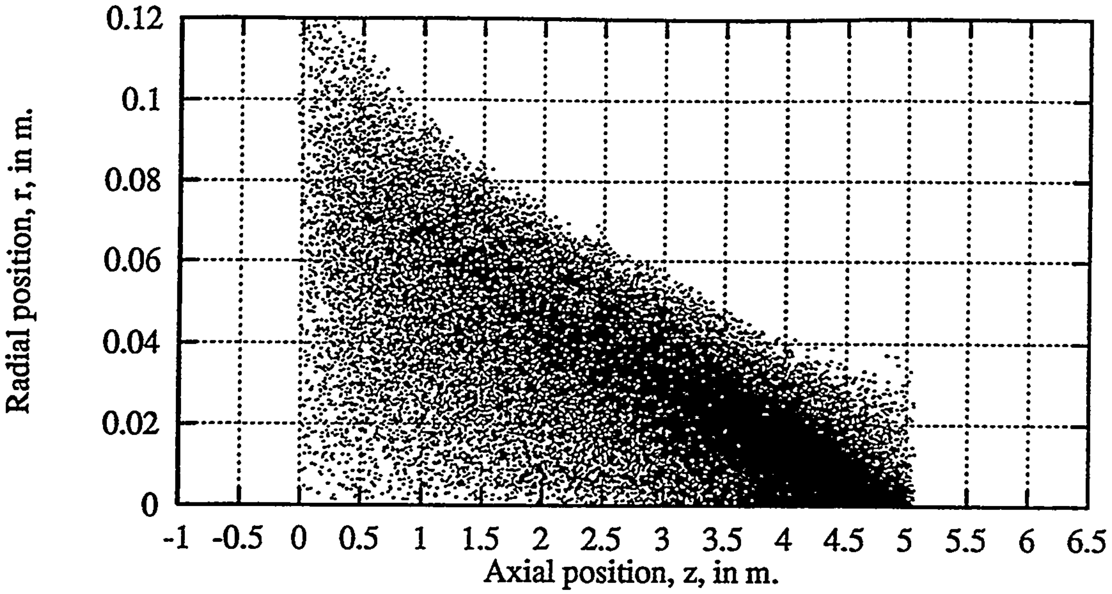

Figure 40: The background gas ions generated by the beam propagating through $4\times10^{14}\,cm^{-3}$ *fluorine.*

Figures (39) and (40) show the electrons and background gas ions in the chamber at the end of the simulation. The electrons, which are much lighter than the background gas ions, get "dragged" along and concentrated in the vicinity of the beam. It had been hoped that these electrons would not only be able to compensate for the extra charge due to the stripping of the beam ions and the presence of any gas ions in the vicinity of the beam, but also substantially neutralize the original beam charge. Any residual electric field, resulting from incomplete neutralization, will have a much larger defocusing effect than in the case of vacuum transport because of the higher charge state of the beam ions.

Figure (41) shows the radial electric field at a radius of $3.05\,cm$ as a function of axial position across the beam when the mid-point of the beam is at $\sim 4.61\,m$ at the end of the simulation; this field is calculated using equation (266) in a manner similar to that for the vacuum case. The dashed line is a result of convoluting the

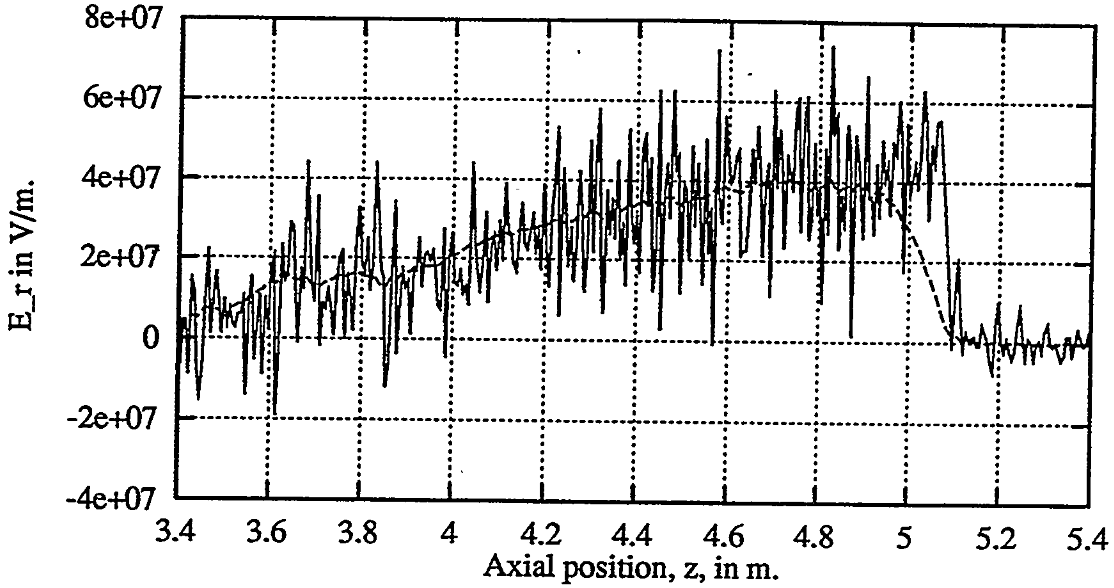

Figure 41: The radial electric field at 3.05 *cm for propagation through* $4\times10^{14}\ cm^{-3}$ *fluorine.*

simulation data with a Gaussian kernal whose full-width at half-maximum is $\sim40\Delta z$, or one-fourth the length of the beam. The average radial electric field across the beam from $\sim$4.14 to 5.08 m is $E_r\simeq3.68\times10^7\ V/m$. If we use the line-charge density for the vacuum case, $\sim4.79\times10^{-5}\ C/m$, and then use the long-beam approximations for the electric field, equation (265), at this radius, $\sim3.05\,cm$, we get $E_r\simeq2.82\times10^7\ V/m$. Even though we used an approximation that neglects the effects of the axial electric field, we see that this field is smaller than the non-vacuum case, suggesting that the electrons are not able to neutralize the extra charge due to the stripping of the beam and the gas ion charge due to ionization of the background gas.

If we ignore the effect of the magnetic "pinch" force, which, in general, is β^2 times the electric force, we can calculate an effective force on an ion at the edge of the beam, $f_r\equiv\langle q\rangle eE_r$, where $\langle q\rangle$ is the average charge-state of the beam ions, and E_r is the electric field at the edge. Although the electric field at the edge is lower than the edge electric field for the vacuum case, $\sim 4.06\times10^{8}\ V/m$, the charge-state has increased, therefore the effective force, $f_r \simeq 6.73\times10^{-11}\ N$, is only slightly larger than that felt by a beam ion at the focal-spot radius for vacuum transport, $f_r \simeq 6.5\times10^{-11}\ N$, which partially explains why the beam starts to expand at this point.

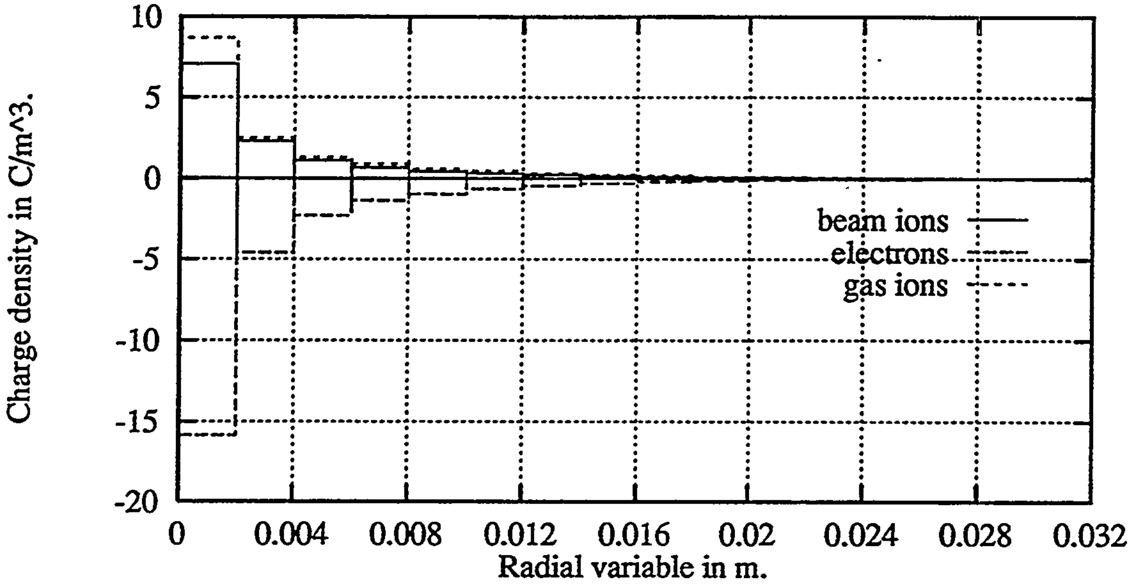

Figure 42: The charge density for propagation through $4\times10^{14}\ cm^{-3}$ *fluorine.*

In order to calculate the extent of the neutralization of the beam and gas ion charge we can look at the charge density across the beam radius. Figure (42) shows the charge density as a function of radius averaged over the entire length of the beam from ~ 4.14 to $5.08\,m$. This is calculated in the same manner as was done before in the case of vacuum transport, except that now $\Delta r \simeq 2\,mm$. The solid lines refer to the beam ions and the dashed and dotted lines refer to the electrons and background gas ions respectively. If we integrate the charge density for the beam ions only over radius to $\sim 3.05\,cm$, we get $\lambda_b \simeq 5.16\times10^{-4}\,C/m$; this agrees well, $\sim 5.59\%$, with the value estimated earlier from the average charge state of the beam ions. For the electrons we get, $\lambda_e \simeq -1.16\times10^{-3}\ C/m$; while for the gas ions, $\lambda_g \simeq 7.0\times10^{-4}\ C/m$, which is comparable to the beam ion charge density. The total charge density of the beam ions, gas ions and electrons is $\lambda \simeq 5.94\times10^{-5}\ C/m$. As in the case of the field, this is larger than the vacuum case of $\sim 4.79\times10^{-5}\ C/m$, which again means that the electrons are not able to neutralize even the excess charge due to the gas ions and the stripping of the beam ions. We calculate a charge neutralization fraction based on the ability of the electrons to not only compensate for the excess positive charge due to stripping and ionization, but also to neutralize the original charge of the beam by $[1-(\lambda/\lambda_b)] \simeq 88.5\%$.

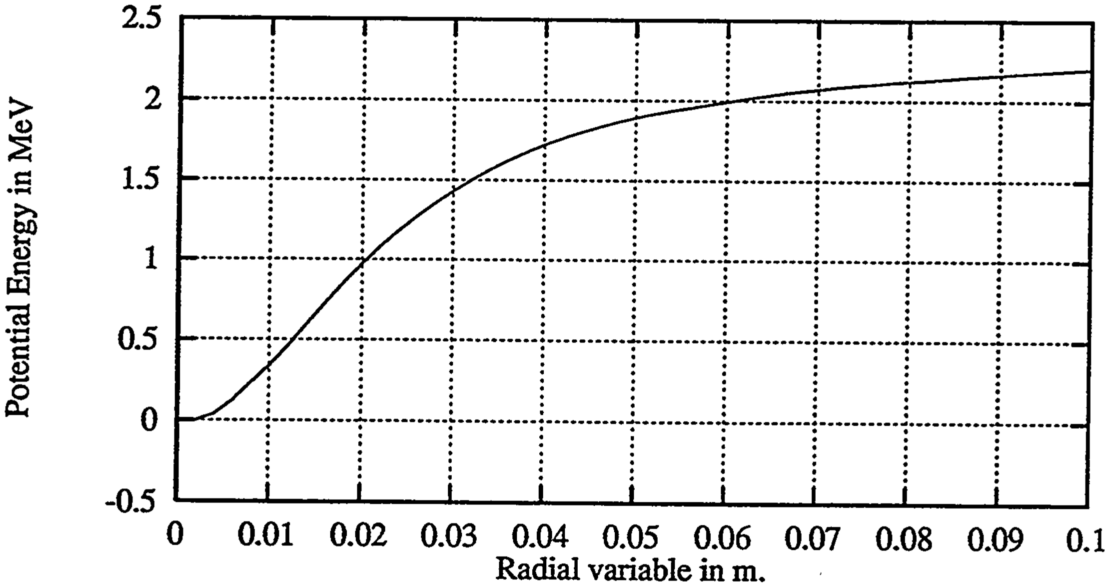

Figure 43: The potential energy for propagation through $4\times10^{14}\ cm^{-3}$ *fluorine.*

To gain some insight into why the electrons are not able to effectively neutralize the beam we look at the beam potential. Figure (43) shows the potential energy of the beam as a function of radius. This is calculated by integrating the radial force on an electron, $(E_r - v_{z,e}B_\theta)$, where E_r and B_θ are, as before, the average radial electric and

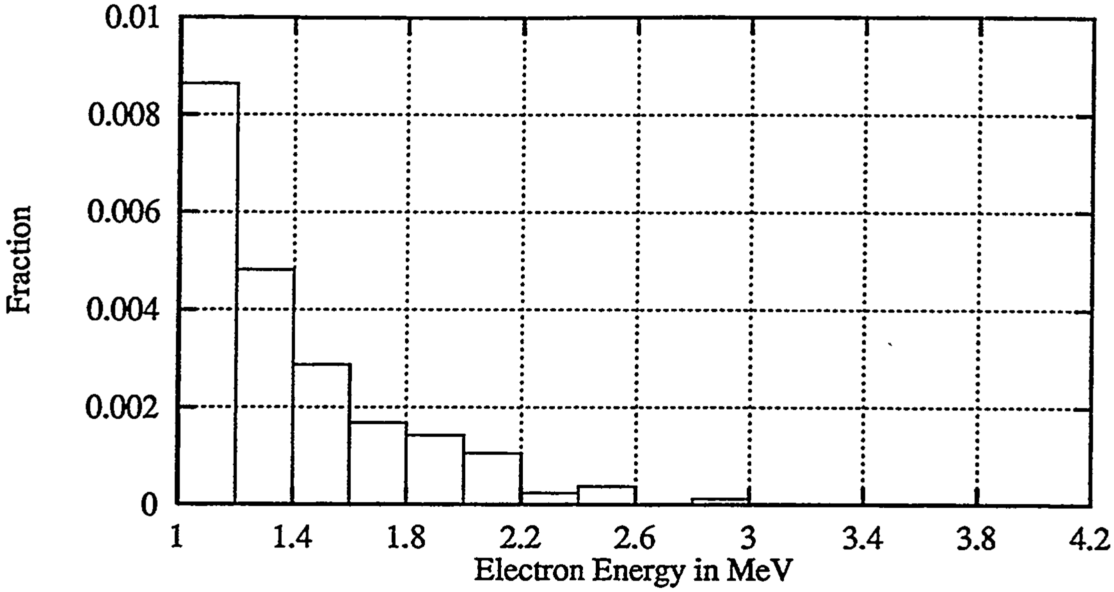

Figure 44: The electron transverse kinetic energy for propagation through $4 \times 10^{14}\, cm^{-3}$ *fluorine.*

azimuthal magnetic fields respectively, and $v_{z,e}$ is the average electron axial velocity. The magnetic force is about $\sim 3\%$ of the electric force, and therefore can be ignored. As can be seen, the potential reaches $\sim 1.45\, MV$ at the edge of the beam, $\sim 3.05\, cm$. Figure (44) shows the distribution of the transverse kinetic energy for the electrons in the vicinity of the beam, from $z \simeq 4.14$ to $5.08\, m$. The plot shows the fraction of electrons with energies greater than $\sim 1\, MeV$. Some electrons can have transverse kinetic energies as high as $\sim 3.26\, MeV$. Electrons with transverse kinetic energies larger than the potential of the beam that are not entirely confined within the beam and therefore cannot contribute effectively to its neutralization. These electrons gain energy from the rapid increase in the beam potential. Because of the high stripping cross sections of fluorine, the beam ions can reach charge states in excess of ~ 6 within the first meter of propagation; the potential from the bare beam, discounting any electrons and gas ions, would then be $\sim 2.46\, MV$. By the time the beam reaches a waist, this bare-beam potential can get as high as $\sim 4.67\, MV$, leading to energetic electrons that can "escape" the potential of the beam.

6.2.2 Numerical Solution for
Flibe Vapor at 1×10^{15} Molecules per c.c

$\Delta r\,(mm)$	$\Delta t\,(ps)$	N_t
8	15	349
8	5	753
8	3	1891
8	2	3125
8	1	13486
4	1	982

Table 8: Number of time steps used for numerical simulation of the beam in $2\times10^{15}\,cm^{-3}$ fluorine.

We now look at the results of the numerical simulations for the beam passing through Flibe background gas at 1×10^{15} molecules per cm^3, which we simulate with $2\times10^{15}\,cm^3$ fluorine. The beam parameters are the same as those used in the previous simulations given in table (5). The reductions in the radial grid division, Δr, and the time division, Δt, are given in table (8). Again, the first time division is set by the CFL condition, while all subsequent times are determined by the electron plasma frequency limit; the other simulation parameters are the same as were used in the vacuum case, $\Delta z\simeq 6\,mm$ and $\Delta N\simeq 1.4\times10^{10}$.

Figure (45) shows the results of the BTRAC simulation for the beam ions at two different times superimposed on the same graph. The first of these is at time "0", the second is at the end of the simulation at time $\sim 35.39\,ns$. As before, the solid line plots the location of the particle with the maximum radial position within a thin, Δz, slice

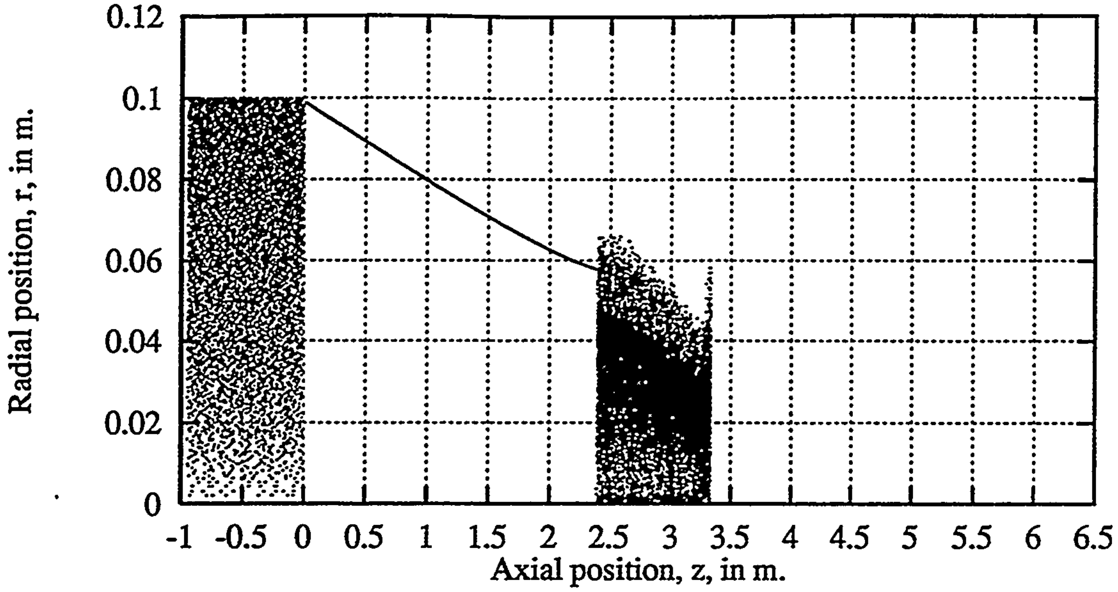

Figure 45: The beam ions for propagation through $2\times10^{15}\ cm^{-3}$ *fluorine.*

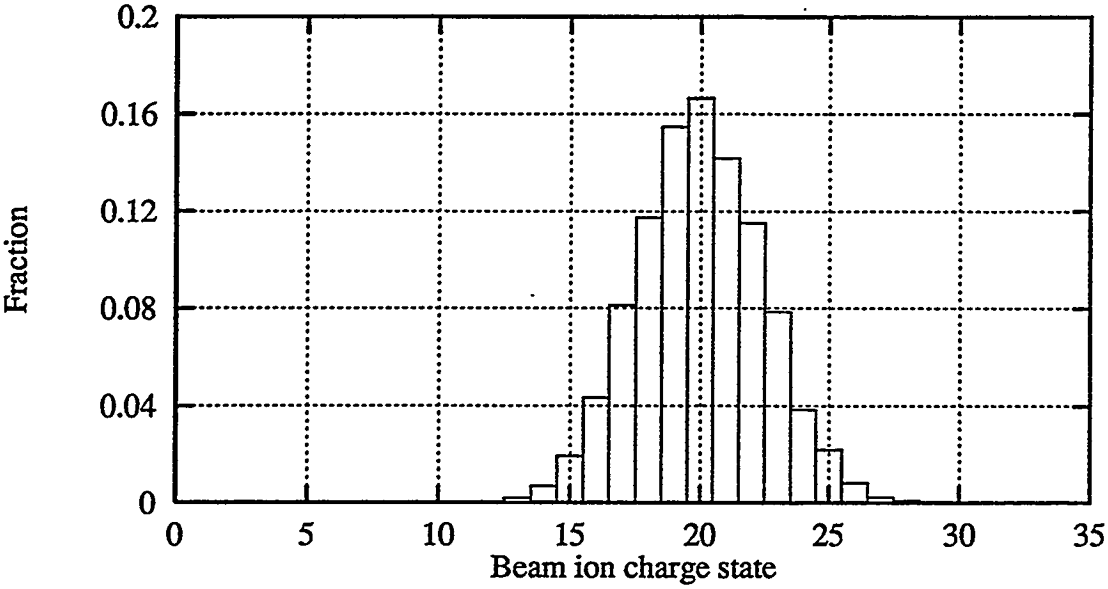

Figure 46: The distribution of beam ion charge states for propagation through $2\times10^{15}\ cm^{-3}$ *fluorine.*

around the mid-point of the beam. As can be seen, the radius of the beam reaches a spot-size of $\sim 5.49\,cm$ at a distance of $\sim 2.86\,m$ from the lens. Again, this spot size is much larger than the $\sim 2\,mm$ achievable in a vacuum; and now the position of this focal spot has moved by about $\sim 2.81\,m$ from the vacuum case. The distribution of charge states of the beam ions at the end of the simulation is shown in figure (46). The average charge state is now ~ 19.98, so that the bare beam line-charge density increases from $\sim 4.79 \times 10^{-5}\,C/m$ to $\sim 9.57 \times 10^{-4}\,C/m$.

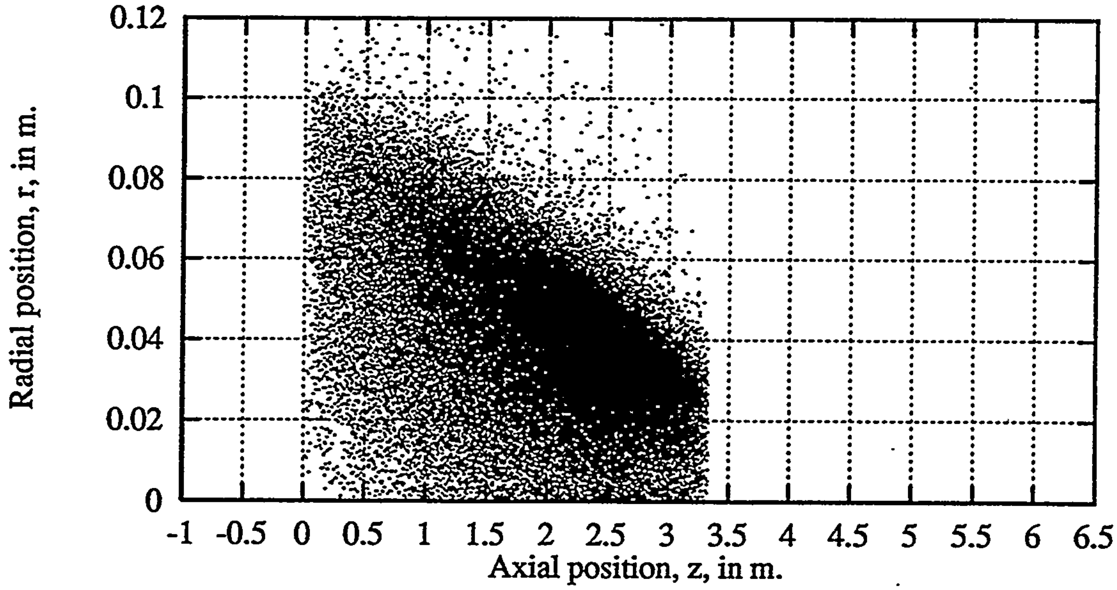

Figure 47: The electrons generated by propagation through $2 \times 10^{15}\,cm^{-3}$ *fluorine.*

Figures (47) and (48) show the electrons and background gas ions in the chamber at the end of the simulation. Again, it had been hoped that the electrons, concentrated in the vicinity of the beam, would partially neutralize both the beam charge and the background gas ions. Figure (49) shows the radial electric field at a radius of $\sim 5.49\,cm$ as a function of axial position across the beam at the end of the simulation. As before, this field is computed using equations (266); and the dashed line is a convolution with a Gaussian kernal of full-width $\sim 40\Delta z$. The average field across

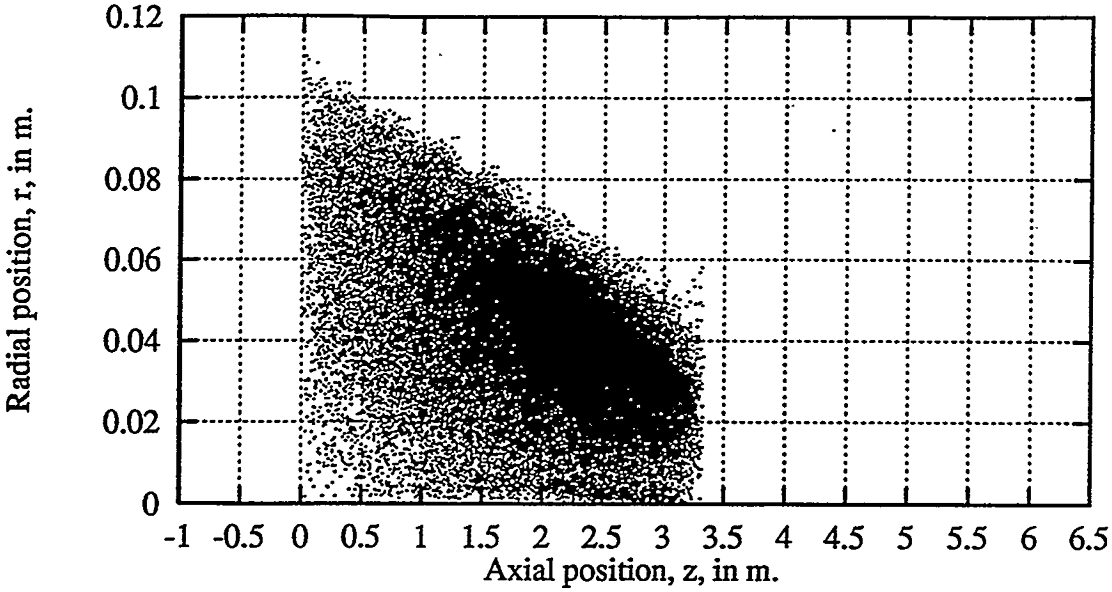

Figure 48: The background gas ions generated by propagation through $2\times10^{15}\,cm^{-3}$ *fluorine.*

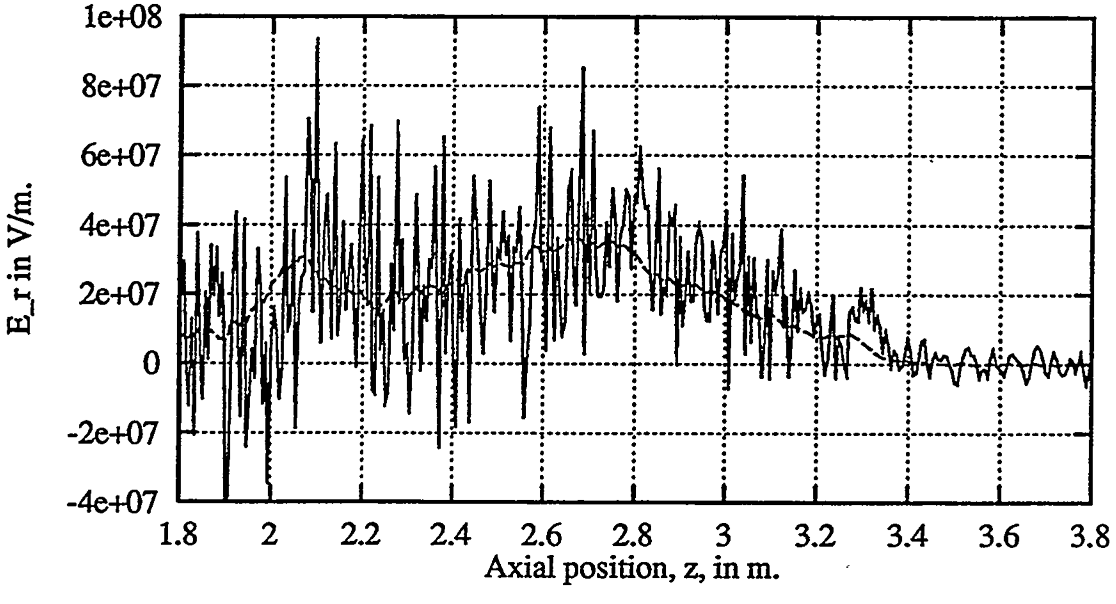

Figure 49: The radial electric field at $5.49\,cm$ *for propagation through* $2\times10^{15}\,cm^{-3}$ *fluorine.*

the beam from $\sim$2.39 to 3.33 m is $E_r \simeq 2.47\times10^7\ V/m$. If we calculate the field of the vacuum case at this radius, $\sim 5.49\,cm$, with the long-beam approximation, equation (265), we get $E_r \simeq 1.57 \times 10^7\,V/m$. Again the field that results from propagation through the background gas is larger than that from vacuum propagation, suggesting incomplete neutralization of the excess charge state of the beam ions from stripping and the gas ions.

We can calculate the electric force on a beam ion at the focal-spot radius, $\sim 5.49\,cm$, $f_r \simeq 7.91 \times 10^{-11}\,N$, which, again, is only slightly larger than the force on a beam ion at the focal-spot radius for vacuum transport, and is the dominant repulsive force on the beam ions causing the beam to expand.

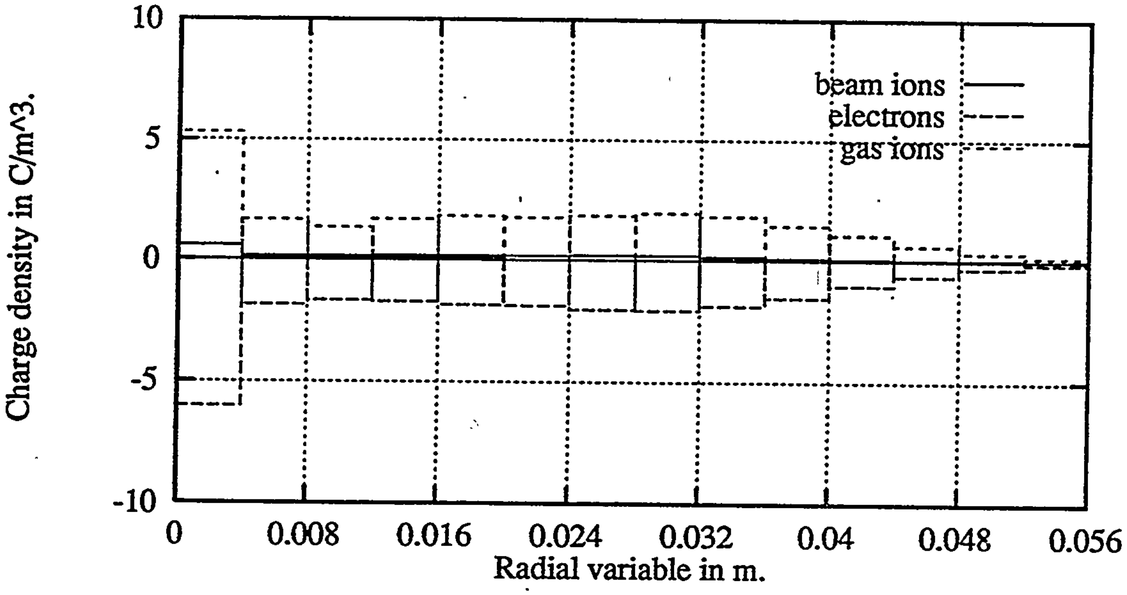

Figure 50: The charge density for propagation through $2 \times 10^{15}\,cm^{-3}$ *fluorine.*

To calculate the extent of the neutralization, we look at the charge density as function of beam radius averaged over the length of the beam ~ 2.39 to $3.33\,m$, figure (50). As before, we calculate this density by averaging over the particles in successive annuli, this time of thickness ~4 mm. The total beam line-charge density, integrated out to radius ~5.49 cm, is $\lambda_b \simeq 8.94\times10^{-4}\ C/m$; this agrees well, ~6.59%, with the value estimated earlier from the average charge state of the beam ions. Similarly for the electrons, $\lambda_e \simeq -1.19\text{x}10^{-2}\ C/m$; and for the gas ions, $\lambda_g \simeq 1.12\text{x}10^{-2}\ C/m$, which is now more than ten times the beam ion density. The total line-charge density is $\lambda \simeq 2.2\text{x}10^{-4}\ C/m$, is substantially higher than the vacuum case of ~4.79x$10^{-5}\ C/m$, meaning that the electrons are not able to neutralize the extra charge of the highly stripped beam ions and gas ions. We calculate a charge neutralization fraction of ~ 75.4%; this is lower than the ~ 88.5% neutralization achieved for propagation through $4\times10^{14}\ cm^{-3}$ density fluorine.

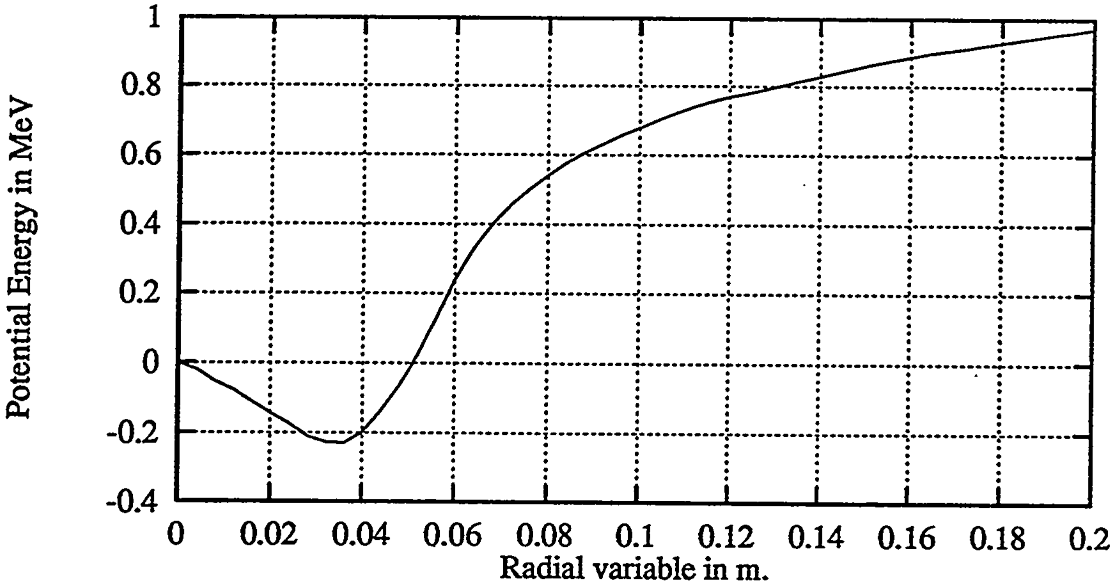

Figure 51: The potential energy for propagation through $2\times10^{15}\ cm^{-3}$ fluorine.

Figure (51) shows the potential energy of the beam as a function of radius, calculated in the same way as before. The potential difference between the minimum point and the edge of the beam, ~ 5.49 cm, is ~ 0.33 MV. Figure (52) shows the

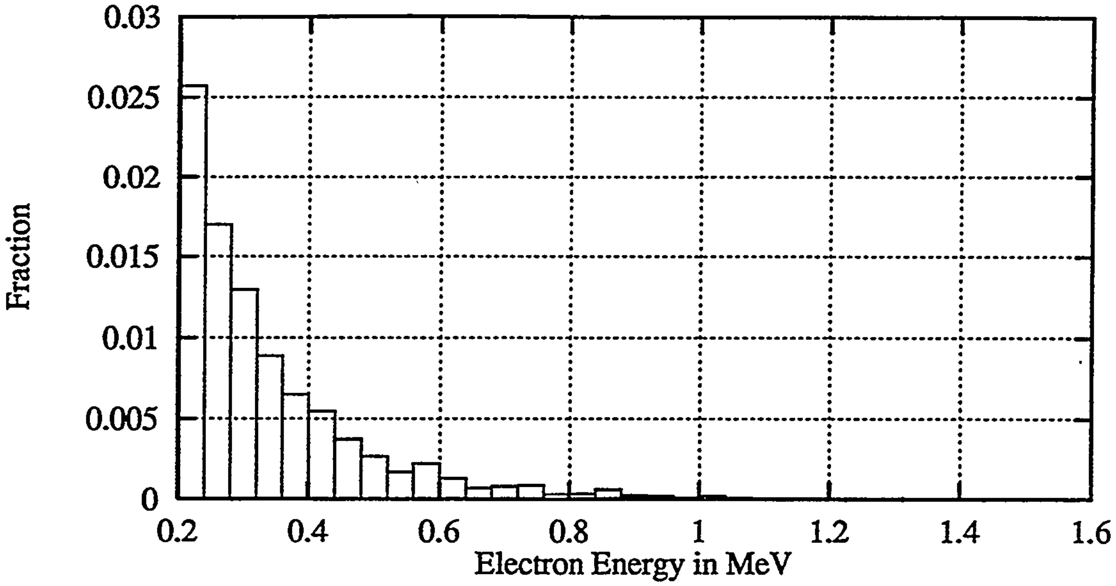

Figure 52: The electron transverse kinetic energy for propagation through $2\times10^{15}\,cm^{-3}$ *fluorine.*

distribution of the transverse kinetic energy for the electrons in the vicinity of the beam. As can be seen, about $\sim 5\%$ of the electrons have energies greater than this potential "well", with some as high as $\sim 1.36\,MeV$. These high-energy electrons contribute only partially to the beam's neutralization. However, from figure (51), we see that the potential has a minimum at $r \simeq 3.6\,cm$, implying a region of better confined electrons in the center of the beam. The charge neutralization fraction, calculated by integrating the line charge density to radius $\sim 3.6\,cm$, is $\sim 85.2\%$; this is about $\sim 10\%$ higher than the total beam neutralization of $\sim 75.4\%$ calculated above. Indeed from figure (45) we see that there exists a "core" of beam ions to a radius of around $\sim 3.6\,cm$ at the mid-point of the beam, $z \simeq 2.86\,m$. One measure of the behavior of this core is the "envelope" radius a, given by $\sqrt{2\langle r^2\rangle}$, where $\sqrt{\langle r^2\rangle}$ is the *rms* radius. At the mid-point of the beam, $a \simeq 4.09\,cm$; and shows no sign of stagnation as the maximum radius does, but continues to decrease.

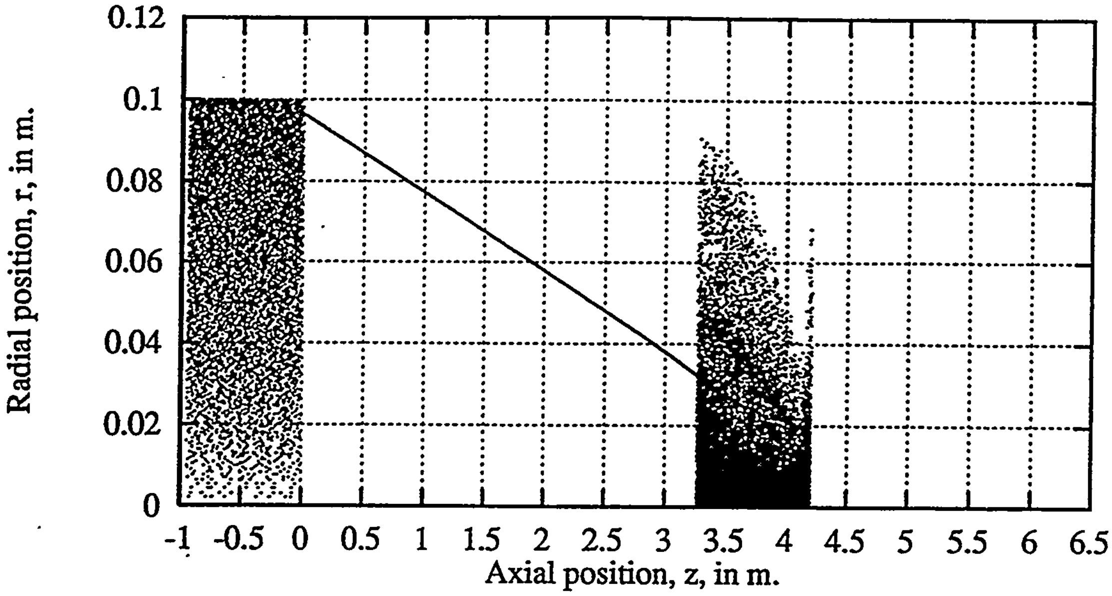

Figure 53: The beam ions for propagation through $2 \times 10^{15}\, cm^{-3}$ *fluorine.*

Figure (53) shows two "snap-shots" of the beam at different times. The first of these is at the start of the simulation, and the second is at $\sim 44.65\, ns$, which is about $\sim 9.26\, ns$ later than the last "snap-shot" of the beam in figure (45); the mid-point is now at $\sim 3.74\, m$. The solid line shows $a \equiv \sqrt{2\langle r^2 \rangle}$ of the mid-point of the beam. As can be seen, the edge radius of this mid-point continues to grow, until it reaches $\sim 6.93\, cm$; however a decreases until it reaches a minimum at $\sim 2.44\, cm$. Although there is still a core of confined beam ions, they are now concentrated within a radius of $\sim 1.5\, cm$ at the mid-point of the beam. The average charge state of the beam has also increased from ~ 19.98 to ~ 22.41 which gives a beam ion line-charge density of $1.07 \times 10^{-3}\, C/m$.

Figure (54) shows the potential energy as a function of radius. As can be seen, the potential minimum has shifted inward to about $\sim 1.5\, cm$ which again coincides with the core of the beam. The potential at the edge of the beam, $r \simeq 6.93\, cm$, is

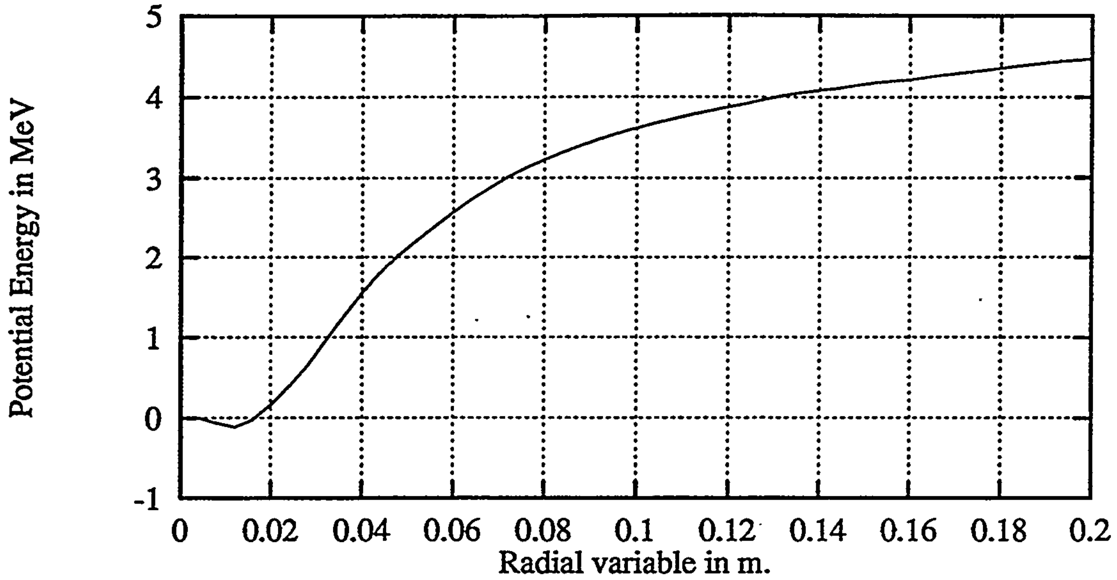

Figure 54: The potential energy for propagation through $2\times10^{15}\,cm^{-3}$ *fluorine.*

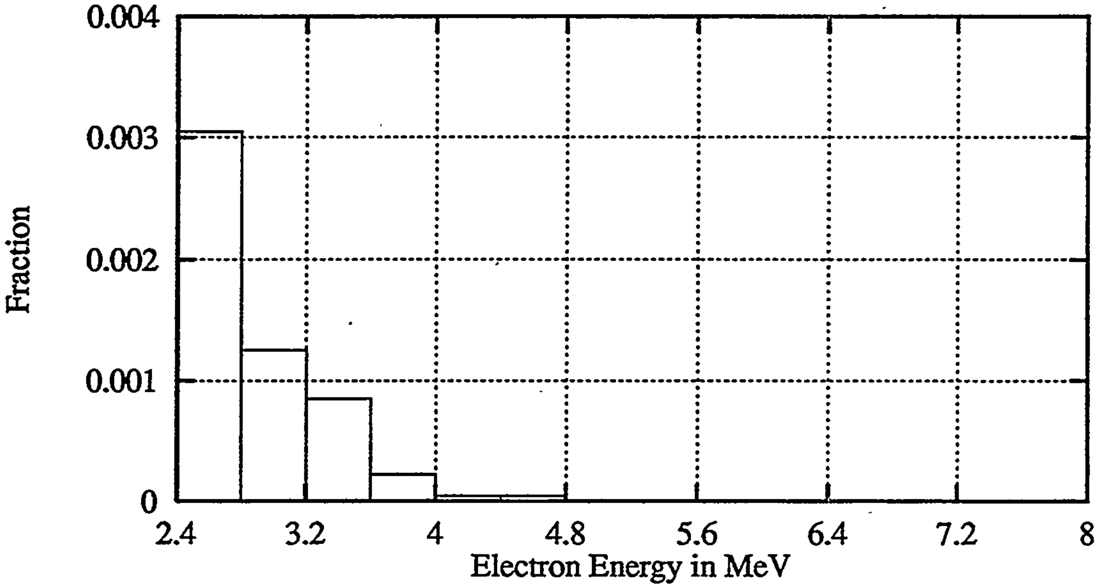

Figure 55: The electron transverse kinetic energy for propagation through $2\times10^{15}\,cm^{-3}$ *fluorine.*

now $\sim 3.03\,MV$. Figure (55) shows the distribution of electron transverse kinetic

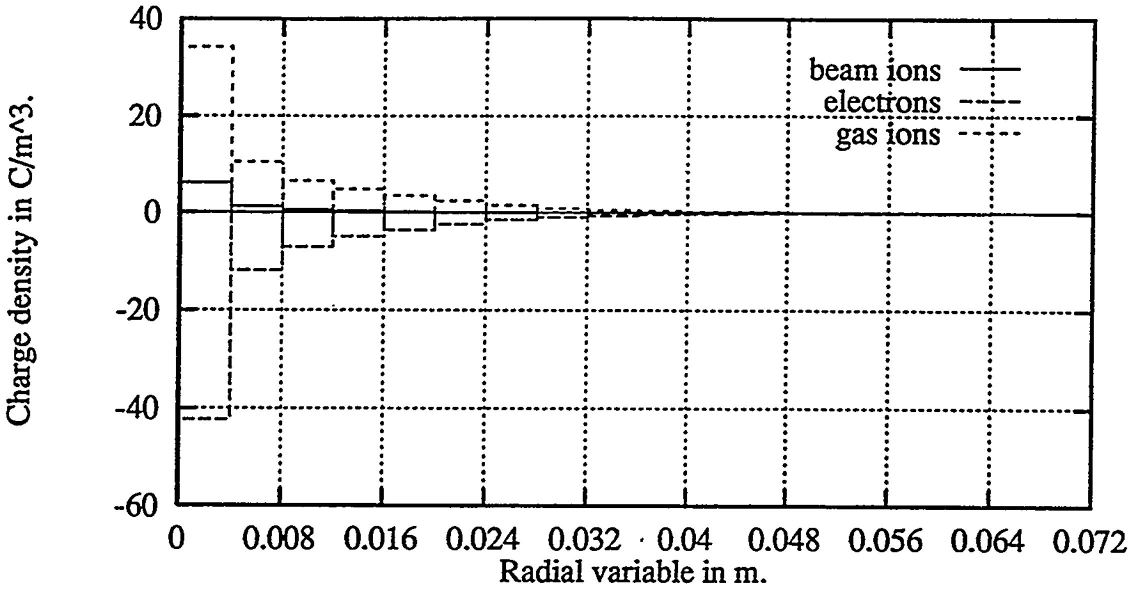

Figure 56: The charge density for propagation through $2 \times 10^{15}\,cm^{-3}$ fluorine.

energy. As can be seen, the electron energies have also increased, and can get as high as $\sim 4.69\,MeV$; these high-energy electrons will not be entirely confined within the beam and provide only partial neutralization. Figure (56) shows the charge densities for the beam ions, electrons, and gas ions, as a function of radius. If we integrate these out to radius $\sim 6.93\,cm$, the edge of the beam, we get $\lambda_b \simeq 1.01 \times 10^{-3}\,C/m$, $\lambda_e \simeq -1.35 \times 10^{-2}\,C/m$ and $\lambda_g \simeq 1.28 \times 10^{-2}\,C/m$. The total charge neutralization has decreased to $\sim 69.6\%$; but in the core of the beam, up to a radius of about $\sim 0.15\,cm$, the charge neutralization is $\sim 98.8\%$, almost $\sim 30\%$ higher than the rest of the beam.

6.2.3 Numerical Solutions for

low-density Flibe Vapor and high-density Lithium Vapor

The previous results have shown that a heavy ion beam with parameters given in table (5) cannot be focused by conventional means to the *mm* size focal spot radii necessary for heavy ion driven inertial confinement fusion in high-density, $\sim 10^{14}$ to 10^{15} molecules per cm^3, Flibe gas. Before proceeding to the case of high-density propagation in chambers that use liquid-lithium as the working fluid, we look at one last Flibe case: low-density, $\sim 10^{13}$ molecules pe cm^3.

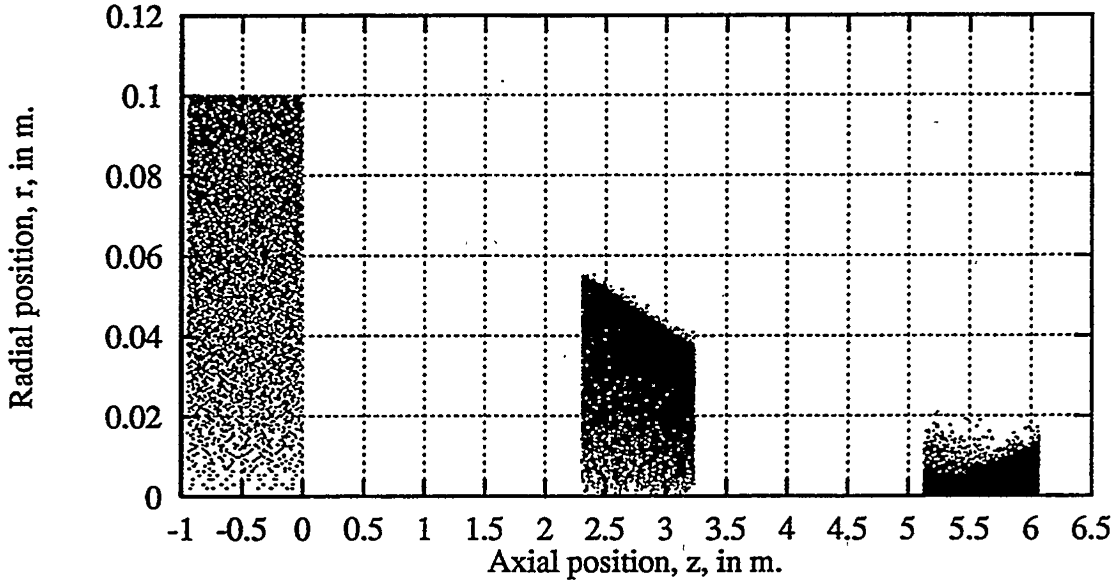

Figure 57: The beam ions for propagation through $2 \times 10^{13}\, cm^{-3}$ *fluorine.*

For $1 \times 10^{13}\, cm^{-3}$, Flibe, the background gas density, as before, is taken to be $2 \times 10^{13}\, cm^{-3}$ atoms of fluorine. The beam is the same as was used in the previous cases. Figure (57) shows the results of a BTRAC simulation. As before the figure shows three "snapshots" of the beam. The first of these is at time "0", the second is at time $\sim 34.4\, ns$, and the third is at time $\sim 64.4\, ns$. At the end of the simulation the mid-point of the beam is at axial location $\sim 5.6\, m$ from the lens. The edge radius of the beam reaches a waist, or focal spot radius, of $\sim 8\, mm$ at this location. Although this is not as good as the case of vacuum propagation where the focal-spot radius was $\sim 2.08\, mm$ at an axial location of $\sim 5.67\, m$, it is considerably better than the ~ 3 to

$5\,cm$ spot sizes for high-density propagation. The beam also has a "core" of better focused ions; the *rms* radius reaches a minimum of $\sim 2.23\,mm$ at an axial location of $\sim 5.33\,m$. The average charge-state of the beam ions is much lower, ~ 1.66, than those seen for propagation through high-density gas. This lower charge state leads to lower beam ion line-charge densities and also lower gas ion line-charge densities because the ionization cross sections depend on the charge state of the beam ions. If we calculate the line-charge densities integrated to $r \simeq 8\,mm$ we get $\lambda_b \simeq 6.43 \times 10^{-5}\,C/m$, which is what we expect for an average charge state of ~ 1.66; $\lambda_e \simeq -5.17 \times 10^{-5}\,C/m$; and $\lambda_g \simeq 4.57 \times 10^{-6}\,C/m$. From these we calculate a charge neutralization fraction, given by $[1-(\lambda/\lambda_b)]$, of $\sim 73.2\%$. Although this is not much better than the fractions achieved at higher densities, leading to comparable residual fields, $E_r \simeq 3.79 \times 10^7\,V/m$ at $r \simeq 8\,mm$, the charge state of the beam ions is more than an order of magnitude lower than the high-density cases, therefore the space-charge defocusing forces are smaller, $f_r \simeq 1.01 \times 10^{-11}\,N$.

We now turn to the case of propagation through high-density, $\sim 10^{14}$ to $10^{15}\,cm^{-3}$, lithium background gas. In their original HYLIFE design, Blink, et al., (1985), proposed using liquid lithium in the chamber as the coolant, to protect the first structural wall and breed tritium, in much the same way as Flibe is used in the HYLIFE-II design by Moir, et al., (1994). From a beam propagation point of view, lithium has an advantage over Flibe; it has a lower atomic number than fluorine, therefore its stripping cross section, which is proportional to the square of the atomic number as seen in equation (247), is much lower than that of fluorine. Figures (58) and (59) show the stripping and ionization cross sections for mercury ions colliding with lithium atoms with velocity $\beta \simeq 0.315$ computed using equations (247). If we compare these cross sections to those for fluorine shown in figures (30) and (31) we see that although the ionization cross sections are the about the same order of magnitude for both gases,

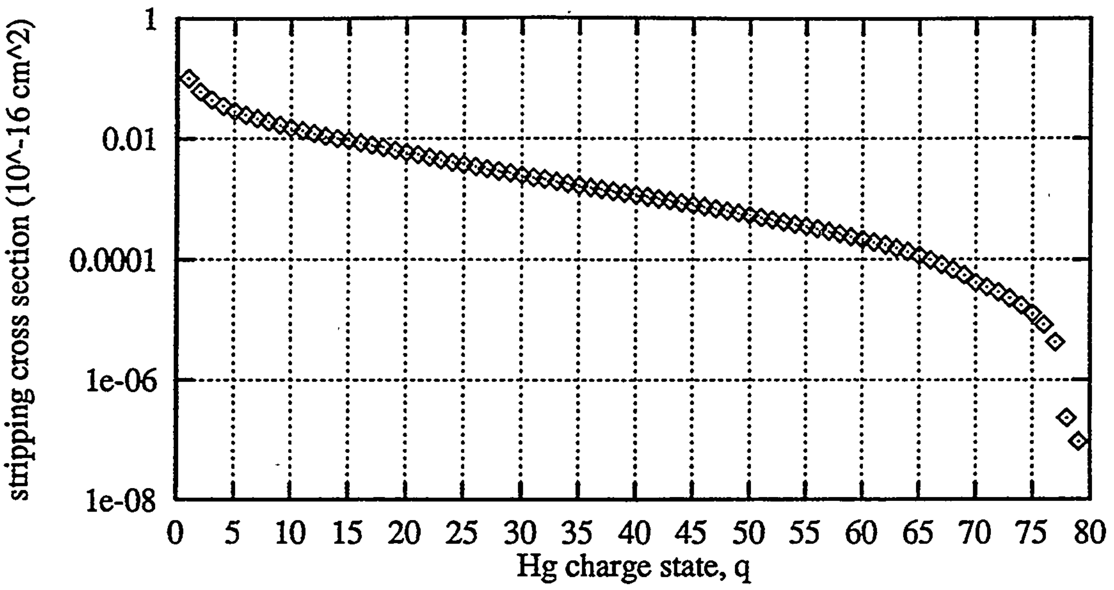

Figure 58: The stripping cross section, $\sigma_{st,q}$

for Hg^{q+} *colliding with neutral lithium at* $\beta = 0.315$.

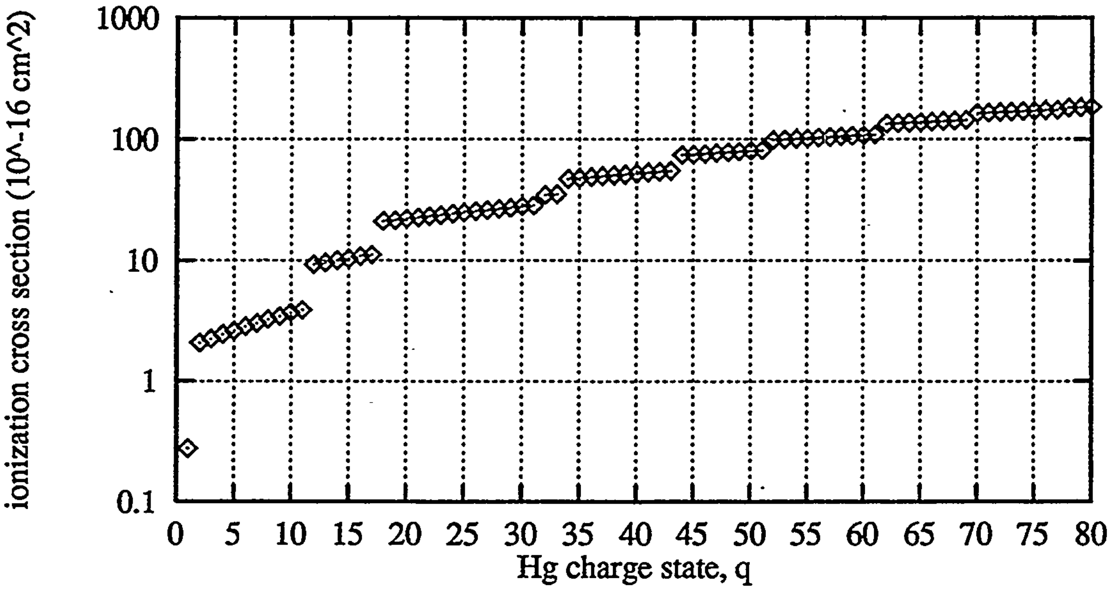

Figure 59: The ionization cross section, $\sigma_{in,q}$

for Hg^{q+} *colliding with neutral lithium at* $\beta = 0.315$.

the stripping cross sections for lithium are almost an order of magnitude lower than that for fluorine. Therefore, even in high-density lithium gas, we expect the charge states of the beam ions to be low.

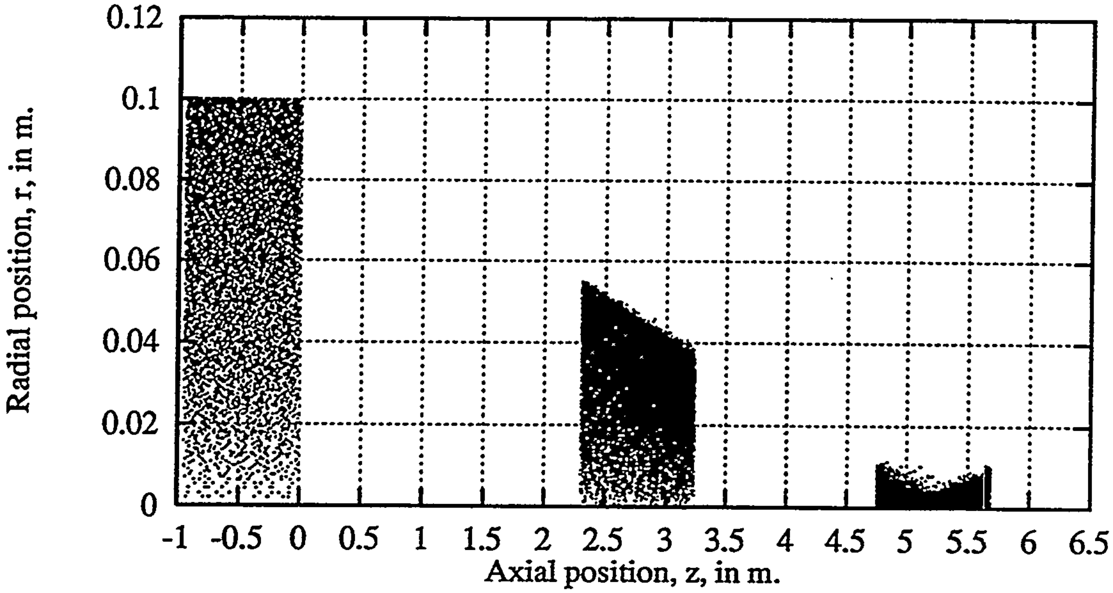

Figure 60: The beam ions for propagation through $2\times10^{14}\,cm^{-3}$ *lithium.*

Figure (60), as before, shows three "snapshots" of a beam of heavy ions propagating through $2\times10^{14}\,cm^{-3}$ lithium. The first of these is at time "0", the second is at time $\sim 34.4\,ns$, and the third is at time $\sim 60.3\,ns$. At the end of the simulation the mid-point of the beam is at $\sim 5.22\,m$ from the lens. The edge radius of the beam at this point is $\sim 3.75\,mm$; which is comparable to the vacuum focal spot radius of $\sim 2.08\,mm$ at an axial location of $\sim 5.67\,m$. As expected, the average charge-state of the beam ions in this case is low, ~ 1.87, as compared with ~ 11.41 for propagation through Flibe gas of the same density. The line-charge densities integrated out to a radius of $\sim 3.75\,mm$ are now, $\lambda_b \simeq 5.12\times10^{-5}\,C/m$, $\lambda_e \simeq -7.14\times10^{-5}\,C/m$ and $\lambda_g \simeq 2.64\times10^{-5}\,C/m$. The neutralization fraction is $\sim 87.7\%$, which is about the same as the neutralization achieved by Flibe at the same density, $\sim 88.5\%$.. Consequently, the radial electric field at $r \simeq 3.75\,mm$ is still as high as $\sim 3.02 \times 10^7\ V/m$; but since the charge-state of the beam ions is small, this field has less of a defocusing effect than comparable fields in the case of propagation through Flibe gas. The force on an ion at the focal-spot radius is about seven times smaller than that for Flibe, $f_r \simeq 9.05 \times 10^{-12}\ N$.

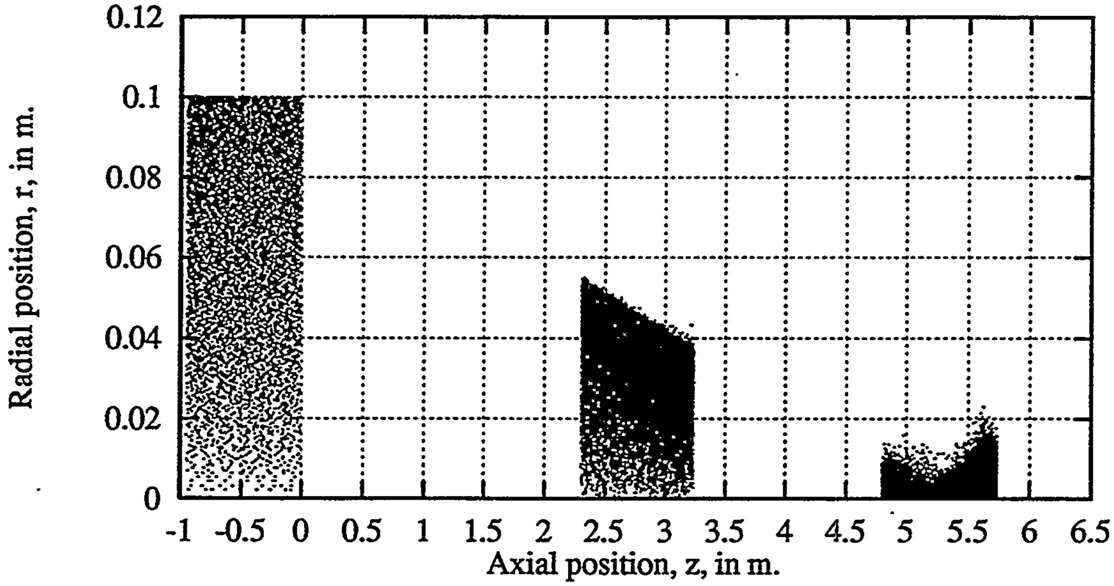

Figure 61: The beam ions for

propagation through $1 \times 10^{15}\ cm^{-3}$ *lithium.*

Finally we look at propagation through $1 \times 10^{15}\ cm^{-3}$ lithium. As before figure (61) shows the beam at three different times, "$0\,ns$", $\sim 34.4\,ns$, and $\sim 60.8\,ns$. The beam reaches a waist, or focal-spot radius of $6.88\,mm$ at a distance of $\sim 5.27\,m$ from the lens. The average charge-state is now higher than the previous case, as expected, ~ 3.96, but still considerably lower than propagation through Flibe at the same density. The radial electric field at $r \simeq 6.88\,mm$ is $\sim 5.01 \times 10^7\ V/m$. The force on a beam ion at the focal-spot radius is now about half that for a beam ion at the focal radius for transport through Flibe gas of the same density, $f_r \simeq 3.18 \times 10^{-11}\ N$.

6.3 Conclusions

We have seen that heavy ion beams used to drive the implosion of a pellet of DT fuel for the effective production of electricity in an ICF power plant, must be focused to *mm* size spot radii on the target in order to yield the high temperatures required for efficient ablation driven implosion. In some power plant designs, the target is surrounded by exposed liquid flows, consisting of lithium compounds, located in the center of a chamber. For efficient electric power production, a pellet must be imploded ~ 5 to 20 times a second. The "liquid-wall" carries away the heat generated from the microexplosion of the pellet, protects the first structural wall of the chamber from damage from the neutrons and breeds tritium. The microexplosion partially vaporizes the liquid resulting in a background gas density in the chamber that can get as high as $\sim 10^{18}$ molecules per cm^3 immediately after a shot. Much of the design of a chamber is devoted to lowering this gas density between subsequent shots to levels that would not impede the ability to focus the beams to the necessary small spot radius. It is therefore of high interest to determine the degree to which clearing between shots is really necessary.

In this thesis we examined the ability to "conventionally" focus a single heavy ion beam in reactor chambers that use Flibe, a molten salt mixture of LiF and BeF_2, or liquid-lithium as the working fluid, with background gas densities in the range of $\sim 10^{14}$ to $10^{15}\,cm^{-3}$. Conventional focusing schemes employ a system of magnetic quadrupoles, the last element of which is located well outside the chamber, perhaps $\sim 5\,m$ away from its center, to focus the beam onto the target. For this study the beam was initially taken to be a uniformly distributed, $\sim 0.94\,m$ long, $\sim 10\,cm$ radius, cylinder consisting of $\sim 4.3\,kA$ of $\sim 10.02\,GeV$, Hg^+ ions. The `BTRAC` code was developed and used to study the propagation of this beam through high-density,

$\sim 4\times10^{14}$ and $\sim 2\times10^{15}$ atoms per cm^3 fluorine gas, used to simulate chambers with Flibe, and $\sim 2\times10^{14}$ and $\sim 1\times10^{15}$ atoms per cm^3 lithium gas.

Our results for vacuum propagation showed that such a beam can indeed be focused to a $\sim 2.08\,mm$ spot-size at a distance of $\sim 5.67\,m$ from the lens. This spot radius is in good agreement, $\sim 5.6\%$, with the solution to the "envelope" equation, even though this solution ignores the effect of the axial electric field. The beam line-charge density was $\sim 47.9\,\mu C/m$, leading to a radial electric field at the edge of the beam, $r \simeq 2.08\,mm$, of $\sim 0.41\,GV/m$, as expected. The azimuthal magnetic field was $\sim 0.46\,T$; but because the beam is sub-relativistic, $\beta \simeq 0.315$, the magnetic pinch forces are typically a tenth of the electric defocusing forces felt by the beam ions. If we ignore this magnetic force the radial electric force felt by a beam ion at the edge of the beam is $\sim 6.5\times10^{-11}\,N$. Any electrons generated from collisions with background gas neutrals will be strongly effected by these fields.

The complicated plasma phenomena that results from propagation through background gas makes analytic methods inadequate for describing the dynamics of the beam. The primary defocusing effect on the beam ions comes from the radial electric force and is a product of two components: the charge state of the beam ions, and the total line-charge density of the beam. The charge-state of the beam ions is determined solely by the stripping cross sections and the density of the background gas. The total line-charge density is the sum of the line-charge densities of the various charged particles in the beam: the beam ions, electrons and background gas ions. The charge-state of the beam ions can influence not only the charge density of the beam ions, but because the ionization cross sections depend on this charge-state, they also influence the electron and gas ion charge densities; furthermore, any radial electric field due to the total line-charge density will strongly effect the transverse dynamics of the electrons and determine their ability to remain confined within the beam and contribute to its neutralization.

In $\sim 4\times10^{14}\,cm^{-3}$ fluorine gas the edge radius of the beam, given by "tracking" the ion with the largest radial position at the axial mid-point of the beam, reached a "waist", or minimum, of $\sim 3.05\,cm$ at an axial location of $\sim 4.61\,m$ from the lens. The larger the focal-spot radius the shorter the distance from the lens to the waist. The average charge-state of the beam ions was ~ 11.41; therefore the beam line-charge density was as high as $\sim 0.52 mC/m$. The ionization mean-free-path at this charge state and background gas density is $\sim 2.78\,cm$, therefore we expect to see a high gas ion line-charge density, $\sim 0.7\,mC/m$. If we assume a uniform radial distribution we can calculate the potential at the edge of the beam due to both these line-charge densities, $\sim 11\,MV$. These high potentials are capable of imparting large transverse energies to the electrons; indeed the electrons had transverse kinetic energies as high as $\sim 3.26\,MeV$. The observed potential at the edge of the beam, calculated by integrating the radial electric field, was $\sim 1.45\,MV$. Electrons with transverse kinetic energies larger than this potential are not effectively confined within the beam. The electron line-charge density was therefore lower than expected, $\sim -1.16 mC/m$, leading to a total line-charge density of $\sim 59.4\,\mu C/m$ and a neutralization fraction of $\sim 88.5\%$. The average radial electric field at the edge of the beam was $\sim 36.8\,MV/m$. Although this field is about a tenth of the strength of the field for the vacuum case, it coupled together with the fact that the average charge-state of the beam ions has increased by more than a factor of ten leads to a defocusing force, $\sim 6.73\times10^{-11}\,N$, which is comparable to that at the smaller waist of the beam for vacuum propagation.

The next case studied was propagation through $\sim 2\times10^{15}\,cm^{-3}$ fluorine gas. In this case beam focused to a spot radius, determined by the outermost beam ion, of $\sim 5.49\,cm$, which, as expected, was located closer to the lens at $\sim 2.86\,m$. The average charge-state of the beam was now almost twice as high, ~ 19.98, leading to a beam line-charge density of $\sim 0.89\,mC/m$. The ionization mean-free-path is now much smaller, $\sim 0.15\,cm$, and the gas ion line-charge density was correspondingly higher, $\sim 11.2\,mC/m$. Again the electron line-charge density was lower than expected, $\sim -11.9\,mC/m$, leading to a total line-charge density of $\sim 0.22\,mC/m$ and a neutralization fraction of $\sim 75.4\%$. The average field at the edge was $\sim 24.7\,MV/m$. Again this field is about a factor of seventeen lower than the vacuum field, but the average charge-state has also gone up by close to a factor of twenty, leading to defocusing forces, $\sim 7.91 \times 10^{-11}\,N$, that are comparable to the forces at the waist of the beam for vacuum propagation.

In both these cases, there exists a "core" of much better focused beam ions. This was evidenced by the fact that the *rms* radius of the beam continued to decrease even after the edge radius reached a waist. In the case of the propagation through $\sim 2 \times 10^{15}\,cm^{-3}$ fluorine it was $\sim 2.89\,cm$ at the time the edge radius was at its minimum, $\sim 5.49\,cm$. The potential of the beam had a "well" with a minimum at $r \simeq 3.6\,cm$. Most of the electrons were concentrated in a central region within this radius; indeed the neutralization fraction in this region was $\sim 85.2\%$, which is more almost 10% higher than the overall beam neutralization. We allowed the beam to propagate past the waist, until the *rms* radius reached a minimum of $\sim 1.73\,cm$, $\sim 3.74\,m$ from the lens; the edge radius of the beam expanded to $\sim 6.93\,cm$. The beam potential at the edge of the beam was now $\sim 3.03\,MV$, with a minimum at $r \simeq 1.5\,cm$. The electrons had maximum transverse kinetic energies of $\sim 4.69\,MeV$, again allowing them to "escape" the beam potential. The overall beam neutralization fraction decreased to $\sim 69.6\%$; but the core, to a radius of $\sim 1.5\,cm$, again had a much better fraction of $\sim 98.8\%$.

We finally looked at propagation through three different gas and density regimes that did yield spot radii that were more in keeping with the requirements for heavy ion driven inertial confinement fusion. The first of these was for low-density Flibe, $\sim 2\times 10^{13}\,cm^{-3}$ fluorine gas. The beam focused to a spot radius of the $\sim 8\,mm$, with a minimum *rms* radius of $\sim 2.23\,mm$. The average charge-state of the beam ions was ~ 1.66, much lower than for propagation through higher density fluorine. We also looked at transport through high-density, lithium background gas for chambers that use liquid-lithium as the working fluid instead of Flibe. Because lithium has a lower atomic number than fluorine, the stripping cross sections for the beam ions are about an order of magnitude smaller. Therefore even for propagation through high-density lithium gas we do not expect the charge-states of the beam ions to get as high as they do for propagation through similar density Flibe. The first of these cases studied was for $\sim 2\times 10^{14}\,cm^{-3}$ lithium. The beam focused to a spot radius of $\sim 3.75\,mm$; and the average charge-states of the beam ions was ~ 1.87. The last case was for propagation through $\sim 1\times 10^{15}\,cm^{-3}$ lithium. The average charge-state was ~ 3.96 and the spot radius was $\sim 6.88\,mm$.

Although we studied the propagation of a beam with only a single, but typical, set of parameters, we found essentially that moderate stripping, to average beam ion charge-states of ~ 4 could be tolerated. Substantially higher charge states, ~ 11.4 to ~ 20, that result from propagation through high-density, $\sim 10^{14}$ to 10^{15} molecules per cm^3, Flibe, not only lead to higher beam ion line-charge densities, but because of the increased ionization of the background gas, also lead to large gas ion line-charge densities. The resultant beam potentials impart considerable transverse kinetic energies to the electrons. These high-energy electrons are not entirely confined within the beam and cannot effectively neutralize the beam and gas ion charge. The residual radial electric fields at the edge of the beam when it reaches a waist of $\sim 3.1\,cm$ to

$\sim 5.5\,cm$, although lower than the fields present in the case of vacuum propagation, when coupled with the higher charge-states of the beam ions results in defocusing forces that are comparable to those at the much smaller waist, $\sim 2.1\,mm$, achievable in vacuum. Stripping cross sections depend roughly on the square of the atomic numbers, therefore propagation through high-density gas, $\sim 10^{14}$ to 10^{15} atoms per cm^3, in chambers that use liquid-lithium as the working fluid results in considerably lower charge states, ~ 1.9 to ~ 4, than for propagation through Flibe background gas of comparable densities, allowing the beam to focus to smaller spot radii, $\sim 3.8\,mm$ to $\sim 6.9\,mm$.

There are several methods that can be employed in reactor designs with conventional focusing systems to achieve smaller spot radii in high-density gas. For instance, Callahan (1995) has shown that it may be possible to overcome the problem of inadequate neutralization by injecting "cold" electrons into the beam to continuously replenish those that are heated and lost. Also, electrons generated by photo-ionization of the background gas by x-rays emitted from the target when the beam impinges on it, which are not accounted for in this study, may further neutralize the beam. Another possibility is to use final focus systems that focus the beam with larger convergence angles, or to simply increase the number of beams thereby lowering the current in each beam. Another strategy is to employ targets that yield similar gain for spot-radii that are larger than the nominal $\sim 2\,mm$.

Ultimately, the various methods for propagating a beam of heavy ions through background gas must be weighed with respect to the cost and safety of the ICF power plant. Allowing for higher-density background gas in the chamber may lead to simpler designs, eliminating the need to drastically lower the density between shots, but the resultant larger focal-spot radii lead to lower target gain and increased plant costs. Increasing the number of beams or focusing with larger convergence angles may require bigger and more complicated final focus systems. And although using liquid-lithium as the working fluid in the chamber instead of Flibe drastically reduces stripping and therefore allows the beam to focus to smaller spot radii for higher background gas densities, there are several safety disadvantages compared with Flibe. These include fire hazard, large tritium inventory, and a greater fluid thickness to contain the fusion neutrons.

References

Abramowitz, M., and I.A. Stegun, *Handbook of Mathematical Functions*, Dover Publications, Inc., 355-433, 1965.

Bangerter, R.O., Targets for heavy-ion fusion, *Fusion Technology*, **13**, 348-355, 1988.

Bangerter, R.O., and D.D-M. Ho, Heavy ion induction linacs for fusion, *Proceedings of the Linac Conference*, 1990.

Bethe, H., Theory of the passage of fast corpuscular rays through matter, *Annalen der Physik*, **5**, 325-400, 1930.

Betz, H-D., Charge states and charge-changing cross sections of fast heavy ions penetrating through gaseous and solid media, *Reviews of Modern Physics*, **44-3**, 465-539, 1972.

Birdsall, C.K., Particle-in-cell charged-particle simulations, plus Monte Carlo collisions with neutral atoms, PIC-MCC, *IEEE Transactions on Plasma Science*, **19-2**, 65-85, 1991.

Birdsall, C.K., and A.B. Langdon, *Plasma Physics via Computer Simulation*, McGraw-Hill, 1985.

Blink, J.A., W.J. Hogan, J. Hovingh, W.R. Meier, and J.H. Pitts, The high-yield lithium-injection fusion-energy (HYLIFE) reactor, UCID-53559, Lawrence Livermore National Laboratory, 1985 (unpublished).

Bohr, N. *The Penetration of Atomic Particles Through Matter*, Munksgaard, København, 63-121, 1948.

Boris, J.P., Relativistic plasma simulation - optimization of a hybrid code, *Proceedings of the Fourth Conference on Numerical Simulation of Plasmas*, 3-67, 1970.

Callahan, D.A., Interactions between neighboring beams in a heavy ion fusion reactor chamber, *Applied Physics Letters*, **67-22**, 3254-3256, 1995.

Callahan, D.A., Chamber propagation physics for heavy ion fusion, *Fusion Engineering and Design*, 1995 (to be published).

Carlson, T.A., C.W. Nestor, Jr., N. Wasserman, and J.D. McDowell, Calculated ionization potentials for multiply charged ions, *Atomic Data*, **2**, 63-99, 1970.

Dawson, J.M., Particle simulation of plasmas, *Reviews of Modern Physics*, **55-2**, 403-447, 1983

Dehmel, R.C., H.K. Chau, and H.H. Fleischmann, Experimental stripping cross sections for atoms and ions in gases, *Atomic Data*, **5**, 231-289, 1973.

Fano, U., and J.W. Cooper, Spectral distribution of atomic oscillator strengths, *Reviews of Modern Physics*, **40-3**, 441-507, 1968.

Hahn, K., and E. Lee, A study of stripped, pinched beam transport for HIF, *Fusion Engineering and Design*, 1995 (to be published).

Hammersley, J.M., and D.C. Handscomb, *Monte Carlo Methods*, Methuen and Co., London, 50-75, 1964.

Hockney, R.W., and J.W. Eastwood, *Computer Simulation using Particles*, Institute of Physics Publishing, 1988.

Hovingh, J., V.O. Brady, A. Faltens, D. Keefe, and E.P. Lee, Heavy-ion linear induction accelerators as drivers for inertial fusion power plants, *Fusion Technology*, **13**, 255-278, 1988.

Inokuti, M., Inelastic collisions of fast charged particles with atoms and molecules - the Bethe theory revisited, *Reviews of Modern Physics*, **43-3**, 297-347, 1971.

Isaacson, E., and H.B. Keller, *Analysis of Numerical Methods*, John Wiley and Sons, 364-530, 1966.

Jackson, J.D., *Classical Electrodynamics*, John Wiley and Sons, Second Edition, 84-135 & 618-653, 1975.

Kapchinskij, I.M., and V.V. Vladimirskij, Limitations of proton beam current in a strong focusing linear accelerator associated with the beam space charge, *Proceedings of the International Conference on High-Energy Accelerators and Instrumentation - CERN*, 274-288, 1959.

Kaufman, A.N., Theoretical plasma physics course notes, Physics 242A, University of California at Berkeley, 1995.

Keefe D., Inertial confinement fusion, *Annual Review of Nuclear and Particle Science*, **32**, 391-441, 1982.

Keski-Rahkonen, O. and M.O. Krause, Total and partial atomic-level widths, *Atomic Data and Nuclear Data Tables*, **14**, 139-146, 1974.

Lee, E.P., Heavy ion driven LMF design concept, LBL-31248, UC-421, Lawrence Berkeley National Laboratory, 1991 (unpublished).

Lee, E.P., and R.K. Cooper, General envelope equation for cylindrically symmetric charged-particle beams, *Particle Accelerators*, **7**, 83-95, 1976.

Lewis, E.E., and W.F. Miller, Jr., *Computational Methods of Neutron Transport*, John Wiley and Sons, 297-360, 1984.

Lindl, J., Development of the indirect-drive approach to inertial confinement fusion and the target physics basis for ignition and gain, *Physics of Plasmas*, **2-1**, 3933-4024, 1995.

Lo, H.H. and W.L. Fite, Electron-capture and loss cross sections for fast, heavy particles passing through gases, *Atomic Data*, **1**, 305-328, 1970.

Mei, K.K., Applied electromagnetic theory course notes, Electrical Engineering 210B, University of California at Berkeley, 1994.

Moir, R.W., M.G. Adamson, R.O. Bangerter, R.L. Bieri, R.H. Condit, C.W. Hartman, P.A. House, A.B. Langdon, B.G. Logan, C.D. Orth, R.W. Petzoldt, J.H. Pitts, R.F. Post, R.A. Sacks, M.T. Tobin, W.H. Williams, T.J. Dolan, G.R. Longhurst, M.A. Hoffman, V.E. Schrock, P.F. Peterson, R.Y. Bai, X.M. Chen, J.C. Liu, D-K. Sze, and W.R. Meier, HYLIFE-II Progress Report, UCID-21816, Lawrence Livermore National Laboratory, 1991 (unpublished).

Moir, R.W., R.L. Bieri, X.M. Chen, T.J. Dolan, M.A. Hoffman, P.A. House, R.L. Leber, J.D. Lee, Y.T. Lee, J.C. Liu, G.R. Longhurst, W.R. Meier, P.F. Peterson, R.W. Petzoldt, V.E. Schrock, M.T. Tobin, and W.H. Williams, HYLIFE-II: A molten-salt inertial fusion energy power plant design - final report, *Fusion Technology*, **25**, 5-25, 1994.

Mur, G., Absorbing boundary conditions for the finite-difference approximation of the time-domain electromagnetic-field equations, *IEEE Transactions on Electromagnetic Compatibility*, **33-4**, 377-382, 1981.

Nakamura, S., *Computational Methods in Engineering and Science*, Robert E. Krieger Publishing Company, 333-388, 1977.

Press, W.H., S.A. Teukolsky, W.T. Vetterling, and B.P. Flannery, *Numerical Recipes in C*, Cambridge University Press, Second Edition, 274-286 & 732-734, 1992.

Prussin, S.G., Nuclear reactions and interactions of radiation with matter course notes, Nuclear Engineering 201, University of California at Berkeley, 1992.

Sevier, K.D., Atomic electron binding energies, *Atomic Data and Nuclear Data Tables*, **24**, 323-371, 1979.

Schlachter, A.S., J.W. Stearns, W.G. Graham, K.H. Berkner, R.V. Pyle, and J.A. Tanis, Electron capture for fast highly charged ions in gas targets: an empirical scaling rule, *Physical Review A*, **27-11**, 3372-3374, 1983.

Schram, B.L., A.J.H. Boerboom, and J. Kistemaker, Partial ionization cross sections for noble gases for electron with energy $0.5-16\,keV$ (I helium and neon), *Physica*, **32**, 185-196, 1966.

Schram, B.L., Partial ionization cross sections for noble gases for electron with energy $0.5-18\,keV$ (II argon, krypton and xenon), *Physica*, **32**, 197-208, 1966.

Slater, J.C., Atomic shielding constants, *Physical Review*, **36**, 57-64, 1930.

Tauschwitz, A., S.S. Yu, S. Eylon, R.O. Bangerter, W. Leemans, C. Peters, J.O. Rasmussen, L. Reginato, J.J. Barnard, and W.M. Sharp, Plasma lens focusing and plasma channel tansport for heavy ion fusion, *Fusion Engineering and Design*, 1995 (to be published).

Vahedi, V. and M. Surendra, A Monte Carlo collision model for the particle-in-cell method: applications to argon and oxygen discharges, *Computer Physics Communications*, **87**, 179-198, 1995.

Verboncoeur, J.P., A.B. Langdon, and N.T. Gladd, An object-oriented electromagnetic PIC code, *Computer Physics Communications*, **87**, 199-211, 1995.

Vujic, J., Numerical methods of reactor analysis course notes, Nuclear Engineering 255, University of California at Berkeley, 1992.

Yee, K.S., Numerical solution of initial boundary value problems involving Maxwell's equations in isotropic media, *IEEE Transactions on Antennas and Propagation*, **14-3**, 302-307, 1966.

Zukerman, D.S., D.E. Driemeyer, L.M. Waganer, and D.J. Dudziak, An induction linac driven heavy-ion fusion systems model, *Fusion Technology*, **13**, 217-254, 1988.

Appendix
BTRAC Code

The "C" code BTRAC was developed to implement the numerical solution for the transport of a beam of heavy ions through background gas. The numerical equations are derived and explained in the preceding sections, and figure (25) shows the flow chart for the algorithm used in the code. We describe here the structure of this code, its syntax, and the input and output files.

A.1 Code Structure

Figure (A.1) shows the block diagram for BTRAC. As can be seen the code is divided into four modules. The first of these is the main program that controls the flow of the other modules in the code, and the input and output of information. The second module does the initialization and is composed of two submodules. The first of these, IFC, initializes the electric and magnetic fields in the system. The Bessel functions needed in this submodule are based on expansions given by Abramowitz and Stegun (1965). The second submodule, LOAD, "loads" the super-beam ions, or initializes their positions and velocities. The random number generators needed in this submodule are taken from Press, et al., (1992). Both IFC and LOAD assume a K-V transverse distribution for the beam and a singular axial velocity for all beam ions; however, the axial spatial distribution is specified by the user.

The next module does the time-step loop and is comprised of three submodules. CPC advances the positions of the particles, and then uses these positions to calculate the current densities; MCC analyzes the collisions between the beam ions and background gas neutrals and then updates the number of beam ions of each charge

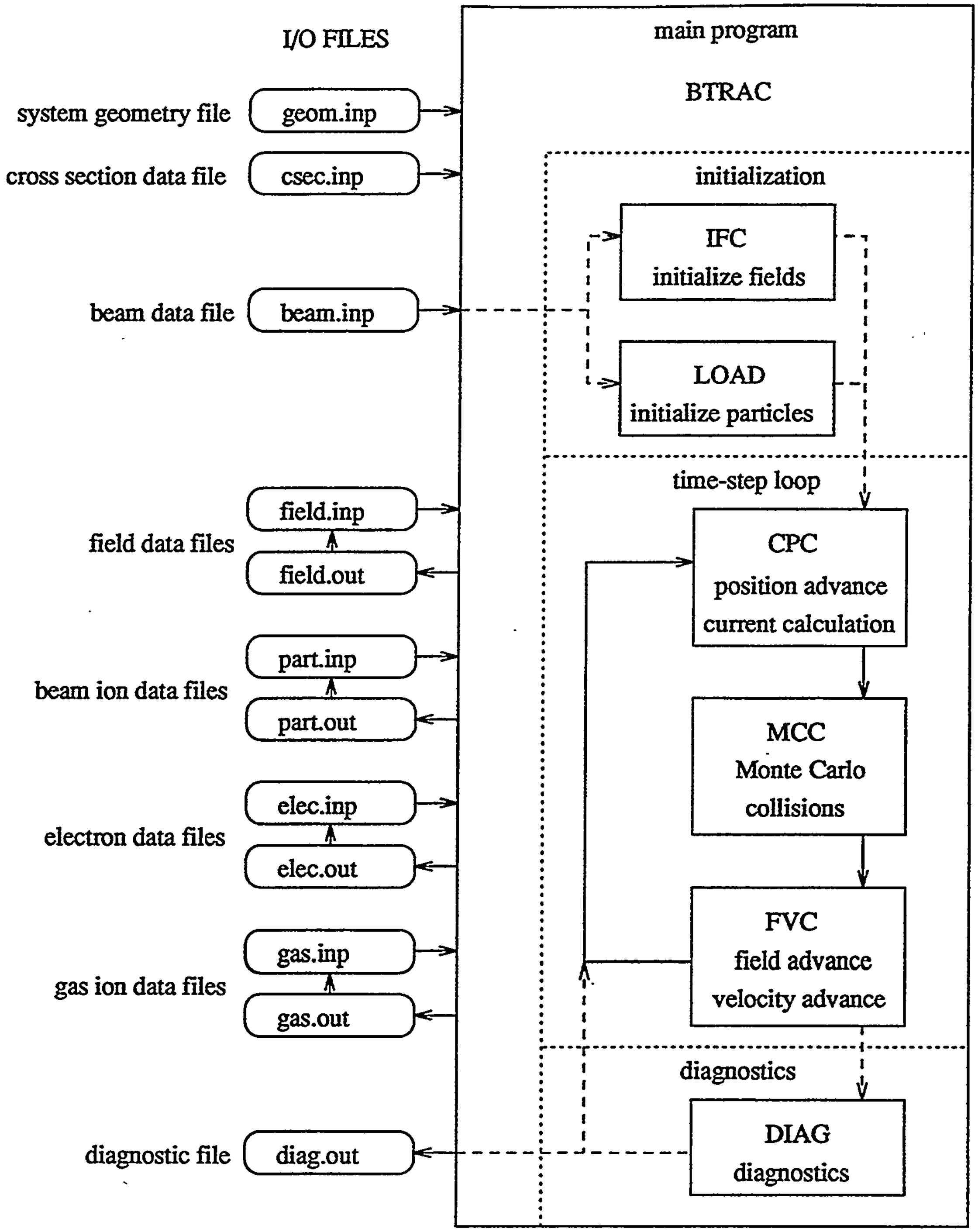

Figure A.1: Block diagram of the `BTRAC` *code.*

state, electrons, and background gas ions; and `FVC` advances the electric and magnetic fields, interpolates the fields to the particle positions and uses these interpolated fields to advance the particle velocities. The random number generators in `MCC` are taken from Press, et al., (1992). Finally the last module does the diagnostics and consists of the single submodule `DIAG`, which, at present, computes the radius of the beam and the electron plasma frequency at the longitudinal mid-point of the beam, and the maximum and average charge-states of the beam ions; from these quantities can be computed the beam current and collision frequency. The plasma and collision frequencies are particularly useful in calculating the time-step accuracy conditions discussed in the previous sections.

A.2 Running the Code

The command line syntax for invoking the code has various options that control which modules in the program are invoked. The syntax for the code is:

```
btrac [-ni] [-nd] [-rn #] i/o-location
```

The command line argument `i/o-location` is the directory location from which the program will take its input files, and to which it will write its output files. At this location there must exist two subdirectories with the titles `input` and `output`. The input files, with extension `inp`, must be located in the subdirectory `input` and the output files, with extension `out`, will be written to the sub-directory `output`.

Regardless of the options with which the code is run, it will always read two input files at the start of a simulation "run" from the `input` subdirectory: `geom.inp`, which contains a description of the simulation environment, and `csec.inp`, which contains the cross section information for the stripping and ionization collisions between the beam ions and background gas neutrals; this latter file is only read if background gas is present, i.e. the chamber is not a vacuum. The code will also write four output files at the end of the "run" to the `output` subdirectory: `field.out`, which contains the electric and magnetic fields on the spatial grid, and `part.out`, `elec.out` and `gas.out`, which contain the positions and velocities of the beam ions, electrons, and background gas ions respectively. The other input and output files are determined by the options used.

A.2.1 The Initialization Option

We shall now discuss each of the command line options in turn. The first of these is `-ni`; this option is used to control the initialization module of the code. Without it the code calls both `IFC` and `LOAD`. In this case, in addition to `geom.inp` and `csec.inp`, another input file, `beam.inp`, which contains a description of the beam, must also exist in the `input` subdirectory. As an example consider the following command line:

```
btrac .
```

The `i/o-location` is the current context, and the code takes the input files from `./input` and will write the output files to `./output`. The code will also display the following information on the screen:

```
Reading in the chamber geometry from file:          ./input/geom.inp
Reading in the cross section data from file:        ./input/csec.inp
Reading in the beam data from file:                 ./input/beam.inp

Computing the initial fields ...
Loading the particles ...

The length of the chamber is ...                    9.000000 m.
The axial grid division is ...                      0.006 m.
The location of the thin lens is ...                5.000000 m.
The radius of the chamber is ...                    0.300000 m.
The radial grid division is ...                     0.008 m.

The number of radial grids is ...                   38
The number of axial grids is ...                    1501
The axial grid location of the target is ...        331

The mass of the beam ion is ...                     200.59 amu.
The average initial charge state per particle is ...1.000000 .
The beam current is ...                             4304.88 A.
The central radius of the beam is ...               0.0989693 m.
```

```
The electron plasma frequency is ...                0 rad/sec.
The mass of the background gas is ...               19 amu.
The background gas density is ...                   4e+20 m-3.

The number of particles per super-particle is ...   1.4e+10 .
The number of super-beam ions to be simulated is ...19080 .
The number of electrons per super-electron is ...   1.4e+10 .
The number of super-electrons is ...                0 .
The number of super-gas particles is ...            0 .

The time division is ...                            1.5e-11 s.
The current simulation time is ...                  0 s.
The head of the beam is at ...                      5.010204 m.
The number of time-steps to hit the target is ...   3868

Please enter in the number of time-steps you wish to simulate:
```

The first three lines inform the user that the environment, cross section and beam input files are being read; if the background gas density is zero, the cross section file is not read. The second two lines tell the user that the code is calling `IFC` and `LOAD` to initialize the fields and load the particles, using the information contained in `./input/beam.inp`. The next eight lines display the environment parameters, shown in figure (12). These are the length of the chamber, $L_c = 9\,m$; the axial grid division, $\Delta z = 6\,mm$; the location of the lens from the target, $L_f = 5\,m$; the radius of the chamber, $R_c = 30\,cm$; the radial grid division, $\Delta r = 8\,mm$; the number of radial grids, $N_r = R_c/\Delta r = 38$; the number of axial grids, $N_z = L_c/\Delta z = 1501$; and the axial grid location of the target, 331, so that the distance between the target and the left open end of the cylinder is $131 \times \Delta z \simeq 1.99\,m$, and the distance between the lens and the right open end is $\sim 2.01\,m$, both about twice the beam length. The next four lines display information about the beam. The mass of the beam ion, $m_b = 200.59\,amu$; the initial charge state of the beam ions, $q = 1$; the beam current, $I_b \simeq 4.3\,kA$; and the initial radius of the beam at its longitudinal mid-point, $a \simeq 10\,cm$. The next three lines display nformation about the background gas and electrons. The electron plasma frequency, ω_{pe}, is computed at the longitudinal mid-point of the beam, and is zero because no electrons have been generated yet; the mass of the background gas atoms, $m_g = 19\,amu$; and the density of the background gas, $n_g = 4 \times 10^{14}\ cm^{-3}$. The next five lines display the super particle information. The superparticle ratio for the beam ions, $\Delta N = 1.4 \times 10^{10}$; the number of super-beam ions, $\sum K_q = 19080$; the superparticle ratio for the electrons and background gas ions, which can be different from that used for the beam ions; and the number of super-electrons, K_e, and super-gas ions, K_g, both of which are zero. The next four lines display the time information. The size of the time-step, $\Delta t = 15\,ps$; the current simulation time, which is zero; the distance of the head of the beam from the target, $\sim 5.01\,m$, so that the beam is located $\sim 1\,cm$ behind the lens initially; and the number of time-steps it will take for the beam to hit the target, $N_t = 3868$. The last line asks the user to enter in the number of time-steps to simulate. If, as an example, we wish to run for 100 time-steps, then we would enter `100` in response; at the end of the "run", the code will display the following information:

```
Please enter in the number of time-steps you wish to simulate:
100
Running the simulation ...
Appending data to diagnostics output file:        ./output/diag.out

The average charge state per particle is ...      1.017453 .
The beam current is ...                           4380.012652 A.
The central radius of the beam is ...             0.0989736 m.

The electron plasma frequency is ...              0 rad/sec.
The number of electrons per super-electron is ... 1.4e+10 .
The number of super-electrons is ...              727 .
The number of super-gas particles is ...          394 .

The current simulation time is ...                1.5e-09 s.
The head of the beam is at ...                    4.868552 m.
The number of time-steps to hit the target is ... 3768

Please enter ...
c :  to print out data and continue simulating
e :  to end simulation and print out data
```

The first line informs the user that the simulation is running; the second line tells the user that the diagnostic information is being written to a file `diag.out` in the subdirectory `output`; we'll discuss the diagnostics in more detail later. The next three lines display updated beam information. The average charge-state of the beam, $\langle q\rangle \simeq 1.02$, indicating that some of the beam ions have been stripped to higher charge states; the current of the beam is now $I_b \simeq 4.4\,kA$, because of the higher charge state beam ions; and the radius of the beam at its longitudinal mid-point is slightly larger than it was before, indicating that this location in the beam has not passed through the lens yet, but has rather expanded due to the space-charge forces of the beam. The next four lines display updated information about the background gas and electrons. The electron plasma frequency at the longitudinal center of the beam is still zero; the super particle ratio for the electrons and background gas ions is $\Delta N = 1.4\times 10^{10}$; the number of super-electrons is now $K_e = 727$, and the number of super-gas ions is $K_g = 394$. The next three lines display the updated temporal information. The current simulation time is now $100\times\Delta t = 1.5\,ns$; the distance of the head of the beam from the target is $\sim 4.87\,m$, indicating that the head of the beam has now passed through the lens, located at $5\,m$, and is $\sim 13\,cm$ beyond it; and the number of time-steps it will take to hit the target is now $N_t = 3768$. Finally the code asks the user to decide either to continue or end the simulation. In both cases the output files `field.out`, `part.out`, `elec.out` and `gas.out` are written to the `output` subdirectory; if other, possibly old, files exist with these names they will be over-written. In the case where "e" is entered, these files are written and the simulation is ended:

```
Please enter ...
c :  to print out data and continue simulating
e :  to end simulation and print out data
e
The field output file is:       ./output/field.out
The particle output file is:    ./output/part.out
The electron output file is:    ./output/elec.out
The gas output file is:         ./output/gas.out
```

If "c" is entered, the files are written and the code asks the user to enter the number of time-steps to simulate, and then continues as before:

```
Please enter ...
c :  to print out data and continue simulating
e :  to end simulation and print out data
c
The field output file is:       ./output/field.out
The particle output file is:    ./output/part.out
The electron output file is:    ./output/elec.out
The gas output file is:         ./output/gas.out

Please enter in the number of time-steps you wish to simulate:
```

We now discuss what happens if we use the `-ni` command line option. In this case the code does not invoke the initialization module, and there is no need for the beam description file `beam.inp`; instead the field and particle information is "loaded" from four files located in the `input` subdirectory. These are `field.inp`, for the electric and magnetic field information, `part.inp`, `elec.inp` and `gas.inp` for the super-beam ion, super-electron and super-gas ion position and velocity information respectively; and are identical to the output files that the code writes with the same prefixes. It is necessary to run the code with this option if one wishes to restart a simulation that one has previously ended. One situation where this may need to be done is if one has to reduce the radial grid size, Δr, or the time division, Δt, or both in order to comply with the accuracy conditions discussed in previous sections. The code allows for Δt reductions by any amount, and Δr reductions by factors of two; the other parameters cannot be changed. The prescription for doing this is to run the simulation for the desired number of time-steps with a certain Δr and Δt. Then end the simulation; at which point the code will write the output files, `field.out`, `part.out`, `elec.out` and `gas.out`, to the `output` subdirectory. These output files should then be copied verbatim to the `input` subdirectory, and the suffixes changed from `out` to `inp`. Then Δr and Δt should be changed in the environment file, `geom.inp`, and finally the simulation should be restarted with the `-ni` option. For example after having ended the above simulation we can restart it with the following command line:

```
btrac -ni .
```

The code again takes its input from the current context, `./input` and will write its output to `./output`. The screen display will now read:

```
Reading in the chamber geometry from file:          ./input/geom.inp
Reading in the cross section data from file:        ./input/csec.inp
Reading in the initial fields from file:            ./input/field.inp
Reading in the initial particle data from file:     ./input/part.inp
Reading in the initial electron data from file:     ./input/elec.inp
Reading in the initial gas data from file:          ./input/gas.inp

The length of the chamber is ...                    9.000000 m.
The axial grid division is ...                      0.006 m.
The location of the thin lens is ...                5.000000 m.
The radius of the chamber is ...                    0.300000 m.
The radial grid division is ...                     0.004 m.

The number of radial grids is ...                   38
The number of axial grids is ...                    1501
The axial grid location of the target is ...        331

The mass of the beam ion is ...                     200.59 amu.
The average initial charge state per particle is ...1.017453 .
The beam current is ...                             4380.01 A.
The central radius of the beam is ...               0.0989736 m.
The central edge emittance of the beam is ...       1.92532e-05 m-rad.

The electron plasma frequency is ...                0 rad/sec.
The mass of the background gas is ...               19 amu.
The background gas density is ...                   4e+20 m-3.

The number of particles per super-particle is ...   1.4e+10 .
The number of super-beam ions to be simulated is ...19080 .
The number of electrons per super-electron is ...   1.4e+10 .
The number of super-electrons is ...                727 .
The number of super-gas particles is ...            394 .

The time division is ...                            1.0e-11 s.
The current simulation time is ...                  1.5e-09 s.
The head of the beam is at ...                      4.868552 m.
The number of time-steps to hit the target is ...   5652

Please enter in the number of time-steps you wish to simulate:
```

Notice that the code no longer requires the beam description file `beam.inp`; however, it does read in the field information file, `field.inp`, and the particle information files, `part.inp`, `elec.inp` and `gas.inp`. It also no longer calls `IFC` and `LOAD` to initialize the fields and particle positions and velocities. The radial grid division, Δr, has been halved from $8\,mm$ to $4\,mm$, and the time-step has been changed from $15\,ps$ to $10\,ps$; consequently the beam will now take $N_t = 5652$ time-steps to hit the target, rather than the 3768 time-steps it needed before. The rest of the display is identical to the case without the `-ni` option shown above; and the simulation proceeds as before.

A.2.2 Other Options

We now turn to the second command line option, `-nd`. This works in a similar manner as the `-ni` option, but controls the diagnostic module instead. Without this option, the diagnostic submodule, `DIAG`, is included in the time-step loop, after the `FVC` submodule as can be seen in figure (A.1). As mentioned above, `DIAG` computes, among other quantities, the plasma frequency and collision frequency, therefore not including the `-nd` option enables the code to warn the user about time-step violations of the accuracy conditions as they occur at every time-step, rather than just at the beginning of a "run". In addition the code will write an output file `diag.out` in the `output` subdirectory. Currently this file contains only the longitudinal postion of the mid-point of the beam with respect to the target, and the radius of the beam at this longitudinal mid-point at every time-step; however, the code can readily be modified to output other information as well. This file is continuously appended; that is, as long as there exists a file `diag.out` in the `output` subdirectory, the code will add new information to it, rather than overwrite it, as it does with the other output files. Including the `-nd` option bypasses this diagnostic submodule, enabling the simulation to run faster. But, the code will no longer have the capability to warn the user about the time-step accuracy condition violations during "run-time", however, it will still report on these at the beginning of a "run". Also the code will not write the output file `diag.out`.

Finally we discuss the `-rn #` command-line option. # is a negative integer used to seed the random number generator for evaluating the collisions between the beam ions and the background gas neutrals. For example `-rn -6785` sets the seed to -6785. This option is useful if the simulation is stopped and then restarted with the `-ni` option, because choosing a new seed number avoids repeating the same collisions as in the previous run. If this option is omitted the default seed is set to `-1`.

A.3 Input and Output Files

We now discuss the format for the various input and output files required by the code. The input files can be divided into two groups, the user generated files: `geom.inp`, `csec.inp` and `beam.inp`; and those supplied by the code: `field.inp`, `part.inp`, `elec.inp` and `gas.inp`. Also the output files can be divided into two categories, those that are always written by the code: `field.out`, `part.out`, `elec.out` and `gas.out`; and those that are controlled by the command line options: `diag.out`.

A.3.1 Input Files

We first look at the user generated input files, `geom.inp`, `csec.inp` and `beam.inp`. The first of these, the system file `geom.inp`, contains a description of the simulation environment:

```
length of chamber in m., axial grid division in m.:
9.00    6.0e-3
radius of chamber in m., radial grid division in m.:
0.30    8.0e-3
distance of the lens from the target in m.:
5.0
time division in sec.:
1.5e-11
gas mass in amu., background gas density in m^3.:
19.0    4e20
```

All units are in *mks*. The odd numbered lines are comments. The second line specifies the length of the chamber, $L_c = 9\,m$, and the axial grid division, $\Delta t = 6\,mm$; the fourth line specifies the radius of the chamber, $R_c = 30\,cm$, and the radial grid division, $\Delta r = 8\,mm$; the sixth line specifies the distance between the target and the lens, $L_f = 5\,m$; the eighth line gives the time division, $\Delta t = 15\,ps$; and the last line gives the mass of the background gas atoms, $m_b = 19\,amu$, and the density of the background gas, $n_g = 4 \times 10^{14}\,cm^{-3}$. The only restriction on the quantities in this file is that the length of the chamber, L_c, should be at least four beam lengths longer than the distance between the target and the lens, L_f; this allows for enough distance between the target and the left-open-end of the cylinder and the lens and the right-open-end as shown in figure (12). When Δr and Δt have to be reduced in order to comply with the accuracy conditions, this is the only file that needs to be modified.

The next input file is the cross section data file, `csec.inp`, which contains the cross section information for the stripping and ionization collisions between the beam ions and background gas neutrals:

```
beam ion atomic number, gas atomic number:
80    9
beam ion velocity in units of c.:
0.315000
ionization energy of background gas in units of eV:
18.670000
chg.  state, ioniz.  ene.  in eV, strip.  c.s., ioniz.  c.s.:
0     +5.700000e+00  +7.869267e+00  +3.771160e-01
1     +1.850000e+01  +2.944619e+00  +4.622557e-01
2     +3.480000e+01  +1.796774e+00  +3.475336e+00
3     +5.290000e+01  +1.302316e+00  +3.724983e+00
4     +7.110000e+01  +1.031858e+00  +4.071314e+00
5     +8.920000e+01  +8.572782e-01  +4.341163e+00
       .
       .
       .
78    +9.225000e+04  +6.854448e-06  +3.032494e+02
79    +9.389000e+04  +2.758458e-06  +3.055453e+02
80    +1.000000e+05  +0.000000e+00  +3.078498e+02
```

The first, third, fifth and seventh lines are comments. The second line specifies the atomic number of the beam ion, $Z_b = 80$, and the atomic number of the background gas atom, $Z_g = 9$; the fourth line gives the axial velocity of the beam ions, $\beta = 0.315$; the sixth line gives the ionization energy of the background gas neutral, $I_{g,0} = 18.67\, eV$; and the rest of the lines, starting with the eighth, give the charge state of the beam ion, q, the ionization energy of the beam ion in eV, $I_{b,q}$, the stripping and ionization cross sections in units of πa_0^2, $\sigma_{st,q}$ and $\sigma_{in,q}$ respectively, for every beam ion from charge state 0 to the maximum charge state. Notice that the ionization energy for the fully stripped beam ion, I_{b,Z_b}, is set to some "dummy" number that is larger than the largest ionization energy value, and that the stripping cross section, σ_{st,Z_b}, is zero.

The last user generated input file is the beam data file, `beam.inp`, which contains a description of the beam used to initialize the fields and load the super-beam ions:

```
length of beam in m., axial beam grid division in m.:
0.99    0.11
real charge/part., real mass/part.  in amu., part./superpart.:
1       200.59    1.4e+10
axial velocity in units of c.:
0.315
radius of beam in m., num.  of superpart., emit.  in m-rad.:
0.1     2120      1.93e-5
0.1     2120      1.93e-5
0.1     2120      1.93e-5
0.1     2120      1.93e-5
0.1     2120      1.93e-5
0.1     2120      1.93e-5
0.1     2120      1.93e-5
0.1     2120      1.93e-5
0.1     2120      1.93e-5
```

All units are in *mks*. The first, third, fifth and seventh lines are comments. The second line specifies the length of the beam, $L_b' = 99\, cm$, and the beam slice thickness, $\delta z' = 11\, cm$, in the frame of the beam, so that these quantities in the frame of the chamber are, $L_b = (L_b'/\gamma) \simeq 94\, cm$ and $\delta z = (\delta z'/\gamma) \simeq 10.4\, cm$; the fourth line gives the charge state of each beam ion in the beam, $q = 1$, the mass of the beam ion,

$m_b = 200.59\,amu$, and the beam ion superparticle ratio, $\Delta N = 1.4 \times 10^{10}$; the sixth line specifies the velocity of the beam, $\beta = 0.315$; and the remaining lines, starting with the eighth, give the beam radius, a_μ, number of super-beam ions, $K_{1,\mu}$, and the emittance, ϵ_μ, for each of the $\mu = L_b/\delta z = 9$ slices in the beam starting with the tail, or the end furthest away from the target, and ending with the head, so that the total number of superparticles is 19080. The restrictions on the quantities in this file are that the number of beam slices should be odd, and the number of super-beam ions in each slice should be even.

This is the extent of the input files that need to be supplied by the user. The other four input files, `field.inp`, `part.inp`, `elec.inp` and `gas.inp`, needed when the `-ni` option is used, are identical to their output counterparts with the same prefixes; indeed, it is imperative that these ouput files not be modified by the user if they are going to subsequently be used as inputs, but simply copied verbatim from the output files.

A.3.2 Output Files

We now turn to the output files; we first look at the mandatory files `field.out`, `part.out`, `elec.out` and `gas.out`. The first of these, `field.out`, contains the electric and magnetic fields on the spatial grid:

```
current time in sec.:
1.500000e-09
radial grid division in m.:
8.000000e-03
the axial grid location of the target:
331
fields in mks (format:  j k Er Ez Bt):
1     1     +0.000000e+00  +0.000000e+00  +0.000000e+00
1     2     +0.000000e+00  +0.000000e+00  +0.000000e+00
1     3     +0.000000e+00  +0.000000e+00  +0.000000e+00
1     4     +0.000000e+00  +0.000000e+00  +0.000000e+00
```

```
1      5      +0.000000e+00  +0.000000e+00  +0.000000e+00
       .
       .
       .
15     1240   +7.392719e+06  +9.680006e+04  -7.696454e-03
15     1241   +7.294208e+06  +1.379422e+05  -8.138589e-03
15     1242   +7.362822e+06  +1.493052e+05  -7.967273e-03
15     1243   +7.385347e+06  +1.435686e+05  -8.354462e-03
15     1244   +7.495720e+06  +2.827732e+05  -7.816303e-03
15     1245   +7.338789e+06  +3.121824e+05  -7.528567e-03
       .
       .
       .
38     1500   +1.226347e+02  +0.000000e+00  -1.558121e-07
38     1501   +1.357009e+02  +0.000000e+00  -5.424388e-07
```

All units are in *mks*. The first, third, fifth and seventh lines are comments. The second line denotes the simulation time at which this file was written, $1.5\,ns$; the fourth line gives the radial grid division, $\Delta r = 8\,mm$; the sixth line gives the axial grid location of the target from the left-open-end, so that the distance between this open-end of the chamber and the target is $331 \times \Delta z \simeq 1.99\,m$; the remaining lines, starting with the eighth, give the grid location, j, k, the radial and axial electric fields, $E_{r,j-1/2,k}$ and $E_{z,j,k+1/2}$, and the azimuthal magnetic field, $B_{\theta,j-1/2,k+1/2}$, for each mesh point shown on the grid in figure (16); where $j=1$ is the grid on the axis, so that the radius $r_{j-1/2}(j=1)=0$; $j=N_r$ is the grid on the conducting wall of the chamber, so that $r_j(j=N_r)=R_c$; and $k=1$ and $k=N_z$ are the left and right open-ends of the chamber respectively.

The next output file is `part.out`, which contains the positions and velocities of the super-beam ions:

```
current time in sec.:
1.500000e-09
real mass/part.  in amu.:
200.590000
part./superpart., num.  of superpart.:
1.400000e+10    19080
axial velocity in units of c.:
0.315000
```

```
particle data in mks (format:  n zp r z vr vt):
1      +1    +6.945126e-02  +4.911978e+00  -1.344088e+06  -7.167006e+03
2      +1    +6.948343e-02  +4.911978e+00  -1.322728e+06  +7.163688e+03
3      +1    +4.949950e-02  +4.947517e+00  -9.276196e+05  +2.958040e+03
4      +1    +4.945327e-02  +4.947517e+00  -9.580874e+05  -2.960805e+03
5      +1    +8.602024e-02  +4.965685e+00  -1.626359e+06  -6.131794e+03
       .
       .
       .
19079  +1    +3.754831e-02  +5.772310e+00  -1.068042e+04  +1.229267e+04
19080  +1    +3.758308e-02  +5.772310e+00  +1.250028e+04  -1.228130e+04
```

Again all units are in *mks*. The first, third, fifth, seventh and ninth lines are comments. The second line denotes the simulation time at which the file was written, 1.5 *ns*; the fourth line gives the mass of the beam ion, $m_b = 200.59\,amu$; the sixth line gives the superparticle ratio for the beam ions, $\Delta N = 1.4\times 10^{10}$, and the number of super-beam ions, $\sum K_q = 19080$; the eighth line gives the axial velocity of the beam ions, $v_z = 0.315c$; the remaining lines, starting with the tenth, list the superparticle number, p, followed by the charge state, q, the radial and axial positions, $r_{q,p}$ and $z_{q,p}$, and the radial and azimuthal velocities, $v_{r,q,p}$ and $v_{\theta,q,p}$, for all the super-beam ions.

The next output file is `elec.out`, which contains the positions and velocities of the super-electrons:

```
current time in sec.:
1.500000e-09
superparticle ratio, number of superelectrons.:
1    728
electron data in mks (format:  n r z vr vt vz gamma):
1    +8.466111e-02  +4.982641e+00
     -1.236253e+07  -5.598579e+05  -6.443189e+03  +1.000853e+00
2    +9.353555e-02  +4.993478e+00
     -1.728865e+07  +6.910066e+06  -9.505799e+07  +1.056676e+00
3    +9.353555e-02  +4.993478e+00
     -2.132151e+07  -1.143232e+06  -8.041249e+05  +1.002550e+00
4    +8.638089e-02  +4.939313e+00
     -1.486332e+07  +9.665768e+05  -9.247005e+07  +1.052695e+00
5    +8.638089e-02  +4.939313e+00
     -1.978246e+07  -1.184661e+05  +2.268508e+06  +1.002213e+00
     .
```

```
        .
        .
727  +8.272075e-02  +5.110175e+00
     +2.425506e+07  -7.121247e+05  +1.847665e+08  +1.276602e+00
728  +7.931396e-02  +5.171986e+00
     +1.631678e+07  -1.302135e+06  +2.275511e+08  +1.541393e+00
```

Again all units are in *mks*. The first, third and fifth lines are comments. The second line denotes the simulation time at which the file was written, 1.5 *ns*; the fourth line gives the super-electron ratio in terms of the super-beam ion ratio in the `part.out` file; in the sixth line of that file the super-beam ion ratio was listed as $\Delta N = 1.4 \times 10^{10}$, so that the super-electron ratio is also 1.4×10^{10}, and the number of super-electrons, $K_e = 728$; the remaining lines, starting with the sixth, list the super-electron number, p, followed by the radial and axial positions, $r_{e,p}$ and $z_{e,p}$, the radial, azimuthal and axial velocities, $v_{r,e,p}$, $v_{\theta,e,p}$ and $v_{z,e,p}$, and the relativistic factor, $\gamma_{e,p}$, for all the super-electrons. Although these lines are shown as split lines, they are single lines in the file.

Finally the last mandatory output file is `gas.out`, which contains the positions and velocities of the super-gas ions:

```
current time in sec.:
1.500000e-09
mass of the gas particle in amu.:
19.000000
superparticle ratio, number of supergasions.:
1   406
gas data in mks (format:  n r z vr vz):
1      +8.466111e-02  +4.982641e+00  +3.893040e+02  +3.826877e+00
2      +9.353555e-02  +4.993478e+00  +4.423860e+02  +3.251314e+01
3      +8.638089e-02  +4.939313e+00  +4.192890e+02  -5.807550e+01
4      +2.705703e-02  +4.937905e+00  +2.971518e+01  -1.045548e+00
5      +7.388687e-02  +4.903455e+00  +3.005444e+02  -1.845459e+02
       .
       .
       .
405    +9.181947e-02  +4.995520e+00  +3.223086e+04  -3.221249e+03
406    +8.761122e-02  +4.998939e+00  +3.016384e+04  -1.348608e+03
```

All units are in *mks*. The first, third, fifth and seventh lines are comments. The second line denotes the simulation time at which the file was written, $1.5\,ns$; the fourth line specifies the mass of the gas atom, $m_g = 19\,amu$; the sixth line gives the super-gas ion ratio in terms of the super-beam ion ratio, similar to the fourth line in the `elec.out` file, so that the super-gas ion ratio is the same as the super-beam ion ratio, and the number of super-gas ions, $K_g = 406$; the remaining lines, starting with the eighth, list the super-gas ion number, p, followed by the radial and axial positions, $r_{g,p}$ and $z_{g,p}$, and the radial and axial velocities, $v_{r,g,p}$ and $v_{z,g,p}$, for all super-gas ions.

This concludes a description of the output files that are always written by the code. The diagnostic output file, `diag.out`, is only written if the code is run without the `-nd` option. The format for this file is:

```
current time in sec.:
0.000000e+00
mid-location (m), avg.  chg.,radius (cm), rms radius (cm)
+5.479623    1.000000    9.896930e+00    6.818661e+00
+5.478206    1.000000    9.896931e+00    6.818661e+00
+5.476790    1.000000    9.896931e+00    6.818661e+00
+5.475373    1.000000    9.896932e+00    6.818661e+00
+5.473957    1.000000    9.896933e+00    6.818661e+00
                 .
                 .
                 .
+5.339388    1.109958    9.897351e+00    6.818905e+00
+5.337971    1.112579    9.897359e+00    6.818910e+00
```

The first and third lines are comments. The second line displays the time at which the present simulation run was started, 0, this is different from the time displayed in the other output files, which is the time at which the simulation run ended, or when those output files were written; the remaining lines, starting with the fourth, give the location of the longitudinal mid-point of the beam with respect to the target in m, the average charge state of the beam, $\langle q \rangle$, the radius of the beam at this point, a, in *cm*, and the *rms* radius, $\sqrt{\langle r^2 \rangle}$, in *cm*. Notice that the head of a beam of length $L_b \simeq 94\,cm$ starts $\sim 1\,cm$ behind the lens located $5\,m$ from the target, and then moves through the lens towards the target, i.e. the location of the mid-point decreases, and the radius expands due to the space-charge forces of the beam; after this mid-point passes through the lens, then the radius will start to decrease. At the end of this run, the beam has moved a distance of $\sim 14\,cm$, signifying a simulation run of 100 time-steps at $\Delta t = 15\,ps$ for a beam with velocity $\beta = 0.315$. Currently these are the only four quantities written to this file; however, the code can be readily modified to print out other information if needed.

A.4 Warning and Error Messages

The code has several error and warning messages. The distinction between these two is as follows: error messages will abruptly terminate the simulation at the point at which the error occurs, without regard to saving the current state of the system; warning messages on the other hand ask the user if they wish to continue the simulation or end it, if the user chooses to end the simulation, all output files with the current state of the simulation, `field.out`, `part.out`, `elec.out` and `gas.out`, are written, and then the simulation is ended.

A.4.1 Error Messages

There are two types of error messages, those that occur before the simulation starts, and those that take place during the simulation. The former are generally a result of checking the validity of the quantities in the input files, for instance the simulation times in all the input files should match, and as such are recoverable in that one simply has to fix the error and attempt the simulation again. One error of this type worth mentioning is the CFL time limit; in this case the error message display may read:

```
*** ERROR
*** The time-step in the geometry file must be less than the CFL limit
    5.000000e-12 s.
*** Terminating the simulation
```

In this example the time-step chosen, $\Delta t = 5\,ps$, violates the CFL limit and must be reduced in the `geom.inp` file before the simulation is attempted again.

The second type of error, the one that occurs during the simulation, is catastrophic in that all information about the present run is lost and none of the output files are written. These are generally a result of memory allocation problems. The only error of this type that is not a memory problem occurs when the beam ions start to hit the conducting wall of the chamber; the error message display reads:

```
*** ERROR
*** Ions are hitting the wall
*** Terminating the simulation
```

In this case the chamber radius, R_c, is too small. Since this quantity cannot be changed in the middle of a run, the entire simulation will have to be redone with a larger radius.

A.4.2 Warning Messages

There are only two warning messages, and both of these have to do with time-step accuracy conditions; the first concerns the electron plasma frequency, and the second concerns the collision frequency. If they occur before the simulation starts, the user can choose to ignore them, and enter in the number of time-steps to simulate, or can reduce the time-division, Δt, in the `geom.inp` file and attempt the simulation again.

If the `-nd` option is not used then the code will also report these warning messages during the simulation:

```
*** WARNING
*** The time-step must be less than the plasma frequency limit
    5.000000e-12 s.
The current simulation time is    1.500000e-09 s.
Please enter ...
c :  to print out data and continue simulating
e :  to end simulation and print out data
```

and

```
*** WARNING
*** The time-step must be less than the collision frequency limit
    5.000000e-12 s.
The current simulation time is    1.500000e-09 s.
Please enter ...
c :  to print out data and continue simulating
e :  to end simulation and print out data
```

In this case the user is asked if the simulation should continue or end; if the user chooses to continue the simulation, the warning messages will not be repeated for the rest of the run; if the user chooses to end the simulation then the appropriate output files are written and the simulation is ended. If the `-nd` option is used then these warning messages will not occur during the simulation, but only at the start and finish of a particular run.